

FILE COPY

4

NUSC Technical Document 6712
15 July 1988

Fluctuating Wall Pressure and Vibratory Response of a Cylindrical Elastic Shell Due to Confined Jet Excitations

K. W. Ng
Launcher and Missile Systems Department

AD-A199 528



Navai Underwater Systems Center
Newport, Rhode Island / New London, Connecticut

DTIC
SELECTED
OCT 1 1 1988
S H D

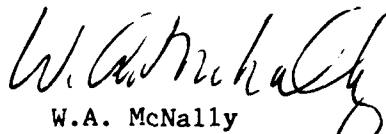
Approved for public release;
distribution is unlimited.

8

PREFACE

This document represents the author's doctoral dissertation submitted for the degree of Doctor of Philosophy in Mechanical Engineering from the University of Rhode Island. This study was partially funded by the Office of Naval Technology (ONT) and the NUSC IR/IED program.

REVIEWED AND APPROVED: 15 JULY 1988

A handwritten signature in dark ink, appearing to read 'W.A. McNally', is positioned above the printed name.

W.A. McNally
Head, Launcher & Missile Systems Department

REPORT DOCUMENTATION PAGE

1a. REPORT SECURITY CLASSIFICATION UNCLASSIFIED			1b. RESTRICTIVE MARKINGS		
2a. SECURITY CLASSIFICATION AUTHORITY			3. DISTRIBUTION/AVAILABILITY OF REPORT Approved for public release; distribution is unlimited.		
2b. DECLASSIFICATION/DOWNGRADING SCHEDULE			5. MONITORING ORGANIZATION REPORT NUMBER(S)		
4. PERFORMING ORGANIZATION REPORT NUMBER(S) TD 6712			7a. NAME OF MONITORING ORGANIZATION		
6a. NAME OF PERFORMING ORGANIZATION Naval Underwater Systems Center		6b. OFFICE SYMBOL (If applicable) Code 8322	7b. ADDRESS (City, State, and ZIP Code)		
6c. ADDRESS (City, State, and ZIP Code) Newport Laboratory Newport, RI 02841-5047		9. PROCUREMENT INSTRUMENT IDENTIFICATION NUMBER			
8a. NAME OF FUNDING/SPONSORING ORGANIZATION Office of Naval Technology		8b. OFFICE SYMBOL (If applicable) OCNR-20	10. SOURCE OF FUNDING NUMBERS		
8c. ADDRESS (City, State, and ZIP Code) Washington, DC 20362		PROGRAM ELEMENT NO	PROJECT NO	TASK NO	WORK UNIT ACCESSION NO
11. TITLE (Include Security Classification) FLUCTUATING WALL PRESSURE AND VIBRATORY RESPONSE OF A CYLINDRICAL ELASTIC SHELL DUE TO CONFINED JET EXCITATIONS					
12. PERSONAL AUTHOR(S) K.W. Ng					
13a. TYPE OF REPORT Final	13b. TIME COVERED FROM TO	14. DATE OF REPORT (Year, Month, Day) 88-07-15	15. PAGE COUNT 246		
16. SUPPLEMENTARY NOTATION					
17. COSATI CODES			18. SUBJECT TERMS (Continue on reverse if necessary and identify by block number)		
FIELD	GROUP	SUB-GROUP	Coherent Structures		
			Flow-induced Noise		
			LDV Measurements		
			Turbulence Calculations		
			Cavitation Noise		
			Confined Jet Flows		
19. ABSTRACT (Continue on reverse if necessary and identify by block number) A theoretical and experimental study was conducted to investigate the flow-induced noise and vibration caused by confined jet flows in a cylindrical duct. Unrestricted pipe flow and flows restricted by various orifices were tested for a wide range of velocities to simulate the flow in piping systems. Wall pressure data showed that the noise levels vary with the pipe's axial location, and the peak noise is located near the end of the jet potential core. A non-dimensional wall pressure spectrum was established for the various confined jets by the Strouhal relationship, where the length scale is the jet hydraulic diameter. This jet pressure spectrum agrees with the wall pressure spectrum of a turbulent boundary layer above a rigid plane. Correlations of wall pressure fluctuations and pipe wall acceleration signals showed that jet flows generate more deterministic features than pipe flow. The coherent functions of the wall pressure and pipe wall acceleration signals are relatively high near the exit of the jet. The high coherence is probably due to the					
20. DISTRIBUTION/AVAILABILITY OF ABSTRACT <input type="checkbox"/> UNCLASSIFIED/UNLIMITED <input checked="" type="checkbox"/> SAME AS RPT <input type="checkbox"/> DTIC USERS			21. ABSTRACT SECURITY CLASSIFICATION UNCLASSIFIED		
22a. NAME OF RESPONSIBLE INDIVIDUAL K.W. Ng			22b. TELEPHONE (include Area Code) (401)841-1908	22c. OFFICE SYMBOL Code 8322	

19. ABSTRACT (Cont'd)

large-scale coherent structures.

An analytical model was developed to study the effect of the turbulent jet flow field on the wall pressure and vibratory motion of the duct wall. Based on flow field measurements, the blocked surface pressure was calculated using Lighthill's method, and then used to drive the fluid-filled shell. The wall pressure and pipe wall acceleration were determined by solving the coupled fluid-solid interaction problem. The wall pressure was obtained by summing the blocked surface pressure and the pressure due to the wall vibration. An amplitude modulated convecting wave field was used to simulate the moving acoustic sources of the jet. The random nature of the turbulent jet was incorporated into the analytical model. Specifically, the acoustic pressure was assumed to result from hydrodynamic pressure fluctuations, which are uncorrelated in the radial direction, but are correlated in the axial direction near the jet exit.

Analytical and experimental results for wall pressure and acceleration then were compared for a wide range of parameters of interest. Results from comparisons showed reasonably good agreement.



Accession For	
NTIS GRA&I	<input checked="checked" type="checkbox"/>
DTIC TAB	<input type="checkbox"/>
Unannounced	<input type="checkbox"/>
Justification	
Ex-	
Description of	
Distribution	
Notes	
A-1	

TABLE OF CONTENTS

	Page
LIST OF ILLUSTRATIONS	iv
LIST OF TABLES	xi
LIST OF SYMBOLS	xii
ACKNOWLEDGEMENTS	xvi
CHAPTER 1. INTRODUCTION	
1. Overview	1
2. Statement of the Problem	2
3. Organization of Dissertation	3
CHAPTER 2. LITERATURE REVIEW	
1. Flow and Acoustic Characteristics of Free-Jet and External Flows	5
2. Shell Vibration	8
3. Flow and Acoustic Measurements	10
4. Coherent Structures	12
5. Confined Jet Flow-Induced Noise	14
CHAPTER 3. THEORETICAL DEVELOPMENT	
1. Introduction	16
2. Near-Field Jet Noise and Blocked Surface Pressure	17
3. Vibratory Response and Pressure Field	22
a. Forced Vibration in Shell	22
b. Pipe Wall Pressure Fluctuations	25
4. Wall Pressure Fluctuations and Forced Vibration in Shell Excited by Random Sources	28

TABLE OF CONTENTS (Cont'd)

	Page
5. Special Case	30
a. Deterministic Approach	31
b. Statistical Approach	32
CHAPTER 4. DESCRIPTION OF EXPERIMENTS	
1. Experimental Data Requirements	37
2. NUSC Acoustic Water Tunnel	38
a. Test Program	38
b. Test Configurations	39
c. Flow Measurement - Mean Velocity Profile	40
d. Acoustic Instrumentation - Wall Pressure Transducers and Accelerometers	41
3. NUSC Flow Loop Facility	42
a. Test Program	42
b. Test Configurations	43
c. Flow Measurements - LDV	44
d. Acoustic Instrumentation - Wall Pressure Transducers and Accelerometers	45
4. Data Reduction	47
CHAPTER 5. EXPERIMENTAL RESULTS AND DISCUSSION	
1. Flow Characteristics	63
2. Acoustic Characteristics	67
3. Vibrational Characteristics	77
4. Effects of Area Ratio, Plate Thickness, and Sharpness	79
5. Measurement Accuracy Summary	80

TABLE OF CONTENTS (Cont'd)

	Page
CHAPTER 6. ANALYSIS AND NUMERICAL RESULTS	
1. Fluid-Filled Shell Vibration	146
2. Near-Field Jet Noise and Blocked Surface Pressure	147
3. Fluid-Coupled Shell Vibration	
with Confined Jet Excitation	151
4. Pipe Wall Pressure due to Flexible Wall Vibration	154
5. Comparison with Experimental Data -	
Jet Flow and Pipe Flow	154
CHAPTER 7. CONCLUSIONS AND RECOMMENDATIONS	190
APPENDIX A. FORMULATION OF THE BLOCKED EXCITATION PRESSURE	A-1
APPENDIX B. EXPERIMENTAL EQUIPMENT	B-1
APPENDIX C. LDV DATA ACQUISITION AND REDUCTION	
1. Instrumentation and Test Procedure	C-1
2. Data Acquisition and Reduction	C-2
APPENDIX D. SUMMARY OF THE FLOW CALCULATIONS USING THE	
K and ϵ MODEL	D-1
BIBLIOGRAPHY	R-1

LIST OF ILLUSTRATIONS

Figure	Page
1-1 Schematic of Present Study	5
3-1 Development of Confined Jet	34
3-2 Noise Model for Fluid-Filled Shell Vibration Excited by a Confined Jet	35
3-3 Coordinate System of the Shell Vibration Problem	36
3-4 Triangular Blocked Pressure Distribution	36
4-1 NUSC Acoustic Water Tunnel	49
4-2 Experimental Setup for Impact Test - Phase I	50
4-3 Photograph of Flow Restrictors - Phase I	51
4-4 Geometry of Flow Restrictors - Phase I	52
4-5 Test Section Instrumentation - Phase I	53
4-6 Data Acquisition System - Phase I	54
4-7 NUSC Flow Loop Facility	55
4-8 Photograph of Flow Restrictors - Phase II	56
4-9 Geometry of Flow Restrictors - Phase II	57
4-10 Photograph of Test Section with Instrumentation	59
4-11 Test Section Instrumentation - Phase II	60
4-12 Details of Hydrophone Attachment	61
4-13 Data Acquisition System - Phase II	62
5-1 Velocity Profiles for Pipe Flow, Circular, Square, and Multiple Circular Jets	82
5-2 Comparison of Pipe Flow Velocity Profile - Data vs Numerical Calculation	83
5-3 Comparison of Circular Jet Velocity Profile - Data vs Numerical Calculation	83
5-4 Streamlines of Recirculation Region	84

LIST OF ILLUSTRATIONS (Cont'd)

Figure	Page
5-5 Comparison of Pipe Flow Velocity Profile with Laufer's Data	84
5-6 Velocity Profiles for Jets at $x = 8.4$ cm	85
5-7 Velocity Profiles for Jets at $x = 14.5$ cm	86
5-8 Velocity Profiles for Jets at $x = 26.2$ cm	87
5-9 Velocity Profiles for Pipe Flow and Far-downstream Jet Flow	88
5-10 Comparison of Pipe Flow Velocity Profile - Data vs Calculation	89
5-11 Comparison of Jet Flow Velocity Profile - Data vs Calculation	89
5-12 Turbulence Intensities of Jet Flow	90
5-13 Turbulence Intensities of Pipe Flow	91
5-14 Skewness of Velocity - Pipe Flow	92
5-15 Flatness Factor- Pipe Flow	93
5-16 Skewness of Velocity - Jet Flow	94
5-17 Flatness Factor - Jet Flow	95
5-18 Velocities, Velocity Fluctuations, Reynolds Stress, and Intensities vs Time	96
5-19 Distribution Function of Axial Velocity	97
5-20 Distribution Function of Radial Velocity	98
5-21 Frequency Spectrum of Axial Velocity	99
5-22 Frequency Spectrum of Radial Velocity	100
5-23 Noise vs Location for Flow Restrictors	101
5-24 Noise vs Location for Pipe Flow	102

LIST OF ILLUSTRATIONS (Cont'd)

Figure	Page
5-25 Correlations of Noise with Velocity	103
5-26 Velocity Exponents for Flow Restrictors	104
5-27 Noise Spectra of Pipe Flow and Circular Jet Flow	105
5-28 Non-dimensional Noise Spectra of Circular Jet Flow	106
5-29 Non-dimensional Noise Spectra of Coannular Jet Flow	107
5-30 Non-dimensional Noise Spectra of Various Flow Restrictors	108
5-31 Transfer Functions of Hydrophone Signals for Pipe Flow	109
5-32 Transfer Functions of Hydrophone Signals for Circular Jet Flow	110
5-33 Transfer Functions of Accelerometers vs Hydrophone Signals for 3:1 Rectangular Jet	111
5-34 Coherence Functions of Hydrophone Signals for Pipe Flow	112
5-35 Coherence Functions of Hydrophone Signals for Circular Jet Flow	113
5-36 Pipe Wall Acceleration Measurement from Acoustic Checkout	114
5-37 Time History of Hydrophone Signals - 1.25-Inch Jet	115
5-38a OASPL vs Location - 0.625-Inch Jet	116
5-38b OASPL vs Location - 0.75-Inch Jet	116
5-38c OASPL vs Location - 1.00-Inch Jet	117
5-38d OASPL vs Location - 1.25-Inch Jet	117
5-38e OASPL vs Location - 1.25-Inch Thin Plate	118
5-38f OASPL vs Location - 1.25-Inch Bevel Plate	118

LIST OF ILLUSTRATIONS (Cont'd)

Figure	Page
5-38g OASPL vs Location - 1.50-Inch Jet	119
5-38h OASPL vs Location - Pipe Flow	119
5-39 Noise vs Location of Circular Jet - Phase I	120
5-40a OASPL vs Velocity - Pipe Flow, 1.25-Inch Thin Plate, 1.25-Inch Bevel Edge Plate	121
5-40b OASPL vs Velocity - 0.625, 0.75, 1.00, 1.50-Inch Jets . . .	122
5-41 Velocity Exponents for Confined Jets	123
5-42a Normalized Noise Spectra - 0.625-Inch Jet	124
5-42b Normalized Noise Spectra - 0.75-Inch Jet	124
5-42c Normalized Noise Spectra - 1.00-Inch Jet	125
5-42d Normalized Noise Spectra - 1.25-Inch Thin Plate	125
5-42e Normalized Noise Spectra - 1.25-Inch Bevel Plate	126
5-42f Normalized Noise Spectra - 1.50-Inch Jet	126
5-43 Normalized Noise Spectra Comparison	127
5-44a Noise Spectra of Cavitating Jet - 0.625-Inch Jet	128
5-44b Noise Spectra of Cavitating Jet - 0.75-Inch Jet	128
5-45a Coherence Function u vs H3 - 0.625-Inch Jet	129
5-45b Coherence Function v vs A3 - 0.625-Inch Jet	129
5-46a Coherence Function u vs H3 - Pipe Flow	130
5-46b Coherence Function v vs A3 - Pipe Flow	130
5-47a Coherence Function H1 vs H3 - 0.625-Inch Jet	131
5-47b Coherence Function H3 vs H5 - 0.625-Inch Jet	131
5-47c Coherence Function H5 vs H7 - 0.625-Inch Jet	132
5-47d Coherence Function H1 vs H5 - 0.625-Inch Jet	132
5-47e Coherence Function H1 vs H7 - 0.625-Inch Jet	133
5-48a Coherence Function H1 vs H3 - Pipe Flow	133

LIST OF ILLUSTRATIONS (Cont'd)

Figure	Page
5-48b Coherence Function H3 vs H5 - Pipe Flow	134
5-48c Coherence Function H5 vs H7 - Pipe Flow	134
5-49 RMS Acceleration Spectra with Impact at $x = 0$ cm	135
5-50 Transfer Functions of Accelerometer Signals with Impact at $x = 0$ cm	136
5-51 Coherence Functions of Accelerometer Signals with Impact at $x = 0$ cm	137
5-52 Pipe Wall Acceleration Spectrum - 0.625-Inch Jet	138
5-53a Coherence Function A1 vs A3 - 0.625-Inch Jet	139
5-53b Coherence Function A3 vs A5 - 0.625-Inch Jet	139
5-54 Coherence Function A3 vs A5 - Pipe Flow	140
5-55a Coherence Function H3 vs A3 - 0.625-Inch Jet	141
5-55b Coherence Function H5 vs A5 - 0.625-Inch Jet	141
5-66a Coherence Function H3 vs A3 - Pipe Flow	142
5-66b Coherence Function H5 vs A5 - Pipe Flow	142
5-57 Velocity Profiles - 1.25-Inch Plate with and without Bevel Edge	143
5-58 Velocity Profiles - 1.25-Inch Thin Plate vs Bevel Edge Plate	144
5-59 Overall Acceleration Level vs Velocity	145
6-1 Dispersion Curve for Free Shell Vibration - Axisymmetric Mode $n = 0$	157
6-2 Velocity Components u , u' , $2u'U$ vs Time	158
6-3a Velocity Data without Interpolation	159
6-3b Velocity Data with Interpolation	159
6-4a Velocity Spectrum without Interpolation	160

LIST OF ILLUSTRATIONS (Cont'd)

Figure	Page
6-4b Velocity Spectrum with Interpolation	160
6-5a Weighting Function - 10 Terms	161
6-5b Weighting Function - 15 Terms	161
6-5c Weighting Function - 20 Terms	162
6-5d Weighting Function - 32 Terms	162
6-5e Weighting Function - 50 Terms	163
6-6a Weighting Function - $x/R = 0.0$	164
6-6b Weighting Function - $x/R = 0.02$	164
6-6c Weighting Function - $x/R = 0.04$	165
6-6d Weighting Function - $x/R = 0.08$	165
6-7 Division of Annular Bands	166
6-8a Magnitude and Phase of $2u/U$ for 0.625-Inch Jet at $x = 0$ cm	167
6-8b Magnitude and Phase of $2u/U$ for 0.625-Inch Jet at $x = 0.25$ cm	168
6-9 Blocked Surface Pressure for 0.625-Inch Jet	169
6-10 Blocked Surface Pressure for Pipe Flow	170
6-11 Blocked Surface Pressure vs Location	171
6-12 Triangular Blocked Pressure Distribution	172
6-13 Wall Acceleration vs Location	172
6-14 Wall Acceleration Spectrum for 0.625-Inch Jet (Deterministic Approach)	173
6-15 Wall Acceleration Spectrum for Pipe Flow (Deterministic Approach)	174
6-16 Wall Acceleration Spectrum for 0.625-Inch Jet (Statistical Approach)	175

LIST OF ILLUSTRATIONS (Cont'd)

Figure	Page
6-17 Wall Acceleration Spectrum for Pipe Flow (Statistical Approach)	176
6-18 Flexible Wall Pressure Spectrum	177
6-19 Wall Pressure Spectra Comparison - 0.625-Inch Jet (Deterministic Approach)	178
6-20 Wall Pressure Spectra Comparison - 1.00-Inch Jet (Deterministic Approach)	179
6-21 Wall Pressure Spectra Comparison - Pipe Flow	180
6-22 Wall Pressure Spectra Comparison - 0.625-Inch Jet.	181
6-23 Wall Pressure Spectra Comparison - 0.75-Inch Jet	182
6-24 Wall Pressure Spectra Comparison - 1.00-Inch Jet	183
6-25 Wall Pressure Spectra Comparison - 1.50-Inch Jet	184
6-26 Wall Pressure Spectra Comparison - 0.625-Inch Jet	185
6-27 Wall Acceleration Spectrum for 0.75-Inch Jet	186
6-28 Wall Acceleration Spectrum for 1.00-Inch Jet	187
6-29 Wall Acceleration Spectrum for 1.50-Inch Jet	188
6-30 Wall Acceleration Spectrum for 0.625-Inch Jet	189
A-1 Distribution of Blocked Excitation Pressure	A-3
A-2 Transformation of $f_2(x)$ to $f_1(x)$	A-4
A-3 Special Case - Triangular Blocked Pressure Distribution . .	A-5
A-4 Representation of $f_1(x)$	A-6
C-1 Schematic of Laser Doppler Velocimeter	C-4

LIST OF TABLES

Table	Page
4-1 Test Conditions - Phase I	39
4-2 Geometry of Flow Restrictors - Phase I	40
4-3 Location of Hydrophones and Accelerometers - Phase I	41
4-4 Test Matrix of Phase II	43
4-5 Geometry of Flow Restrictors - Phase II	44
4-6 Location of Hydrophones and Accelerometers - Phase II	47
5-1 Values of Velocity Exponents for Flow Restrictors - Phase I	68
5-2 Values of Velocity Exponents - Phase II	74
5-3 Summary of Measurement Accuracy	81
6-1 Material Properties for Numerical Calculations	147
B-1 List of Instrumentation - Phase I	B-1
B-2 List of Instrumentation - Phase II	B-2

LIST OF SYMBOLS

A_o	constant
a	mean radius of shell
C_1	constant
C_2	constant
C_d	flow discharge coefficient
C_u	constant
c_f	sound speed in the fluid
c_l	extensional phase speed of the shell material
D	pipe diameter
d	jet diameter
d_f	fringe spacing
F_o	unit force
f	frequency
f_D	frequency of laser light intensity
G	Green's function / generation term in K and ϵ equation
g_c	gravitational constant
H_{ij}	velocity source term in equation (9)
h	thickness of shell
J	Bessel function
j	$\sqrt{-1}$
K	turbulence energy
k	wavenumber / constant
k_c	convective wavenumber = ω/V_c
k_r	radial wavenumber
k_s^r	non-dimensional radial wavenumber
k_u	convective wavenumber = $\omega/V_c + k_{ns}$

LIST OF SYMBOLS (Cont'd)

L	half width of the triangular pressure distribution
L_{ij}	elements of operator in shell vibration equation
M_{ij}	velocity source term in equation (5)
m_s	mass density of shell
n	structural mode
P	mean pressure
P_o	magnitude of blocked pressure
p	instantaneous pressure / flexible wall pressure
p_a	acoustic pressure
p_b	blocked surface pressure
p_r	pressure excitation in the r direction
p'	pressure fluctuations
r	radial location / radius of orifice
R	radius of pipe
St	Strouhal number
S_ϕ	source term
s	source due to velocity fluctuations
t	time
U	displacement in axial direction / mean velocity in axial direction
U_i	velocity component perpendicular to the optical axis
u	instantaneous velocity in axial direction
u'	velocity fluctuation in axial direction
u^+	normalized velocity, $u^+ = u/u^*$
u^*	friction velocity
V	wall displacement in circumferential direction / mean velocity in radial direction

LIST OF SYMBOLS (Cont'd)

V_c	convection velocity
V_j	jet velocity
v	instantaneous velocity in radial direction
v'	velocity fluctuation in radial direction
W	wall displacement in radial direction
\dot{W}	wall velocity in radial direction
\ddot{W}	wall acceleration in radial direction
x	axial location
Y	transfer mobility
y^+	normalized parameter in appendix D

Subscripts

f	fluid
i	index = 1, 2, 3
j	index = 1, 2, 3
n	radial mode number / order of Bessel function
s	structure / branch number

Greek Letters

β	thickness parameter, $\beta^2 = h^2/12a^2$
	orifice to pipe radius ratio, $\beta = r/R$
Γ_ϕ	diffusivity constant
γ^2	coherence function
δ_{ij}	Kronecker delta function
ϵ	energy dissipation
ϵ_n	constant = 1 or 0

LIST OF SYMBOLS (Cont'd)

θ	circumferential direction
λ	laser light wavelength
μ	absolute viscosity
μ_t	turbulent viscosity
ν	Poisson's ratio
ξ_m	constant = $k_r r$
ρ	density
σ_k	constant = 0.9
σ_ϵ	constant = 1.3
ν	kinematic viscosity
ϕ	angle between two laser light beams / parameter in appendix C
ϕ_{mn}	expression defined in equation (7)
ω	circular frequency
Ω	non-dimensional frequency, $\Omega = \omega a / c_1$
\wedge	Fourier transform
∇^2	differentiation operator
$\langle \rangle$	time average
$*$	complex conjugate

ACKNOWLEDGEMENTS

I would like to express my gratitude to Professor Peter R. Stepanishen for his invaluable and patient guidance throughout the course of study. Also, I am indebted to the other members of the doctoral committee, Professor Frank M. White and Professor Martin H. Sadd, for their kind advice during the course of this research.

In addition, I would like to acknowledge several of my colleagues at the Naval Underwater Systems Center for their assistance; especially, Mr. Kenneth M. LaPointe for his assistance in phase II of the experimental study, Mr. James M. Gutkowski for his assistance in phase I of the experimental study, Miss Janet L. Williams for her assistance in computer programs relating to the shell vibration problem, and Mr. William J. Conforti of the Publications Department for his editorial comments. Also, I wish to express my gratitude to the management of the Launcher and Missile Systems Department for their continuing interest and support of this study.

This study was partially supported by the Office of Naval Technology (ONT) under the Covert Launch Technology Program and by the Naval Underwater Systems Center's Independent Research/Independent Exploratory Development Program.

Finally, I wish to extend my deepest appreciation to my wife, Shirley, for her enduring gifts of love and constant encouragement, and to our daughters, Melissa and Janice, for their patience and understanding during this effort.

CHAPTER 1

INTRODUCTION

1. Overview

It is well known that sound is generated from pressure fluctuations in a fluid medium. The turbulent shear in wall-bounded flows is usually associated with intense pressure fluctuations that result in high acoustic radiation. Specific examples of flow processes that have attracted a great deal of attention are turbulent jet flows, flow through restrictors, flow over cavities, wakes, turbulent boundary layer flows, cavitating flows, and unsteady flows.

Turbulent flow with structural interaction, commonly known as the flow-induced noise problem, is complex and has been the subject of acoustic research in recent decades. Previous studies of flow-induced noise and vibration have been both analytical and experimental in nature. The analytical formulation of the problem is based on the laws of physics, such as conservation of mass, momentum, and energy. With reasonable assumptions, certain simple problems can be solved analytically. In recent years, with the advances in the speed and mass storage capabilities of computers, some flow-induced noise problems have been simulated or solved numerically with some success. However, for most practical problems, the flow is complex and the geometry is difficult to describe. In these cases, an experimental approach has to be employed.

The subject of flow-induced noise and vibration involves the simultaneous study of fluid dynamics, vibration, and acoustics. Thus, typical flow-induced noise problems are associated with the generation of turbulence, the unsteadiness of fluid motions, and the interaction

with the structures and the sound field.

In general, flow-induced noise is caused by the quadrupole character of the turbulent boundary layer fluctuations which is often referred to as "pseudo sound." Although the pseudo sound is a near-field phenomenon, it has a strong influence on neighboring structures. Flexible structures, such as thin shells, cylinders, and plates, can be set into vibration by these local pressure fluctuations. Sound waves are then generated that propagate over long distances and can be observed in the far field as "flow-induced noise or sound." The near-field flow-induced noise phenomenon due to turbulent jet flows in a pipe is the scope of this study.

2. Statement of the Problem

This study deals with the internal sound field and vibratory response of the pipe wall generated by the turbulence of confined jets in a pipe. The specific objectives are to: (1) Investigate and characterize the noise generating mechanisms of the confined jet mixing; (2) Determine the noise source strength of confined jets with various configurations and area ratios, as well as orifice plate thickness and sharpness; (3) Develop analytical model to study the effect of the turbulent jet flow field on wall pressure and vibratory motion of the duct wall; (4) Verify the analytical model with experimental data. This investigation is limited to the study of water jet flow in a thick-wall elastic pipe with the jet operated at constant speed.

This investigation focuses primarily on the understanding of piping system noise. Turbulence-generated noise due to high velocity flow through valves and restrictors has been identified as one of the major noise contributors in submarines and industrial piping systems. To

predict and reduce piping system noise, a better understanding of the noise generating mechanisms and their interaction with the flow field and neighboring structures is needed. The noise characteristics of flow through valves and restrictors with air, steam, and gases have been studied quite extensively. However, studies of the noise characteristics of water flow through valves and regulators have been limited, and the understanding of flow-induced noise is far from satisfactory. To some extent, the noise of cavitating jets has been investigated from the considerations of hydrodynamic performance and structural fatigue, but less so from the flow-induced noise point of view. Some other flow-related issues that have some relevance to this study are: the flow performance or measurement accuracy of orifice flow meters, arterial stenosis - the flow of blood in the vicinity of a restriction in the arteries, and the performance of jet pumps.

The approach to this confined jet flow-induced noise problem can be represented by the block diagram shown in figure 1-1. For discussion purposes, the diagram is divided into two tasks - the experimental study and theoretical development or noise modeling. The experimental study focuses on the characterization of flow-induced noise of confined jets and acquisition of flow and acoustic data for numerical calculations and comparisons. The theoretical development deals with the formulation of wall pressure and acceleration predictions.

3. Organization of Dissertation

This dissertation is organized as follows. Chapter 1 contains the introductory material, i.e., an overview of this study and a statement of the problem. A literature review in the specific areas relating to this study is presented in chapter 2. The areas include: flow and

acoustic characteristics of free-jet and external flows, shell vibration, flow and acoustic measurements, coherent structures, and confined jet flow-induced noise. Chapter 3 describes the theoretical development. It starts with the formulation of near-field pressure due to the turbulent jet flow field, fluid-coupled shell vibration with jet excitation source, and total wall pressure evaluation from a deterministic point of view, then followed by the development based on a statistical approach. Lastly, a special case for the confined jet is presented. Experimental setups, test facilities, test program, test configurations, flow and acoustic instrumentation are described in chapter 4. Experimental results - which include discussions of flow, wall pressure, and acceleration measurements, effects of area ratio, plate thickness, and a measurement accuracy summary are presented in chapter 5. Chapter 6 presents and discusses numerical results of the wall pressure and pipe wall acceleration of confined jet flows. It also contains results from the numerical calculations and comparisons with the experimental data. Conclusions and recommendations are contained in chapter 7. Background material, such as the formulation of the blocked excitation pressure for the calculation of pipe wall response, a list of experimental equipment, a brief discussion of the laser Doppler velocimeter (LDV) data acquisition and reduction, and a summary of flow calculations using the K and ϵ model, are included in the appendixes. A complete bibliography follows the appendixes.

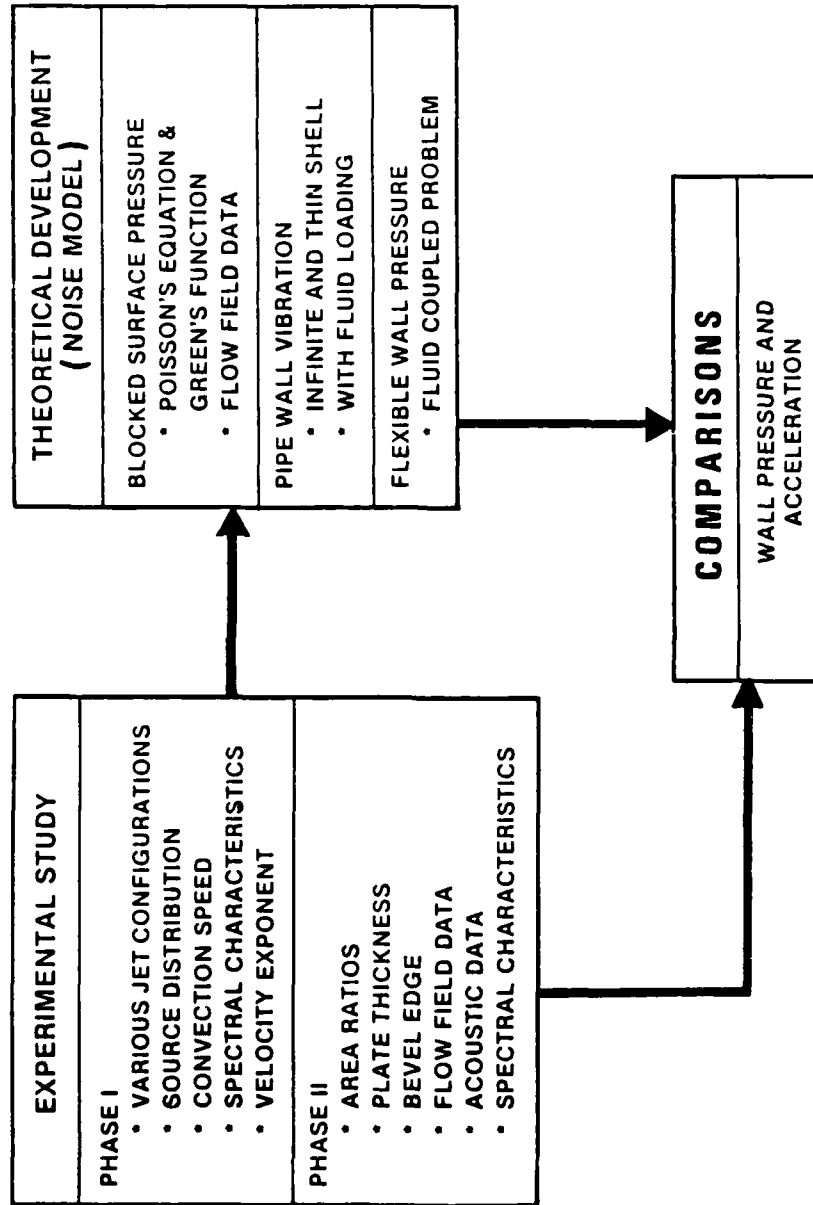


Figure 1-1. Schematic of Present Study

CHAPTER 2

LITERATURE REVIEW

The literature review in this chapter is divided into five sections, each of which covers a topic that is closely related to confined jet flow-induced noise. The five sections are:

1. Flow and acoustic characteristics of free-jet and external flows
2. Shell vibration
3. Flow and acoustic measurements
4. Coherent structures
5. Confined jet flow-induced noise.

1. Flow and Acoustic Characteristics of Free-Jet and External Flows

Aerodynamically generated sound from the mixing of a free turbulent jet was first formulated by Lighthill (1952), and subsequently refined and extended by Ffowcs Williams (1963), Ribner (1964), and many others. Lighthill postulated that turbulent shear stresses act as a source of sound. He derived an inhomogeneous wave equation by combining the continuity and momentum equations. He concluded that jet noise is related to the jet velocity and its velocity fluctuations, the so-called Reynolds stresses.

Davies et al. (1963) presented the noise characteristics of a cold-air jet and related the noise to the turbulence characteristics. Measurements of fluctuating turbulent stresses in the mixing layer of the jets were conducted by Bradshaw (1964), Jones (1969), and Laufer (1973) using hot-wire anemometry. Recently, the flow field of turbulent jets and its fluctuating stresses were measured by Johnson and Bennett (1981), and Ahuja et al. (1985) using a laser Doppler

velocimeter. Even with the advances in flow field measurement and instrumentation, accurate description of the Reynolds stresses still poses a challenge to the experimenters.

Numachi et al. (1960) investigated the effects of cavitation on the discharge coefficient of a sharp-edged orifice plate with reference to various degrees of cavitation. Experimental data substantiated the fact that cavitation can exist to a minimum cavitation number of 0.2. In addition, it was found that the use of air-inhalation to suppress the noise and vibration from the cavitation has no effect on the discharge coefficient. Oba et al. (1978) studied the effect of polymer on a cavitating jet and found that polymer can shift the peak in acoustic energy between 100 Hz and 20 kHz. Flow characteristics of water jets were investigated by Krothapalli et al. (1981) using hot-wire anemometry. In their report, flow field data were presented for rectangular and multiple jets.

Turbulence-generated noise (or flow noise) due to external flows, and its interaction with structures has been studied quite extensively since the 1960s. Analytical and experimental studies on external flow noise have been conducted by Willmarth (1962), Bradshaw (1965), Corcos (1967), Kline (1967), Maidanik (1967), Haddle and Skudrzyk (1969), Ffowcs Williams (1982), Chase (1986), and many others; however, the understanding of flow noise and its interaction with structures is still far from satisfactory.

Meecham and Ford (1958) showed that the self-noise power spectrum is proportional to $\omega^{-3.5} M^{2.5}$ at high frequencies, where ω is the frequency and M is the Mach number. The spectrum at the high-frequency end is universal and is independent of the details of the driving mechanism. At low frequencies, the spectrum is proportional to $\omega^4 M^3$,

and it depends on the distribution and decay of large-scale eddies.

Experimental investigation of the effect of a flexible wall on boundary noise was conducted by Dinkelacker (1966); however, his results were inconclusive. Haddle and Skudrzyk (1969) measured the flow noise of a torpedo-shaped body and concluded that direct radiation from the turbulence was the dominant noise mechanism. Dowling (1983) extended Lighthill's theory and studied turbulent boundary layer noise over a flexible surface. Wall pressure spectra were calculated using Green's function and assuming isotropic turbulence. Li (1986) analyzed the mechanical and flow-induced vibrations on plates and cylindrical shells in a dense fluid. A brief but rather good review and discussion of the flow noise problem is given by Rijnja (1981).

2. Shell Vibration

Several excellent texts have been written on the shell vibration problem. The text by Kraus (1967) is a classic on thin shell theory. Leissa (1973) summarized natural frequencies and mode shapes of various shells with complex configurations and boundary conditions. The fluid-coupled shell vibration problem has been presented by Fahy (1985) and Junger and Feit (1986).

Greenspon (1960) studied the dynamic behavior of an infinitely long thick cylindrical shell surrounded by water. The shell was excited by axially symmetric forces. A solution was obtained by coupling the three-dimensional elasticity equations with fluid pressure in the cylindrical shell. In his follow-on paper, Greenspon (1961) presented the free and forced vibrations of infinitely long, thick and thin cylindrical shells surrounded by water. Exact elasticity theory was used to treat unpressurized shells, and an approximate shell theory was

employed to treat effects on static pressure of internal fluid and structural damping.

Tang (1966) presented the steady-state response of an infinitely long shell subjected to moving axisymmetric ring loads. The complex Fourier transform was used to obtain the exact solution. Numerical results for shells of Maxwell materials with various viscous damping coefficients under various velocities of moving loads were given. Kumar (1972) reported a theoretical study of the dispersion of axially symmetric waves in empty and fluid-filled cylindrical shells of various wall thickness. The analysis was based on the exact three-dimensional equations of linear elasticity, and his findings present a measure for the comparison of various shell theories.

Stepanishen (1982) presented an approach to evaluate the external pressure field and vibratory response of a finite fluid-loaded cylindrical shell. He combined a generalized Fourier series or in vacuo eigenfunction expansion of the shell velocity field with a Green's function and integral equation representation of the excitation. General integral expressions were presented for the self-radiation and interaction impedances. Numerical results were given for the acoustic impedances as a function of mode shape and frequency.

Au-Yang (1986) reviewed the hydrodynamic mass approach to the solution of dynamic problems of the fluid-coupled shell. Simplified equations for computing the hydrodynamic masses and subsequent solution of the eigenvalue problem were presented. Methods of incorporating the hydrodynamic mass concept into finite element structural analysis were described.

The vibration of fluid-filled shell with line and monopole noise sources was presented in a series of papers by Fuller (1981, 1982, 1983,

1984, 1986). Fuller solved the fluid-coupled shell vibration problem for an infinite pipe using the spectral equations of motion. Force input mobilities and energy flow in the pipe were obtained for a thin steel pipe with various circumferential modes.

3. Flow and Acoustic Measurements

Turbulent pipe flow is a classic problem and has been studied quite extensively from the fluid dynamic and turbulence point of view. Laufer (1952) provided a good data base on the velocity and velocity intensity measurements of turbulent pipe flow. Extensive flow measurements were conducted on the pipe and free jet using hot-wire anemometry during the 1950s, 1960s, and 1970s.

Since the mid-1960s, much attention has been given to aircraft engine noise problems. Subsequently, a large effort has been focused on aircraft jet exhaust noise investigations. Analytical and experimental studies were conducted by aircraft engine manufacturers and universities on the aeroacoustic characteristics of free jets. Flow and acoustic measurements of an air jet discharged to an open field have been reported and they provide a good understanding of the noise-generation and propagation processes.

The use of a hot-wire for measurement of the turbulent jet flow field has been reported by many, including Bradshaw (1964), Jones (1969), Kovasznay (1970), Laufer (1973), and Chan and Ko (1978). With the introduction of laser Doppler velocimetry (LDV) in the early 1970s, a wide spectrum of experimental investigations has been reported using LDV for flow field measurements. Detailed discussions of the use of LDV for flow measurements have been documented in texts by Drain (1980) and Durst et al. (1981).

In underwater acoustics, much emphasis has been focused on submarine quieting and sonar performance since the end of World War II. Accordingly, the flow-induced noise problem has become the subject of extensive studies. Measurement of sound pressure in a turbulent flow over the flat surface of a hydrophone has become one of the crucial issues. The hydrophone senses the total pressure on its sensitive area in which the maxima and minima of the pressure wave can cancel each other. Hence, the hydrophone becomes sensitive only to pressures with wavelengths that are longer than the linear dimension of its sensitive area. For smaller wavelengths, its sensitivity gradually decreases.

Corcos (1967) introduced the hydrophone correction factor as the ratio of the measured spectral density of the flow-induced noise to the actual spectral density. Measurements of wall pressure under the turbulent boundary layers, and the effects of hydrophone geometry on noise were addressed by Willmarth and Wooldridge (1962), Haddle and Skudrzyk (1969), Geib (1969), and Rijnja (1981). It has been reported that rectangular or elliptical hydrophones are less sensitive to flow noise if the largest cross-section is oriented in the direction of the flow. Values for the hydrophone size correction were published by Gilchrist and Strawderman (1965). Blake (1986) stated that for $\omega d/U_\infty > 1.2$, where d is the diameter of the pressure transducer, a hydrophone correction must be applied. According to Rijnja (1981), to suppress the flow-induced noise in hydrophones, it is desirable to employ hydrophones that are larger than the largest wavelength that is likely to occur. But, on the other hand, the hydrophone should be small relative to the acoustic wavelength.

Haddle and Skudrzyk (1969) provided an excellent review on the physics of flow noise and presented some data on the turbulent boundary

layer noise. The measurement of flow noise was conducted with a rotating cylinder arrangement or the use of a torpedo-shaped body that is released from the bottom of a deep lake, running upward by its own buoyancy. Hydrophones were mounted in the nose and the sides of the body, while the noise was recorded by built-in instrumentation.

Measurement of airborne noise in ducts has been conducted and reported by Dyer (1958). Karvelis and Reethof (1977) had performed wall pressure measurement in a duct with air flow and presented a method to correlate the wall pressure signals. Kershen and Johnston (1981) used the modal separation technique to quantify the airborne noise in a duct.

Farabee and Casarella (1986) reported the wall measurements beneath a separated and reattached boundary layer for flow over forward and backward steps. They showed that the maximum noise spectrum is found at the reattachment point with a 6.0 ratio of axial location to step. Keith and Tourish (1987) measured and quantified the fluctuating wall pressure and mean velocity profiles for the turbulent boundary layer on the top and bottom walls of a rectangular duct.

4. Coherent Structures

Orderly structures have long been observed in connection with the instability of shear layers, such as ring vortices from a jet nozzle. Since the early 1970s, there has been an upsurge of research activity in the study of large-scale coherent structures related to turbulent shear flows. It was speculated that these orderly or deterministic large-scale structures play an important role in turbulence mixing and its noise production. The large-scale structure is characterized by coherent vorticities with length scales on the order of the width of the mixing layer. The occurrence and significance of these large-scale

coherent structures in jet flows were first recognized by Townsend (1956) as "big eddies."

Subsequently, experimental studies related to the identification of coherent structures via controlled excitation, and measurements of coherent structure properties were conducted by Kovasznay (1970); Crow and Champagne (1971); Laufer, Kaplan and Chu (1973); Winant and Browand (1974); and Hussain (1980). Crow and Champagne (1971), who used a loudspeaker upstream of the nozzle to impose a periodic surging of controllable frequency and amplitude at the exit, studied the response downstream with hot-wire anemometry and Schlieren photography. They discovered that surging amplifies the corresponding instability waves. Winant and Browand (1974) pointed out that the growth of turbulent shear flow is due to the pairing of coherent structures. A rather comprehensive review of coherent structures is given by Roshko (1976).

Sarohia and Massier (1978) conducted experimental studies of coherent structures on jets and found the occurrence of coherent structures at the first seven jet diameters. Chan and Ko (1978) observed the existence of coherent structures in the outer mixing layer of an annular jet. Ho and Huang (1982) presented the vortex pairing and merging of the mixing layer under the so-called "collective interaction" process. Thomas and Bull (1983) studied the wall pressure in the turbulent boundary layer and observed some sort of deterministic motion of the large-scale structures. Recent analytical and experimental studies of coherent structures in jets were documented by Long and Arndt (1984), Ahuja and Blakney (1985), Lam and Ko (1986), Zaman (1986), and Bennett et al. (1987).

Large-scale structures called puffs and slugs were found in the transition region of pipe flow and were reported by Wygnanski (1973).

Based on the experimental evidence and results of the coherent structures, Liu (1974), Mankbadi and Liu (1981), and Acton (1980) modeled the large eddies in a two-dimensional plane jet and an axisymmetric jet, and their numerical results are consistent with many features of the non-linear behavior observed experimentally. Furthermore, Liu attempted to predict the noise characteristics of a plane jet and his results were in good agreement with experimental data. Abdallah (1984) studied the flow and pressure field of an arterial stenosis and suggested that the flow field is dominated by the large-scale structures near the exit of the jet. A comprehensive discussion of coherent structures was held in the Second International Symposium on Turbulent Shear Flows in 1979 and proceedings were documented by Bradbury et al. (1980).

5. Confined Jet Flow-Induced Noise

Since the early 1970s, because of the concern with noise problems in industrial plants, large efforts have been directed at the reduction of piping system noise. Piping system noise due to valves and regulators, and sound transmission loss through pipe walls have been investigated by Clinch (1970), Walter (1979), Fagerlund (1979), Ng (1980), Loh (1981), Norton and Bull (1984), and many others. The study of piping system noise was limited to the decoupled problem by treating the acoustic field and structural vibration independently. The decoupled assumption is valid for the flow of air, steam and gases through valves.

Clinch (1970) described the results of an analytical and experimental investigation of the flow-induced vibrations of thin-walled pipes by the passage of fully-developed turbulent water flow. Random

vibration theory, similar to the acceptance theory developed by Powell (1958), was used to predict the response of thin-walled pipes to the turbulent wall pressure field at high-order modes and frequencies. Walter (1979) and Fagerlund (1979) presented methods to calculate the pipe wall sound transmission loss. Walter utilized the deterministic approach, whereas Fagerlund used statistical energy analysis. Both techniques showed good agreement with experimental data.

Loh (1981) and Ng (1980) investigated valve noise generation and radiation experimentally and reported that airborne noise is related to the flow velocity raised to the sixth power. Bull and Norton (1980) studied the coincidence of the internal sound field with pipe structural response. A comprehensive review of piping system noise was given by Reethof (1978).

The acoustic characteristics of air jet flow in pipes has been investigated by Stahl (1985,1986). He showed that turbulence fluctuations dominate in the region of flow separation downstream of an orifice plate. The sound field of circular jets has been characterized with a range of flow velocities and jet-to-pipe area ratios. He reported that the wall pressure fluctuations are related to the velocity to the fourth power.

Abdallah (1984) investigated the distribution and statistical characteristics of the wall pressure fluctuations and the velocity fluctuations of a confined jet. The confined jet was produced by the flow of water through a restriction, which was an attempt to simulate an arterial stenosis. She related the near-field pressure to the turbulent flow field of the jet by Poisson's equation, and she used the Green's function to satisfy the boundary conditions on a cylindrical rigid surface.

CHAPTER 3

THEORETICAL DEVELOPMENT

1. Introduction

The physical problem under investigation is illustrated in figure 3-1. In general, a low-to-moderate flow approaches the flow restriction in a pipe. A high-velocity jet is formed at the vena contracta immediately downstream of the orifice plate. Near the orifice plate, the jet is surrounded by a low velocity recirculation zone or reversed flow region. Further downstream, the jet shear layer grows until it reattaches to the pipe wall. As shown in the figure, the flow field can be divided into two regions; namely, the recirculating or developing region and the fully developed region. The developing region of the jet is the noise production area in which the flow and noise characteristics are very similar to those of a free jet. In this region, the jet mixing noise is the dominant noise mechanism. However, the flow field can be modified by the presence of the pipe wall, which can alter the noise generation. As compared to a free jet, the confined jet differs significantly in acoustic radiation, propagation, and fluid/structural interaction processes.

The acoustic pressure at the wall in figure 3-1 is a superposition of two components: a blocked surface pressure and a pressure due to the induced vibration of the shell. The blocked surface pressure is defined as the near-field pressure generated by the fluid on the pipe wall surface, but with the surface rigid. This pressure is primarily due to the near-field hydrodynamic component of the turbulent jet flow which is influenced by its small scale and large-scale or coherent structures. Near the exit of the jet, coherent structures play an important role in

turbulence mixing and noise production. Further downstream, the activity of jet mixing decreases; the large-scale turbulence cascades to fine scales, and the flow and acoustic characteristics approach that of pipe flow.

A schematic of the jet flow-induced noise model is shown in figure 3-2. In brief, the model is summarized as follows: Based on flow field measurements, the blocked pressure is calculated using the Lighthill method via the Poisson's equation. The blocked excitation pressure then is used to drive the fluid-filled shell. The pipe wall acceleration and the associated wall pressure are determined by solving the coupled fluid solid interaction problem. Finally, the total wall pressure is obtained by summing the blocked pressure and the pressure due to the wall vibration.

In the following sections, the development of the analytical model for the evaluation of pipe wall pressure and acceleration is presented. First, the development of the expressions for wall pressure and shell vibratory response based on a deterministic approach is introduced, then followed by the development based on a statistical approach. Lastly, a special case for the confined jets is discussed.

2. Near-Field Jet Noise and Blocked Surface Pressure

In this section, the equation relating the pressure fluctuations to the fluctuations in momentum is derived. A solution of the equation (Poisson's equation) is developed utilizing a Green's function method. The equation for evaluating the pressure fluctuations or blocked surface pressure is presented. This development is similar to that of Abdallah (1984).

Consider the flow field of a turbulent jet as shown in figure 3-1.

The flow and pressure are governed by the conservation of mass and momentum equations for incompressible fluids. The conservation of mass is given by

$$\partial u_i / \partial x_i = 0 , \quad (1)$$

and conservation of momentum by

$$\frac{\partial u_i}{\partial t} + u_j \frac{\partial u_i}{\partial x_j} = -\frac{1}{\rho} \frac{\partial p}{\partial x_i} + \nu \frac{\partial^2 u_i}{\partial x_j \partial x_j} , \quad (2)$$

where u and p are the instantaneous velocity and pressure, respectively. By taking the divergence of equation (2) and applying the equation of conservation of mass, equation (2) becomes

$$\frac{1}{\rho} \nabla^2 p = - \frac{\partial^2}{\partial x_i \partial x_j} u_i u_j . \quad (3)$$

In turbulent flow, the instantaneous velocity and pressure can be written as the sum of the mean and fluctuating quantities, i.e.,

$$p = P + p' ,$$

$$u_i = U_i + u_i' . \quad (4)$$

By substituting equation (4) into equation (3) and averaging with respect to time, the equation relating the fluctuating pressure and momentum can be written in the form of Poisson's equation, i.e.,

$$\nabla^2 p' = -M_{ij} , \quad (5)$$

where

$$M_{ij} = \rho \frac{\partial^2}{\partial x_i \partial x_j} (u_i' u_j' - \overline{u_i' u_j'} + 2U_i u_j') .$$

Here, the overbar denotes the time-averaged value. The fluctuating pressure in equation (5) is the near-field pressure generated by the

turbulent jet. It does not propagate as sound and thus is referred to as "pseudo sound." Furthermore, the blocked surface pressure noted earlier is equivalent to p' at the surface of the rigid wall (see figure 3-2).

To solve the Poisson's equation, a Green's function in cylindrical coordinates $G(r, \theta, x/r_0, \theta_0, x_0)$ is constructed (see figure 3-3). The Green's function represents the response at point (r, θ, x) due to a unit point source at (r_0, θ_0, x_0) . The source term in equation (5) consists of the pressure fluctuations or sources at (r_0, θ_0, x_0) . The solution of Poisson's equation in terms of the Green's function can be interpreted as the result of summing responses due to the distribution of source fluctuations. This solution of Poisson's equation can be expressed as

$$p'(r, \theta, x) = \int_V M_{ij} G(r, \theta, x/r_0, \theta_0, x_0) dV - \int_S \frac{\partial p'}{\partial r} G(r, \theta, x/r_0, \theta_0, x_0) dS, \quad (6)$$

where $G(r_0, \theta_0, x_0)$ is the solution of the nonhomogeneous equation

$$\nabla^2 G = -\frac{1}{r} \delta(r - r_0) \delta(\theta - \theta_0) \delta(x - x_0),$$

which satisfies the boundary condition $\partial G / \partial r = 0$ at the wall (i.e., $r = D/2$).

The Green's function $G(r, \theta, x/r_0, \theta_0, x_0)$ has been shown to be (see Abdallah (1984))

$$G(r, \theta, x/r_0, \theta_0, x_0) = \sum_{n=0}^{\infty} \sum_{m=1}^{\infty} \frac{\epsilon_n}{\pi D} \frac{\xi_{mn}}{\xi_{mn}^2 - n^2} \frac{1}{J_n^2(\xi_{mn})} \phi_{mn}(r_0, \theta_0) \cdot \phi_{mn}(r, \theta) \exp(-2\xi_{mn}|x-x_0|/D), \quad (7)$$

where

$$\begin{aligned} \phi_{mn}(r, \theta) &= J_n(2\xi_{mn}r/D) \cos[n(\theta - \theta_0)], \\ \epsilon_n &= 1 \quad n = 0, \\ \epsilon_n &= 2 \quad n \neq 0. \end{aligned}$$

J_n is the Bessel function of the first kind of order n , and ξ_{mn} satisfies the equation $J_n'(\xi_{mn}) = 0$.

As shown by Abdallah (1984), the pressure gradient at the wall is

$$\frac{\partial p'}{\partial r} = -\mu \left[\frac{\partial}{\partial r} \left(-\frac{1}{r} \frac{\partial v_{\theta}'}{\partial \theta} + \frac{\partial v_x'}{\partial x} \right) \right] = -\mu \left[\frac{\partial}{\partial \theta} \left(-\frac{1}{\partial r} \frac{v_{\theta}'}{r} \right) + \frac{\partial}{\partial x} \left(\frac{\partial v_x'}{\partial r} \right) \right]. \quad (8)$$

At high Reynolds numbers, the dipole term is small as compared with the Reynolds shear stress component of the quadrupole source. An order of magnitude analysis shows that the ratio of the volume integral to the surface integral in equation (6) is $(uL/\nu)^{1/2}$, where L is the length scale (i.e. radius of the pipe), u is the turbulent velocity scale, and ν is the kinematic viscosity. Experimental work by Olsen, Miles, and Dorsch (1972) has shown that the surface dipole term is indeed small.

By neglecting the surface dipole term, equation (6) can be written as

$$p'(r, \theta, x) = \int_V G(r, \theta, x/r_0, \theta_0, x_0) \frac{\partial^2}{\partial x_i \partial x_j} H_{ij} dV, \quad (9)$$

where

$$H_{ij} = -\rho(u_i' u_j' - \overline{u_i' u_j'} + 2U_i u_j') .$$

Using the identity

$$\frac{\partial}{\partial x_i} G \frac{\partial H_{ij}}{\partial x_j} - \frac{\partial}{\partial x_j} H_{ij} \frac{\partial G}{\partial x_i} = G \frac{\partial^2 H_{ij}}{\partial x_i \partial x_j} - H_{ij} \frac{\partial^2 G}{\partial x_i \partial x_j}$$

to eliminate $G(\partial^2/\partial x_i \partial x_j)H_{ij}$ and then applying the divergence theorem

$$\int_s A \cdot n \, ds = \int_v \nabla \cdot A \, dV$$

equation (6) becomes

$$p'(r, \theta, x) = \int_v H_{ij} \frac{\partial^2 G}{\partial x_i \partial x_j} dV + \int_s G n_i \frac{\partial}{\partial x_j} H_{ij} dS - \int_s n_j H_{ij} \frac{\partial G}{\partial x_i} dS . \quad (10)$$

Because the velocity vanishes at the surface, the wall pressure fluctuation then becomes

$$p'(D/2, \theta, x) = \int_v H_{ij} \frac{\partial^2 G}{\partial x_i \partial x_j} dV . \quad (11)$$

According to equation (11), the wall pressure fluctuation can be evaluated by multiplying the source magnitude H_{ij} at each point of the flow field by the corresponding local weighting function $\partial^2 G/\partial x_i \partial x_j$ and integrating over the whole source volume.

Consider the case of an axisymmetric jet whose principal mean velocity is the axial component, i.e., $U_i = (U_x, U_r, 0)$ and $\partial/\partial x \ll \partial/\partial r$. The continuity equation can be written as

$$\frac{1}{r} \frac{\partial}{\partial r} r U_r + \frac{\partial U_x}{\partial x} = 0 ,$$

which gives U_r/U_x of the order l/L where l and L are the length scales in the r and x direction, respectively. Assuming an axially symmetric source distribution (i.e., $\partial/\partial\theta = 0$) and $n = 0$, equation (11) becomes

$$p'(D/2, x) = \rho \int_V (u_i' u_j' - \overline{u_i' u_j'} + 2u_i' U_j \delta_{j1}) \frac{\partial^2 G}{\partial x_i \partial x_j} dV , \quad (12)$$

where the Green's function is

$$G(D/2, x/r_o, x_o) = \sum_{m=1}^{\infty} \frac{1}{\pi D} \frac{1}{\xi_m} \frac{J_o(2\xi_m r_o/D)}{J_o(\xi_m)} \exp(-2\xi_m |x-x_o|/D) .$$

Differentiating Green's function with respect to x_o and r_o , the local weighting function $\partial^2 G / \partial x_i \partial x_j$ becomes

$$\frac{\partial^2 G}{\partial x_o \partial r_o} = - \frac{4}{\pi D^3} \sum_{m=1}^{\infty} \frac{\xi_m J_1(\xi_m r_o/R)}{J_o(\xi_m)} \exp(-\xi_m |x-x_o|/R) . \quad (13)$$

3. Vibratory Response and Pressure Field

An approach is presented in this section to evaluate the vibratory response and pressure field of a fluid-filled shell excited by a harmonic, axisymmetric axially varying blocked pressure. The vibratory response is presented first, then followed by the pressure due to the wall vibration.

a. Forced Vibration in Shell

Consider a thin circular shell of infinite length, which is filled with a dense fluid (i.e., water). The vibratory motion of the shell can

be described by the Donnell-Mushtari shell equations as presented by Stepanishen (1982) as

$$\begin{bmatrix} L_{ij} \end{bmatrix} \begin{bmatrix} U \\ V \\ W \end{bmatrix} - m_s \frac{\partial^2}{\partial t^2} \begin{bmatrix} U \\ V \\ W \end{bmatrix} = - \begin{bmatrix} p_x \\ p_\theta \\ p_r \end{bmatrix} + \begin{bmatrix} 0 \\ 0 \\ p_a \end{bmatrix}, \quad (14)$$

where U , V , and W are the axial, circumferential, and radial components of the displacement vector in the x , θ , and r directions. The L_{ij} 's are differential operators, m_s is the mass density per unit area of the shell, and p_x , p_θ , and p_r are the mechanical excitations per unit area which act on the shell in the x , θ , and r directions. The additional pressure p_a is the acoustic pressure which acts on the shell as a result of the excitation of the fluid via the vibration of the shell. Figure 3-3 depicts the cylindrical co-ordinate system used in this problem.

To analyze the response of a cylindrical shell to a generalized excitation pressure, it is convenient to express the shell displacements and excitation pressure as Fourier transforms,

$$U = \frac{1}{\sqrt{2\pi}} \int_{-\infty}^{\infty} \sum_s \sum_n \hat{U}_{ns} \cos(n\theta) \exp[jk_{ns}x - j\omega t + j\pi/2] dk_{ns}, \quad (15a)$$

$$V = \frac{1}{\sqrt{2\pi}} \int_{-\infty}^{\infty} \sum_s \sum_n \hat{V}_{ns} \sin(n\theta) \exp[jk_{ns}x - j\omega t] dk_{ns}, \quad (15b)$$

$$W = \frac{1}{\sqrt{2\pi}} \int_{-\infty}^{\infty} \sum_s \sum_n \hat{W}_{ns} \cos(n\theta) \exp[jk_{ns}x - j\omega t] dk_{ns}, \quad (15c)$$

$$p_r = \frac{1}{\sqrt{2\pi}} \int_{-\infty}^{\infty} \sum_s \sum_n \hat{p}_r \cos(n\theta) \exp[jk_{ns}x - j\omega t] dk_{ns}. \quad (15d)$$

Substituting equations (15-a) through (15-d) into the original equations of motion (equation (14)) of the fluid-filled shell gives the spectral equations of motion for $p_x = p_\theta = 0$:

$$\begin{bmatrix} L_{11} & L_{12} & L_{13} \\ L_{21} & L_{22} & L_{23} \\ L_{31} & L_{32} & L_{33} \end{bmatrix} \begin{bmatrix} \hat{U}_{ns} \\ \hat{V}_{ns} \\ \hat{W}_{ns} \end{bmatrix} = \begin{bmatrix} 0 \\ 0 \\ \hat{p}_r \Omega^2 / \rho_s h \omega^2 \end{bmatrix}. \quad (16)$$

The elements of the differential operator L_{ij} are given by

$$\begin{aligned} L_{11} &= -\Omega^2 + (k_{ns}a)^2 + \frac{1}{2}(1-\nu)n^2, \\ L_{12} &= \frac{1}{2}(1+\nu)n(k_{ns}a), \\ L_{13} &= \nu(k_{ns}a), \\ L_{21} &= L_{12}, \\ L_{22} &= -\Omega^2 + \frac{1}{2}(1-\nu)(k_{ns}a)^2 + n^2, \\ L_{23} &= n, \\ L_{31} &= L_{13}, \\ L_{32} &= L_{23}, \\ L_{33} &= -\Omega^2 + 1 + \beta^2[(k_{ns}a)^2 + n^2]^2 - FL, \text{ and} \\ FL &= \Omega^2(\rho_f/\rho_s)(a/h)(k_s^r a)^{-1}[J_n(k_s^r a)/J_n'(k_s^r a)]. \end{aligned} \quad (17)$$

In these expressions, Ω is the non-dimensional frequency $\Omega = \omega a/c_1$; c_1 is the extensional phase speed of the shell material; k_{ns} is the structural wavenumber; a is the mean radius of the shell; ν is the Poisson's ratio; β is the thickness parameter given by $\beta^2 = h^2/12a^2$; n is the circumferential order of the shell; and the fluid loading term FL is associated with the acoustic pressure which is due to the presence of fluid acting on the shell wall. In the FL term given by Fuller (1983), ρ_f is the fluid density, ρ_s is the density of the shell material, and h

is the shell thickness. The non-dimensional radial wavenumber k_s^r can be written in terms of the shell non-dimensional frequency and axial wavenumber as

$$k_s^r a = \pm [\Omega^2 (c_l/c_f)^2 - (k_{ns} a)^2]^{1/2} . \quad (18)$$

The solution of the forced vibration problem can be obtained via the Fourier transform technique. From the spectral equations of motion (equation 16), the spectral radial displacement, as a function of $k_{ns} a$, is

$$\hat{w}_{ns} = \hat{p}_r \frac{\Omega^2}{\rho_s h \omega^2} \frac{L_{11} L_{22} - L_{12} L_{21}}{\det |L|} . \quad (19)$$

The radial displacement is obtained by performing the inverse transform on equation (19). It should be noted that for the axisymmetric case, (i.e., $n = 0$) the differential operators L_{12} , L_{21} , L_{23} , and L_{32} in equation (16) vanishes. Thus, in the axisymmetric case, the radial displacement becomes

$$w(x) = \frac{1}{\sqrt{2\pi}} \frac{\Omega^2}{\rho_s h \omega^2} \int_{-\infty}^{\infty} \hat{p}_r \frac{L_{11} L_{22}}{\det |L|} \exp(jk_s x) dk_s . \quad (20)$$

The integral in equation (20) can be solved using the residue theorem. Consequently, the radial velocity and acceleration can be obtained by multiplying equation (20) by $-j\omega$ and $(j\omega)^2$ respectively.

b. Pipe Wall Pressure Fluctuations

As discussed previously, the pipe wall pressure is the sum of the blocked surface pressure and pressure contribution from the pipe wall vibration. Evaluation of the blocked surface pressure was presented in

section 2 of this chapter. Here, the pressure due to the wall vibration is developed.

Consider an infinite-length shell with radius a , filled with dense fluid (i.e., water). The shell is set in motion by axisymmetrically distributed sources on the inside of the pipe. The pressure due to the vibratory motion of the pipe wall is governed by the Helmholtz equation:

$$[\nabla^2 + k^2] p(r, x) = 0 . \quad (21)$$

Introducing the Fourier transform pair

$$\hat{p}(r, k_x) = \int_{-\infty}^{\infty} p(r, x) \exp(-jk_x x) dx ,$$

and

$$p(r, x) = \frac{1}{2\pi} \int_{-\infty}^{\infty} \hat{p}(r, k_x) \exp(jk_x x) dk_x ,$$

the Fourier transform of equation (21) is

$$[\nabla_r^2 + (k^2 - k_x^2)] \hat{p}(r, k_x) = 0 , \quad (22)$$

where ∇_r^2 is the operator in cylindrical coordinates defined as

$$\nabla_r^2 = \frac{d^2}{dr^2} + \frac{1}{r} \frac{d}{dr} ,$$

and $k_r^2 = k^2 - k_x^2$, where k_r , k , and k_x are the radial, acoustic, and axial wavenumbers, respectively. The solution of equation (22) can be written as

$$\hat{p} = A_0 J_0(k_r r) , \quad (23)$$

where J_0 is the Bessel function of order zero and A_0 is to be determined. Applying the boundary condition at the wall, $r = a$,

$$\left. \frac{d}{dr} \hat{p} \right|_{r=a} = -jk\rho_f c_f \hat{W} , \quad (24)$$

the constant A_0 can be expressed as

$$A_0 = - \frac{jk\rho_f c_f}{k_r J_0'(k_r a)} \hat{W} , \quad (25)$$

$$\text{where } \hat{W} = \frac{a F_0}{c_1^2 2\pi\rho_s h} \left[\frac{L_{11}L_{22}}{\det|L|} \right] (-j\omega) .$$

Equation (23) now becomes

$$\hat{p}(a, k_x) = \left[\frac{-jk\rho_f c_f}{k_r J_0'(k_r a)} J_0(k_r a) \right] \hat{W}(a, k_x) . \quad (26)$$

By taking the inverse transform, the pressure is

$$p(a, x) = - \frac{\rho_f c_f F_0 \omega}{4\pi^2 c_1^2 \rho_s h} \int_{-\infty}^{\infty} \frac{ka}{k_r a} \frac{J_0(k_r a)}{J_0'(k_r a)} \left[\frac{L_{11}L_{22}}{\det|L|} \right] \exp(jk_x x) dk_x a . \quad (27)$$

The form of the complex integral, equation (27), is very similar to equation (20). Again, using the residue theorem, the pressure due to shell wall vibration at $x = 0$ can be written as

$$p(a, x) = -j \frac{F_o \omega^2}{2\pi c_l^2} \left(\frac{\rho_f}{\rho_s} \right) \frac{a}{h} \sum_{s=1}^{\infty} \frac{J_o(k_r a) [L_{11} L_{22}]}{(k_r a) J_o'(k_r a) \det|L|} \exp(jk_x x) \quad , \quad (28)$$

where the terms in the sum are evaluated at the poles of the integrand and ' represents differentiation with respect to the argument. Lastly, the pipe wall pressure is evaluated by summing the blocked surface pressure, equation (12) and the pressure due to the shell wall vibration, equation (28).

4. Wall Pressure Fluctuations and Forced Vibration in Shell Excited by Random Sources

In this section, the expressions for the wall pressure and shell vibratory response are developed from the statistical point of view. The starting equations are based on the deterministic approach as presented in the last two sections.

It is well known that turbulent jet flow is a random process in space and time. Therefore wall pressure and flow-excited vibration fields associated with the confined jets are also random functions of space and time. To quantify the wall pressure and pipe wall vibratory response, the statistical or averaging method must be used.

First, consider the blocked surface pressure that is due to the near-field hydrodynamic component of the axisymmetric turbulent jet flow. The equation relating the blocked surface pressure to the fluctuations in momentum is presented in equation (12), i.e.,

$$p_b(x, a) = \int_V s(x_0, r_0) \frac{\partial^2 G}{\partial x_0 \partial r_0}(x, a | x_0, r_0) dV,$$

where $s(x_0, r_0)$ is the source at point (x_0, r_0) and is given by

$$s(x_0, r_0) = \rho (u_i' u_j' - \overline{u_i' u_j'} + 2u_i' U_j \delta_{j1}).$$

The complex conjugate of blocked pressure $p_b(x, a)$ at point x' is

$$p_b^*(x', a) = \int_{V'} s^*(x_0', r_0') \frac{\partial^2 G^*}{\partial x_0' \partial r_0'}(x', a | x_0', r_0') dV'. \quad (29)$$

By multiplying equation (12) with equation (29) and ensemble averaging the product, the following expression for the cross spectral density of the pressure is obtained:

$$\begin{aligned} \langle p_b(x, a) p_b^*(x', a) \rangle = & \iint_V \langle s(x_0, r_0) s^*(x_0', r_0') \rangle \frac{\partial^2 G}{\partial x_0 \partial r_0}(x, a | x_0, r_0) \\ & \cdot \frac{\partial^2 G^*}{\partial x_0' \partial r_0'}(x', a | x_0', r_0') dV dV'. \end{aligned} \quad (30)$$

The mean squared blocked pressure at a point x is simply obtained by letting $x' = x$ in equation (30).

In order to determine the velocity of the wall as a function of axial position, the transfer mobility $Y(x-x_0)$, which is defined as the ratio of pipe wall radial velocity at x' to a ring excitation force applied at point x_0 is now introduced. It then follows from the preceding definition and equation (20) that $Y(x-x_0)$ can be expressed as:

$$Y(x-x_0) = \frac{-j\Omega^2}{2\pi\omega_p h} \int_{-\infty}^{\infty} \frac{L_{11}L_{22}}{\det|L|} \exp[-jk_s(x-x_0)] dk_s, \quad (31)$$

which can be simply evaluated using the residue theorem. Finally, after a straight forward application of superposition, it follows that the wall velocity can be expressed as

$$\dot{W}(x) = \int_{x_0} Y(x-x_0) p_b(x_0, a) dx_0. \quad (32)$$

An expression for the mean squared velocity of the wall as a function of position can now be obtained. Following a similar procedure of the blocked pressure, the cross spectral density of the velocity can be expressed as

$$\langle \dot{W}(x) \dot{W}^*(x') \rangle = \int_{x_0} \int_{x'_0} Y(x-x_0) Y^*(x'-x'_0) \langle p_b(a, x_0) p_b^*(a, x'_0) \rangle dx_0 dx'_0. \quad (33)$$

The mean squared velocity of the wall as a function of x is simply obtained from equation (33) by letting $x' = x$. It is noted that the cross spectral density of the blocked pressure, as specified in equation (30) is contained in equation (33).

5. Special Case

The evaluation of the fluid-coupled shell vibration problem with a specific blocked pressure distribution is presented in this section. Results are presented for both deterministic and random blocked surface pressure. A relatively simple form of an amplitude modulated convecting wave field is used as the blocked surface pressure for the deterministic analysis.

The blocked surface pressure for the random case is intended to represent the physics of the confined jet flow. More specifically, the cross spectral density of the pressure is assumed to result from hydrodynamic pressure fluctuations which are uncorrelated in the radial direction, but are correlated in the x direction near the jet exit. The uncorrelated pressure fluctuations in the radial direction reflect the random motion of the turbulent jet, whereas the correlated pressure fluctuations in the x direction reflect the motion of the large-scale coherent structures near the jet exit. This assumption will be further discussed in chapter V - Experimental Results and Discussion.

a. Deterministic Approach

The pressure field of a confined jet is represented here as an amplitude modulated convection term, which simulates the moving acoustic sources of the jet. Each source or turbulent eddy is a function of axial location x and convection velocity V_c . The large eddies and turbulent fluctuations are moving downstream at a convection velocity that is about 0.6 of the jet exit velocity. Accordingly, the convecting blocked pressure can be described by

$$p_b(a, x) = P_0(x) \exp(-jk_c x) \quad , \quad (34)$$

where $P_0(x)$ is assumed to be a triangular pressure distribution as shown in figure 3-4; and k_c is the convecting wavenumber given by $k_c = \omega/V_c$.

The Fourier transform of the triangular blocked pressure can be expressed as

$$P_b = \frac{2P_0}{jk_u} \exp(-jk_u L) \left[\exp(jk_u L/2) \frac{\sin(k_u L/2)}{k_u L/2} - 1 \right] , \quad (35)$$

where L is the half width of the triangular pressure excitation; k_u is

the wavenumber including the convection effect, and is defined as $k_u = \omega/V_c + k_{ns}$. Equation (35) represents a convecting wave field of the turbulent jets and its derivation is shown in appendix A.

After substituting equation (35) into equation (20), and evaluating the integral using the residue theorem, the resultant radial acceleration becomes

$$\ddot{W} = -j \frac{P_o \omega^2}{\rho_s c_l^2 h} \sum_{s=1}^{\infty} \frac{L_{11} L_{22}}{\det |L|'} \exp(jk_s x) \frac{\exp(-jk_u L)}{jk_u} \cdot \left[\exp(jk_u L/2) \frac{\sin(k_u L/2)}{k_u L/2} - 1 \right], \quad (36)$$

where the terms in the sum are evaluated at the poles of the integrand and ' represents differentiation with respect to the argument.

b. Statistical Approach

The expression for evaluating the cross spectral density of the blocked pressure is presented in equation (30). In this special case, it was assumed that the pressure fluctuations are uncorrelated in the radial direction, and the local weighting function $\partial^2 G / \partial x_i \partial x_j$ can be approximated by a Dirac delta function in the x direction. These assumptions are discussed in more detail in chapters 5 and 6. With these assumptions, equation (30) could be simplified and the mean squared blocked pressure can be expressed as

$$\langle p_b(x, a)^2 \rangle = \int_V \langle s(r_o)^2 \rangle \left[\frac{\partial^2 G}{\partial x_o \partial r_o}(x, a | x_o, r_o) \right]^2 dV. \quad (37)$$

In the pipe wall response calculations, it was assumed that the blocked pressure has a triangular distribution, and the pressure

fluctuations are correlated in the x direction. Again, these assumptions are discussed in chapters V and VI. With these assumptions, equation (33) could be reduced to

$$\begin{aligned} \langle \dot{W}(x) \dot{W}^*(x') \rangle = P_o^2 \int_{x_o'}^{x_o} \int_{x_o}^{x_o'} Y(x-x_o) Y^*(x'-x_o') A(x_o) A^*(x_o') \\ \cdot \exp[-j\omega/V_c(x_o-x_o')] dx_o dx_o' , \end{aligned} \quad (38)$$

where $A(x)$ is the triangular pressure distribution given in figure 3-4.

Experimental flow field data will be used for the calculation of blocked surface pressure. Since results from the experimental investigation can shed some light on the nature of the acoustic sources of the turbulent jets and its blocked surface pressure distribution, presentation and discussion of the numerical results of the pipe wall acceleration is continued in chapter 6 after the presentation of the experimental data.

This chapter has introduced the near-field jet noise and blocked surface pressure, fluid-coupled shell vibration, and pipe wall pressure fluctuations from both deterministic and statistical point of views. A special case of the triangular pressure distribution has been presented and discussed. Since the excitation source of the jet is based on experimental data (i.e., turbulent jet flow field), it is more effective to present and discuss the numerical results after the presentation and discussion of the experimental data and results in chapter 5. Accordingly, the numerical results of the noise model of the confined jet are presented in chapter 6.

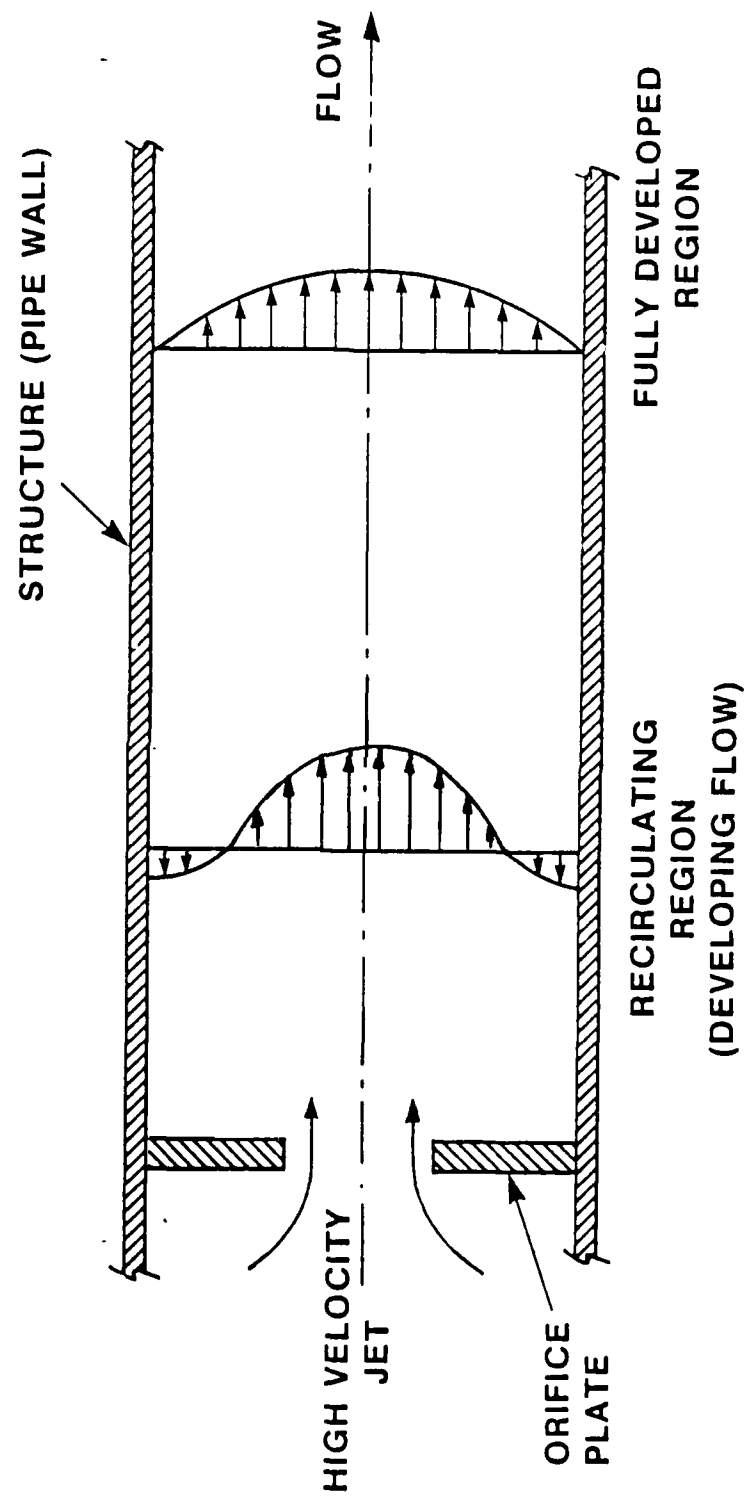


Figure 3-1. Development of Confined Jet

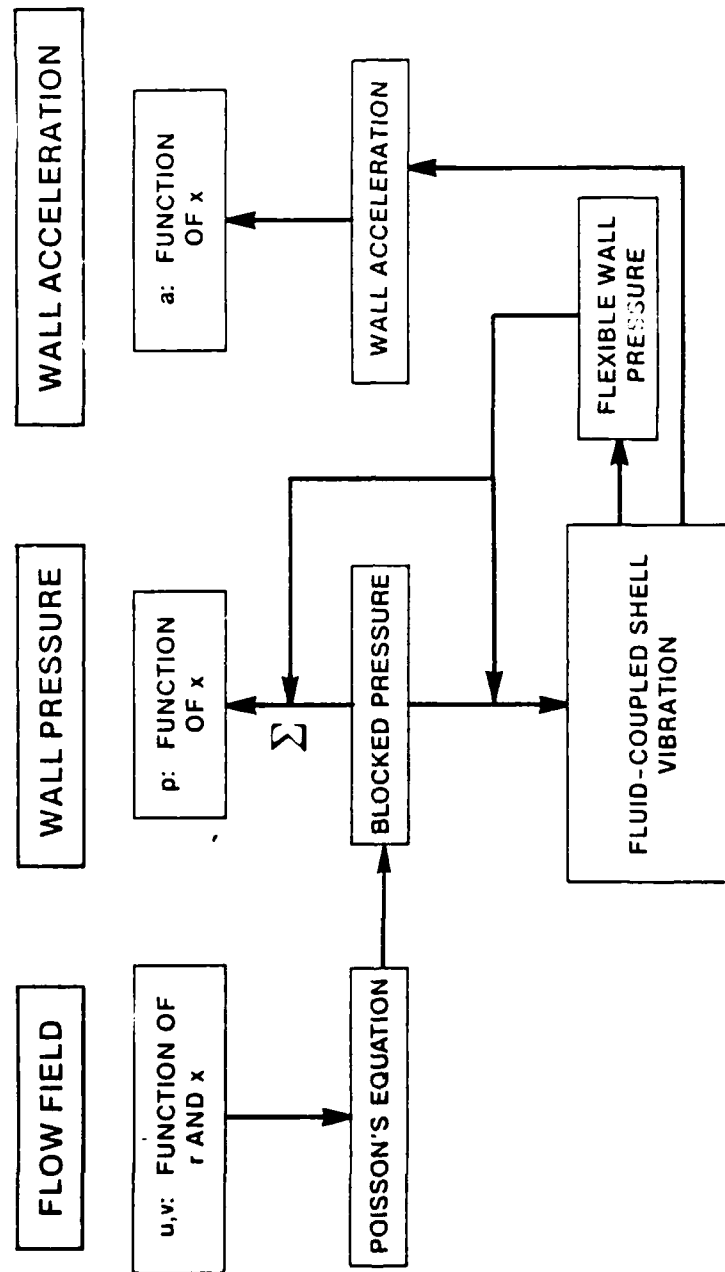


Figure 3-2. Noise Model for Fluid-Filled Shell Vibration
Excited by a Confined Jet

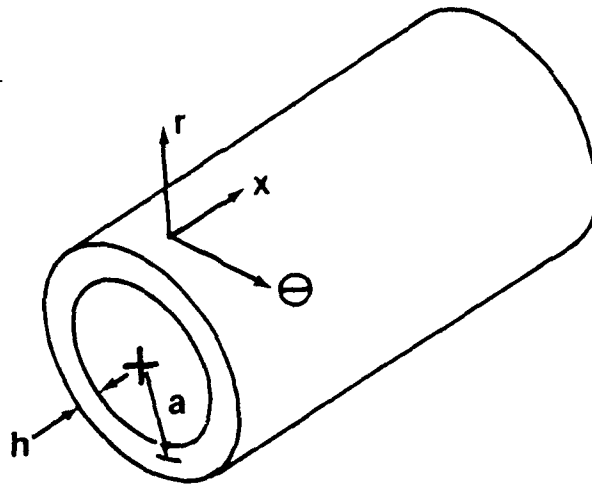


Figure 3-3. Coordinate System of the Shell Vibration Problem

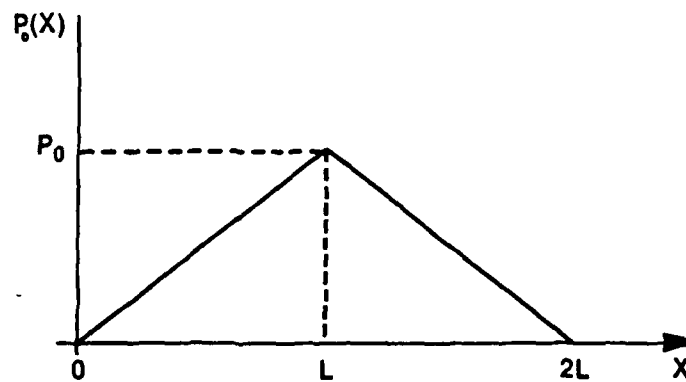


Figure 3-4. Triangular Blocked Pressure Distribution

CHAPTER 4

DESCRIPTION OF EXPERIMENTS

The experiments were conducted to quantify the flow characteristics and noise generating mechanisms of the confined jets. Turbulent jet flow field data were measured for calculating the wall pressure and acceleration from an analytical model of the test configuration. In addition, wall pressure and pipe wall acceleration measurements were taken for comparison with the numerical results from the analytical model.

The experimental study consisted of two phases: Phase I involved study of the noise characteristics of various confined jet flows, and phase II investigated the flow and acoustic characteristics of circular confined jets with various area ratios. Phase I was conducted at the Naval Underwater Systems Center Acoustic Water Tunnel in New London, Connecticut. Phase II was conducted at the Naval Underwater Systems Center Flow Loop Facility in Newport, Rhode Island.

1. Experimental Data Requirements

Instantaneous velocity measurements were made at the jet developing region. The velocity components consist of the axial velocity u and the radial velocity v . From the instantaneous velocities, mean and fluctuating quantities were calculated. From the flow field measurements, the flow characteristics of the various confined jets were quantified. Simultaneously, pipe wall pressure and acceleration were measured for further data correlations. Acoustic characteristics of the confined jets were investigated and quantified. Other parameters, such as convection velocity and jet source strength distribution, were also determined.

2. NUSC Acoustic Water Tunnel

Phase I of the experimental study was conducted at the Naval Underwater Systems Center (NUSC) Acoustic Water Tunnel. As shown in figure 4-1, the acoustic water tunnel is a closed-loop system having a 8.9-cm (3.5-in.) ID circular and 10.2-cm / 30.5-cm (4-in. / 12-in.) rectangular test sections. The experiments were conducted in the circular Butyrate (elastic) test section, in which the pipe wall thickness is about 12.7 mm (0.5 in.). Water was pumped through this section at controlled centerline velocities ranging from approximately 4.6 to 15.2 m/sec (15 to 50 ft/sec). Noise reduction techniques have been incorporated in the design of the tunnel to prevent pump and piping noise from entering the test section through either structural or fluid paths. Some of the quieting features include the use of Neoprene screens, Butyrate plastic pipe, and nylon-reinforced fire hose to reduce the background noise. A detailed description of the acoustic water tunnel is given by Carey et al. (1967).

a. Test Program

Tests were run on the various flow configurations, including pipe flow and flow restrictors with the following pressure differentials across the restrictors: 2.76, 6.21, 9.65, 15.2, and 22.8×10^5 pascals (4,9,14,22, and 33 psi), and temperature at 21 °C (70 °F). These pressure differentials correspond to velocities ranging from 4.6 to 12.8 m/sec (15 to 42 ft/sec) through the orifice of the flow restrictors. The test conditions are summarized in table 4-1.

Table 4-1. Test Conditions - Phase I

Configuration	Flow Velocities (ft/sec)					
	15	22	28	35	42	50
No Flow (pump on, valved closed)	X	X	X	X	X	-
Circular Jet	X	X	X	X	X	-
Square Jet	X	X	X	X	X	-
2:1 Rectangular Jet	X	X	X	X	X	-
3:1 Rectangular Jet	X	X	X	X	X	-
Multiple Circular Jet	X	X	X	X	X	-
Coannular Jet	X	X	X	X	X	-
Slotted Jets	X	X	X	X	X	-
Pipe Flow	X	-	X	X	X	X

Impact testing was conducted on the Butyrate test section to determine the structural response of the test section. An impulse force was applied at various locations and the vibratory responses were measured at several points on the pipe wall (see figure 4-2).

b. Test Configurations

The flow configurations tested during phase I of the experimental study include: pipe flow, and flow restrictors with circular, coannular, and rectangular cross-sectional areas, as well as multiple circular and

slotted jets. Photographs and drawings of the flow restrictors tested are shown in figures 4-3 and 4-4. Note that the area of the various restrictor orifices was kept constant at about 6.45 sq. cm (1 sq. in.). Details of the flow restrictors geometry are summarized in table 4-2.

Table 4-2. Geometry of Flow Restrictors - Phase I

Configuration	Dia. (in.)	Length (in.)	Width (in.)	No. of Orifices	Perimeter (in.)	Hydraulic Dia. (in.)
Circular Jet	1.125	--	--	1	3.53	1.125
Square Jet	--	1.0	1.0	1	4.0	1.0
2:1 Rectangular Jet	--	1.4375	0.6875	1	4.25	0.93
3:1 Rectangular Jet	--	1.78125	0.5625	1	4.6875	0.855
Multiple Circular	0.5	--	--	5	7.854	0.5
Coannular Jet	$D_0=2.0$ $D_1=1.625$	--	--	1	11.388	0.35
Slotted Jets	--	1.0	0.2	5	12.0	0.333
Pipe Flow	3.5	--	--	--	11.0	3.5

Note: Orifice plate thickness is 9.5 mm (3/8 in.).

c. Flow Measurement - Mean Velocity Profile

Velocity profiles were measured at 25.4 cm (10 in.) downstream of the orifice plate using a Pitot tube. The probe was traversed across the inside diameter of the test section to obtain the averaged velocity profile.

d. Acoustic Instrumentation-Wall Pressure Transducers and Accelerometers

Wall pressure fluctuation and acceleration measurements were made using miniature Acoustic Research Corp. Model LD-107 M2 hydrophones flush-mounted on the inside wall of the pipe and Endevco Model 2220 C accelerometers mounted on the outside wall. Locations of the hydrophones and accelerometers are tabulated in table 4-3 and shown in figure 4-5.

Table 4-3. Location of Hydrophones and Accelerometers - Phase I

Hydrophones	H1	H2	H3	H4	H5	H6	H7	H8
Location (inches from orifice plate)	1.5	2	3	6	8	12	24	-24
Accelerometers	A1	A2	A3	A4				
Location (inches from orifice plate)	0	-24	1.5	24				

Hydrophone and accelerometer data were amplified and signal-conditioned by Ithaco Model 455 amplifiers and then FM recorded on a Honeywell Model 5600 B 14-channel analog tape recorder running at a tape speed of 76.2 cm/sec (30 in./sec). Acoustic data were monitored online by a Spectral Dynamics Model SD-375 frequency analyzer and simultaneously recorded on tapes for further data correlations and analyses. In addition, temperature and pressures, such as pressure differential, were recorded by a Honeywell UDC 500 Digital Controller

and Meriam mercury manometers, respectively. A schematic of the data acquisition system is shown in figure 4-6, and a list of instrumentation is given in table B-1 of appendix B.

3. NUSC Flow Loop Facility

Phase II of the experimental study was conducted at the Naval Underwater Systems Center (NUSC) Flow Loop Facility. This test facility is a closed-loop system with a 30,000-liter (7925-gallon) constant-head reservoir where the water surface is exposed to the atmosphere. The test section (figure 4-7) consists of a 5.1-cm (2.0-in.) I.D. plexiglass pipe with flange to flange dimension of 49.9 cm (19.25 in.) and pipewall thickness of 6.4 mm (0.25 in.). Water was pumped through the test section at controlled velocities ranging from 4.6 to 12.2 m/sec (15 to 40 ft/sec). A 3.1-m (10-ft) long flexible hose was installed at the upstream of the test section to reduce the structureborne and fluidborne noise generated by the 150-horsepower pump. The combination of a 7.6-cm (3-in.) control valve downstream and a 5.1-cm (2-in.) ball valve upstream of the test section provided control of flow through the orifice plate. The valve was located upstream of the flexible hose so that the unwanted noise produced by the valve could be attenuated by the flexible hose.

a. Test Program

The tests consisted of acoustic and flow measurements of the confined jet flows produced by the various orifice plates. The flow velocities through the orifices ranged from 4.6 to 12.2 m/sec (15 to 40 ft/sec), and temperature was maintained at 27 °C (80 °F). Test conditions are summarized in table 4-4.

Table 4-4. Test Matrix of Phase II

Configuration	Flow Velocities (ft/sec)						
	15	20	25	30	35	40	45
0.625-in. Orifice	X	-	(X)	X	(X)	X	-
0.75-in. Orifice	(X)	X	X	-	(X)	X	-
1.00-in. Orifice	-	X	X	X	X	(X)	X
1.25-in. Orifice	-	(X)	X	-	(X)	(X)	-
1.50-in. Orifice	-	X	X	X	(X)	X	-
1.25-in. Orifice (Thin Plate)	-	X	X	X	X	(X)	-
1.25-in. Orifice (Bevel Edge)	-	X	X	X	X	(X)	-
Pipe Flow	X	X	(X)	X	-	-	-

Note: () indicates LDV measurements.

b. Test Configurations

The flow configurations tested during phase II included: pipe flow, and circular flow restrictors with the pipe-to-orifice jet area ratios of 10.24, 7.11, 4.00, 2.56, and 1.78. In addition, orifice plates with various thickness and orifice edge sharpness (i.e., bevel edge) were tested. Photographs and drawings of the orifice plates are shown in figures 4-8 and 4-9. Table 4-5 tabulates the flow restrictor geometries.

Table 4-5. Geometry of Flow Restrictors - Phase II

Configuration	Dia. (in.)	Plate Thickness (in.)	$\beta=r/R$	Area Ratio
0.625-in. Orifice	0.625	0.1875	0.3125	10.24
0.75-in. Orifice	0.75	0.1875	0.3750	7.11
1.00-in. Orifice	1.00	0.1875	0.5000	4.00
1.25-in. Orifice	1.25	0.1875	0.6250	2.56
1.50-in. Orifice	1.50	0.1875	0.7500	1.78
1.25-in. Orifice (Thin Plate)	1.25	0.1250	0.6250	2.56
1.25-in. Orifice (Bevel Edge)	1.25	0.2500	0.6250	2.56
Pipe Flow	2.00	-	1.0000	1.00

Note: Orifice plate thickness was 4.8 mm (0.1875 in.).

c. Flow Measurements - LDV

Flow measurements were made on a the TSI System 9100-11, three-beam, two-component laser Doppler velocimeter (LDV). The LDV system employed in this study used the dual-beam optics concept. The dual-beam operating principle is based on the scattering of light from a small particle traversing the measurement or probe volume. The probe volume occurs at the intersection of two equal-intensity coherent laser light beams. The LDV optics were arranged to obtain the minimum-beam

waist diameter at the probe volume location. The intersection of two coherent laser light beams at the probe volume caused an interference fringe pattern to occur with a fringe spacing $d_f = \lambda / [2 \sin (\phi/2)]$, where λ is the laser light wavelength and ϕ is the angle between the two laser light beams. Light scattered from the particle traversing the probe volume was collected and focused onto the photomultiplier. The frequency of the light intensity f_D arriving at the photodetector was related to one component $f_D = U_1/d_f$, where U_1 is the velocity component perpendicular to the optical axis and in the plane of the two laser light beams. Further descriptions of dual-beam laser Doppler velocimetry, including the frequency shift used to prevent flow direction ambiguity, are presented in TSI LDV instrumentation manual (1982), and texts by Drain (1980), and Durst et al. (1981). The LDV data acquisition and reduction methods used in phase II were similar to those employed by Lefebvre (1987), and are briefly described in appendix C.

Axial and radial velocity components were simultaneously measured at 3 axial locations ($x = 8.4, 14.5$, and 26.2 cm or $3.3, 5.7$, and 10.3 in.) and 12 radial locations ($r = 0.0$ to 2.4 cm or 0.0 to 0.95 in.). Also, attempts were made to measure the normal pipe wall velocity for a few selected test conditions. The data sampling frequency was 10 kHz and the sampling time was 9 seconds. Furthermore, velocity measurements were taken at $x = 36.6$ cm (14.4 in.) and 183.9 cm (72.4 in.) for the 1.25-in. thin plate to provide far downstream data for fully developed jet flow.

d. Acoustic Instrumentation - Wall Pressure Transducers and Accelerometers

Wall pressure measurements were obtained using flush-mounted

hydrophones located downstream of the orifice plate. A photograph of the test section with instrumentation is shown in figure 4-10. Hydrophone and accelerometer locations are shown in figure 4-11. The wall pressure measurements were made by Wilcoxon model H506-1 hydrophones. Details of the hydrophone attachment are shown in figure 4-12. During the installation of hydrophones, a 0.8-mm (1/32 in.) thick elastomer layer was filled over the hydrophone sensing surface to provide a smooth surface with the pipe wall. The diameter of the hydrophone is 5.6 mm (0.22 in.). An experiment was conducted to determine the effective hydrophone sensing area using the technique developed by Gilchrist and Strawderman (1965). Results showed the ratio of effective radius to actual radius ranged from 50 to 74 percent. Calibration curves of the hydrophone from the manufacturer were utilized for the calculation of wall pressure fluctuations.

Pipe wall acceleration signals were acquired by several accelerometers located downstream of the orifice plate (figure 4-11). The structureborne noise signals were measured by Endevco model 2220 C accelerometers. Calibration of the accelerometers was performed using the B & K Type 4294 Calibrator. A known signal - 1 g at 160 Hz was applied at the accelerometers and signals were recorded.

Hydrophone and accelerometer locations as referenced to the orifice plate are summarized in table 4-6.

Table 4-6. Location of Hydrophones and Accelerometers - Phase II

Hydrophones	H1	H2	H3	H4	H5	H6	H7	H8
Location (inches from orifice plate)	2.5	2.5	4	6	9	9	12	14
Accelerometers	A1	A2	A3	A4	A5	A6		
Location (inches from orifice plate)	-10.5	2.5	4	6	9	12		

A MASSCOMP MC-5500 data acquisition system was utilized to acquire and process all data. The system is a 32-bit, Unix-based, embedded processor minicomputer configured with a high-capacity hard disk (133 Mbytes); a 16-channel, analog input board; and three digital input boards. This system has the capability of acquiring both analog and digital data simultaneously. In the phase II experiments, the LDV data were in digital form, whereas all acoustic and flow instrumentation had analog output of ± 5 volts. Simultaneously, hydrophone and accelerometer signals were recorded on a Honeywell Model 5600 E 14-channel analog tape recorder running at a tape speed of 76.2 cm/sec (30 in./sec). A list of instrumentation used in phase II of this experimental study is contained in table B-2 of appendix B.

4. Data Reduction

Acoustic and velocity data acquired by the MASSCOMP system were processed by the Interactive Laboratory System (ILS) digital signal processing and analysis software supplied by Signal Technology, Inc.

Analog and digital data were preprocessed prior to the data reduction by the ILS package. Data filtering, signal time histories, frequency spectra, data averaging, and signal correlations were performed on the acoustic data and LDV data. The analog (acoustic) data recorded were played back on a Nicolet Model 660 B dual-channel FFT spectrum analyzer for additional data correlations and analyses. A schematic of the data acquisition and reduction system is shown in figure 4-13.

The processed LDV data and acoustic data are presented in chapter 5. In general, the data are presented in the following sequence and format:

Flow Data:

- a. velocity and turbulence intensity versus time
- b. velocity and turbulence intensity spectra
 versus radial and axial location
- c. statistical measure of velocities - skewness and
 flatness factor versus radial location

Acoustic Data:

- a. signal versus time
- b. narrowband and one-third-octave spectra
- c. signal correlations - transfer function, coherence function,
 transmissibility of acceleration and pressure, auto correlation
 and cross correlation functions

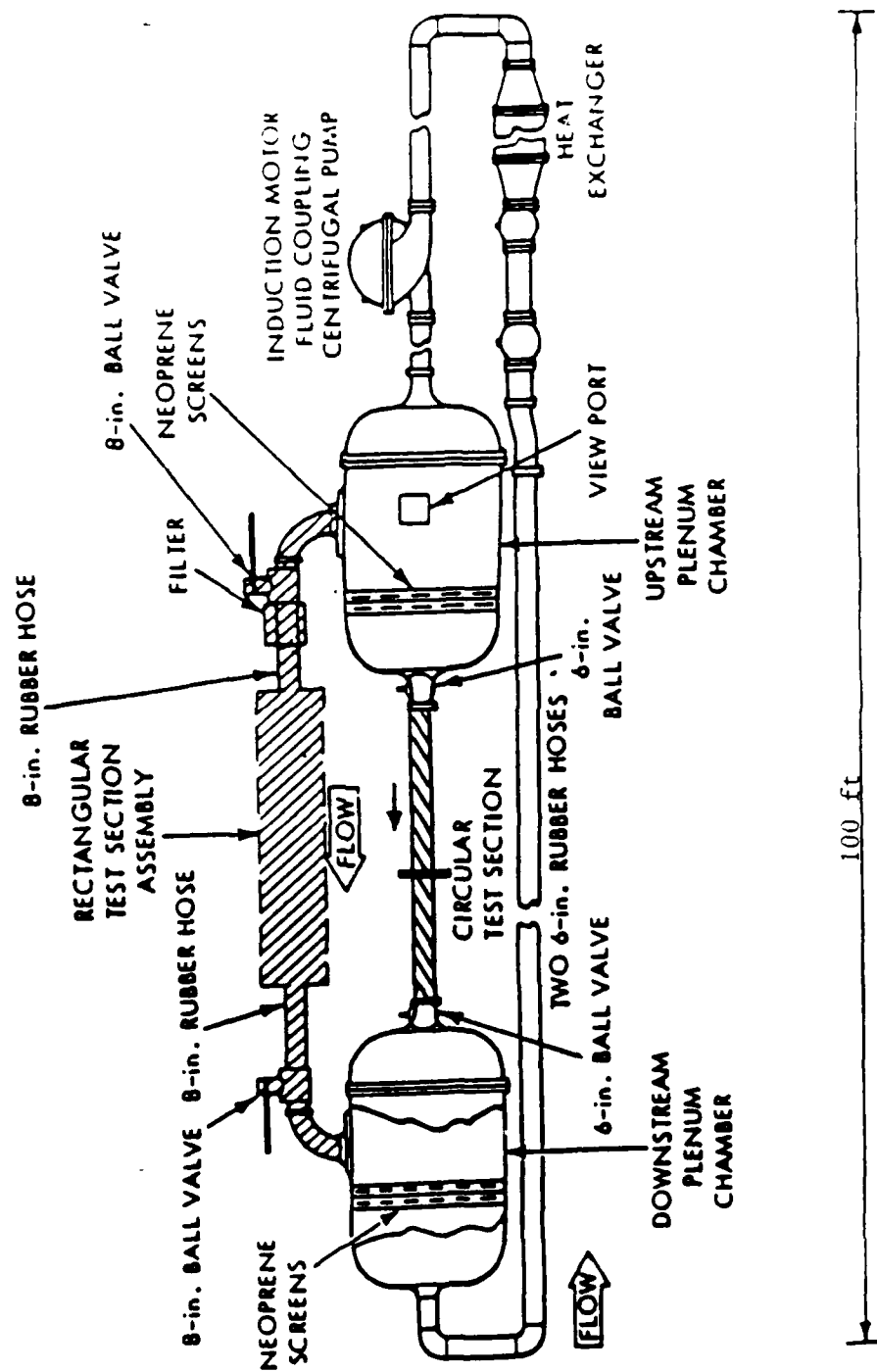


Figure 4-1. NUSC Acoustic Water Tunnel

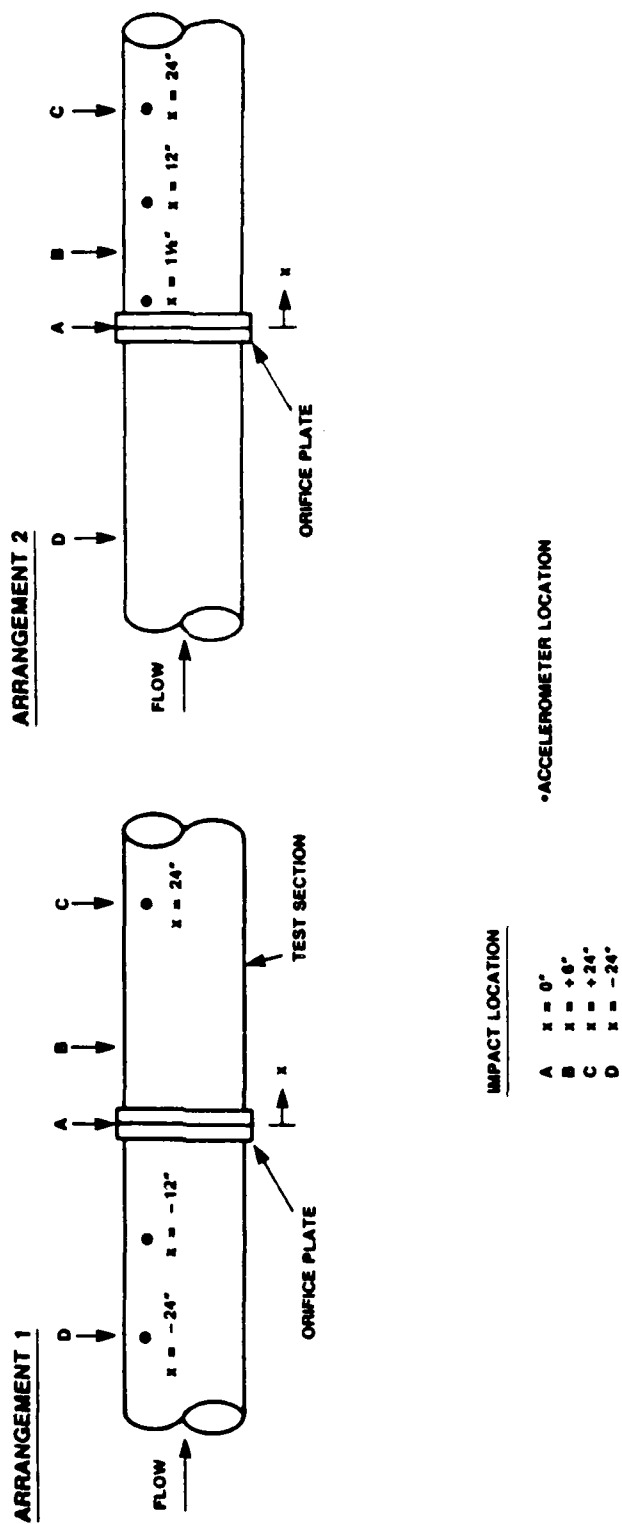
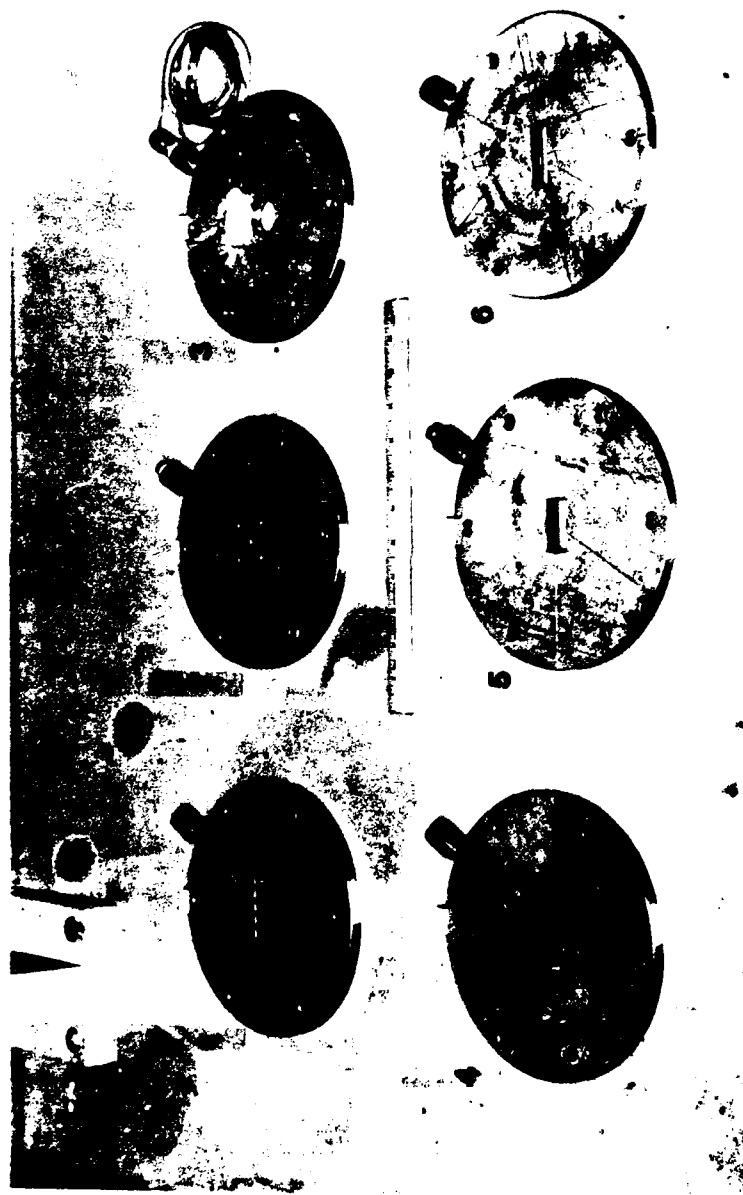


Figure 4-2. Experimental Setup for Impact Test - Phase I



- | | |
|----------------------|--------------------|
| 1) SLOTTED JETS | 4) COANNULAR |
| 2) MULTIPLE CIRCULAR | 5) 2:1 RECTANGULAR |
| 3) CIRCULAR JET | 6) 3:1 RECTANGULAR |

Figure 4-3. Photograph of Flow Restrictors - Phase I

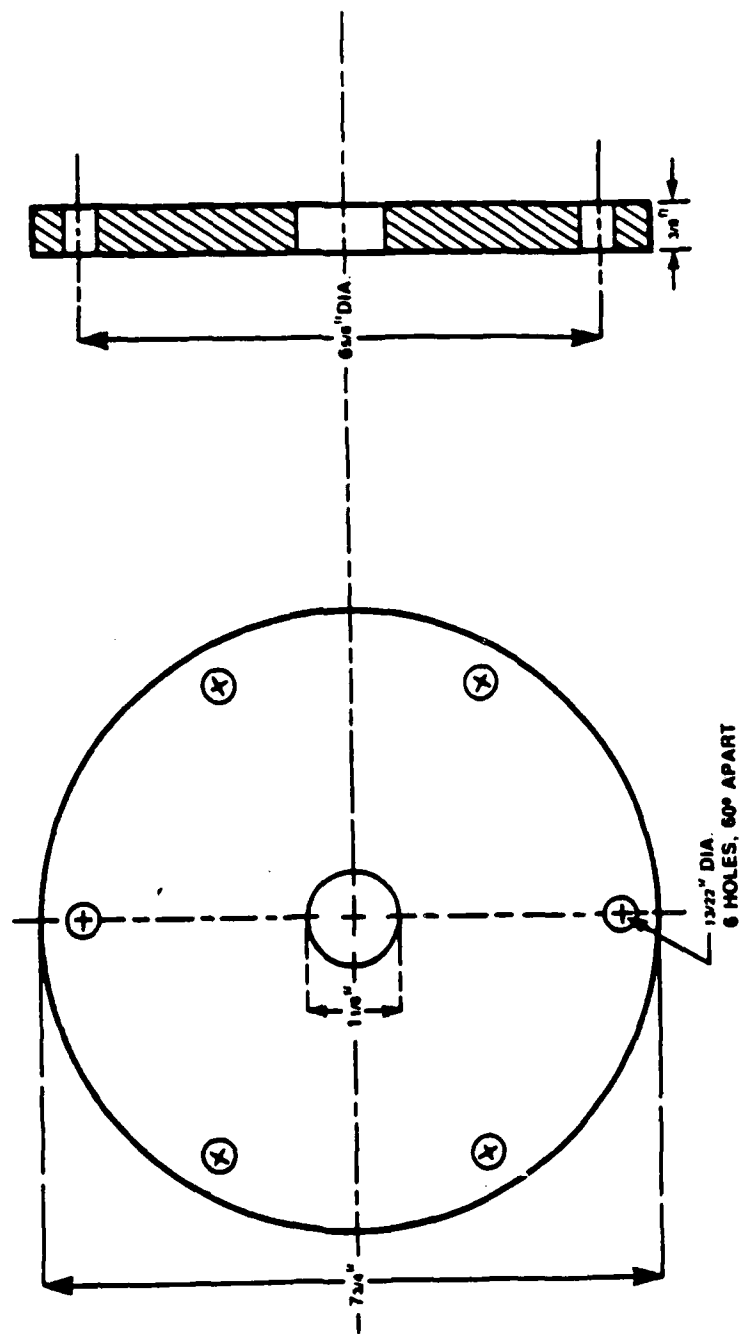


Figure 4-4. Geometry of Flow Restrictors - Phase I

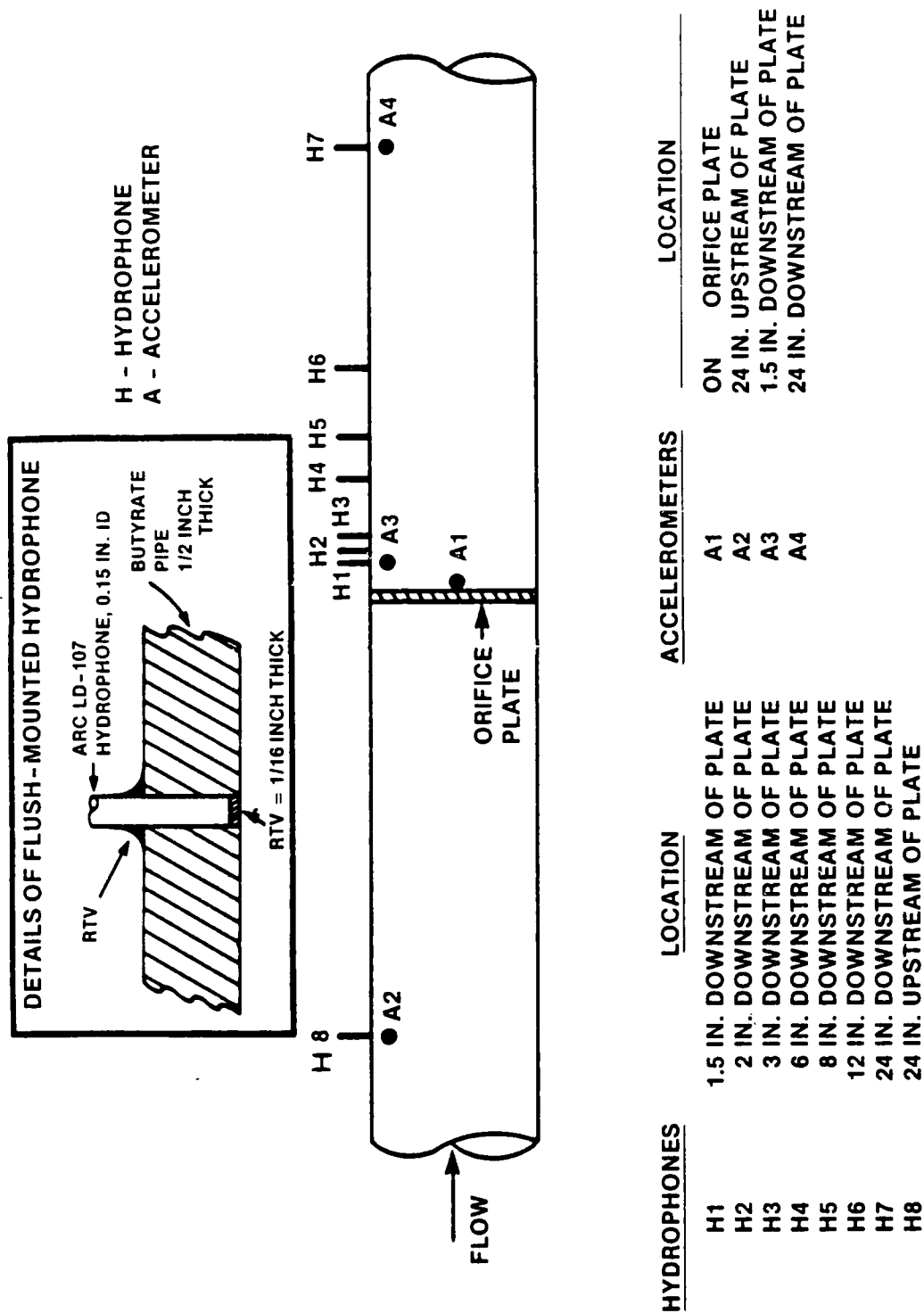


Figure 4-5. Test Section Instrumentation - Phase I

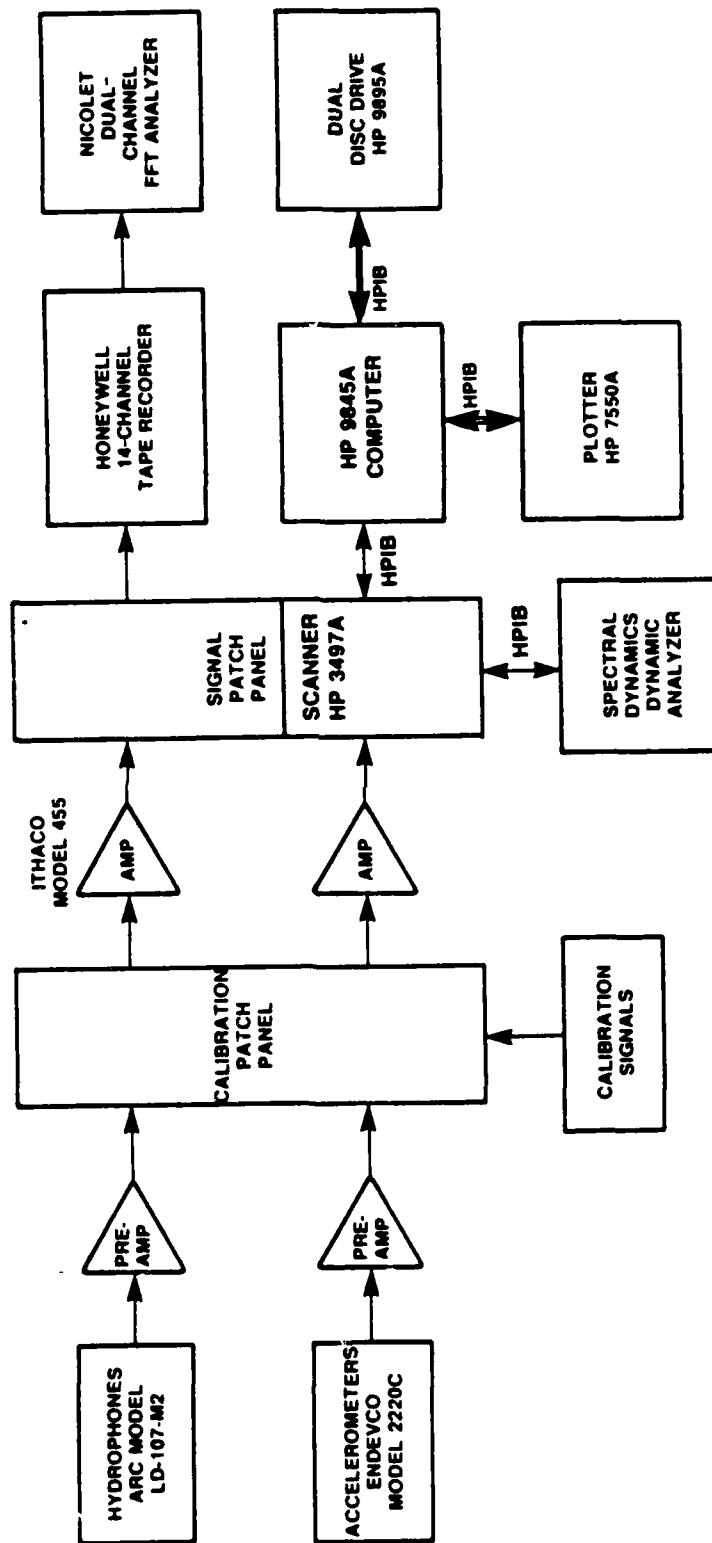


Figure 4-6. Data Acquisition System - Phase I

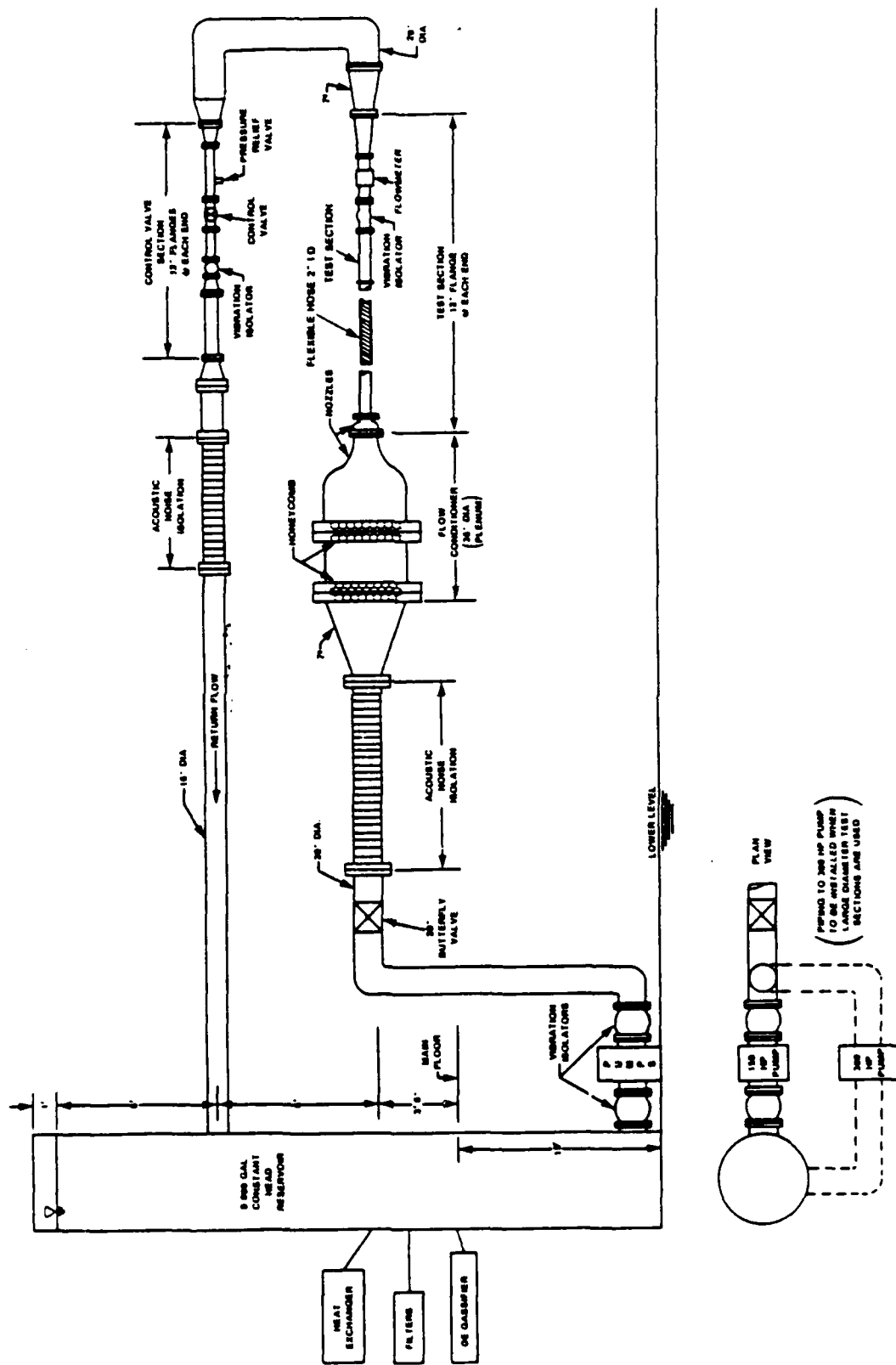


Figure 4-7. NUSC Flow Loop Facility

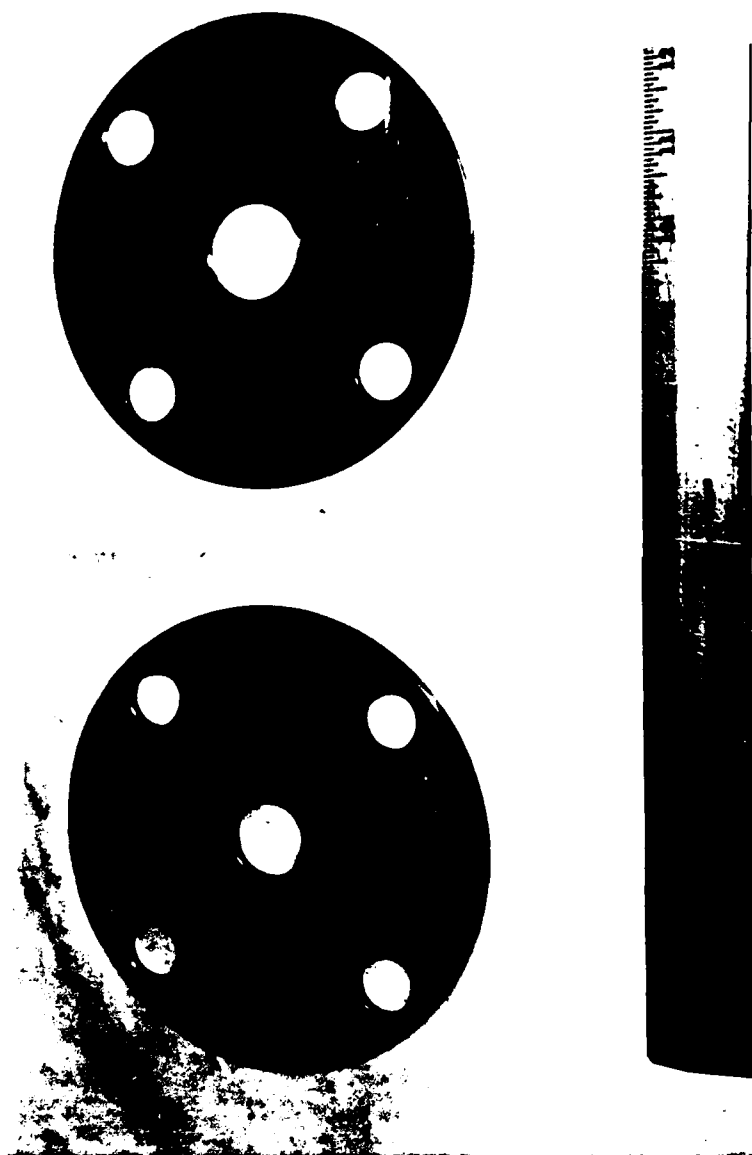


Figure 4-8. Photograph of Flow Restrictors - Phase II

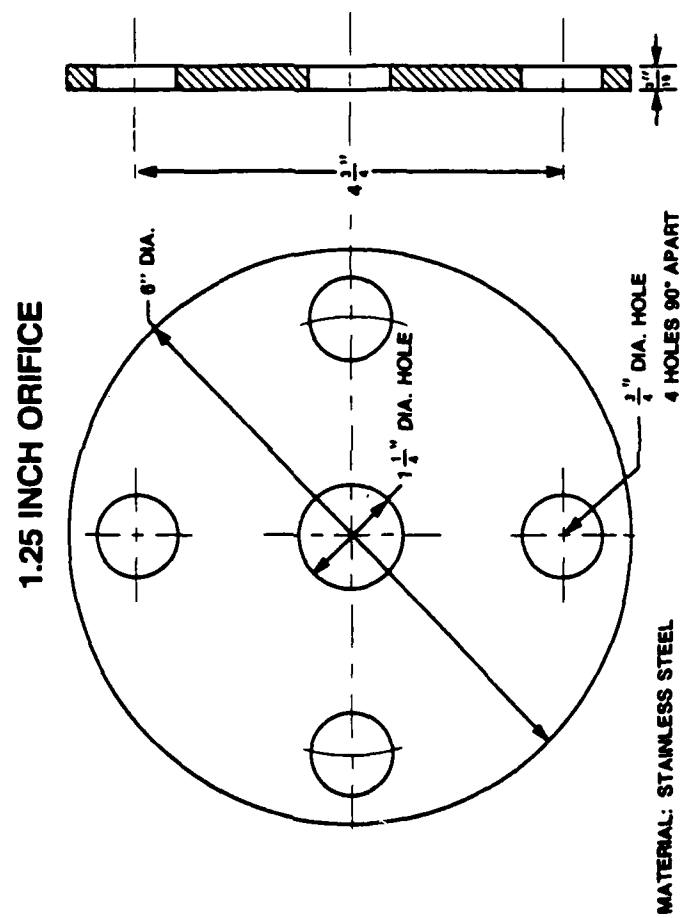
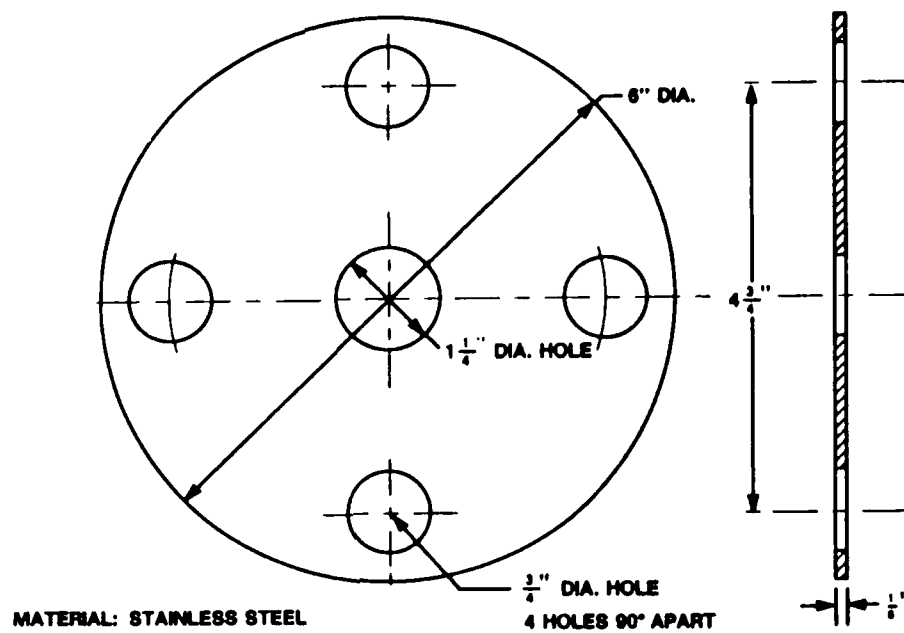


Figure 4-9. Geometry of Flow Restrictors- Phase II

1.25 INCH ORIFICE (THIN PLATE)



1.25 INCH ORIFICE (BEVEL EDGE)

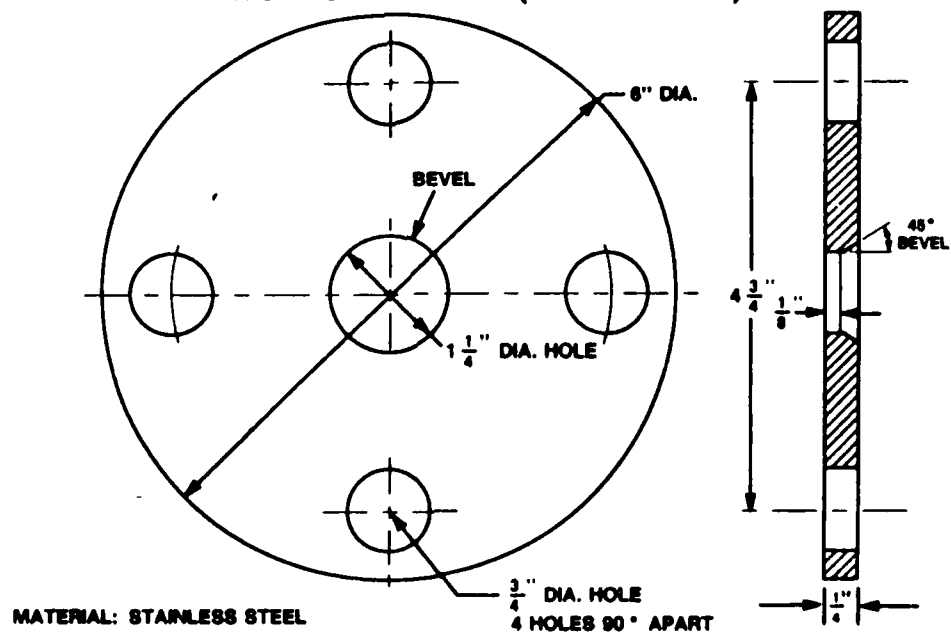


Figure 4-9. Geometry of Flow Restrictors- Phase II (Cont'd)

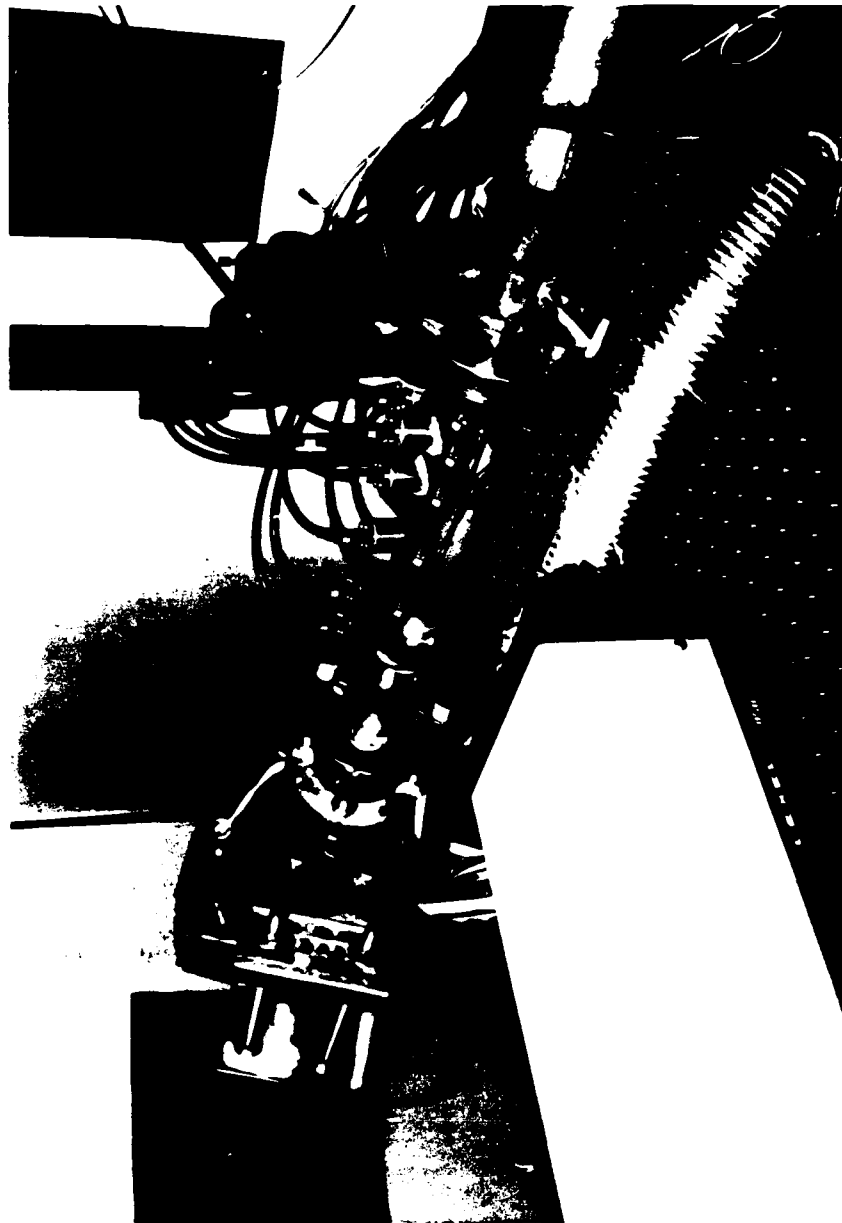
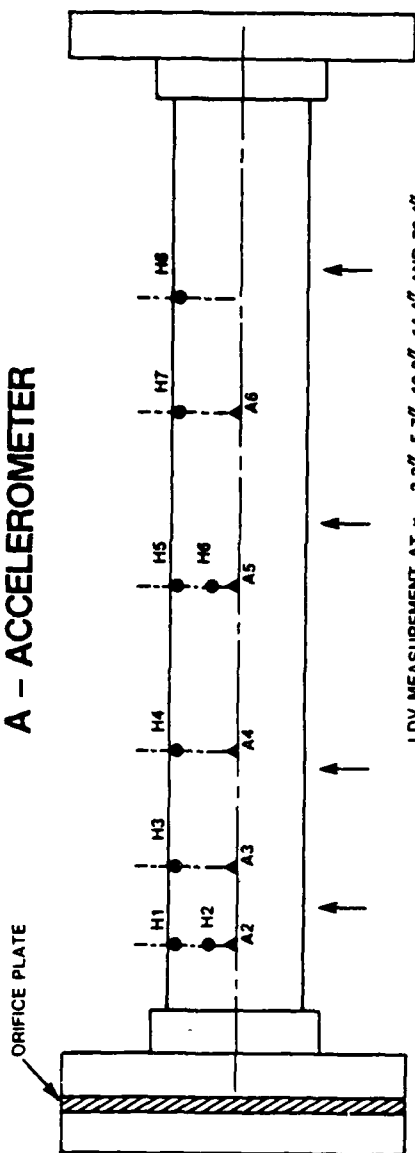


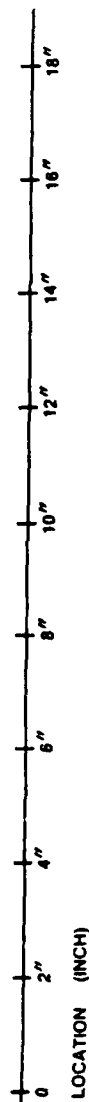
Figure 4-10. Photograph of Test Section with Instrumentation

H - HYDROPHONE
A - ACCELEROMETER



LDV MEASUREMENT AT $x = 3.3''$, $5.7''$, $10.3''$, $14.4''$ AND $72.4''$

→ FLOW



HYDROPHONES LOCATION X INCH	1	2	3	4	5	6	7	8
	2.5	2.5	4	6	9	9	12	14

ACCELEROMETERS LOCATION X INCH	1	2	3	4	5	6	9	12
	-10.5	2.5	4	6	9	12		

Figure 4-11. Test Section Instrumentation- Phase II

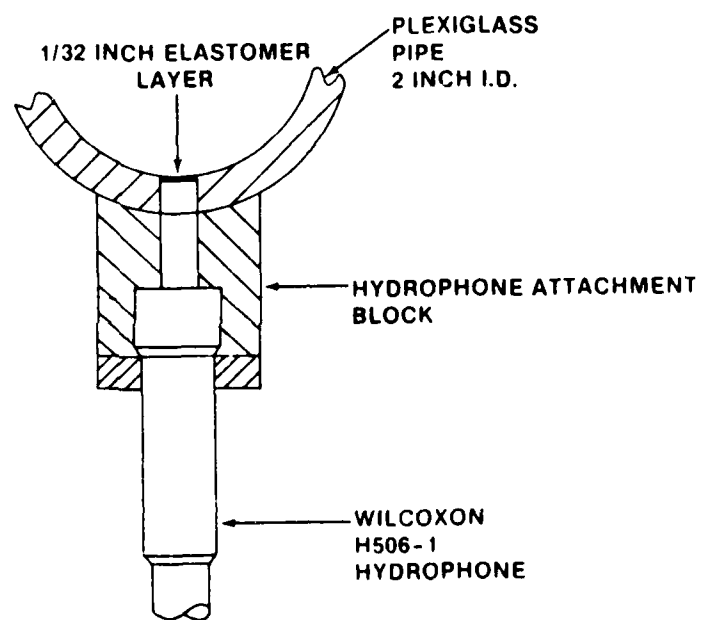


Figure 4-12. Details of Hydrophone Attachment

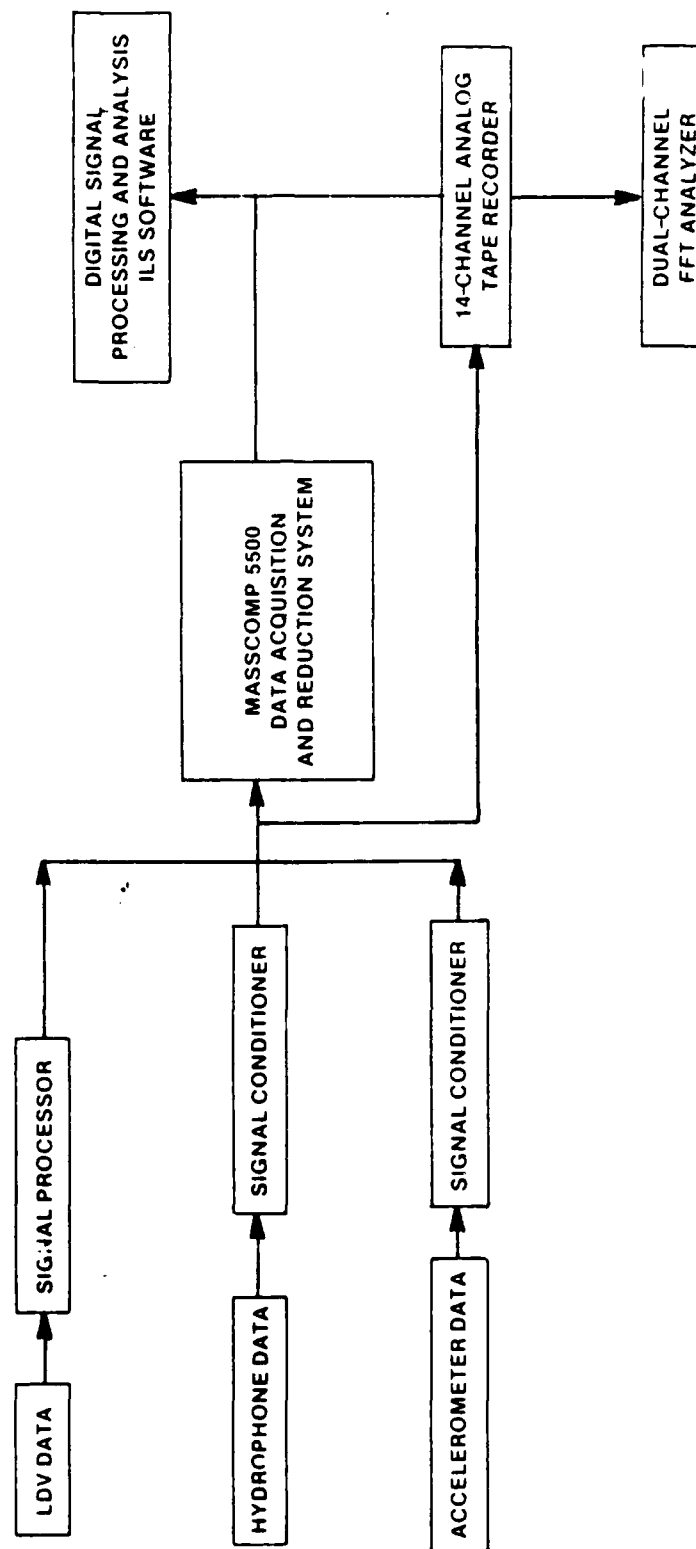


Figure 4-13. Data Acquisition System - Phase II

CHAPTER 5

EXPERIMENTAL RESULTS AND DISCUSSION

In this chapter, results from the experimental program are presented. The discussion and presentation of the data are arranged in the following manner:

1. Flow characteristics
2. Acoustic characteristics
3. Vibrational characteristics

In each section, results from phase I of the experimental program are presented first, then followed by results from phase II.

1. Flow Characteristics

a. Phase I Study of Various Confined Jet Flows - Velocity Profile Measurements

To understand the flow characteristics of pipe flow and flow restrictors, mean velocity profiles were measured at 25.4 cm (10.0 in.) downstream of the orifice plate. Typical plots of the normalized velocity versus radius for pipe flow and flow restrictors - circular, square, and multiple circular jets are shown in figure 5-1. As shown, pipe flow and multiple circular jets have a flat velocity profile, whereas circular and square jets have a relatively sharp profile.

Results of the mean velocity profiles from the experiment were compared with the calculations using the K and ϵ model (turbulence energy and dissipation equations). Details of the flow calculations were presented by Ng (1986), and a summary is presented in appendix D. Typical comparisons of the velocity profiles are shown in figures 5-2 and 5-3 for pipe flow and the circular jet, respectively. As shown, the calculated profiles are in good agreement with the measurements. In

addition, the streamlines were also calculated. These lines show the recirculation region behind the orifice plate (figure 5-4). The negative velocities shown in figure 5-3 are due to flow recirculation.

b. Phase II Study of Flow and Acoustic Characteristics
of Circular Confined Jets

(1) Velocity Profile Measurements

To validate the velocity measurements, the LDV data were compared with the pipe flow data from Laufer (1952). Comparisons of the mean velocity profiles are shown in figure 5-5. In the present study, the pipe flow Reynolds number ranges from 2.8×10^5 to 4.7×10^5 . As shown, the LDV data compare reasonably well with Laufer's data. In addition, flow rates were calculated by integrating the velocity profiles; results showed the calculated values were within 3 percent of the flowmeter measurements.

Mean normalized velocity (U/U_j) profiles of the confined jets are shown in figures 5-6 through 5-8 for the three axial locations, i.e., $x = 8.4$, 14.5 , and 26.2 cm (3.3 , 5.7 , and 10.3 in.). As shown in figure 5-6, the jet velocity profiles are relatively sharp at $x = 8.4$ cm. For the smaller jets, negative velocities that correspond to flow recirculation can be seen near the wall. Because of data acquisition problem, no data are plotted for radius ratio (r/R) of 0.6 and greater for the 1.00 -in. diameter jet. Further downstream, i.e., at $x = 14.5$ and 26.2 cm, the velocity profiles are flatter (see figures 5-7 and 5-8).

It has been mentioned previously that further downstream the jet flows eventually develop to pipe flow. To confirm this trend, velocity measurements were taken far downstream from the orifice plate; indeed, measurements showed that, at 36 pipe diameters downstream, the velocity

profile approaches the fully developed pipe flow profile. Comparisons of the far-downstream jet flow profiles with the pipe flow are shown in figure 5-9.

As was similarly done in phase I, the measured velocity profiles were compared with the calculations using the K and ϵ model. Comparisons of the measured and calculated velocity profiles are shown in figures 5-10 and 5-11 for pipe flow and the 0.625-in. diameter jet respectively. As illustrated, the measured data compared well with the calculation for pipe flow and reasonably well for jet flow.

(2) Turbulence Intensity Profile

Based on the instantaneous velocity measurements, the fluctuating quantities (such as turbulence intensities and Reynolds stresses) were calculated. Plots of the intensities u'^2/V_j^2 , v'^2/V_j^2 , and $u'v'/V_j^2$ are shown in figures 5-12 and 5-13 for the 1.25-in. diameter jet and pipe flow, respectively. Note that in the jet flow the profile of the axial velocity fluctuations u'^2 are similar to the mean velocity profile. The radial velocity fluctuations v'^2 show a peak value at the shear layer of the jet. The Reynolds stress $u'v'$ is relatively low as compared with the turbulence intensities. In pipe flow, the turbulence intensities increase toward the wall, whereas the Reynolds stress is quite constant and lower than the turbulence intensities.

(3) Skewness and Flatness Factors

The third and fourth moments, i.e., skewness and flatness factors, were calculated according to the relationship given by Hinze (1975). Figures 5-14 and 5-15 depict the skewness and flatness factors of the axial velocity u and radial velocity v components for pipe flow. As shown, the skewness of the v component ranges from 1 to 3, and the skewness of the u component ranges from -0.5 to 0.5. It should be noted

that the skewness factor is 0 and flatness factor is 3 for a Gaussian (normal) distribution. This implies that the distribution of the u component is more Gaussian. Typical skewness and flatness factors for the 0.625-in. diameter jet are shown in figures 5-16 and 5-17. Again, the distribution of the u component is more Gaussian, and the skewness and flatness factors of the v component are higher than the u component.

(4) Spectral Characteristics of the Velocities

Based on the velocity measurements, the velocity fluctuations, turbulence intensities, and Reynolds stresses were calculated. Typical time histories of the various velocity quantities are shown in figure 5-18 for the 1.5-in. diameter jet. The velocity quantities include instantaneous velocities u and v , velocity fluctuations u' and v' , Reynolds stress $u'v'$, and turbulence intensities u'^2 and v'^2 . The corresponding distribution function of the axial and radial velocity components are shown in figures 5-19 and 20. To illustrate the spectral characteristics, instantaneous frequency spectra of the u and v velocity components are shown in figures 5-21 and 5-22. In general, the spectral amplitude of the u component has a relatively rapid decay, whereas the spectral amplitude of the v component is quite constant.

During the test, considerable care and effort were spent to increase the LDV data rate and signal-to-noise ratio; nevertheless, the data rate was only up to 5 kHz, which is about half the sampling frequency. Also, the measurements near the wall suffered from a high noise problem, such as due to the light reflection from the pipe wall surface. Thus, in interpreting the LDV data, the high frequency information, (i.e., above 2.5 kHz) should not be considered.

2. Acoustic Characteristics

a. Phase I Study of Various Confined Jet Flows

Frequency analyses and data correlations were performed on the wall pressure and acceleration signals. Root mean square (rms) spectra, as well as the transfer function, coherence function, and cross correlation function, were obtained using a dual-channel spectrum analyzer. Data averaging (sum averaged of 4 samples) was applied on frequency spectra, transfer functions, and coherence functions. Velocity across the orifice plate was calculated using the measured differential pressure according to the following relationship:

$$V_j = C_d \sqrt{(2\Delta P g_c) / [\rho(1-\beta^4)]},$$

where $C_d = 0.6$, ΔP is the differential pressure, g_c is the gravitational constant, ρ is the density of water, and β is the orifice radius to pipe radius ratio, i.e., $\beta = d/D$.

(1) Broadband Noise Characteristics

A typical plot of overall sound pressure levels versus pipe axial location for the various flow restrictors is shown in figure 5-23. The overall sound pressure level is the band level from 70 to 2000 Hz, which was calculated from the wall flush-mounted hydrophone measurements by using the calibration curves and bandwidth correction. According to the relationship given by Bakewell (1962) on the pressure correction due to finite size of the transducer, the correction factor is about 0.93. Since the correction factor is close to unity, no correction was applied on the wall pressure measurements.

As shown in figure 5-23, the plots of the various restrictors are similar in that the peak noise is located about 15.2 cm (6 in.) downstream of the orifice plate. This distance is equivalent to about 6

jet diameters and, according to jet flow theory, corresponds to the end of the jet potential core. It should be noted that the peak noise levels are about 15 dB above the upstream levels. This result is quite similar to the mixing noise of free subsonic jets from Ahuja et al. (1985). Note that in pipe flow (i.e., without a flow restrictor) the noise levels are quite constant (figure 5-24).

(2) Scaling of Noise with Jet Velocity

Plots of overall sound pressure level versus jet exit velocity are shown in figure 5-25 for the various jet configurations. The noise levels are based on measurements from hydrophone 1, which was located at 3.8 cm (1.5 in.) downstream of the orifice plate. As shown, the pipe flow data yield a velocity exponent of 4.4 while the average of flow restrictors data also yield a velocity exponent of 4.4. This velocity exponent is in good agreement with the results from Stahl (1985). Values of the averaged velocity exponents for the other hydrophones are tabulated in table 5-1 and shown in figure 5-26.

Table 5-1. Values of Velocity Exponents for Flow Restrictors - Phase I

Hydrophone Number	H1	H2	H3	H4	H5	H6	H7
Velocity Exponent	4.4	4.8	5.0	4.6	4.5	4.2	3.7

These velocity exponents were obtained using the first-order polynomial least-squares fit of data. The variances of the least-squares fit are less than 1.5 dB. As shown in table 5-1, the velocity exponents of the flow restrictors range from 3.7 to 5.0. Note that the exponent increases in the downstream direction; it reaches the

maximum value at hydrophone 3 (7.6 cm or 3 in. downstream of the orifice plate) and then it decreases. Haddle and Skudrzyk (1969) have documented that flow noise is due mainly to the dipole-type source; and, theoretically, dipole source noise is related to the flow Mach number raised to the sixth power or is equivalent to velocity exponent of 6. The difference with the theoretical value is probably due to the flow-induced vibration component or structural response of the piping systems.

(3) Spectral Noise Characteristics

The spectral noise characteristics of pipe flow and confined jet flow are shown in figure 5-27. The narrowband spectra of pipe flow and circular jet flow (restrictor flow) are plotted and compared with the background noise, which is mainly due to the pump. As shown, the pipe flow spectrum is relatively smooth and straight whereas the circular jet spectrum is not smooth and decays faster than the pipe flow spectrum. Note that both flow noise spectra are about 40 dB higher than the background noise, which indicates the good quality of noise measurements in the water tunnel.

Figure 5-28 shows the non-dimensional one-third-octave noise spectra of the circular jet as measured by hydrophone 1. The adjusted one-third-octave noise levels were plotted against the Strouhal number. The noise levels were adjusted for fluid density, jet diameter, and velocity according to

$$\Delta dB = 10 \text{ Log } (d \rho^2 V_j^3) ,$$

where d is the jet diameter, ρ is the density, and V_j is the jet velocity. The Strouhal number is defined as

$$St = fd/V_j ,$$

where f is the frequency. As shown in figure 5-28, the noise spectra

collapsed reasonably well.

The non-dimensional noise spectra of the various flow restrictors are quite similar, except that the coannular and slotted jets show more high-frequency noise. This high-frequency noise is depicted in figure 5-29 for the coannular jet. For the complicated flow restrictor configuration, the hydraulic diameter was used as the length scale in the Strouhal relationship. Calculated values of the hydraulic diameters of the various flow restrictors were given earlier in table 4-2.

Typical non-dimensional noise spectra for the various flow restrictors at hydrophone 4 are shown in figure 5-30. As with the circular jet spectra (figure 5-28), the noise spectra at the other hydrophones collapsed quite well. The collapsed curve (spectrum) can be represented by using the third-order polynomial least-squares fit:

$$Y = 94.678 - 18.651X - 16.183X^2 - 7.874X^3 ,$$

where Y is the one-third-octave noise level, and X is the logarithm of the Strouhal number.

(4) Cross Correlation of Signals

Cross correlations of two hydrophone signals, as expressed in terms of the transfer function, are presented in figures 5-31 and 5-32. Transfer function is the complex ratio of cross spectrum G_{AB} to input power spectrum G_{AA} . It defines the phase lag and gain introduced by a transmission system excited by input $A(t)$ and responding with output $B(t)$. Typical transfer functions of the hydrophone signals, such as hydrophone 1 vs hydrophones 2, 3, 4, 5, 6, and 7 for pipe flow are shown in figure 5-31. In each plot, the upper trace is the phase angle between the correlated signals, whereas the lower trace is the magnitude of the transfer function. As shown in figure 5-31, the phase angles between the hydrophone signals are quite random, which indicates that

the wall pressures at the various locations on the pipe wall are random or uncorrelated.

Typical transfer functions of the hydrophone signals for the circular jet are shown in figure 5-32. The circular jet data are quite representative of the various flow restrictors and, for brevity, only the circular jet transfer functions and coherence functions are presented. As compared with those for pipe flow, the transfer functions of the hydrophone signals for circular jet flow are more deterministic. The phase angle is relatively small and constant for hydrophones with small separation (e.g., hydrophone 1 versus hydrophone 2 and hydrophone 1 versus hydrophone 3). As the hydrophone separation increases, the phase angle increases with frequency.

Typical transfer functions of the accelerometer signal versus the various hydrophone signals for the 3:1 rectangular jet are shown in figure 5-33. Note that the results from the correlation of accelerometer versus hydrophone signals are similar to the hydrophone signals. Based on the phase angle information, the convection velocity of pipe flow was calculated to be about 0.6 of the free-stream velocity.

Coherence functions of the hydrophone signals for pipe flow and circular jet flow are shown in figures 5-34 and 5-35. Coherence function is a real spectrum "power squared" ratio indicating the linear cause/effect relationship between input $A(t)$ and output $B(t)$. The coherence function γ^2 has a value lying between 0 and 1 that provides an unambiguous indication of the causal relationship between the input and output. If $\gamma^2 = 1$, the two signals are correlated; whereas $\gamma^2 = 0$, the two signals are uncorrelated. As shown in figure 5-34, the pipe flow coherence functions are relatively low. This result is consistent with the data shown in figure 5-31 in that the hydrophone signals are

uncorrelated. The coherence functions for circular jet flow are shown in figure 5-35, and they are higher than those for pipe flow. In particular, the coherence function near the jet exit is higher than those further downstream. This high coherence function has been attributed to the highly correlated pressure fluctuations due to the large-scale structures in jet flow. Sarohia and Massier (1978), Long and Arndt (1984), and Abdallah (1984) have reported that a significant part of the pressure fluctuations near the exit of the jet was contributed by the interaction and merging processes of these large-scale coherent structures.

b. Phase II Study of Flow and Acoustic Characteristics of Circular Confined Jets

Frequency analyses and data correlations were performed on the velocity, wall pressure and acceleration signals. Root mean square (rms) spectra, as well as the transfer functions, coherence functions, and cross correlation functions, were obtained using the (ILS) digital signal processing and analysis software as described in section 4 of chapter 4. Data averaging based on sum averaged of 4 samples was applied on the frequency spectra and coherence functions.

(1) Acoustic Checkout of the Flow Loop Facility

Prior to the actual data collection phase (phase II) of the experimental program, an acoustic checkout of the Flow Loop Facility was conducted. Pipe wall acceleration measurements were taken at the various locations of the flow loop. The objective was to assess the background noise, pump noise, and water flow noise levels. Results of the noise measurements are shown in figure 5-36. The rms acceleration spectra are shown for the following conditions: pump off, pump on with no flow, and pipe flow at 4.9 m/sec (16 ft/sec) and 9.8 m/sec (32 ft/sec).

In figure 5-36, the upper trace corresponds to the accelerometer signal downstream of the flow conditioner, and the lower trace is the acceleration measurement at the test section. In the pump off condition, the electronic noise (such as 60 Hz) dominates the noise spectra. Once the pump starts up, the fundamental blade passage frequency at 146 Hz and its harmonics can be observed. It should be pointed out that the pump was designed to operate at a constant pump speed. As shown, the acceleration levels at the test section are quite independent of flow velocity.

From these measurements, it was concluded that the pump noise could be a potential noise source at the low frequencies (i.e., below 300 Hz). To minimize this problem, a 10-ft-long flexible hose designed for structureborne noise isolation was installed upstream of the test section. Subsequent noise measurements showed that the flexible hose reduced the pump noise level by as much as 20 dB at the low frequencies.

(2) Signal Versus Time Plots

Typical hydrophone signal versus time plots are depicted in figure 5-37 for the 1.25-in. jet. It can be seen that the amplitude of the wall pressure signals stays constant in the first few jet diameters, then decreases further downstream. A better description of the wall pressure as a function of axial location is presented in the next section.

(3) Broadband versus Axial Location

Plots of overall sound pressure level (OASPL) versus axial location are shown in figures 5-38a through 5-38h. The overall sound pressure levels are broadband levels that cover the frequencies from 200 Hz to 5 kHz. As shown in figure 5-38h, the broadband levels are quite constant

for pipe flow. For the various jets, the broadband levels stay almost constant for the first few jet diameters, then they decay in the downstream direction.

As noted earlier, the broadband levels increase toward the end of the jet potential core, then they decrease in the downstream direction. Because of the wide separation of hydrophones near the exit of the jets, the details of the growth region were lost. For comparison and reference purposes, plots of the broadband levels versus axial location are shown in figure 5-39 for the circular jet from the phase I test program. As shown, the pressure fluctuations increase toward the end of the jet potential core, then they decrease with distance.

(4) Scaling of Noise with Jet Velocity

As in phase I, the overall sound pressure levels of hydrophone 1 were plotted versus jet velocities. Plots of pressure levels with $10 \log V_j$ are shown in figures 5-40a and 5-40b for the various jets and for pipe flow. Values of the velocity exponents are tabulated in table 5-2 and results are presented in figure 5-41.

Table 5-2. Values of Velocity Exponents - Phase II

	Jet Configuration						
	Pipeflow	0.625	0.75	1.00	1.25 Thin	1.25 Bevel	1.50
Exponent	3.4	5.1	3.9	4.3	3.7	3.1	2.8

The velocity exponent of the 0.625-in. diameter jet is consistent with the results from phase I (table 5-2). Again, these velocity exponents are in good agreement with the results of Stahl (1985). The value of the velocity exponent reported by Stahl is 4. It should be noted that

in figure 5-41, the value of the velocity exponent decreases with increasing jet diameter.

(5) Spectral Characteristics

Non-dimensional one-third-octave wall pressure spectra are shown in figures 5-42a through 5-42f for the various jets. The adjusted or shifted one-third-octave levels were plotted against the Strouhal number according to equations defined earlier. The collapsed noise spectrum obtained from phase I using the third-order polynomial least-squares fit, is also shown in the figures for comparison. As shown, the normalized spectra collapse rather well for the range of velocities tested and, most important of all, they agree reasonably well with the least-squares fit of spectral data from phase I. Note that comparison with the least-squares fit of data is excellent for the larger jets. However, the collapsed noise spectra of the 0.625 and 0.75-in. diameter jets are lower than the least-squares fit of data.

To measure the quality of the normalized jet spectra, the collapsed jet spectrum (least-squares fit of data from phase I) is plotted and compared with the results from Bakewell et al. (1962), Schloemer (1974), and Willmarth and Wooldridge (1962). As shown in figure 5-43, the least-squares fit of spectral data compares well with the others' published data. The difference in the high frequencies is probably due to the hydrophone correction. As mentioned previously, no correction was applied on the wall pressure measurements because of the small size of the hydrophone. Also, it should be pointed out that the normalized pressure spectra referenced from Bakewell et al., Schloemer, and Willmarth and Wooldridge were based on the measurement of turbulent boundary layer (TBL) from external flows. It is quite remarkable that the wall pressure spectra of the confined jets agree well with the TBL

using hydraulic diameter as the length scale for the jets.

(6) Cavitating Jet Noise Characteristics

Most of the data presented and discussed so far are for non-cavitating jets. During the test, the smaller jets were intentionally operated in cavitating condition for a few selected runs. The objective was to quantify the noise characteristics of cavitating confined jets. Typical wall pressure spectra are shown in figures 5-44a and 5-44b for the 0.625 and 0.75-in. diameter jets. The noise spectra of the cavitating jets exhibit a double-peak characteristics. The second peak is probably due to the cavitation noise. Similar results were previously observed from valves operating under cavitating conditions (see results reported by Ng and Sonderegger (1982)).

(7) Coherence of Hydrophone Signals with Flow Field Data

Typical coherence functions of hydrophone data with flow field data are shown in figures 5-45 and 5-46 for the 0.625-in. diameter jet flow and pipe flow, respectively. Figure 5-45a shows the coherence of hydrophone data at hydrophone 3 with the axial velocity u measured at $x = 8.2$ cm. As presented previously, both the u component and hydrophone data (figure 5-21 and figure 5-27) show similar spectral characteristics in which the spectral levels decay quite rapidly. However, their coherence function as shown in figure 5-45a is relatively low, ranging from 0.1 to 0.6. Similar results are shown in figure 5-45b for the v velocity component (measured at $x = 8.2$ cm) and acceleration data. Again, similar trends are shown in figures 5-46a and 5-46b for pipe flow. As mentioned previously, the data rate of the LDV system was less than 5000 samples per second and, certainly, it could affect the coherence with the acoustic data.

(8) Coherence of Hydrophone Signals

Typical coherence functions between hydrophone signals are shown in figures 5-47 and 5-48 for the 0.625-in. diameter jet and pipe flow, respectively. Figures 5-47a through 5-47e show the correlation functions between hydrophones, such as hydrophone 1 versus hydrophone 3, hydrophone 3 versus hydrophone 5, etc. As illustrated, the coherence functions are relatively high, in particular for frequencies below 600 Hz. The high coherence functions between the hydrophones imply that the pressure fluctuations or blocked pressure generated by the confined jet are highly correlated in the x direction. As discussed before, this high coherence for jet flow could be attributed to the large-scale coherent structures. Similarly, coherence functions between the various hydrophone signals are shown in figures 5-48a through 5-48c for pipe flow. However, the coherence functions for pipe flow are lower than those for jet flow, which indicate that the blocked pressure are uncorrelated for pipe flow. This trend is consistent with the phase I data shown in figures 5-34 and 5-35.

3. Vibrational Characteristics

a. Phase I Study of Various Confined Jet Flows

To determine the structural characteristics of the test section, impact testing was conducted. RMS acceleration spectra of the various accelerometers with an impulse force at the orifice plate location ($X = 0$ cm) are shown in figure 5-49. The spectral plots show that the pipe response was quite symmetric, in that the acceleration levels at 61 cm (24 in.) upstream are very similar to those at 61 cm (24 in.) downstream. Note that the structural response is dependent on the axial location. The corresponding transfer functions and coherence functions are shown in figures 5-50 and 5-51.

To simulate the peak noise location, the impulse force was applied at 15.2 cm (6 in.) downstream of the orifice plate. RMS spectra, transfer functions and coherence functions of the various accelerometer signals were obtained. Again, similar results were observed in that the accelerometer signals were highly correlated.

b. Phase II Study of Flow and Acoustic Characteristics of Circular Confined jets

(1) Pipe Wall Acceleration - Spectral Characteristics

A typical pipe wall acceleration spectrum is shown in figure 5-52 for the 0.625-in. diameter jet. Relative to the wall pressure spectra, the acceleration spectra contain more high-frequency component. The lower frequency peak at around 300 Hz is related to the first harmonic of the blade passage frequency of the pump. Though a flexible hose was installed upstream of the test section, blade passage frequencies of the pump have been observed for the lower jet flow condition.

(2) Coherence of Accelerometers Signals

Coherence functions of the accelerometer signals are shown in figures 5-53 and 5-54 for jet flow and pipe flow, respectively. Figures 5-53a and 5-53b show the coherence functions of the accelerometer signals for the 0.625-in. diameter jet. As illustrated, the coherence functions between the accelerometers are high. Again, the high coherence functions are due to the highly correlated pressure fluctuations that are contributed by the large-scale structures. The coherence between the accelerometer signals as shown in figure 5-54 is relatively low for pipe flow. This result is consistent with the hydrophone data presented previously.

(3) Coherence of Accelerometer Signals with Hydrophone Signals

Typical coherence functions of the hydrophone signal with accelerometer signal are depicted in figures 5-55 and 5-56 for the 0.625-in. diameter jet flow and pipe flow, respectively. Again, the results are consistent with the correlations with hydrophones and accelerometers as presented. In summary, jet flow has higher coherence than pipe flow in terms of correlations between hydrophone data and accelerometer data.

4. Effects of Area Ratio, Plate Thickness, and Sharpness

The effect of jet area ratio on the flow field is significant. Results of area ratio on flow velocity can be seen in figures 5-6 through 5-8. Near the jet exit, such as in the jet developing region, the jet flow is highly dependent on the area ratio. For example, a larger recirculation region can be seen near the pipe wall for the smaller jets; and the velocity profile of the larger jets is flatter. The effects of plate thickness and edge sharpness on the flow profiles are minimal. Comparison of normalized velocity (U/U_j) profiles for the 1.25-in. plate with and without a bevel edge is shown in figure 5-57. Figure 5-58 shows the normalized velocity profiles of the 1.25-in. plate with a bevel edge versus the 1.25-in. thin plate. As illustrated, their velocity profiles are almost identical.

As with the flow field, the effect of jet area ratio on noise is substantial. The effect of area ratio on noise can be seen in figures 5-38a through 5-38g, in which the area ratio has a definite effect on the wall pressure distribution. Also, as shown in figure 5-41, the velocity exponent decreases with increasing jet diameter. Furthermore, similar results can be seen in figure 5-59, which is a plot of broadband acceleration levels versus jet velocity for the various confined jets.

Consistent with the flow field, the effects of plate thickness and edge sharpness on noise are insignificant.

As discussed and presented previously, correlations of the wall pressure and pipe wall acceleration data indicated that jet flows have higher coherence functions than the pipe flow. From a data correlation point of view, jet flows are more deterministic than pipe flow. The highly correlated behavior of the wall pressure and pipe wall acceleration are probably due to the large-scale coherent structures of jet flows. Recently, several experimenters (i.e., Hussain (1980), Abdallah (1984), Ahuja et al. (1985), and Bennett et al. (1987)) have reported the occurrence of coherent structures in free jet flows as well as confined jet flows; and, to some extent, they have related the coherent structures to noise production.

5. Measurement Accuracy Summary

Based on measurement accuracies of the instrumentation and error analysis, measurement uncertainties in flow parameters (i.e., velocity, temperature, and flow rate) and acoustic data were assessed. Table 5-3 is a summary of the measurement accuracy of this experimental study. All accuracies or uncertainties are based on a 95-percent confidence level.

Table 5-3. Summary of Measurement Accuracy

Measurement	Accuracy/Uncertainty
<u>Phase I:</u>	
Jet velocity	± 3.5 percent
Temperature	$\pm 0.1^{\circ}\text{C}$
Wall pressure	± 1.5 dB
Acceleration	± 2.0 dB
<u>Phase II:</u>	
Flow rate or average velocity	± 1.0 percent
Temperature	$\pm 0.05^{\circ}\text{C}$
LDV axial velocity	± 1.0 percent
LDV radial velocity	± 3.0 percent
Wall pressure	± 1.5 dB
Acceleration	± 1.5 dB

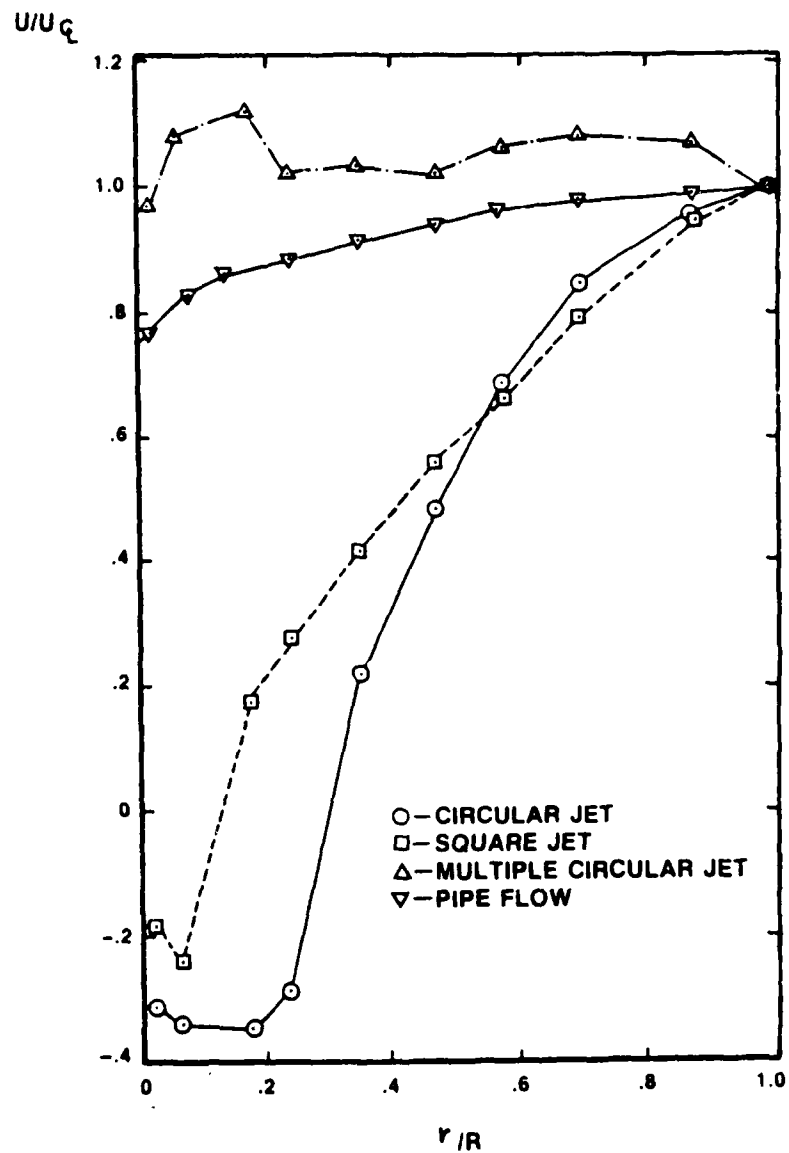


Figure 5-1. Velocity Profiles for Pipe Flow, Circular, Square, and Multiple Circular Jets

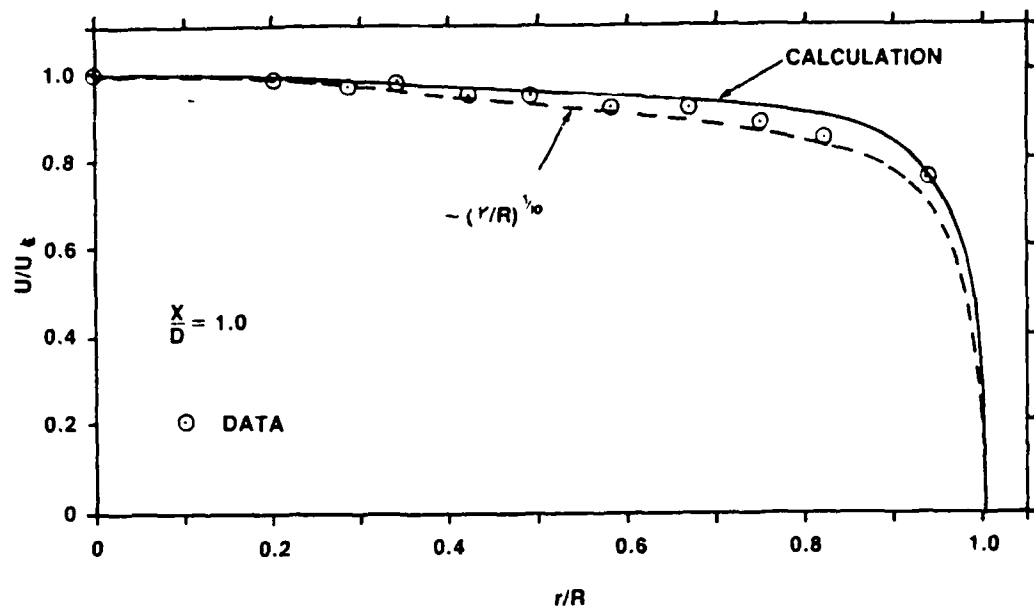


Figure 5-2. Comparison of Pipe Flow Velocity Profile - Data vs Numerical Calculation

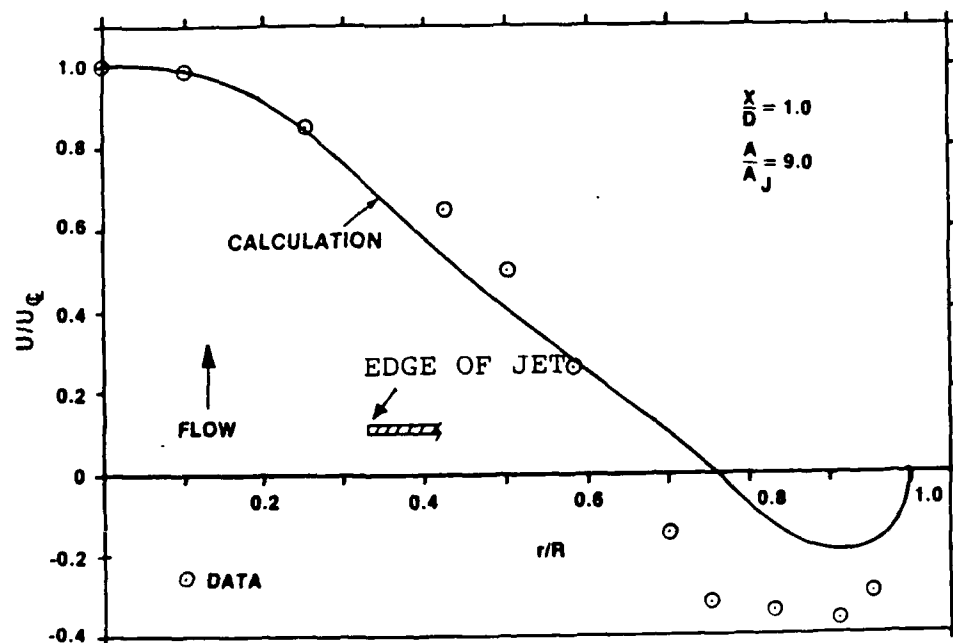


Figure 5-3. Comparison of Circular Jet Velocity Profile - Data vs Numerical Calculation

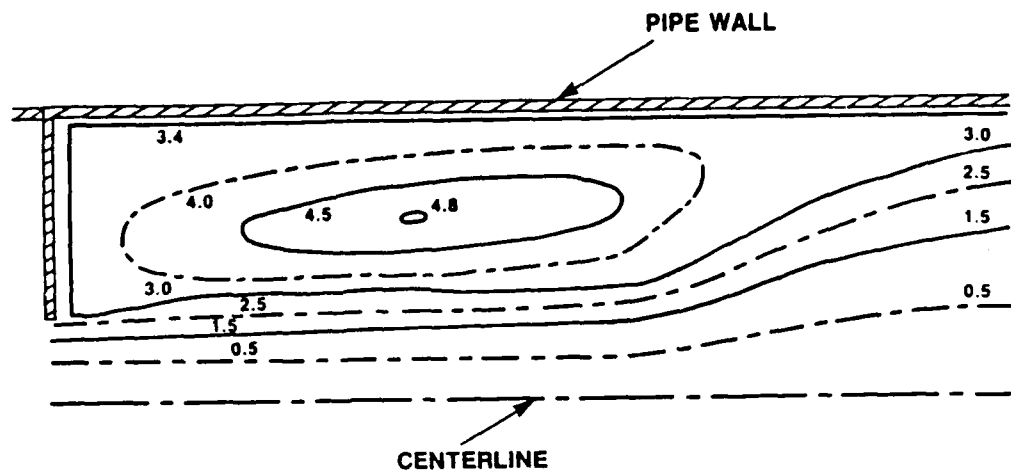


Figure 5-4. Streamlines of Recirculation Region

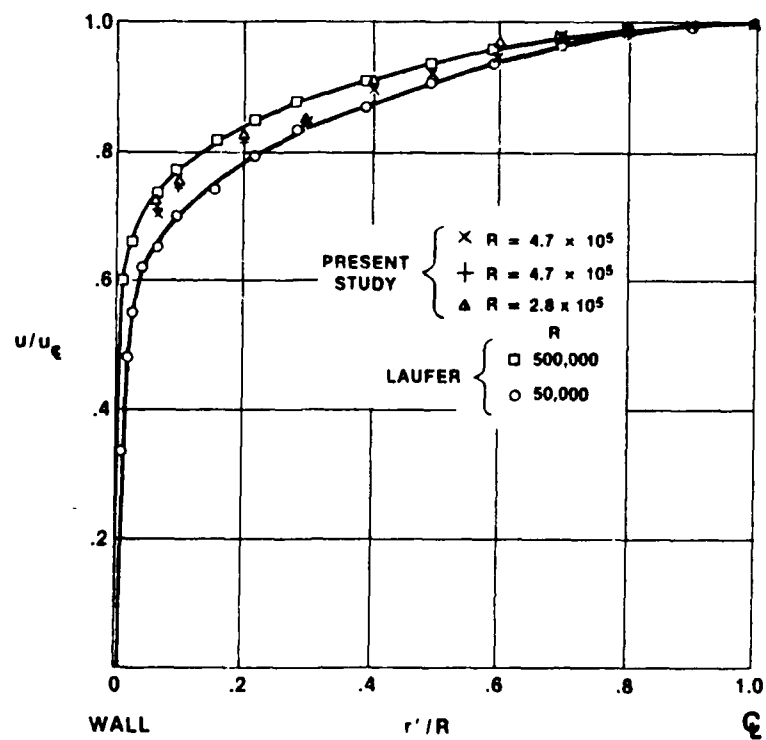


Figure 5-5. Comparison of Pipe Flow Velocity Profile with Laufer's Data

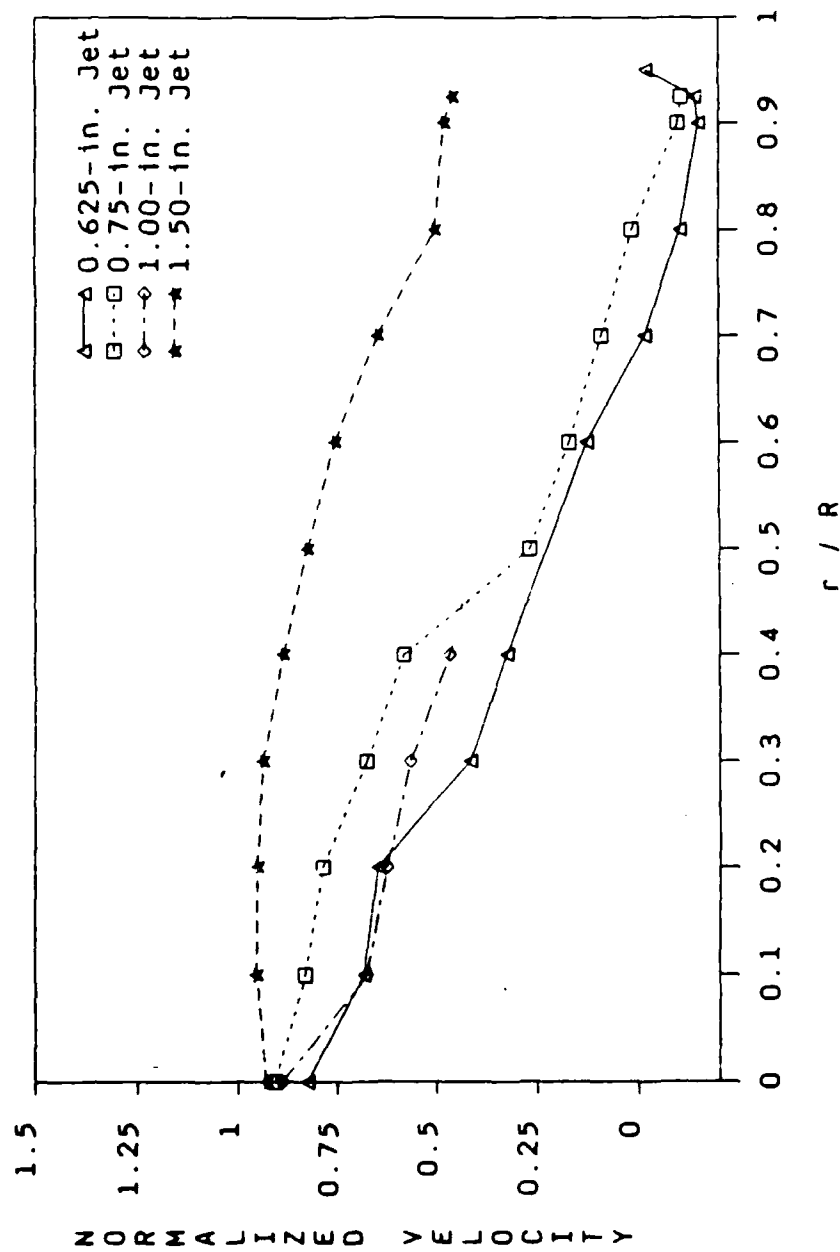


Figure 5-6. Velocity Profiles for Jets at $x = 8.4$ cm

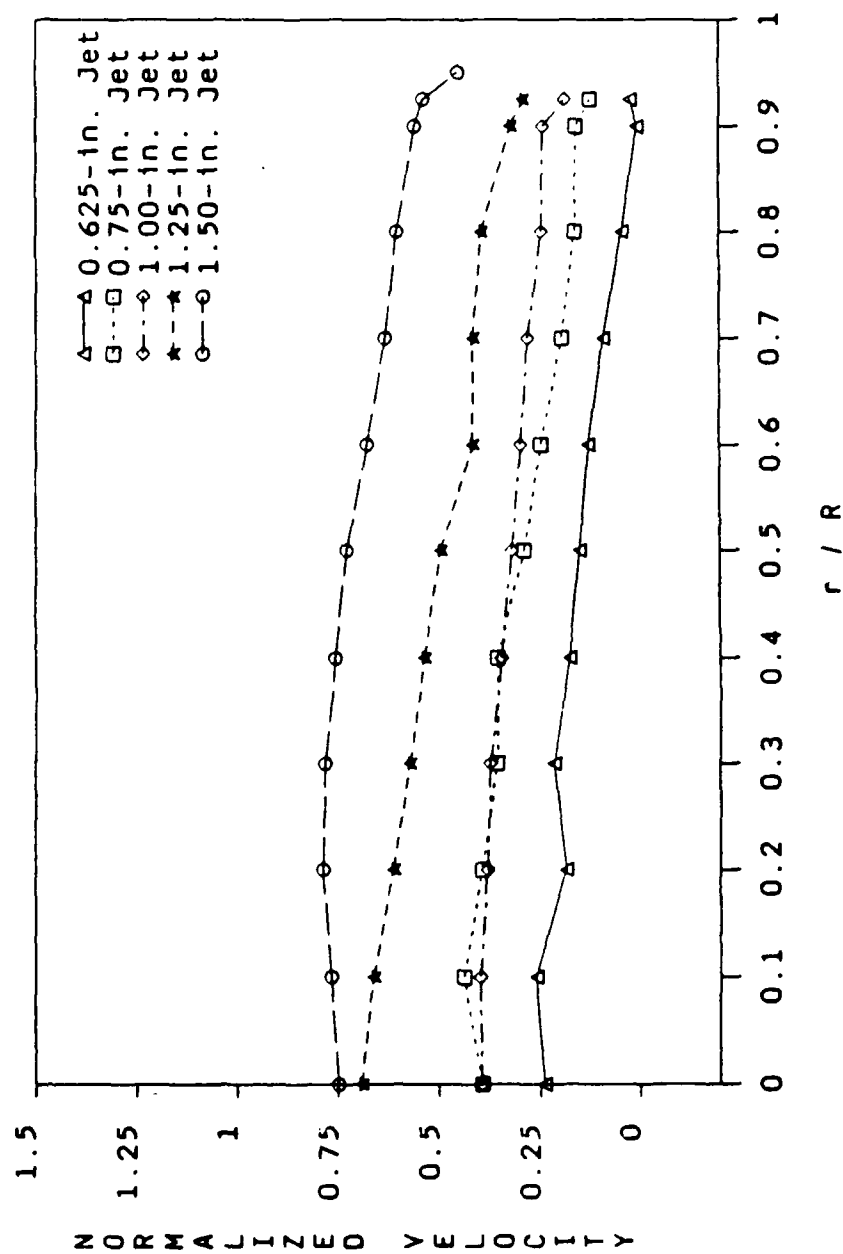


Figure 5-7. Velocity Profiles for Jets at $x = 14.5$ cm

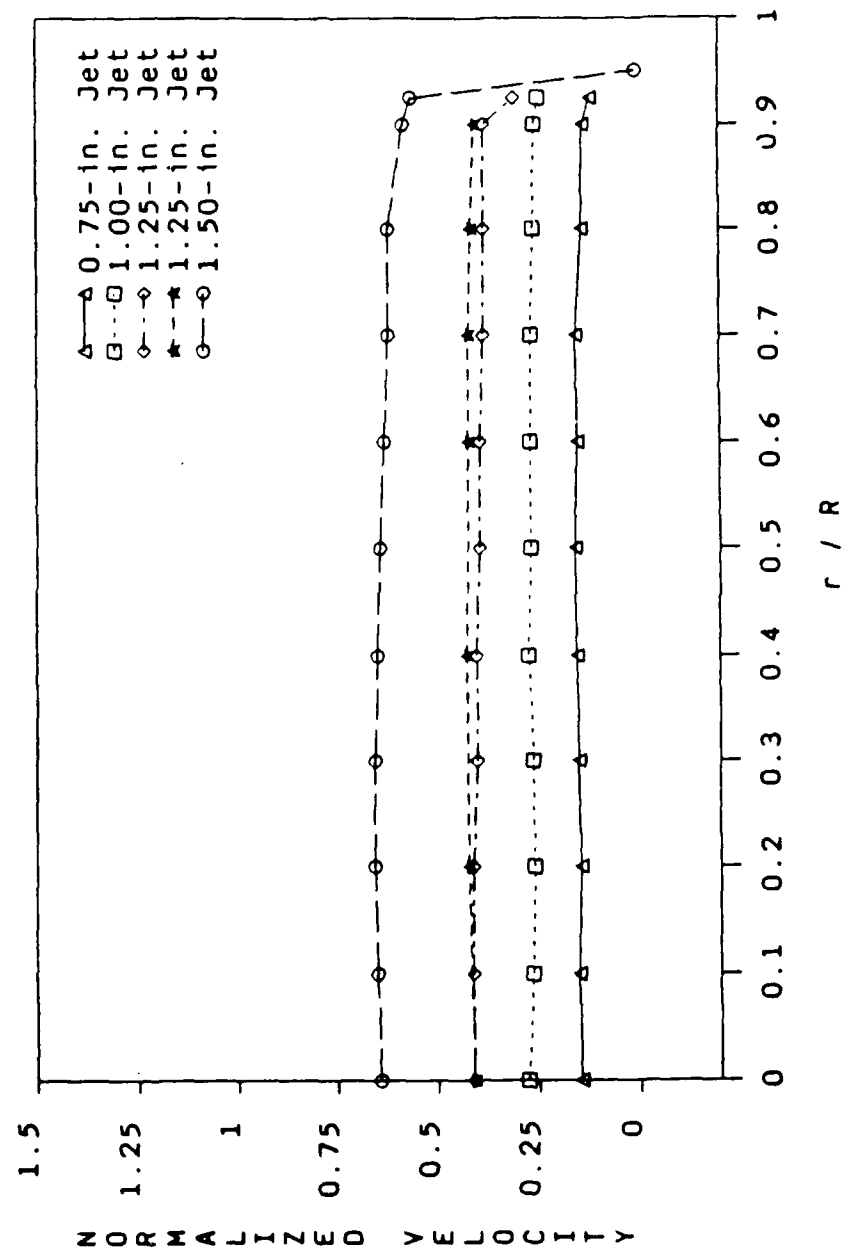


Figure 5-8. Velocity Profiles for Jets at $x = 26.2$ cm

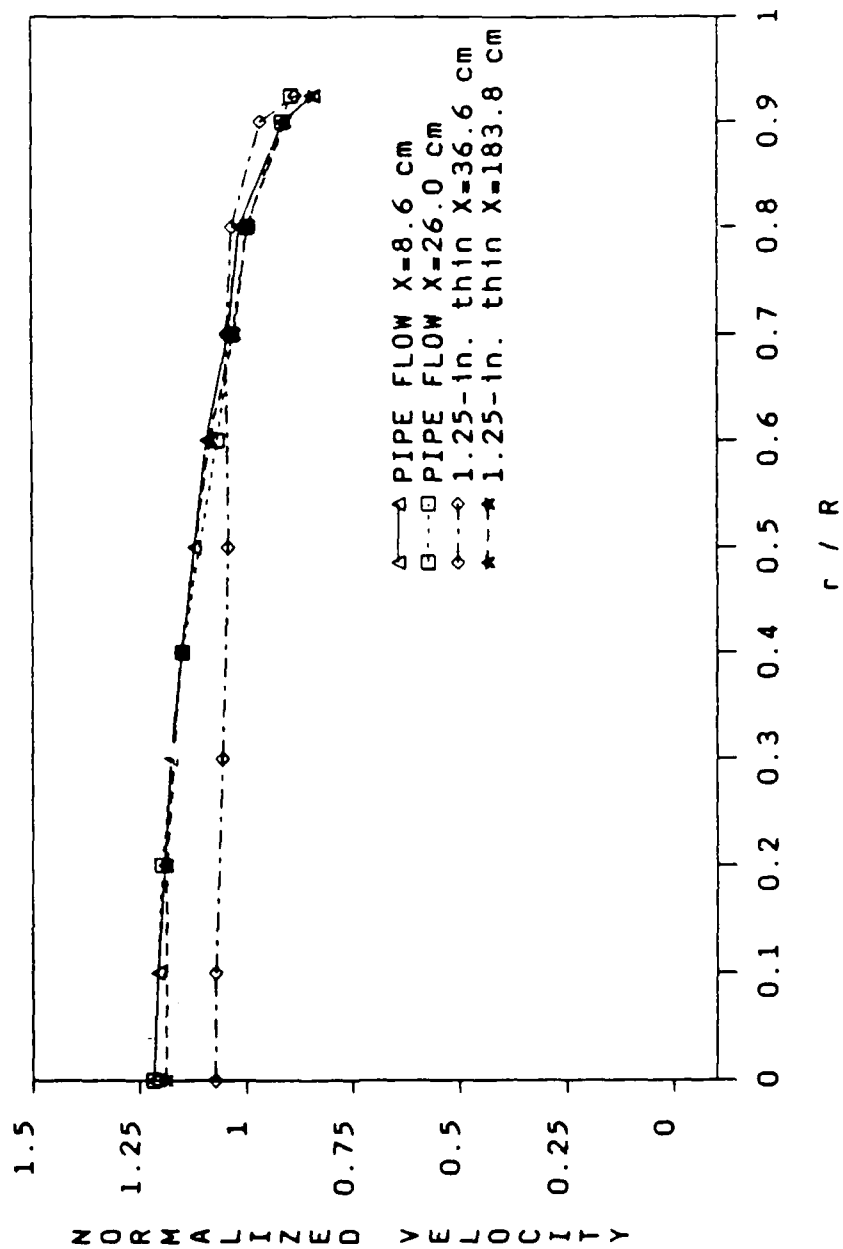


Figure 5-9. Velocity Profiles for Pipe Flow and Far-downstream Jet Flow

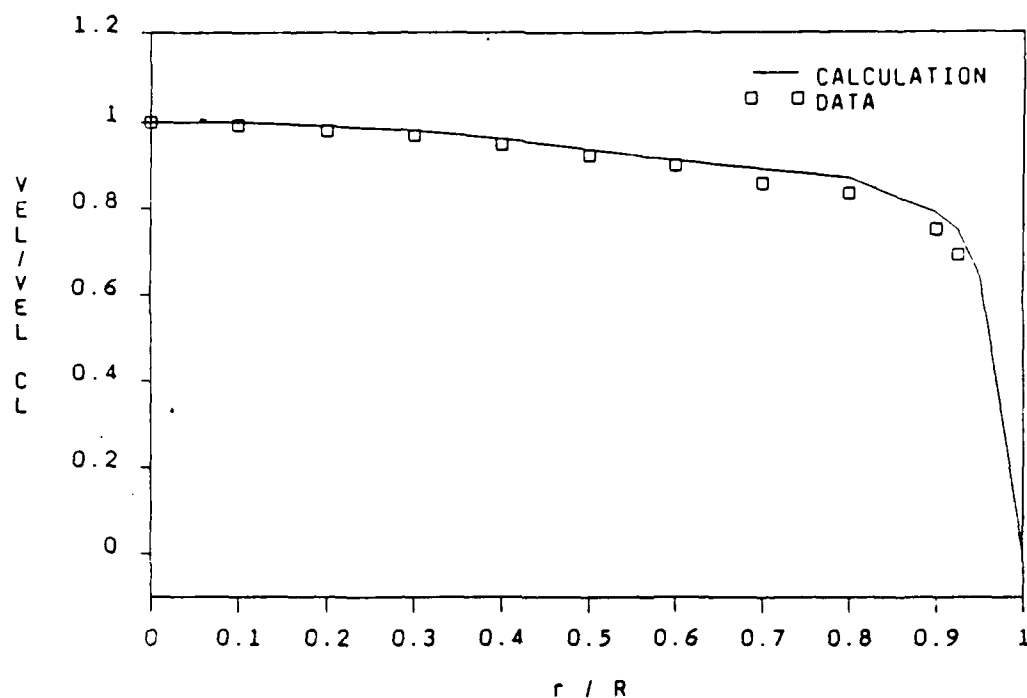


Figure 5-10. Comparison of Pipe Flow Velocity Profile -
Data vs Calculation

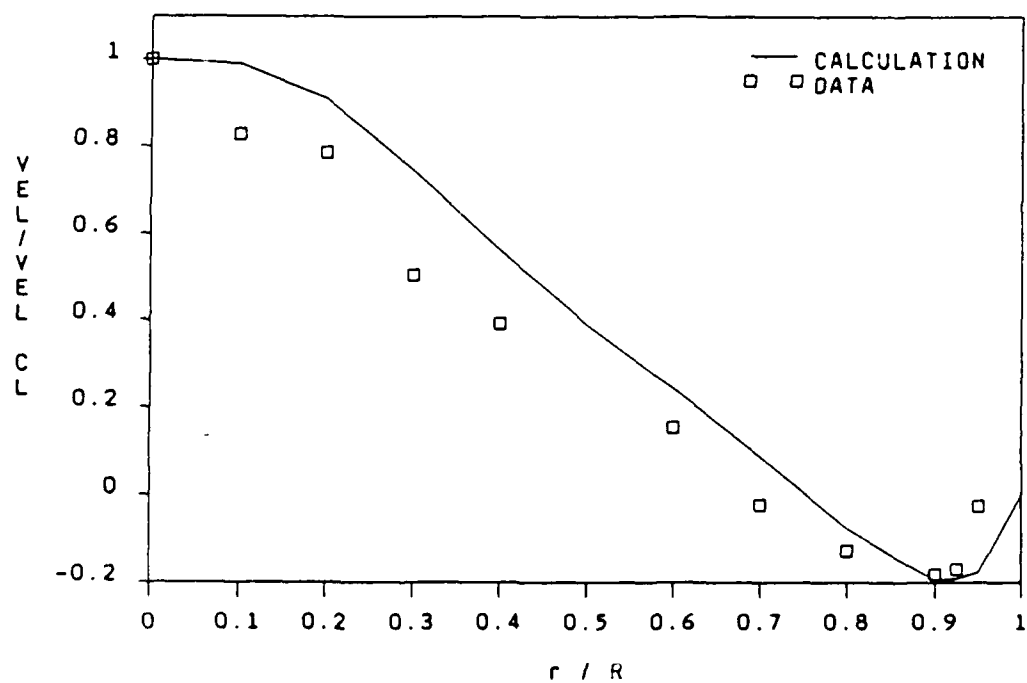


Figure 5-11. Comparison of Jet Flow Velocity Profile -
Data vs Calculation

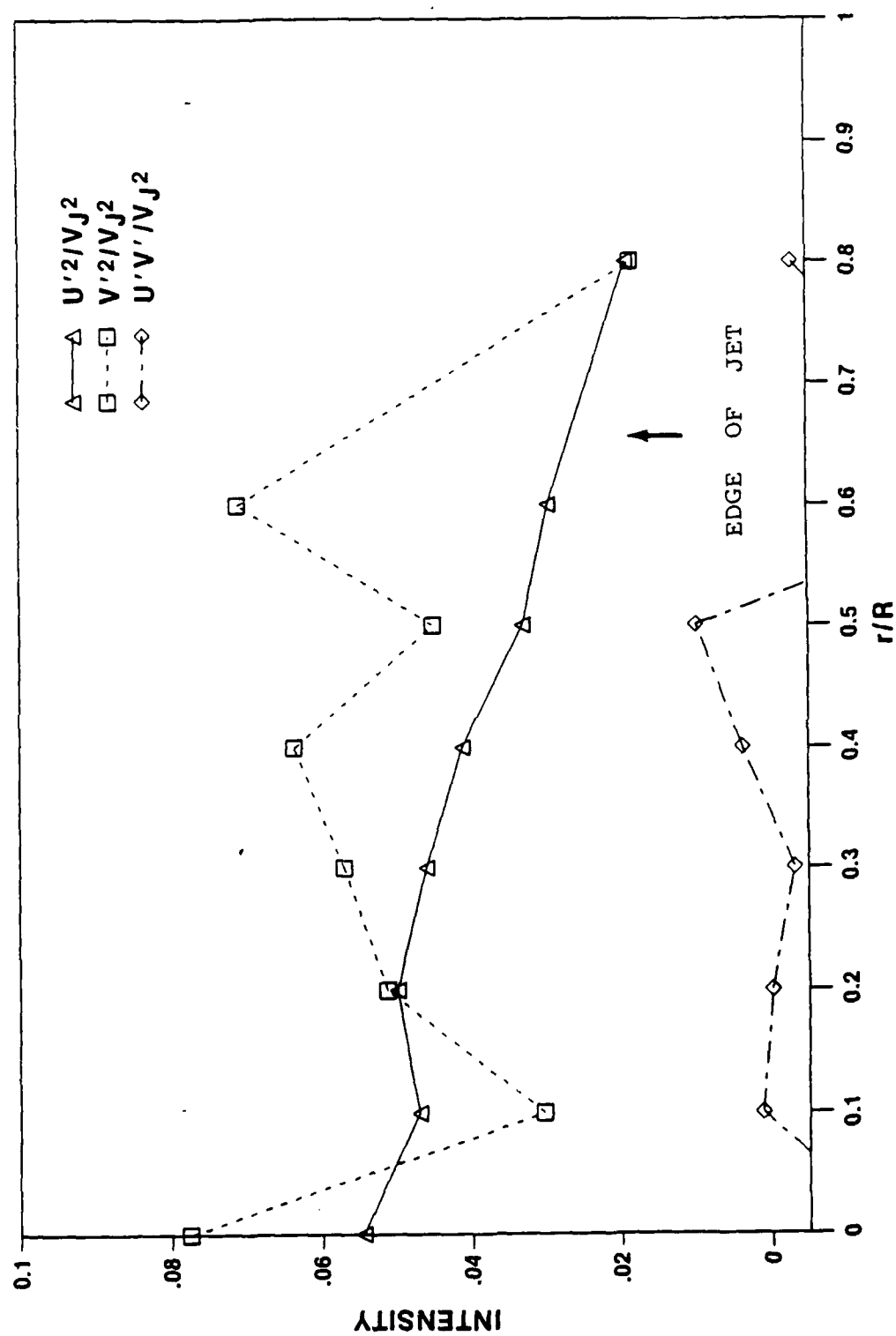


Figure 12. Turbulence Intensities of Jet Flow

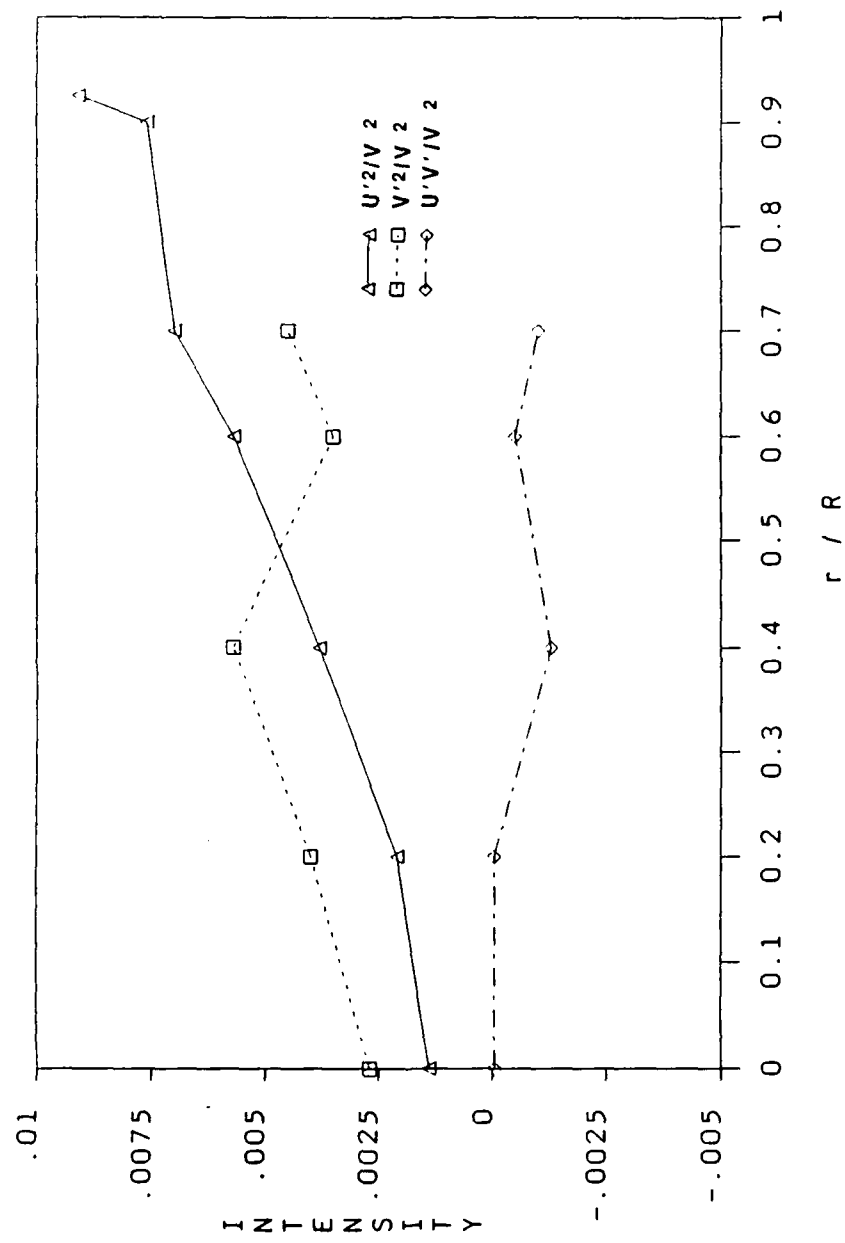


Figure 5-13. Turbulence Intensities of Pipe Flow

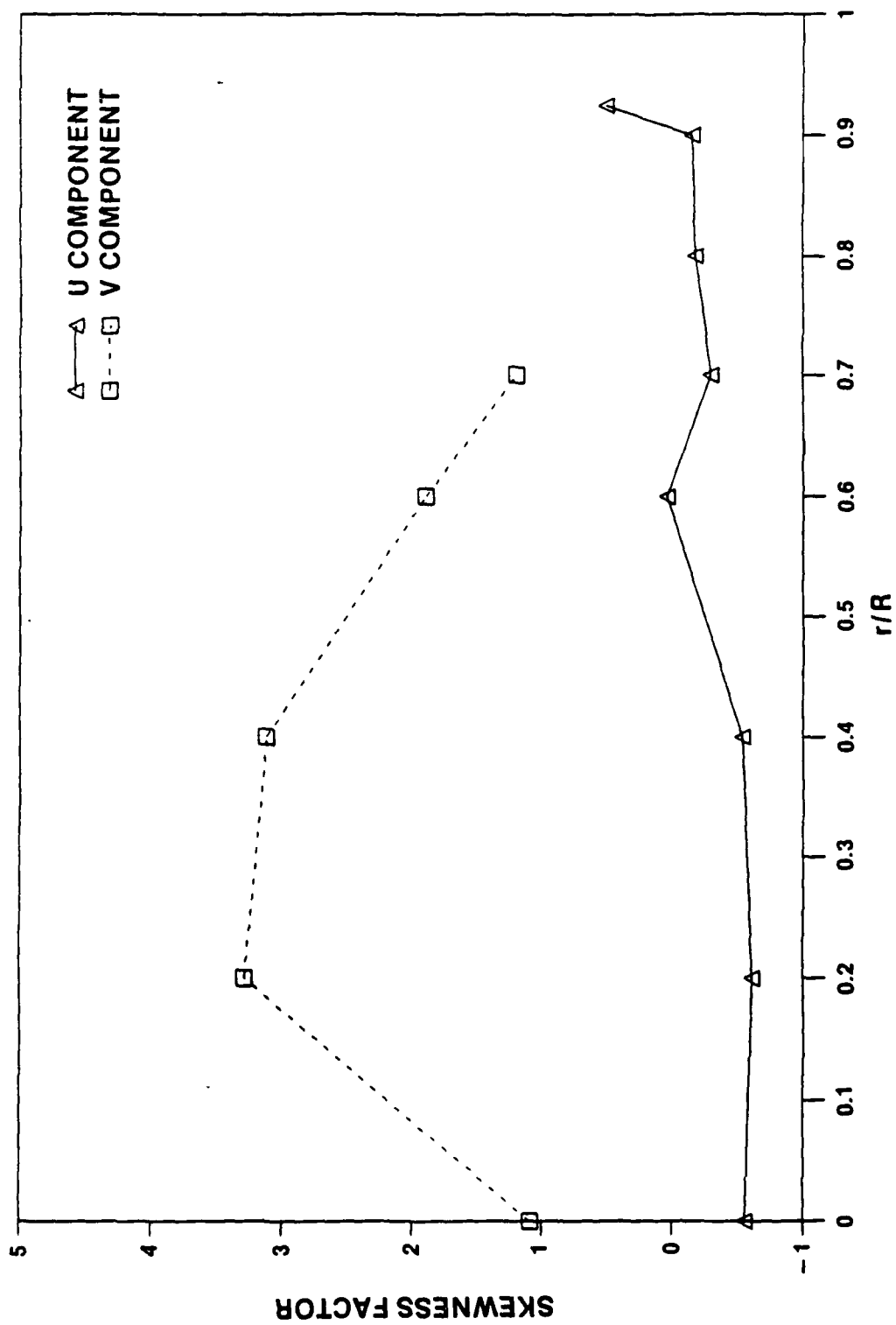


Figure 5-14. Skewness of Velocity - Pipe Flow

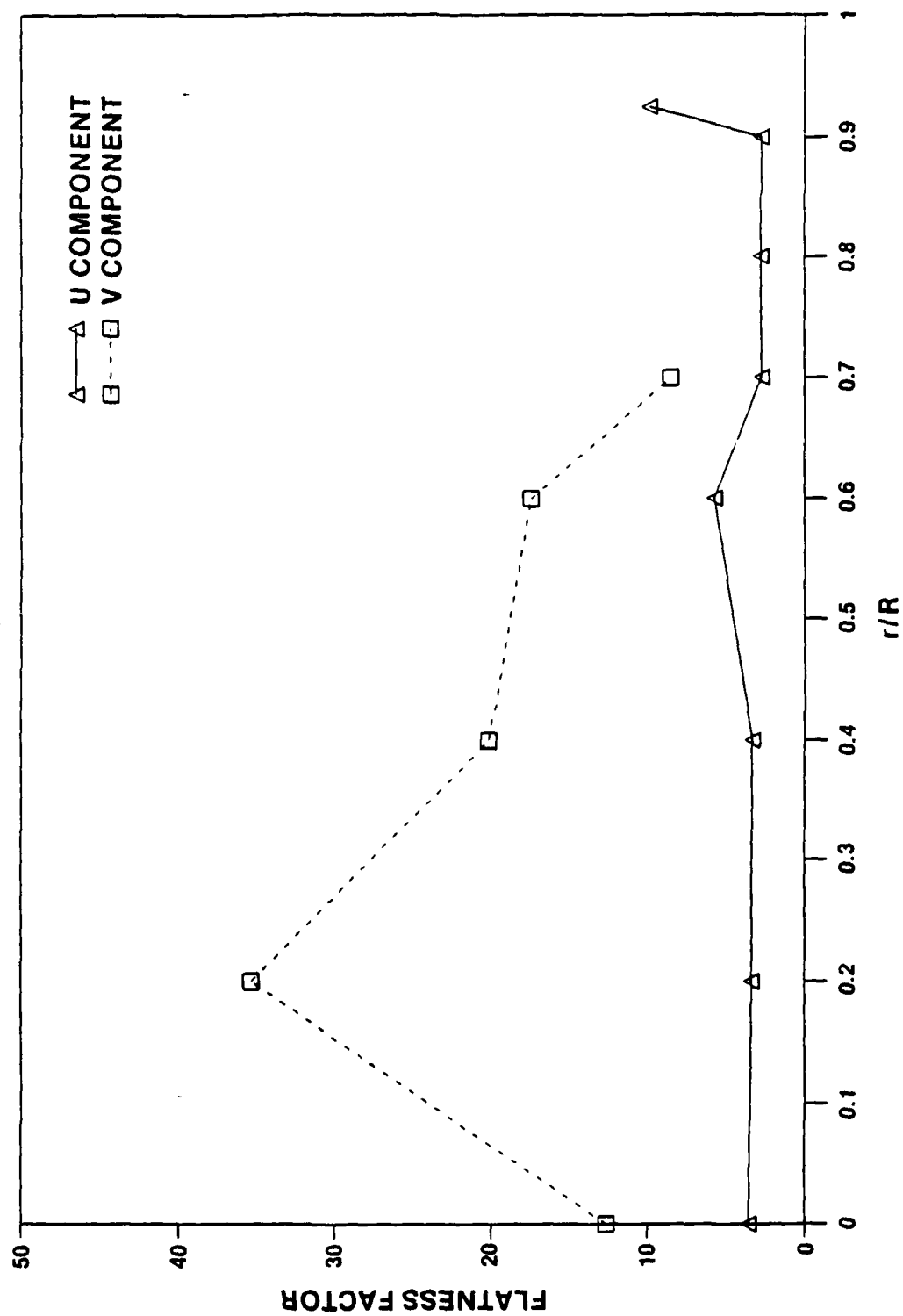


Figure 5-15. Flatness Factor - Pipe Flow

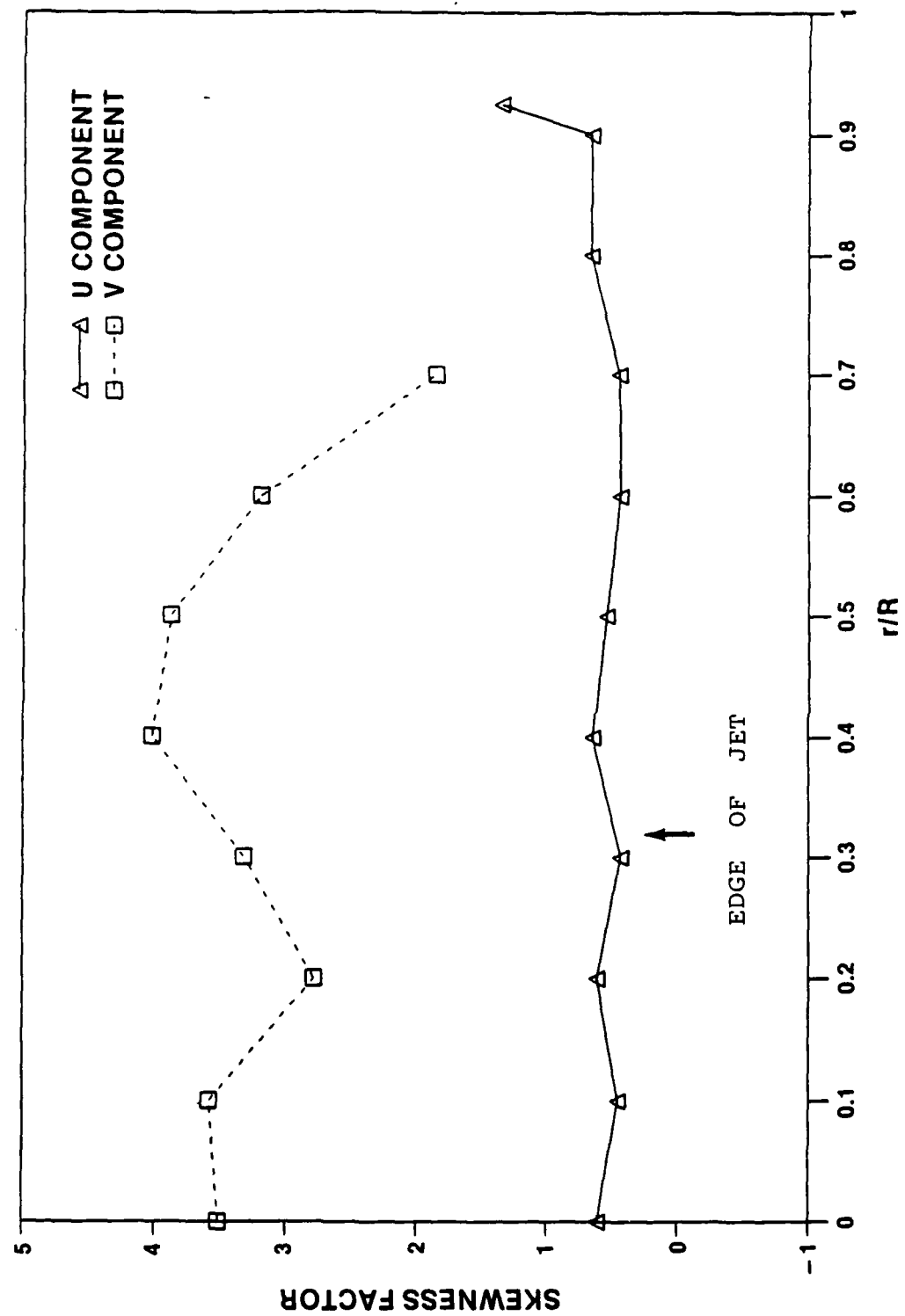


Figure 5-16. Skewness of Velocity - Jet Flow

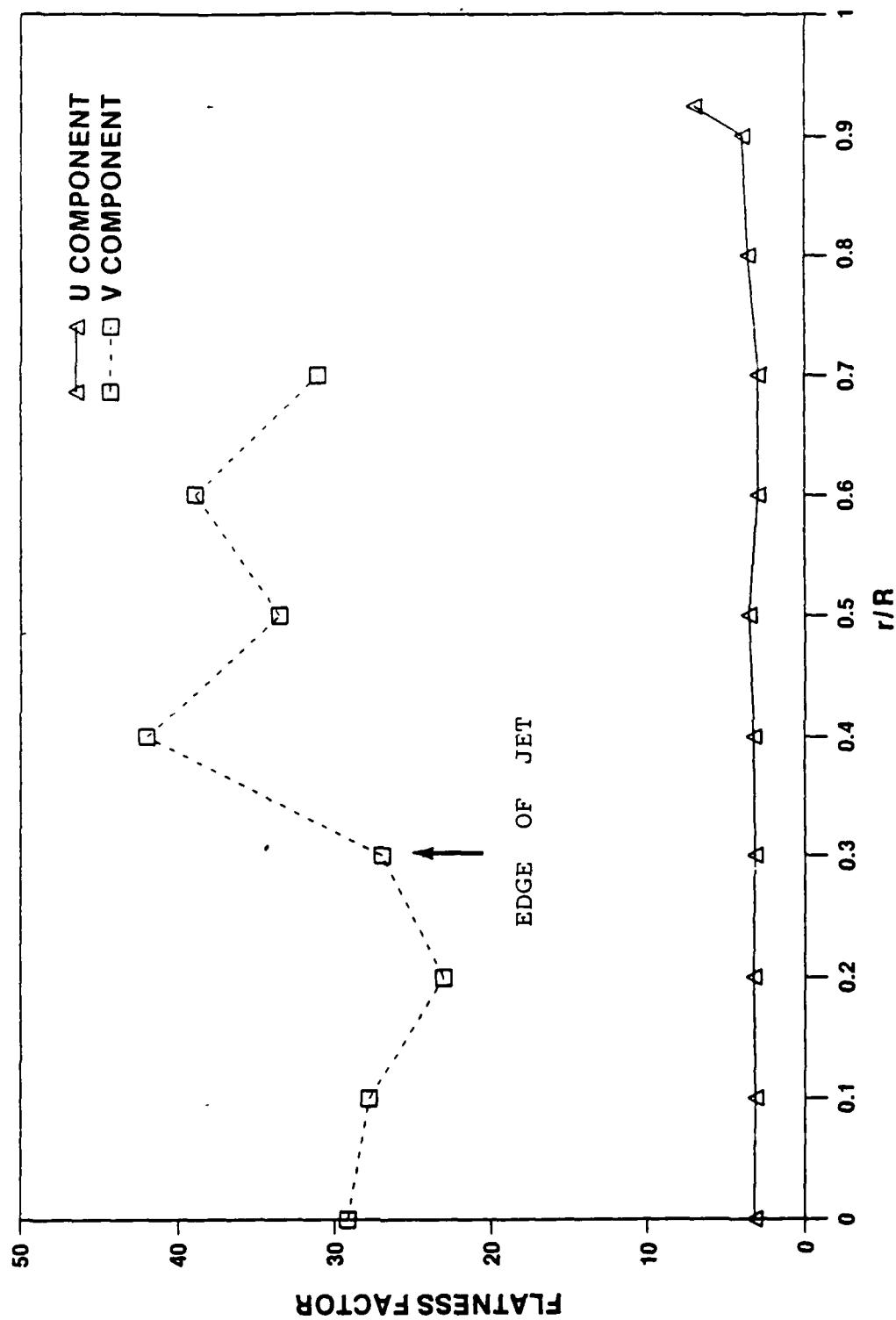


Figure 5-17. Flatness Factor - Jet Flow

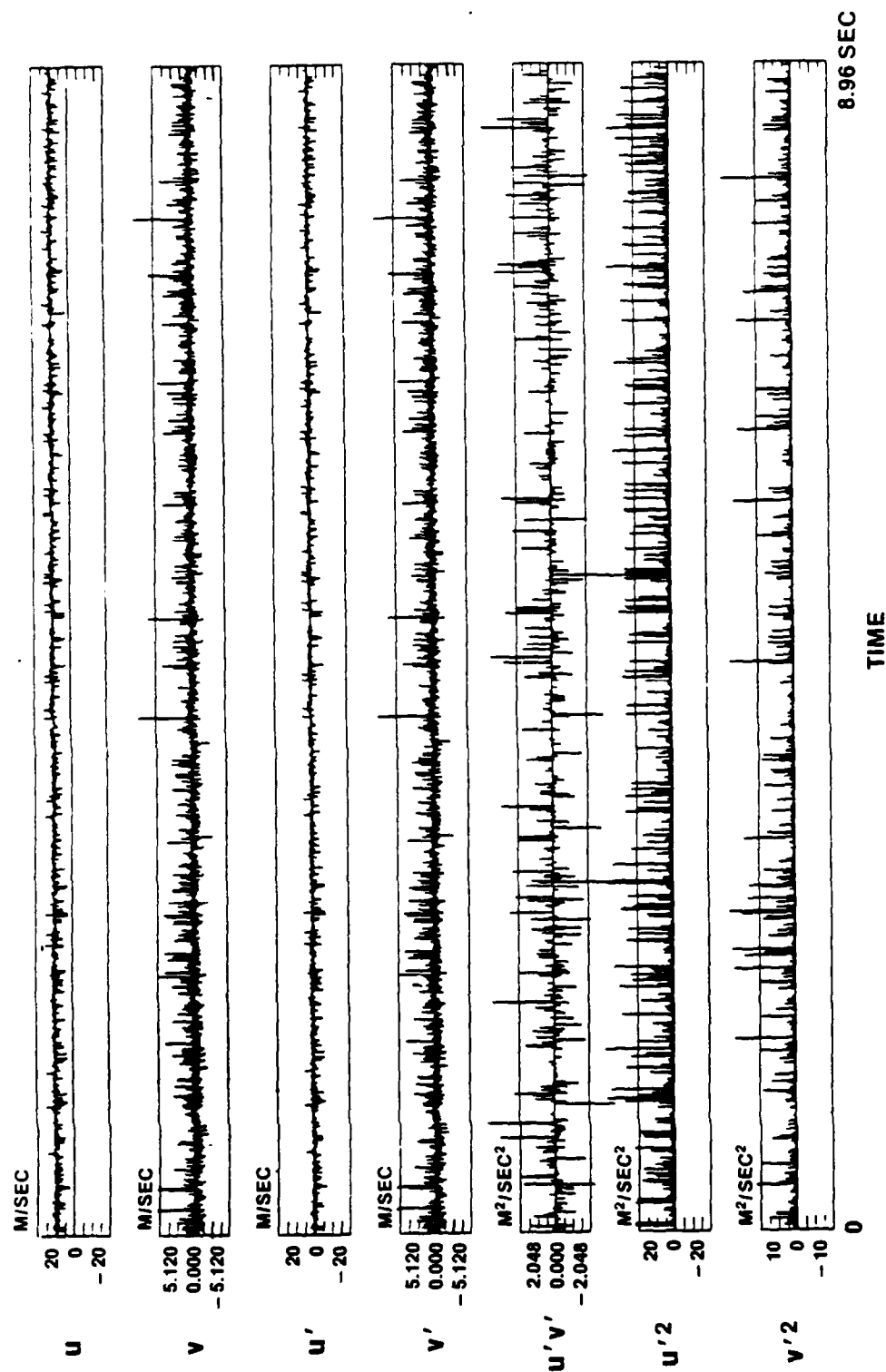


Figure 5-18. Velocities, Velocity Fluctuations, Reynolds Stress, and Intensities vs Time

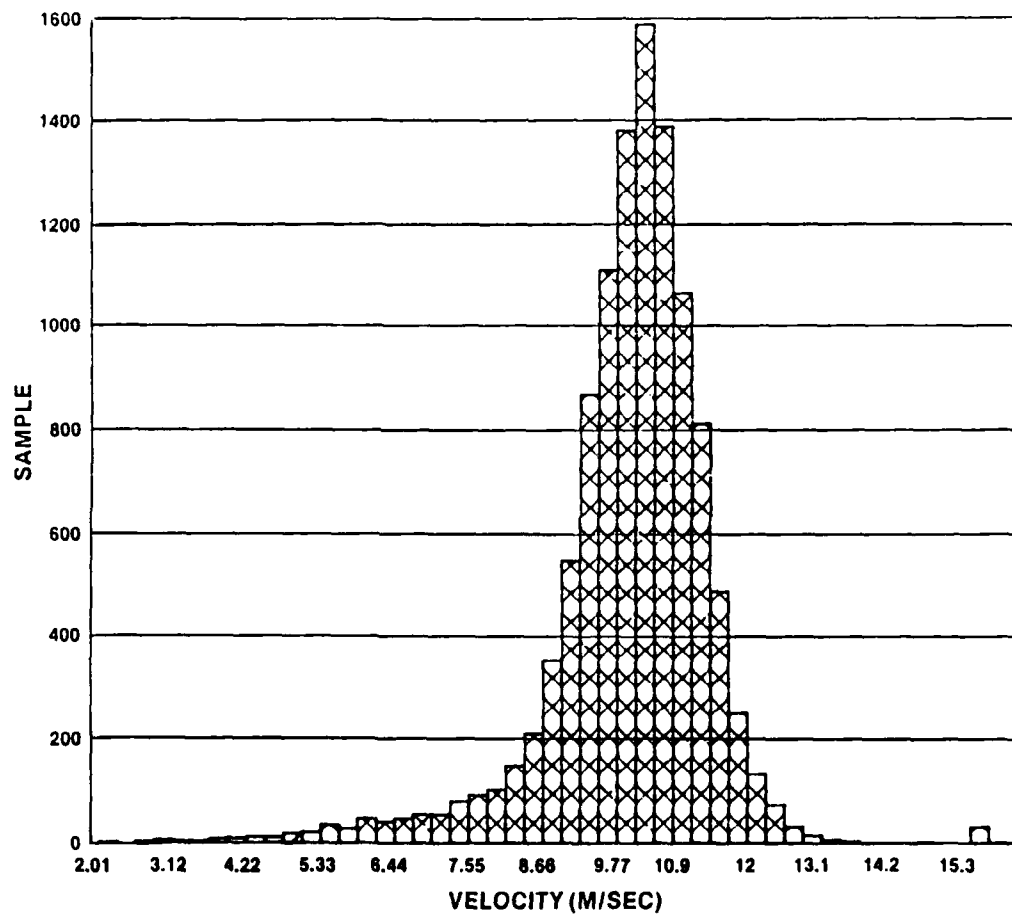


Figure 5-19. Distribution Function of Axial Velocity

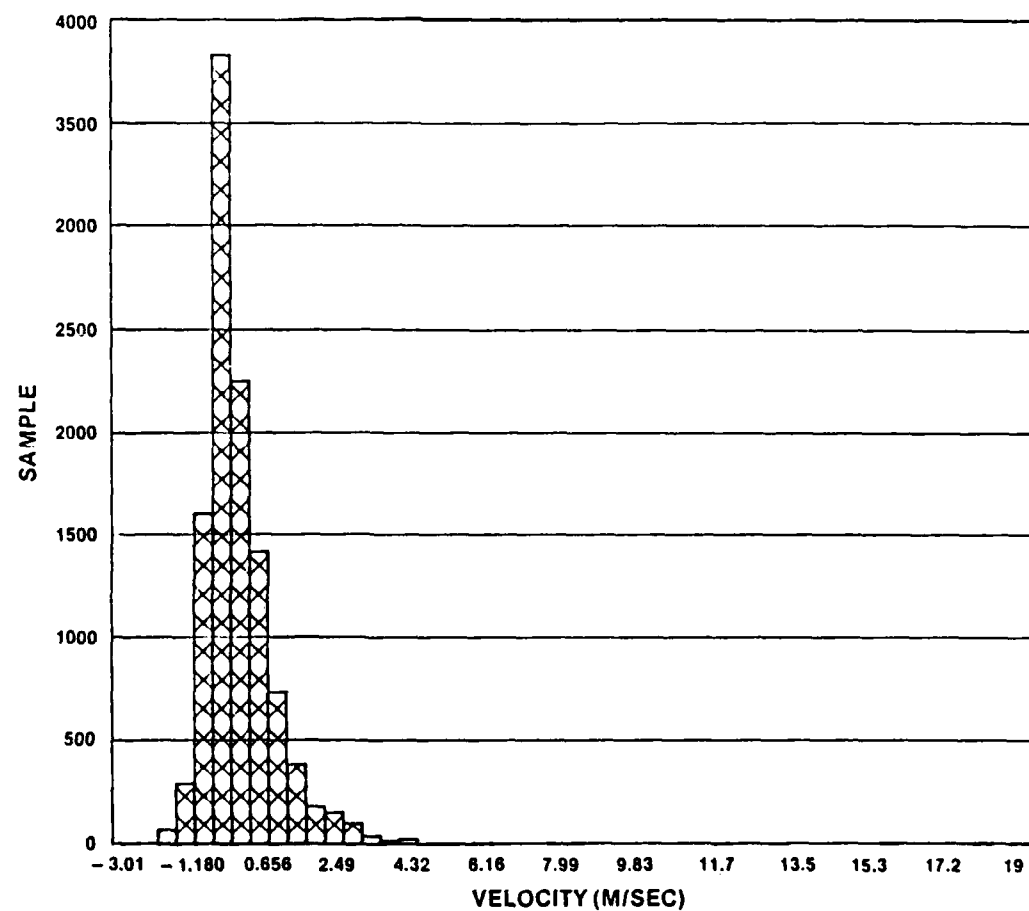


Figure 5-20. Distribution Function of Radial Velocity

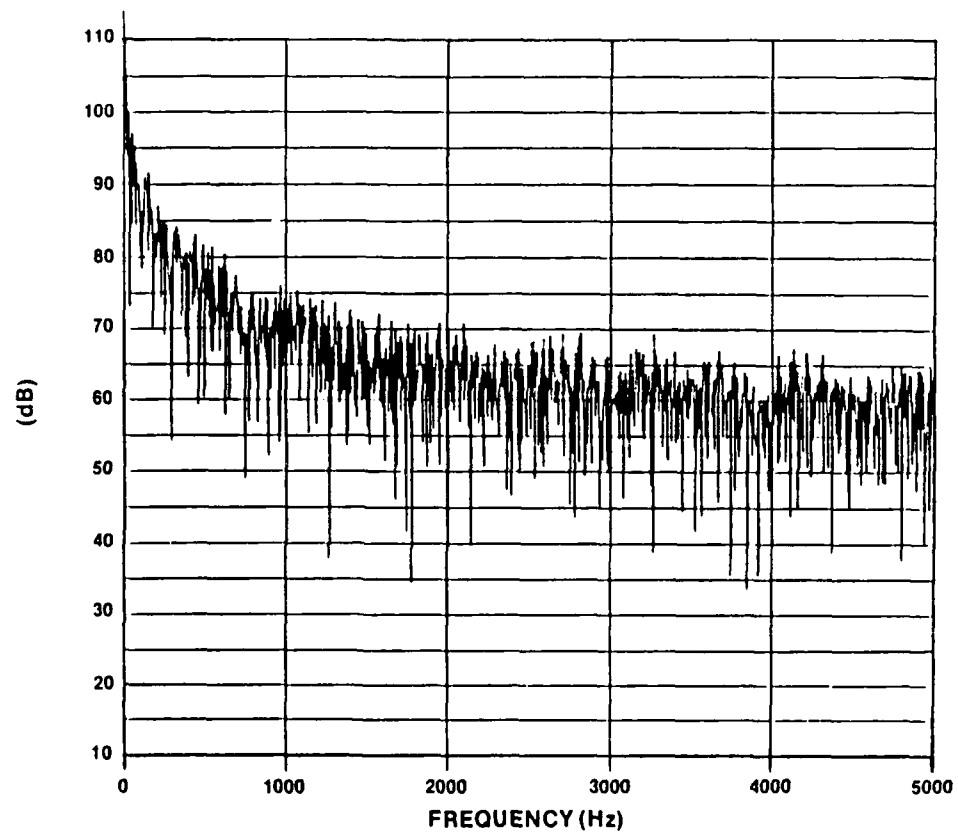


Figure 5-21. Frequency Spectrum of Axial Velocity

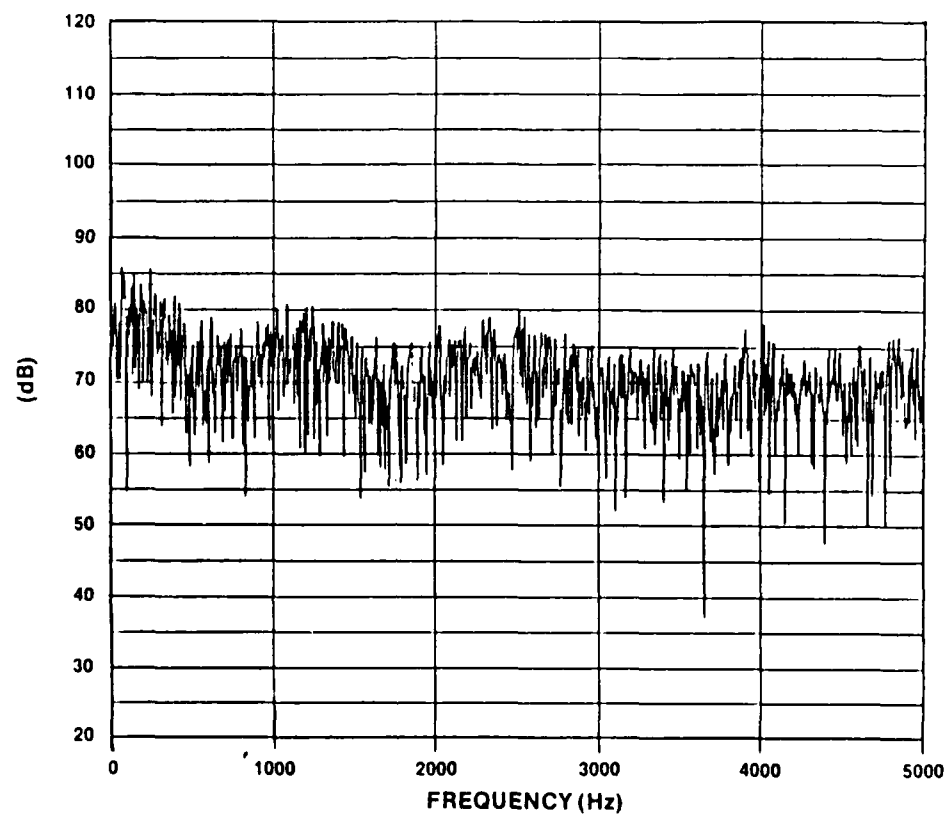


Figure 5-22. Frequency Spectrum of Radial Velocity

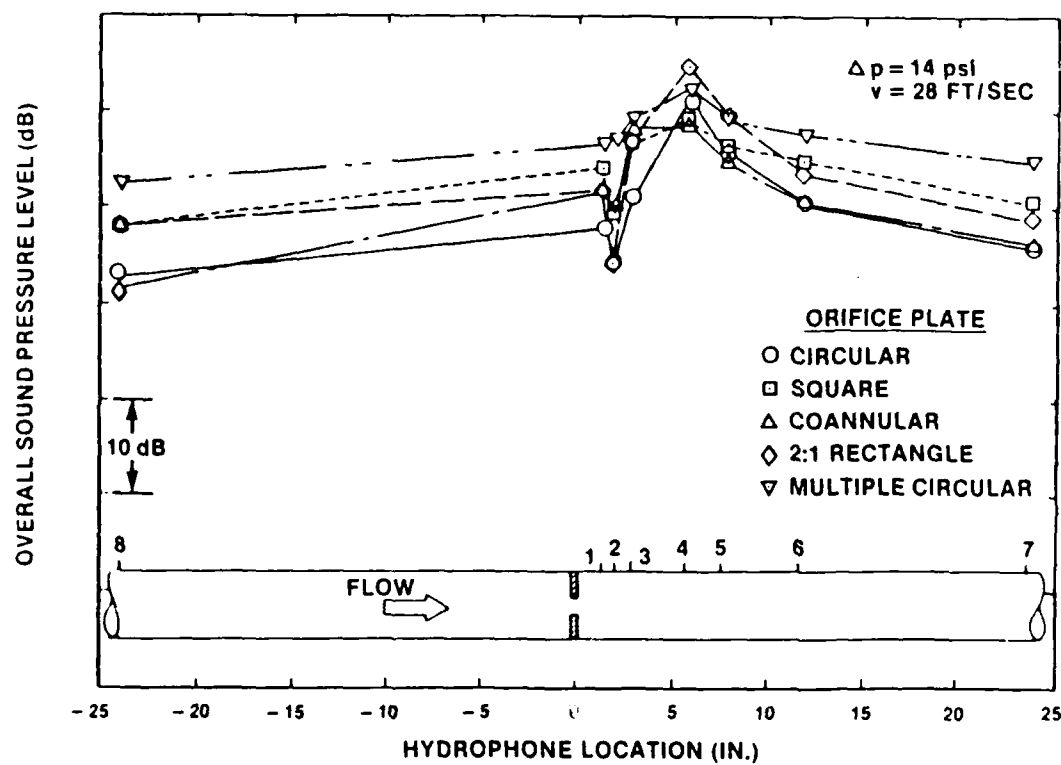


Figure 5-23. Noise vs Location for Flow Restrictors

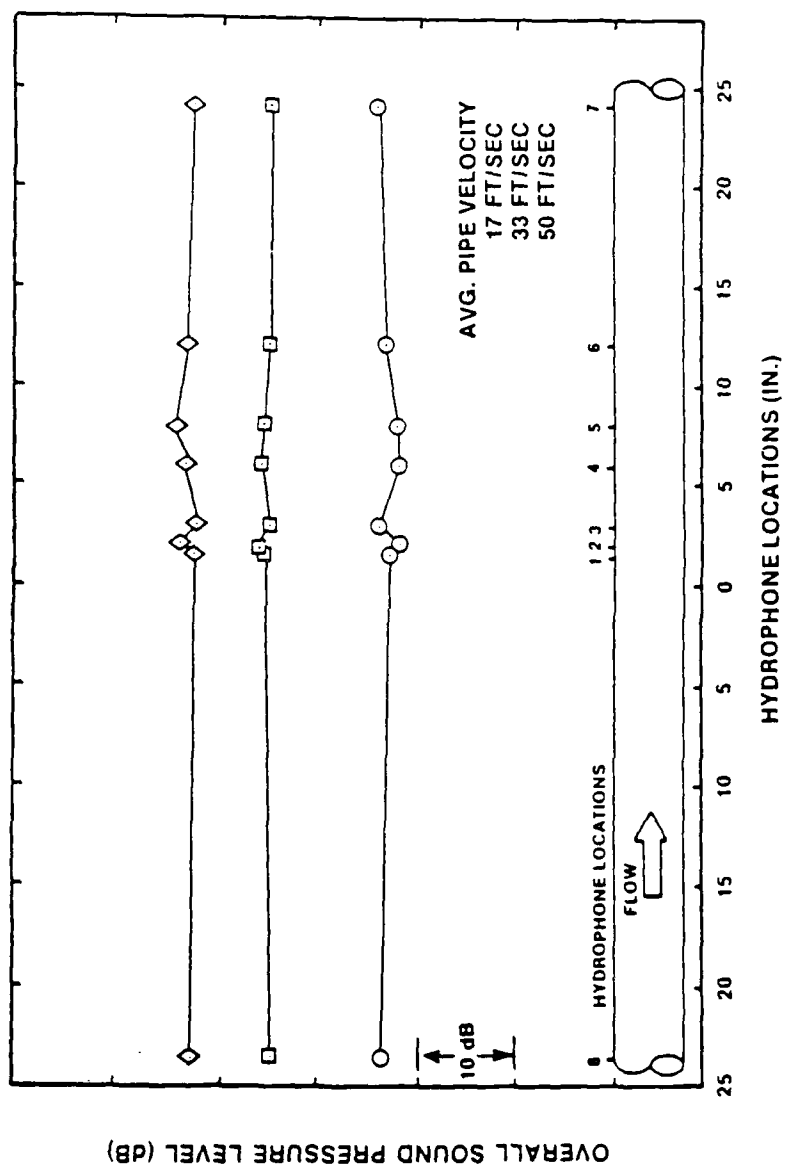


Figure 5-24. Noise vs Location for Pipe Flow

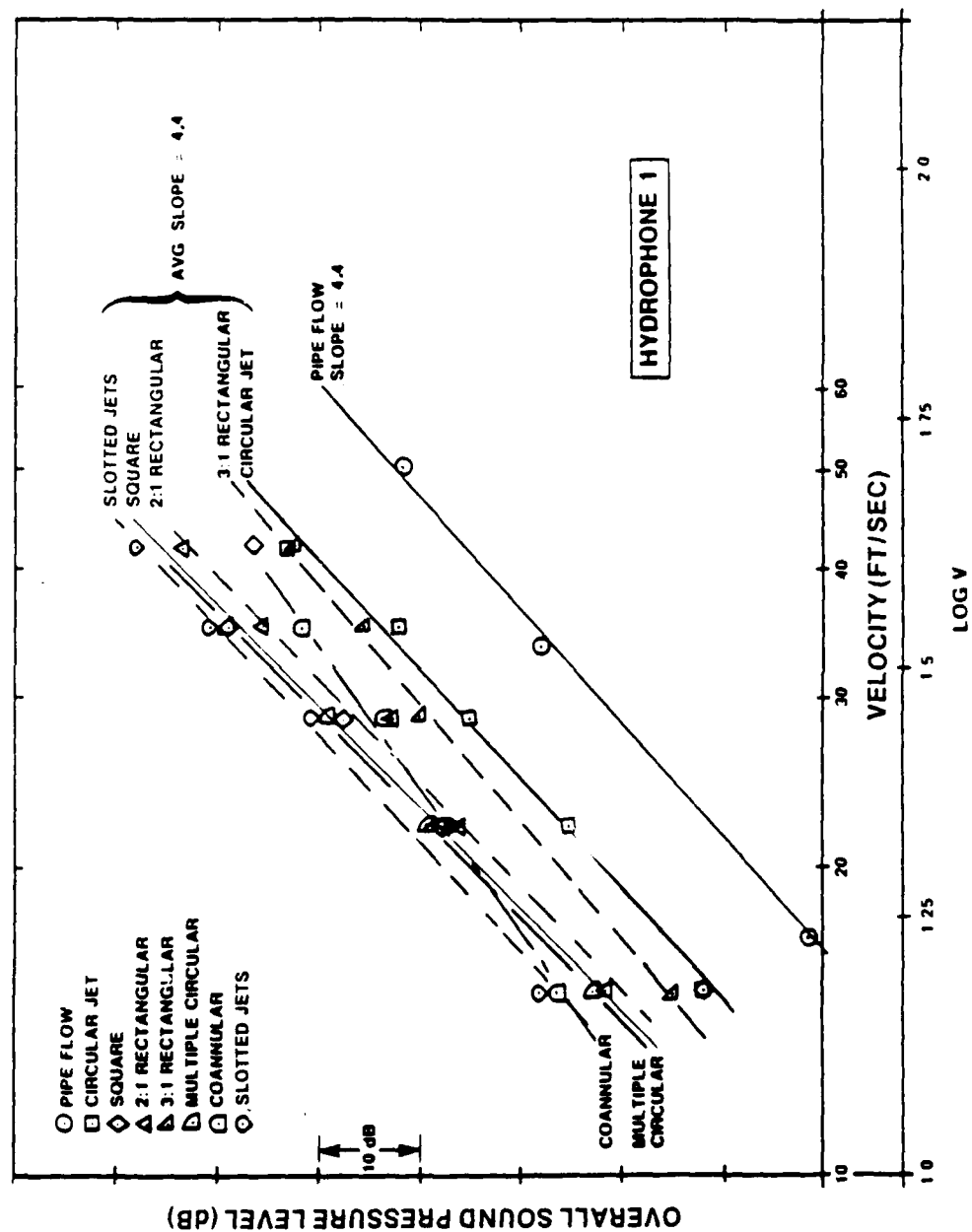


Figure 5-25. Correlations of Noise with Velocity

LEAST-SQUARES FIT OF DATA, STANDARD DEVIATION < 1.5 dB

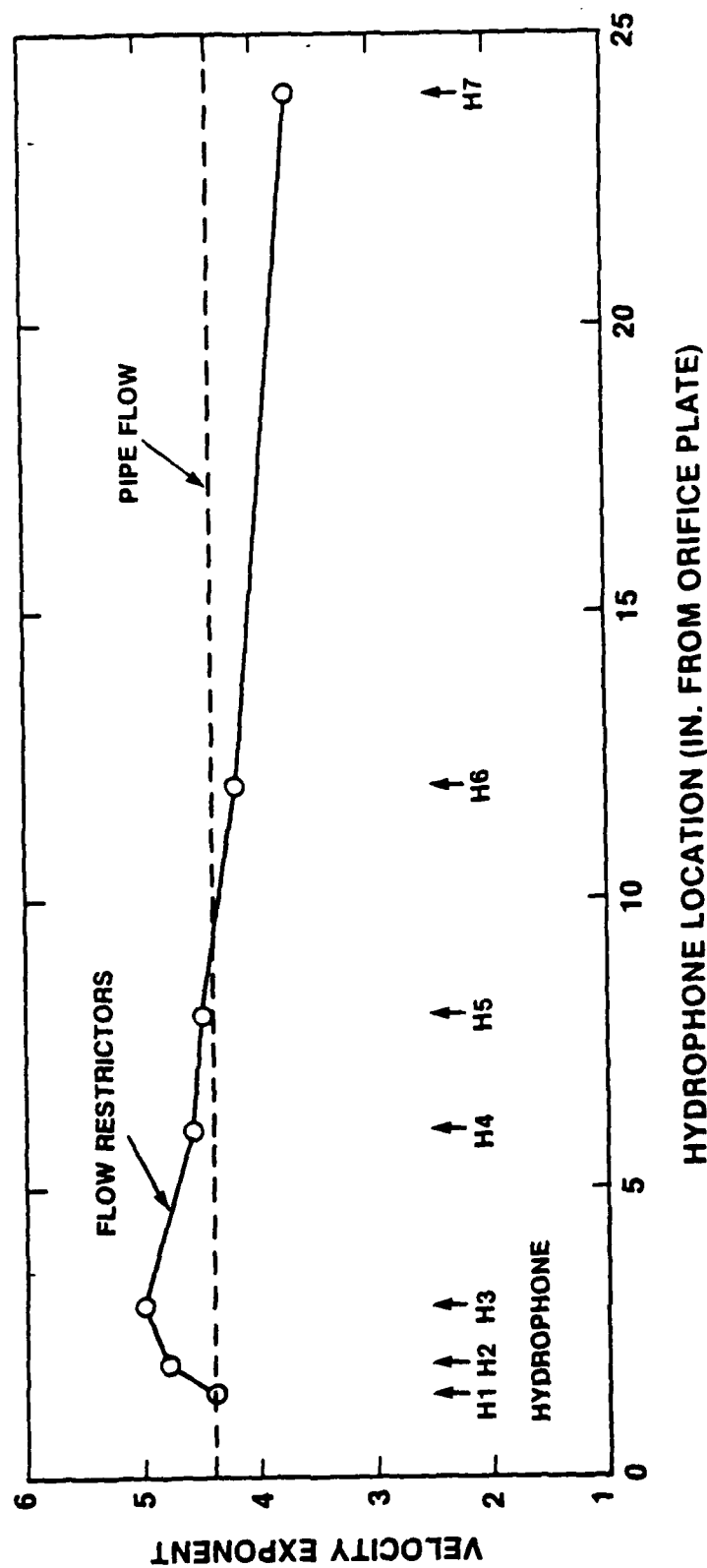


Figure 5-26. Velocity Exponents for Flow Restrictors

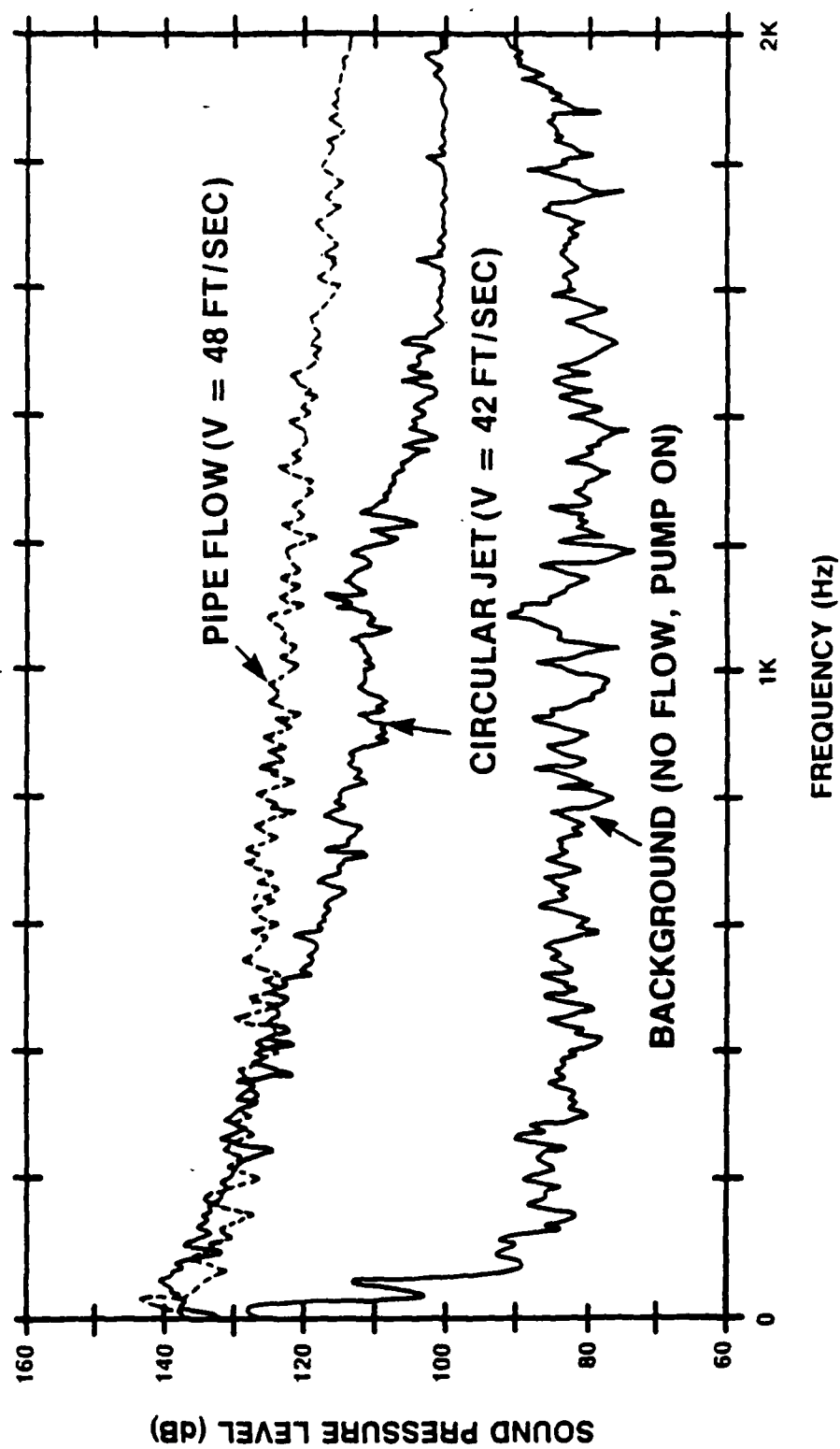


Figure 5-27. Noise Spectra of Pipe Flow and Circular Jet Flow

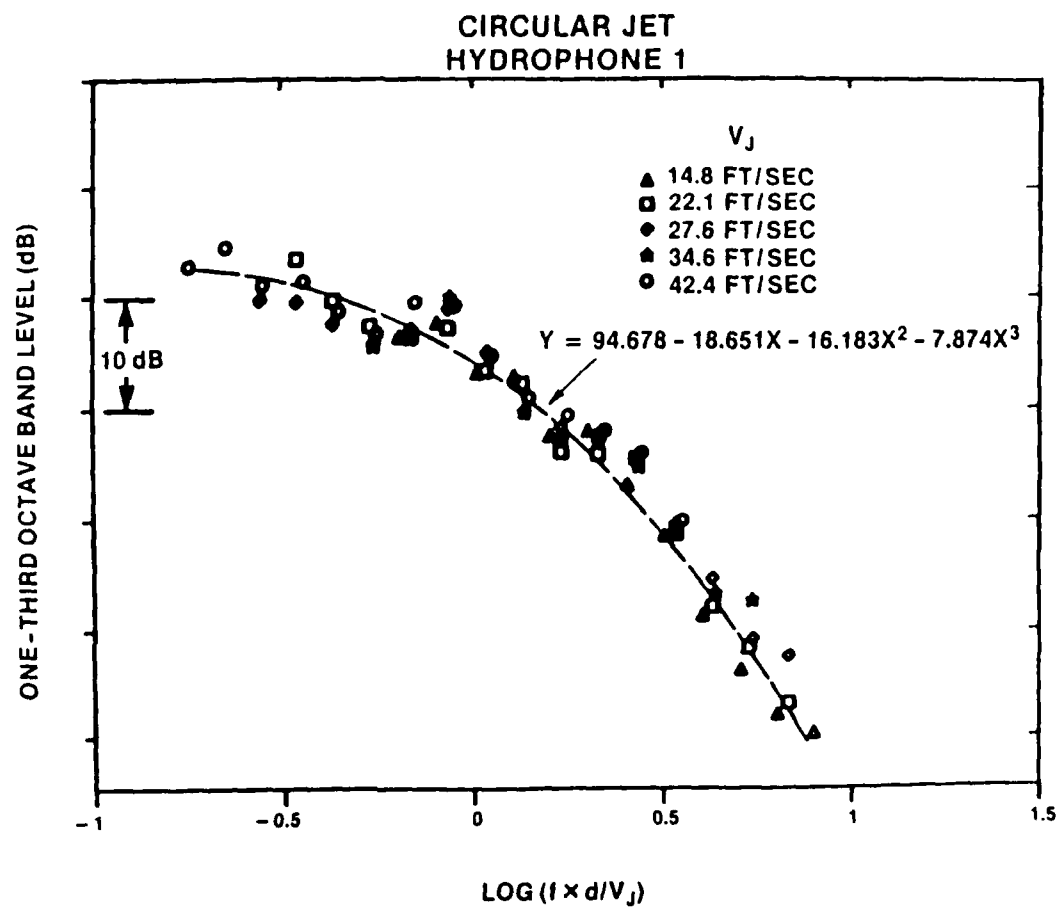


Figure 5-28. Non-dimensional Noise Spectra of Circular Jet Flow

COANNULAR JET HYDROPHONE 1

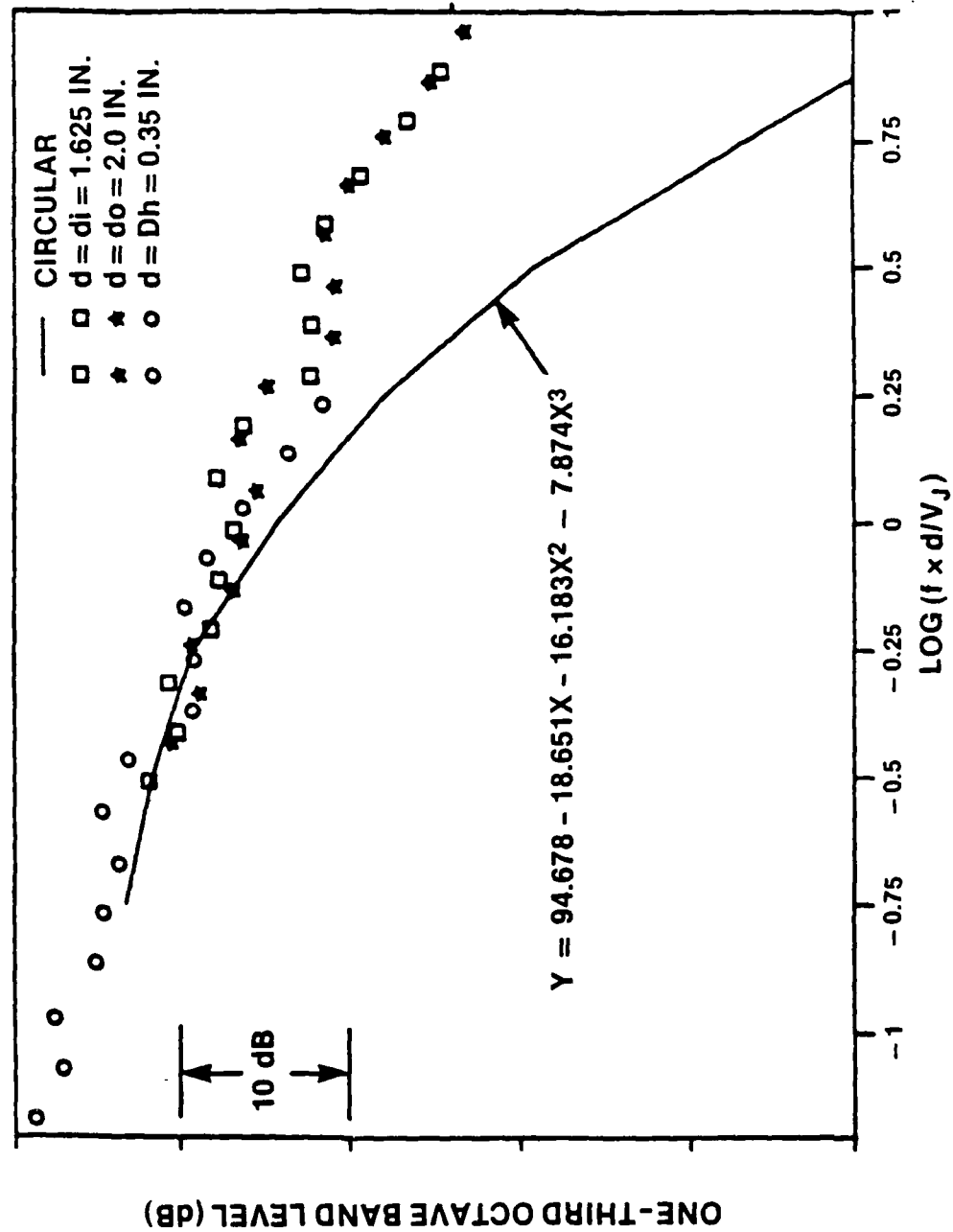


Figure 5-29. Nondimensionalized Noise Spectra of Coannular Jet Flow

VARIOUS FLOW RESTRICTORS HYDROPHONE 4

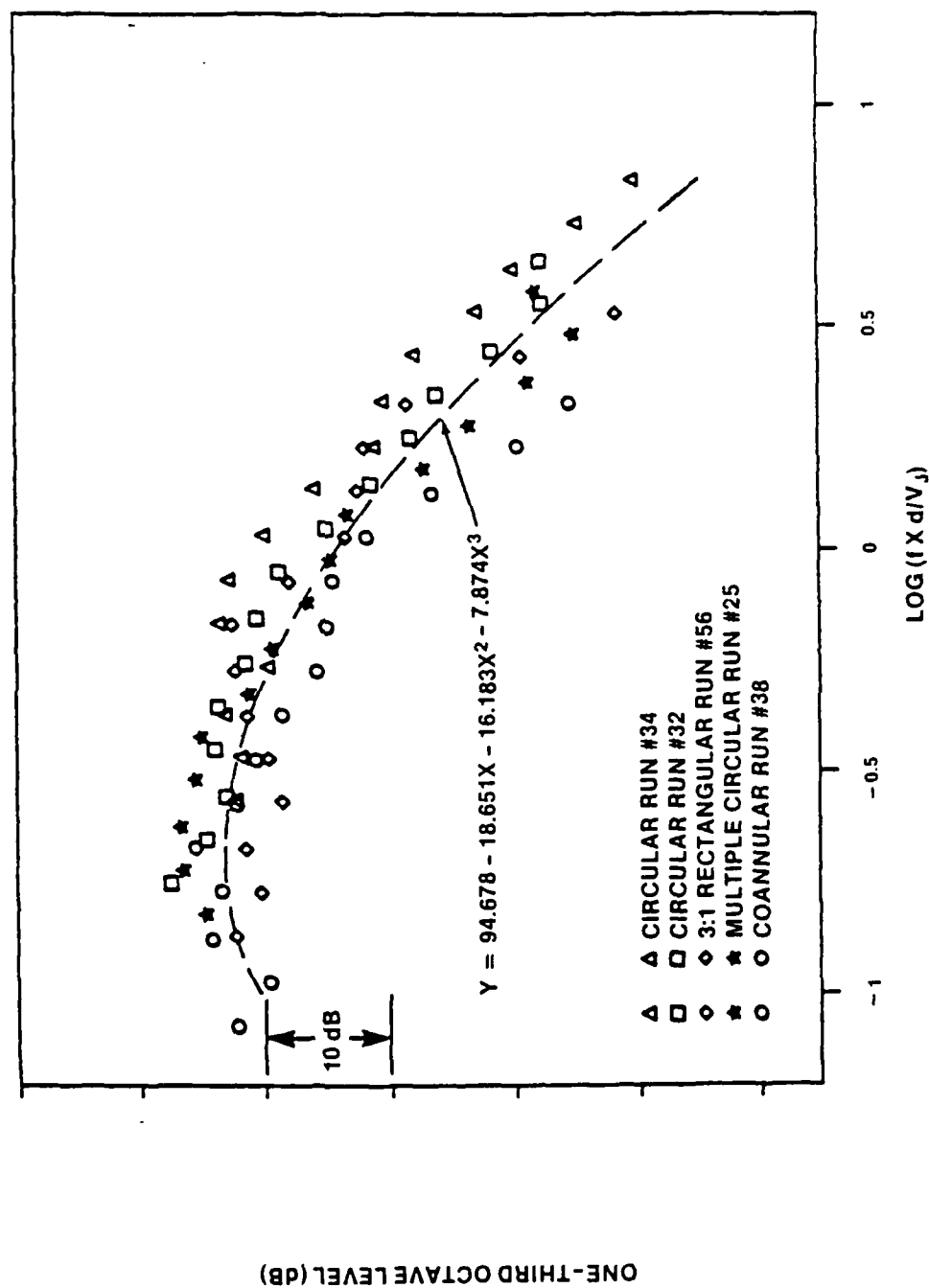


Figure 5-30. Non-dimensional Noise Spectra of Various Flow Restrictors

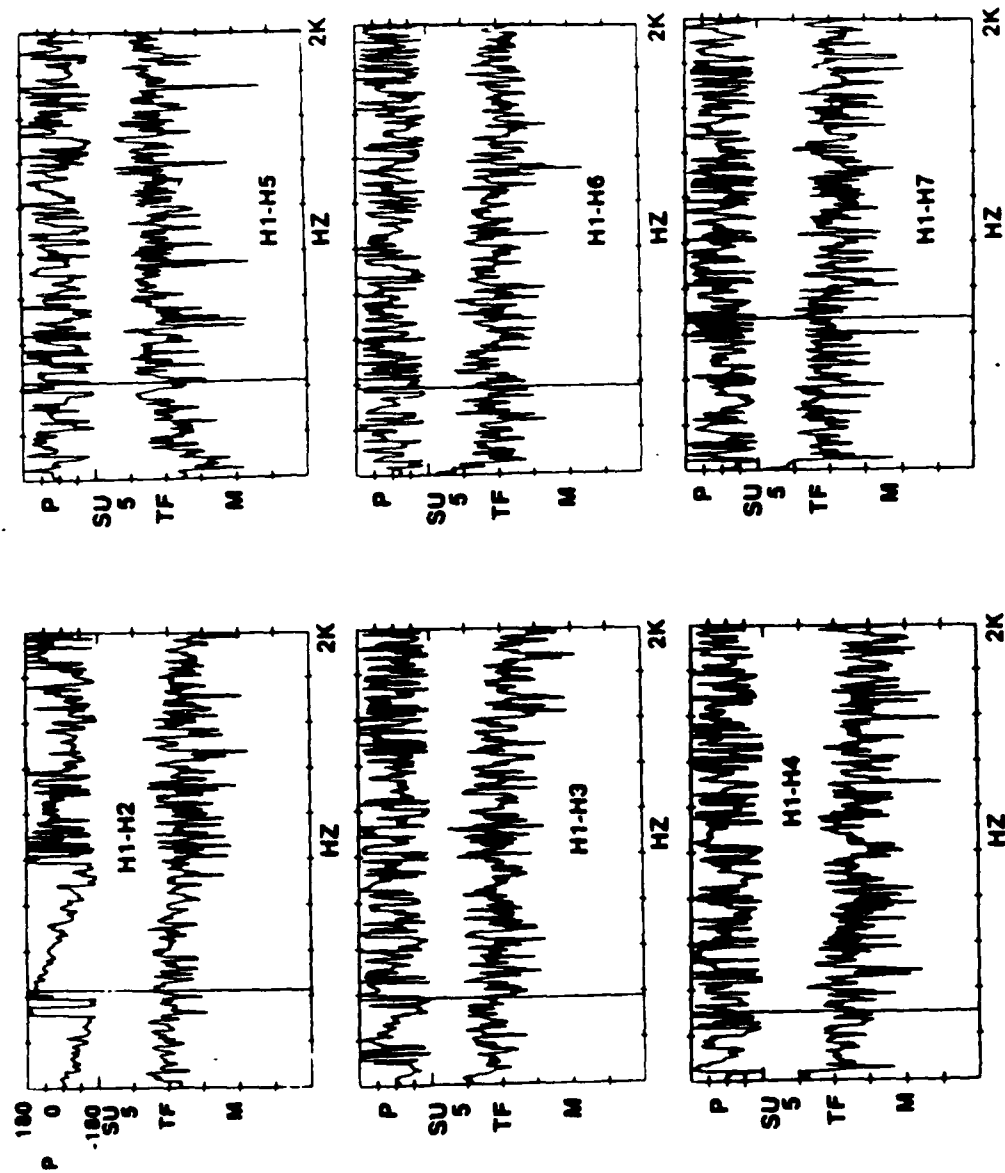


Figure 5-31. Transfer Functions of Hydrophone Signals for Pipe Flow

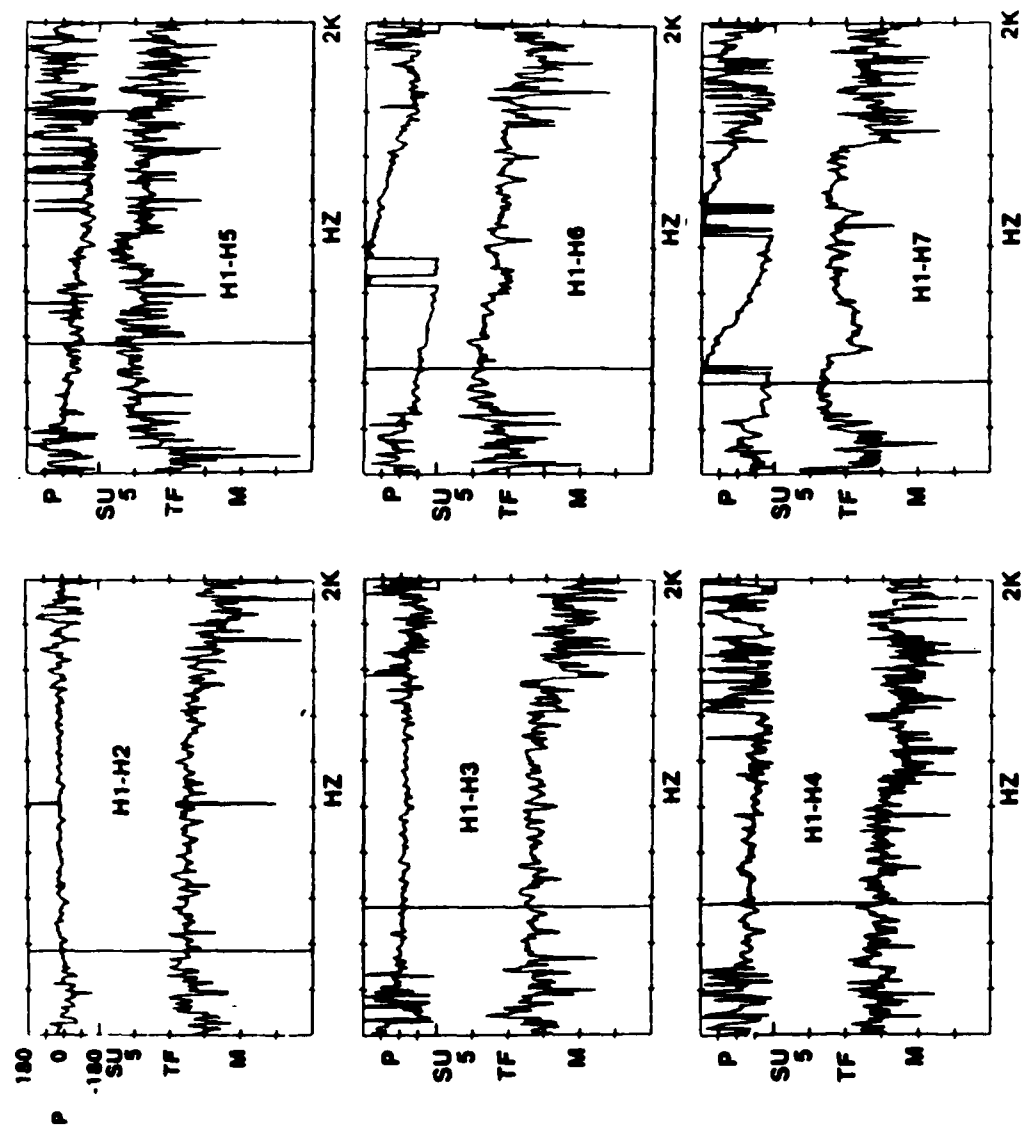


Figure 5-32. Transfer Functions of Hydrophone Signals for

Circular Jet Flow

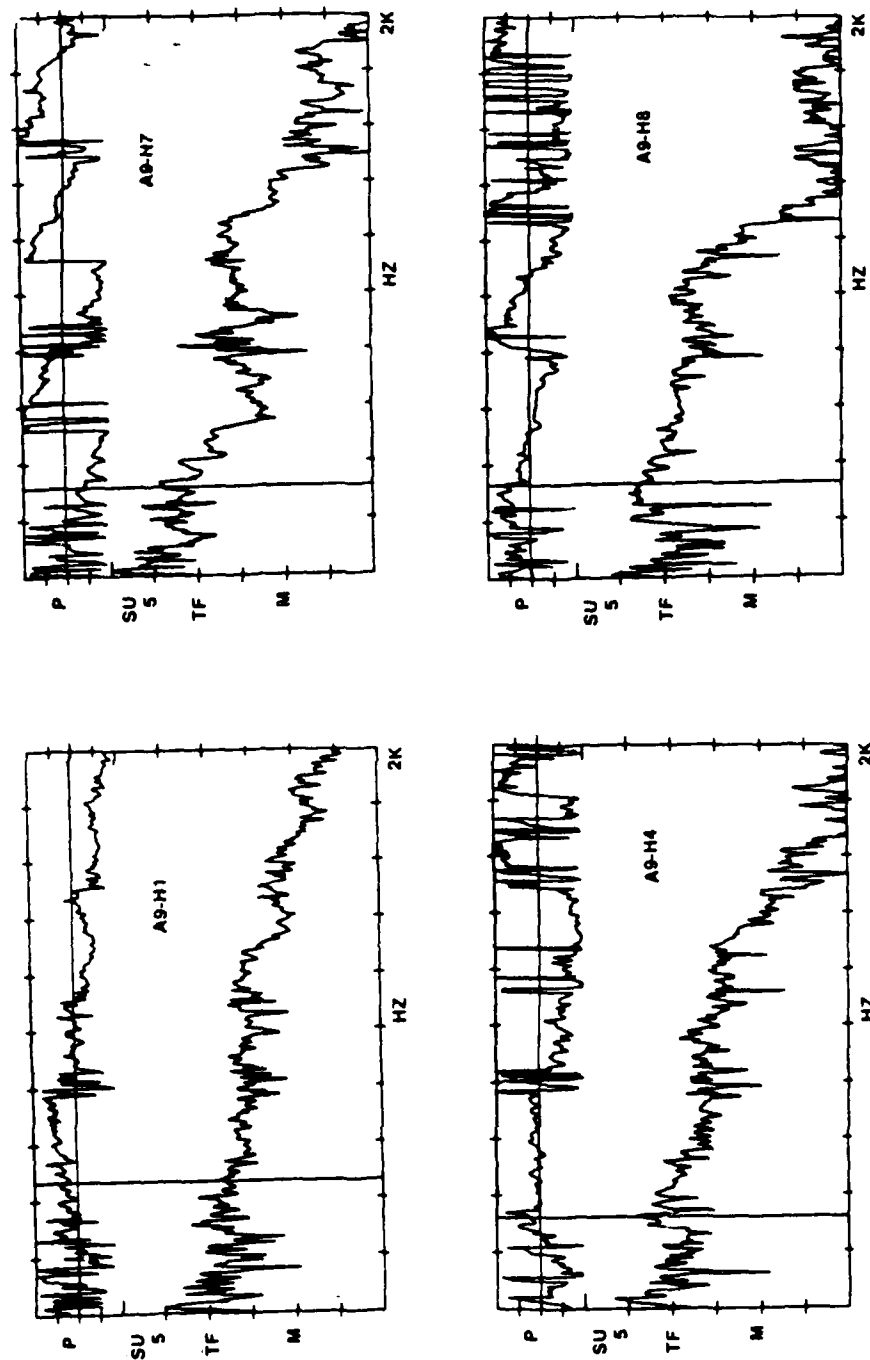


Figure 5-33. Transfer Functions of Accelerometers vs
Hydrophone Signals for 3:1 Rectangular Jet

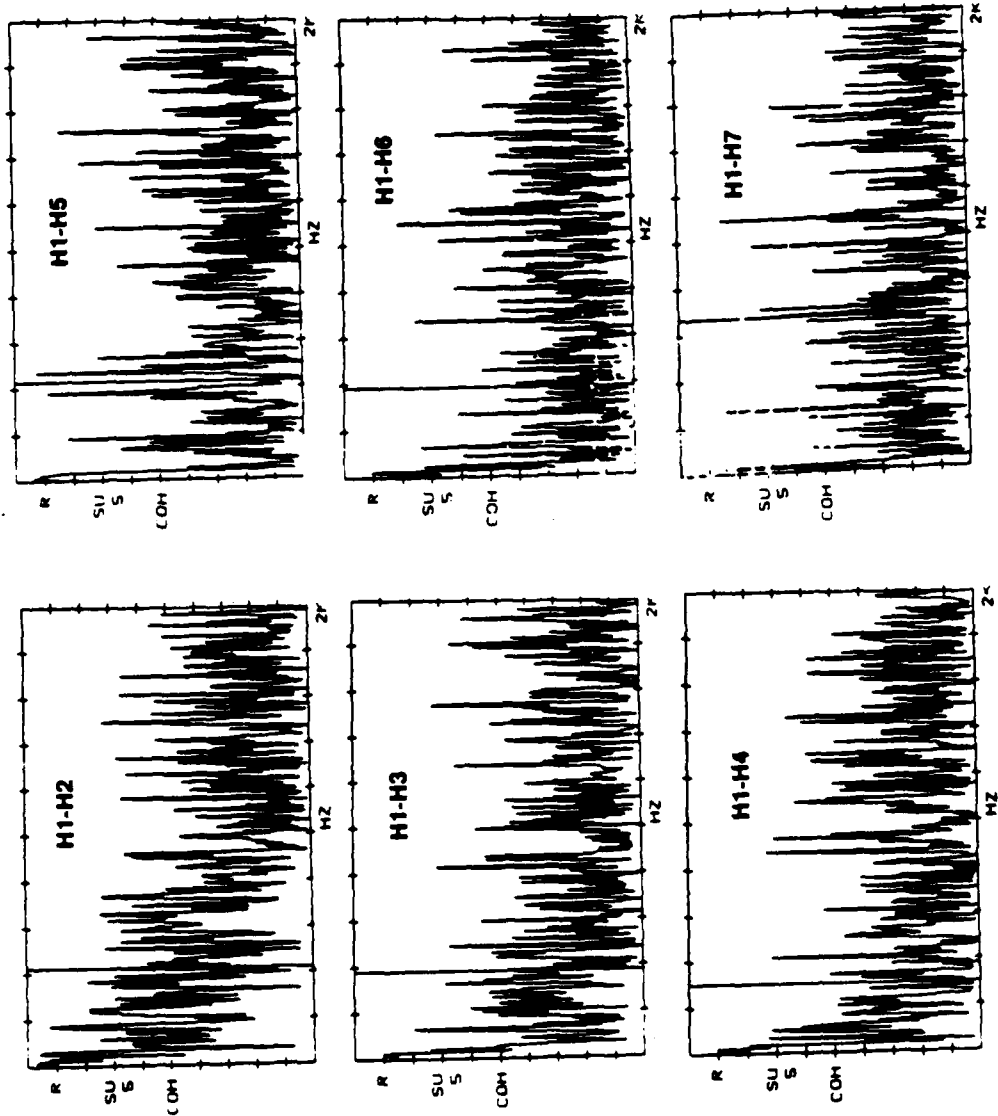


Figure 5-34. Coherence Functions of Hydrophone Signals for Pipe Flow

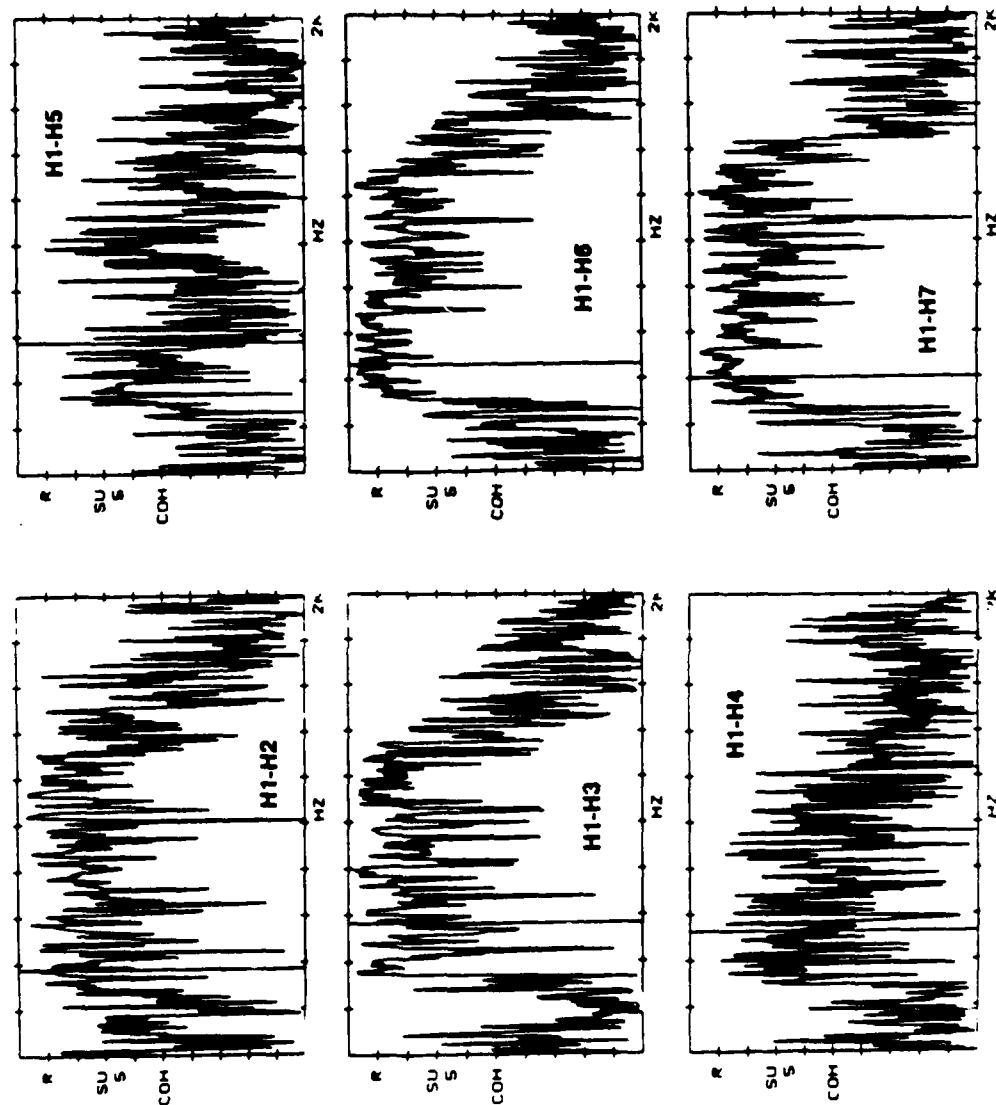


Figure 5-35. Coherence Functions of Hydrophone Signals for
Circular Jet Flow

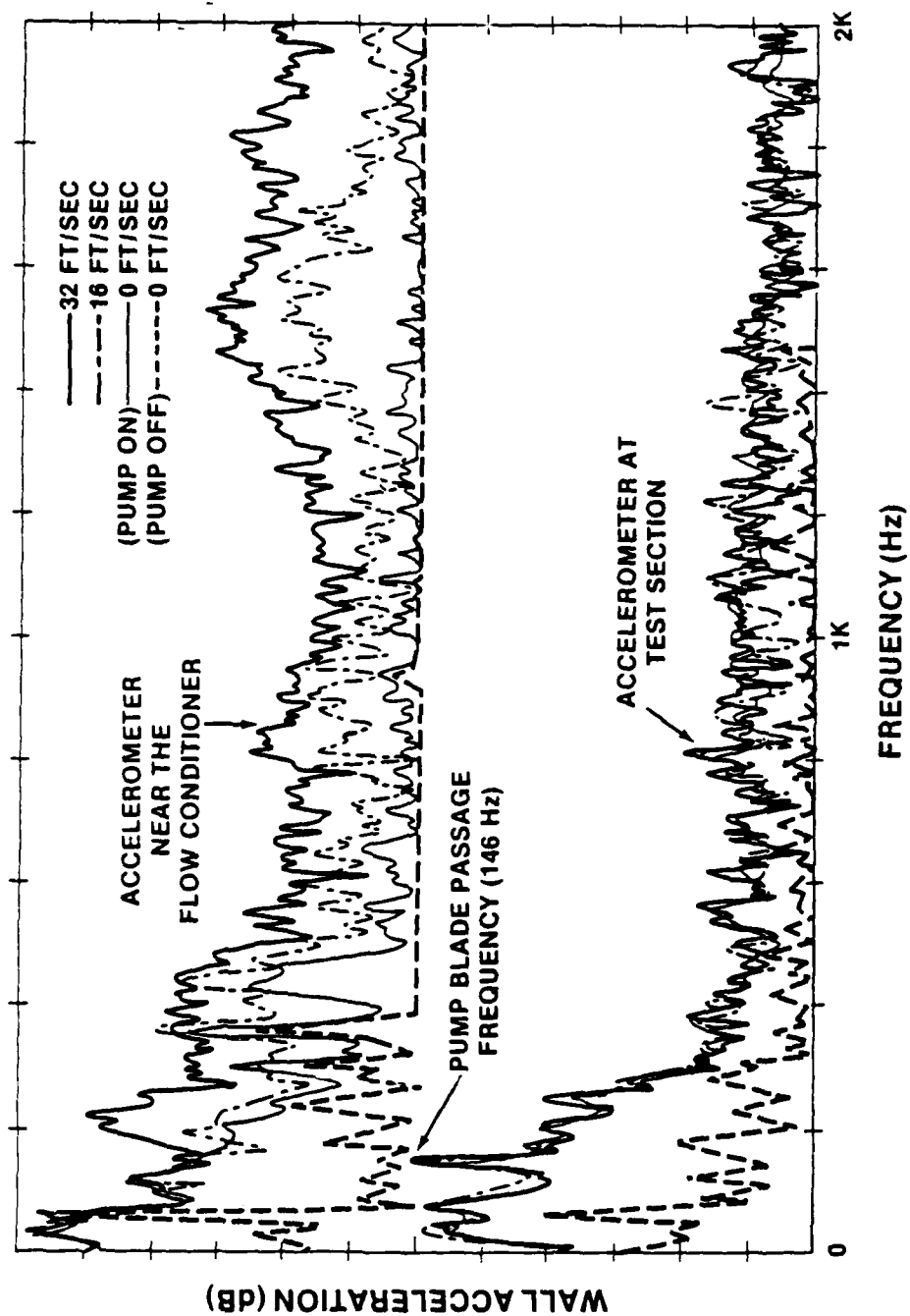


Figure 5-36. Pipe Wall Acceleration Measurement from Acoustic Checkout

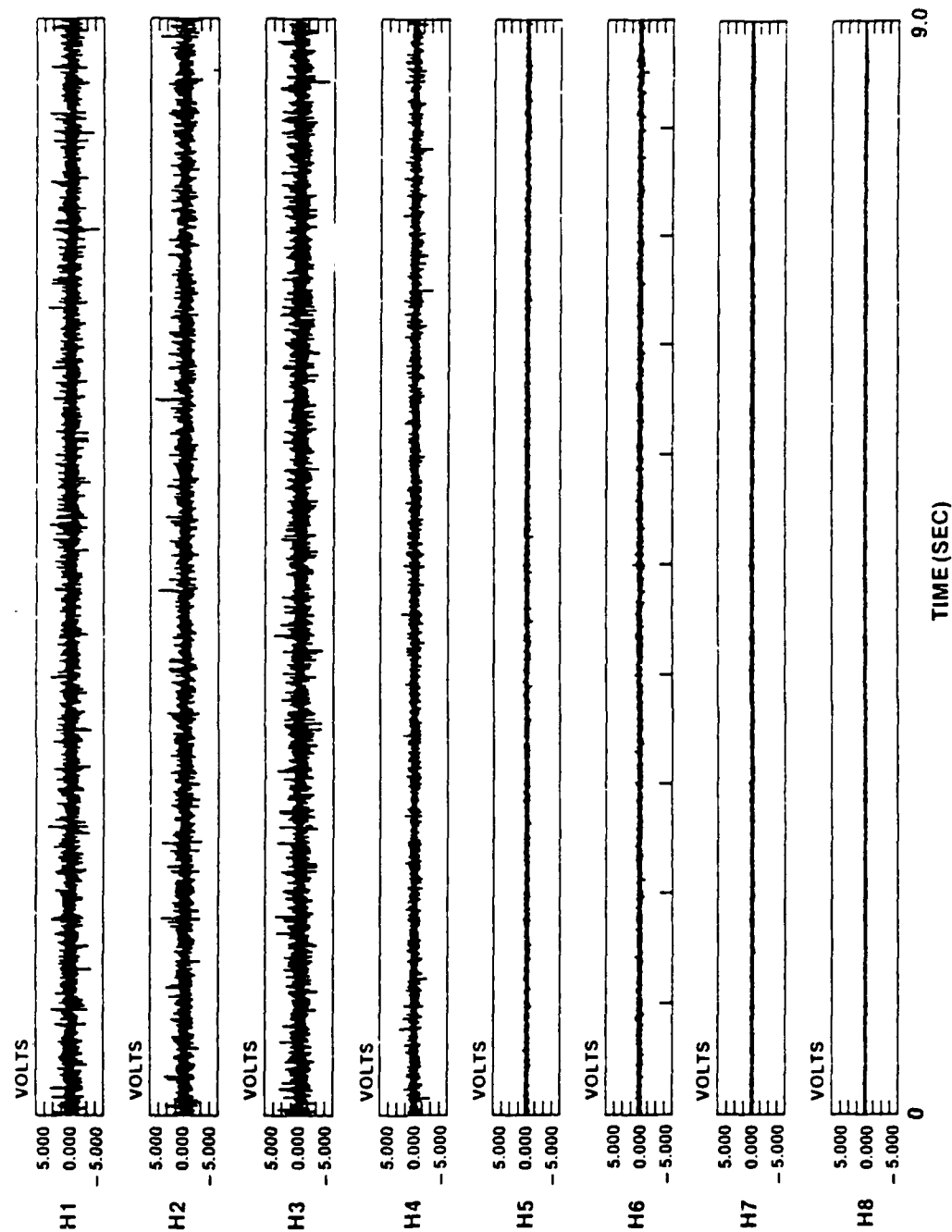


Figure 5-37. Time History of Hydrophone Signals - 1.25-Inch Jet

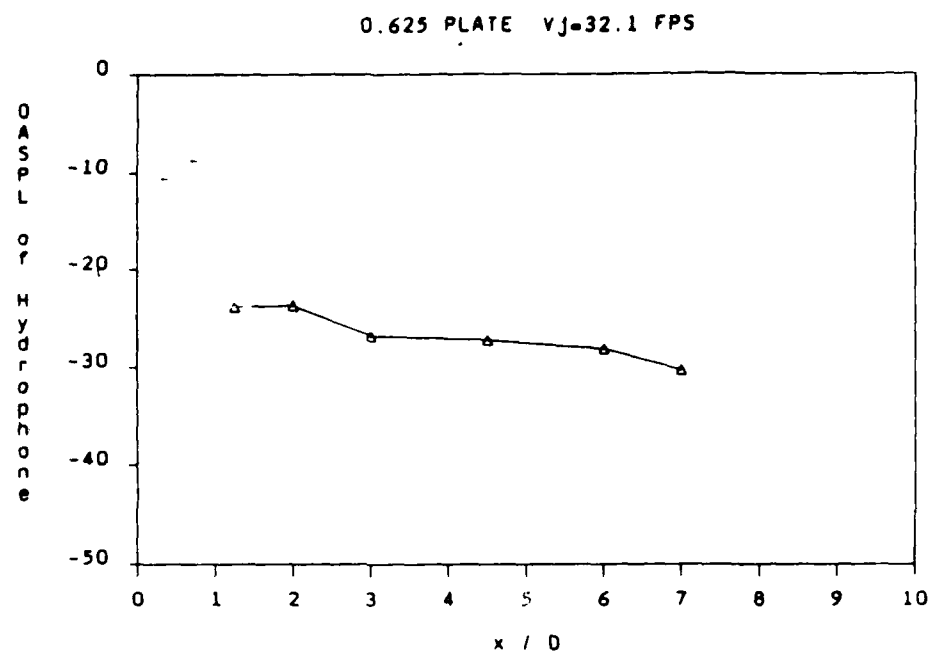


Figure 5-38a. OASPL vs Location - 0.625-Inch Jet

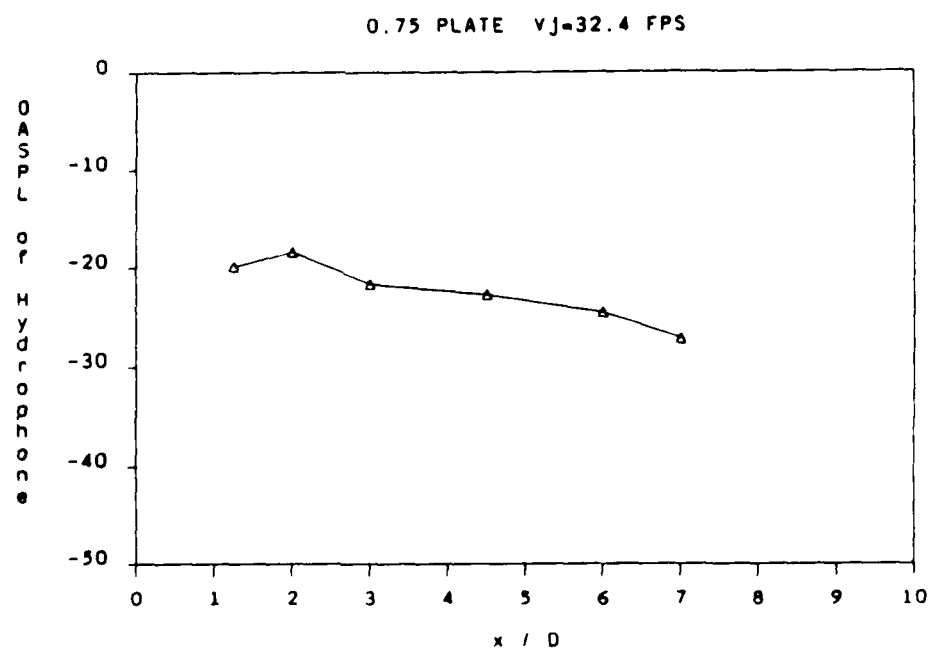


Figure 5-38b. OASPL vs Location - 0.75-Inch Jet

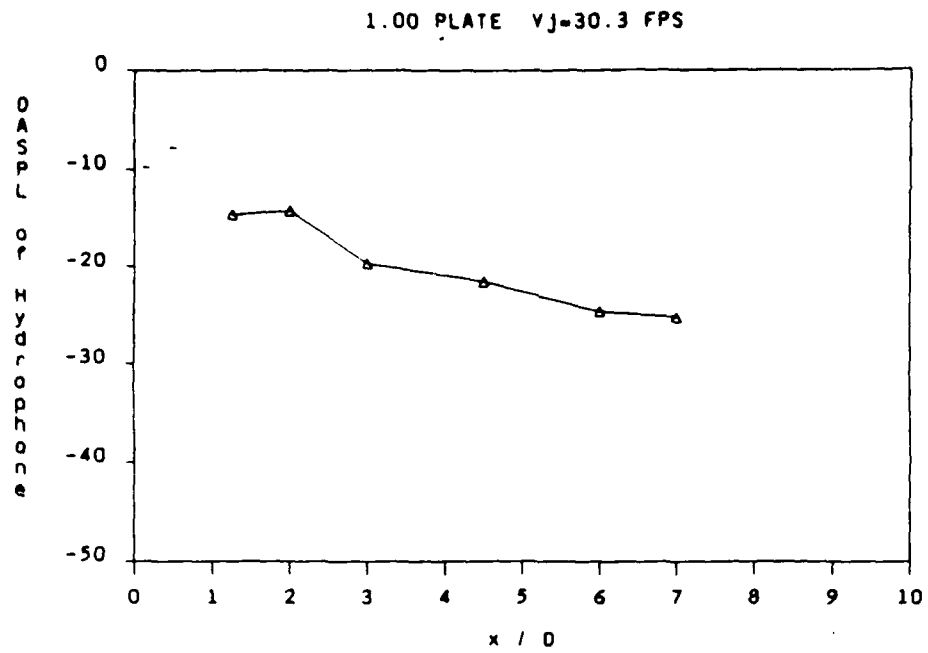


Figure 5-38c. OASPL vs Location - 1.00-Inch Jet

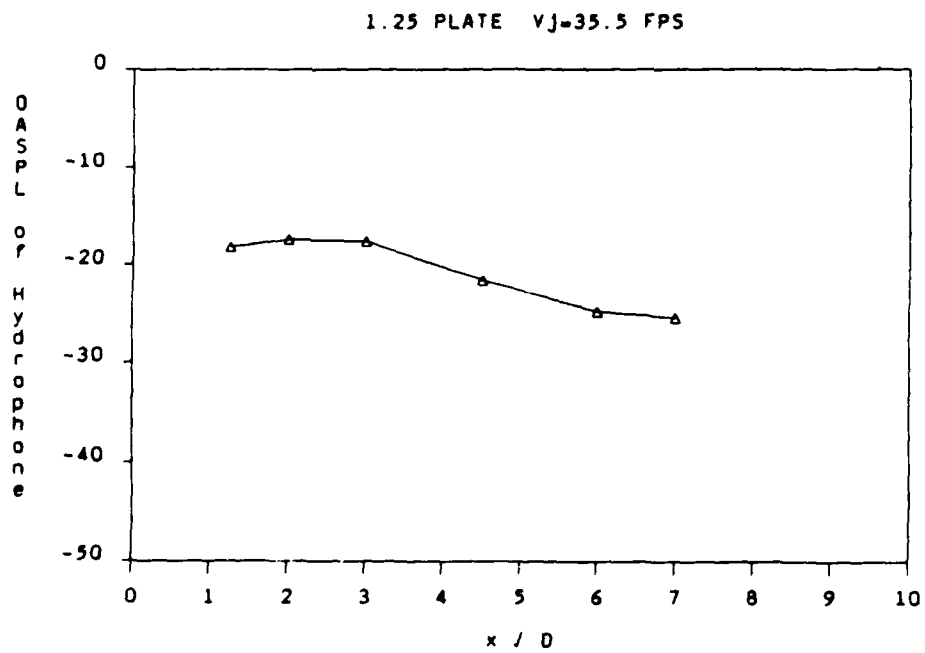


Figure 5-38d. OASPL vs Location - 1.25-Inch Jet

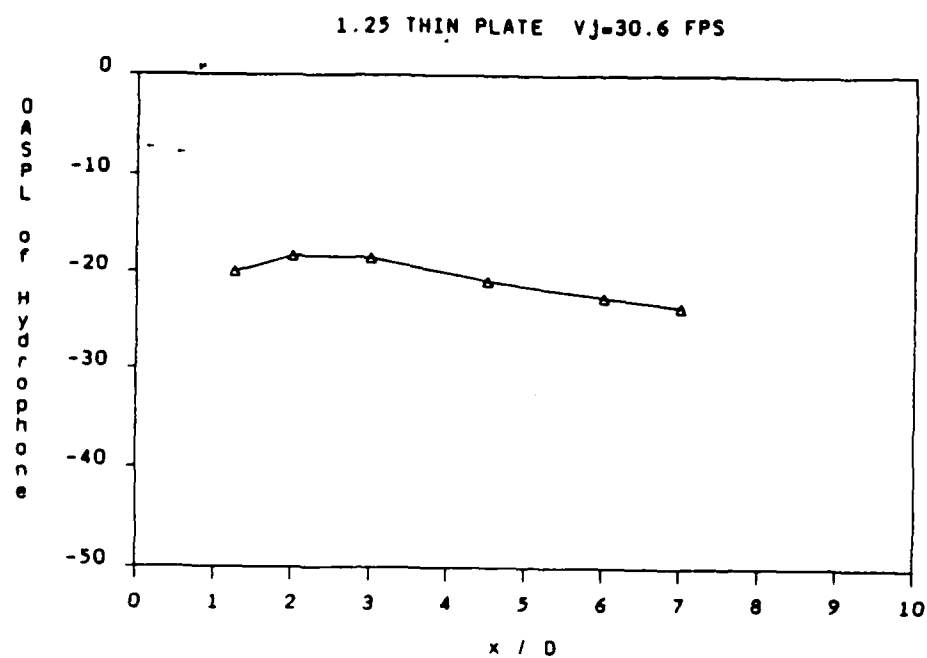


Figure 5-38e. OASPL vs Location - 1.25-Inch Thin Plate

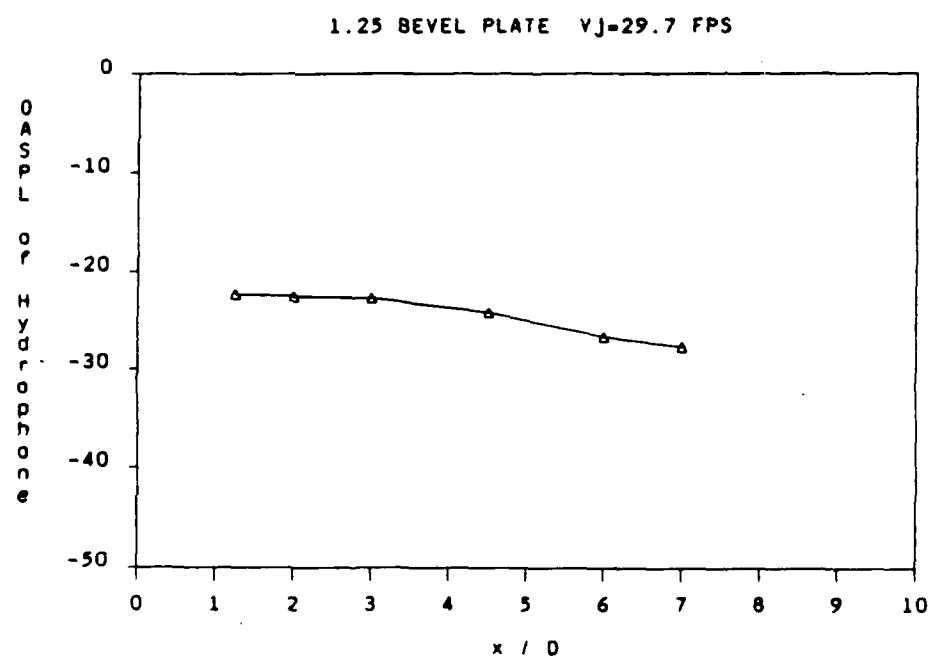


Figure 5-38f. OASPL vs Location - 1.25-Inch Bevel Plate

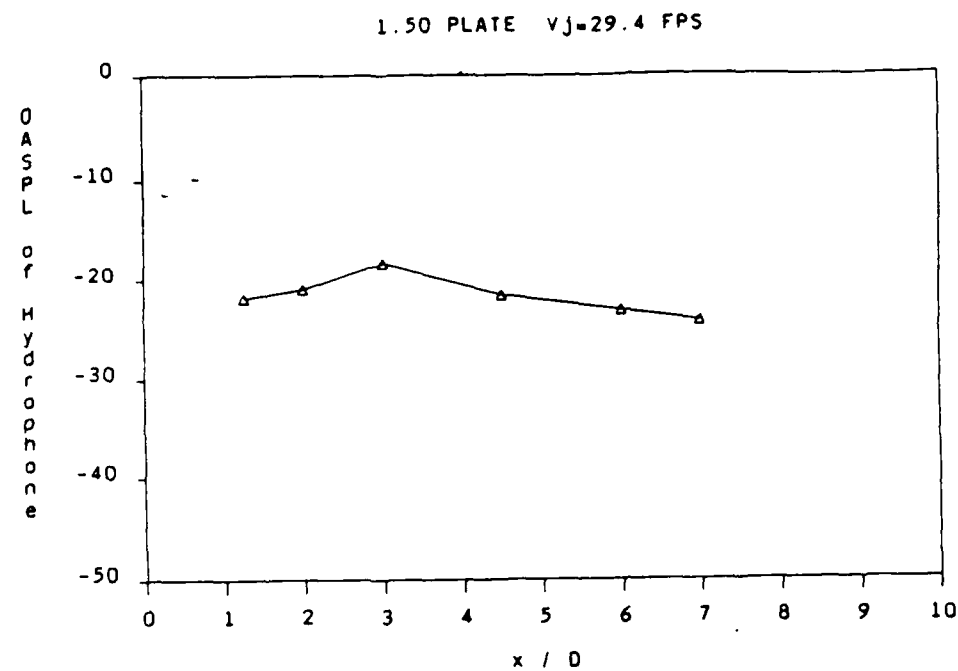


Figure 5-38g. OASPL vs Location - 1.50-Inch Jet

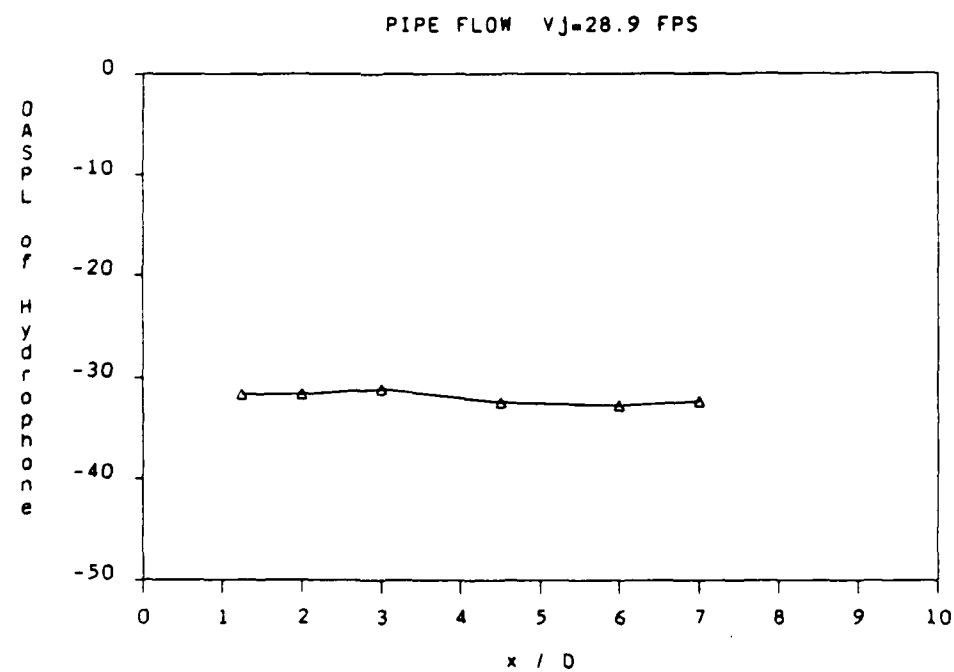


Figure 5-38h. OASPL vs Location - Pipe Flow

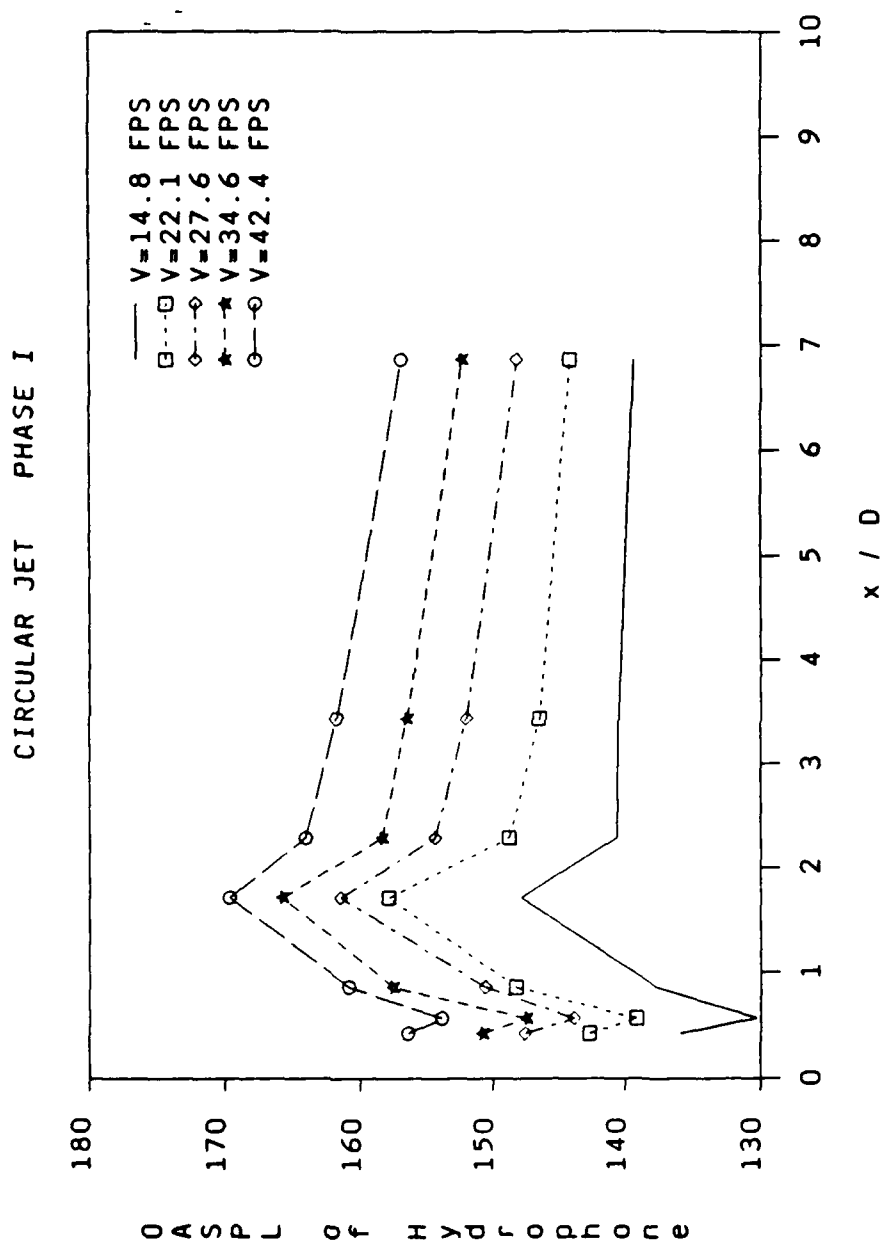


Figure 5-39. Noise vs Location of Circular Jet - Phase I

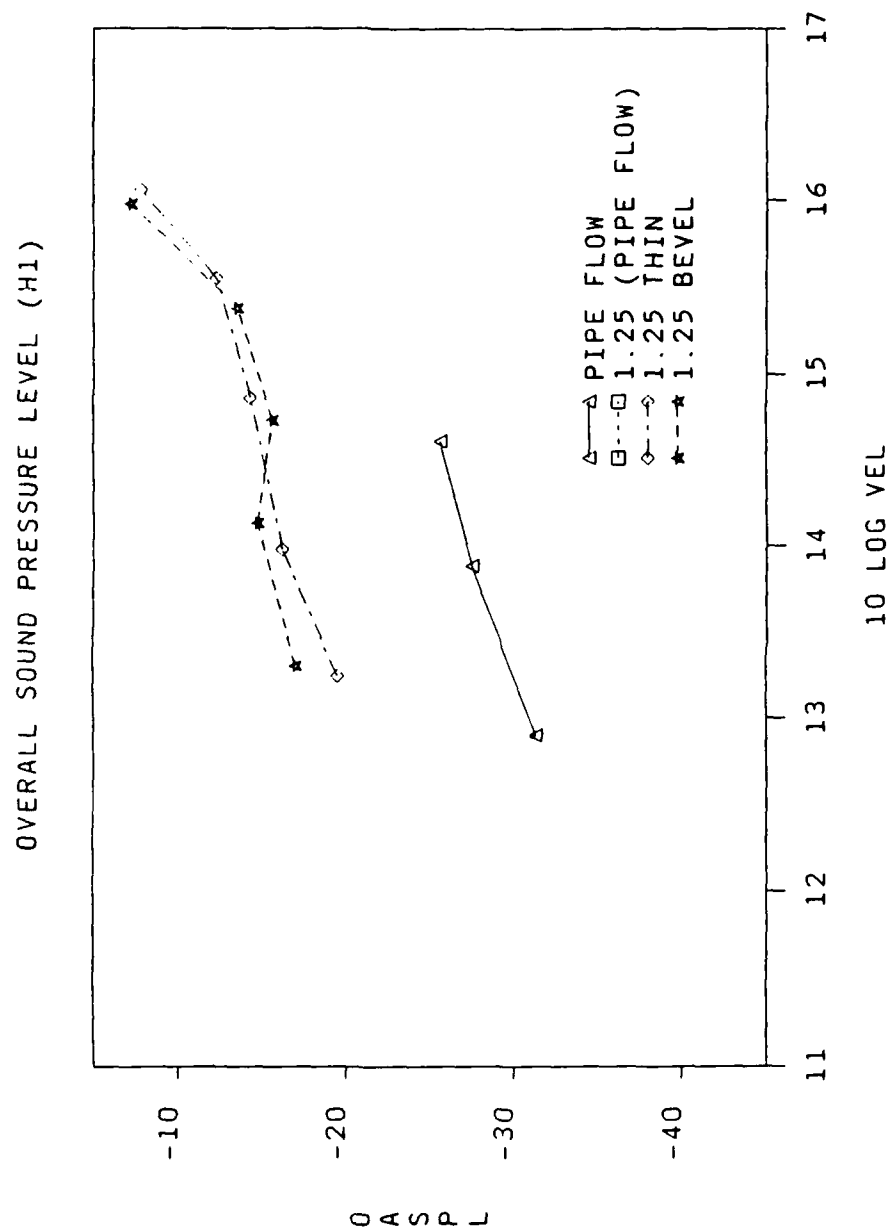


Figure 5-40a. OASPL vs Velocity - Pipe Flow, 1.25-Inch Thin Plate, 1.25-Inch Bevel Edge Plate

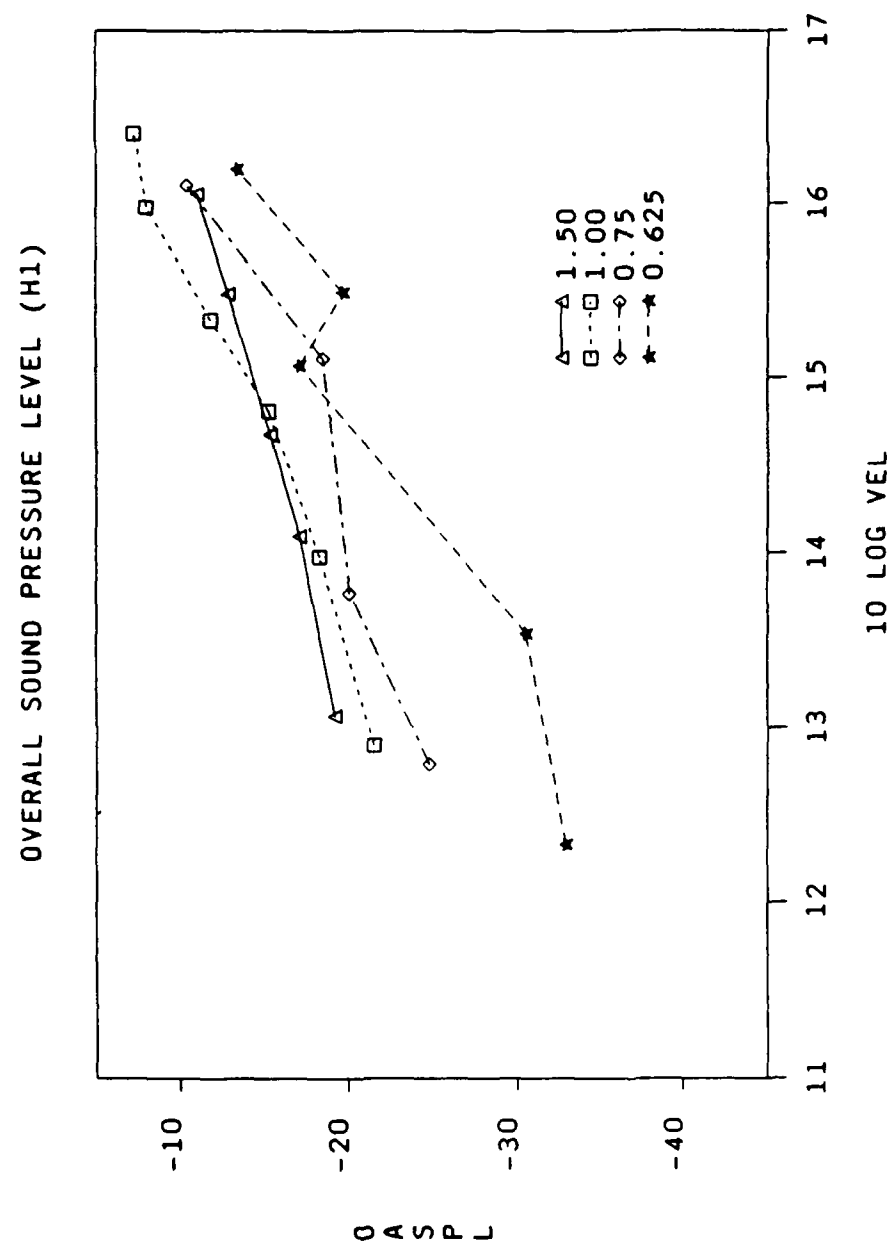


Figure 5-40b. OASPL vs Velocity - 0.625, 0.75, 1.00, 1.50-Inch Jets

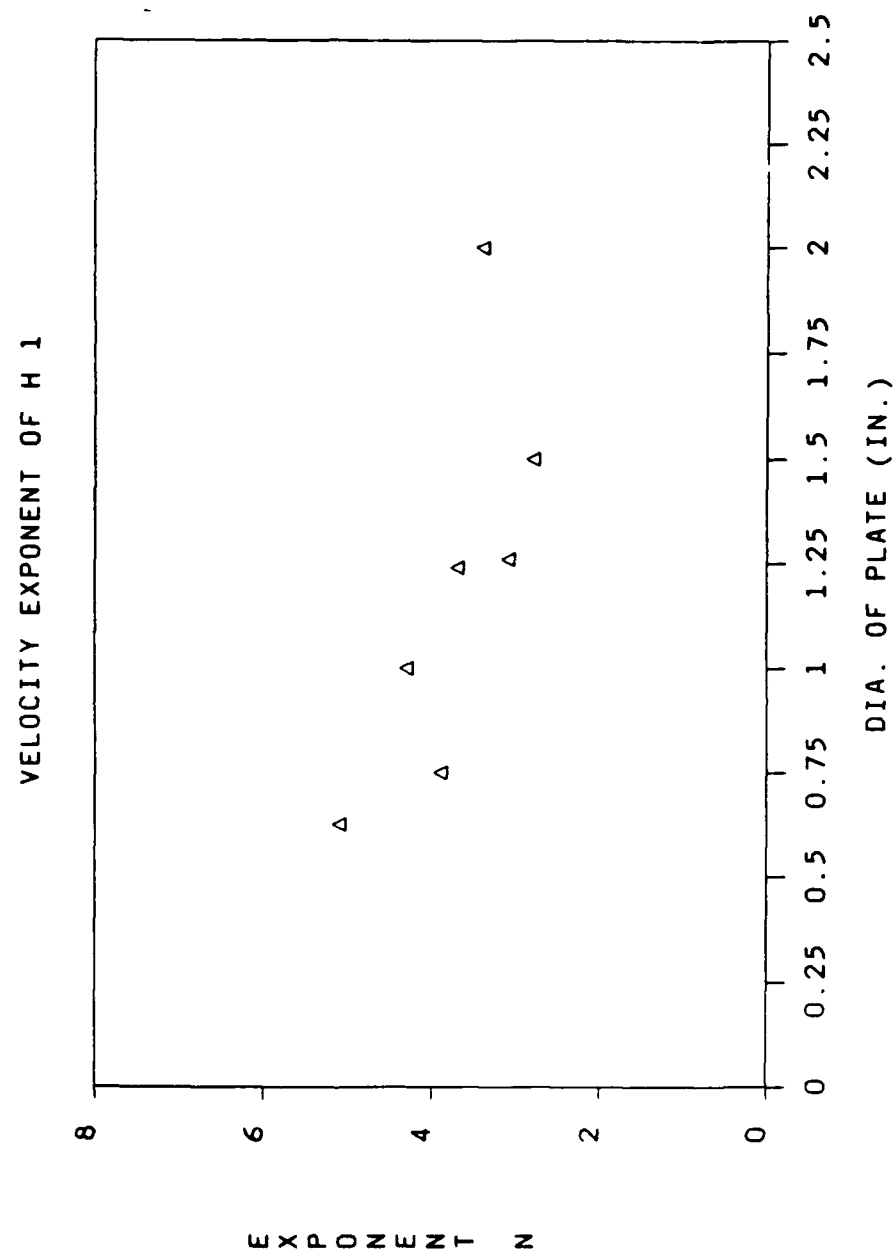


Figure 5-41. Velocity Exponents for Confined Jets

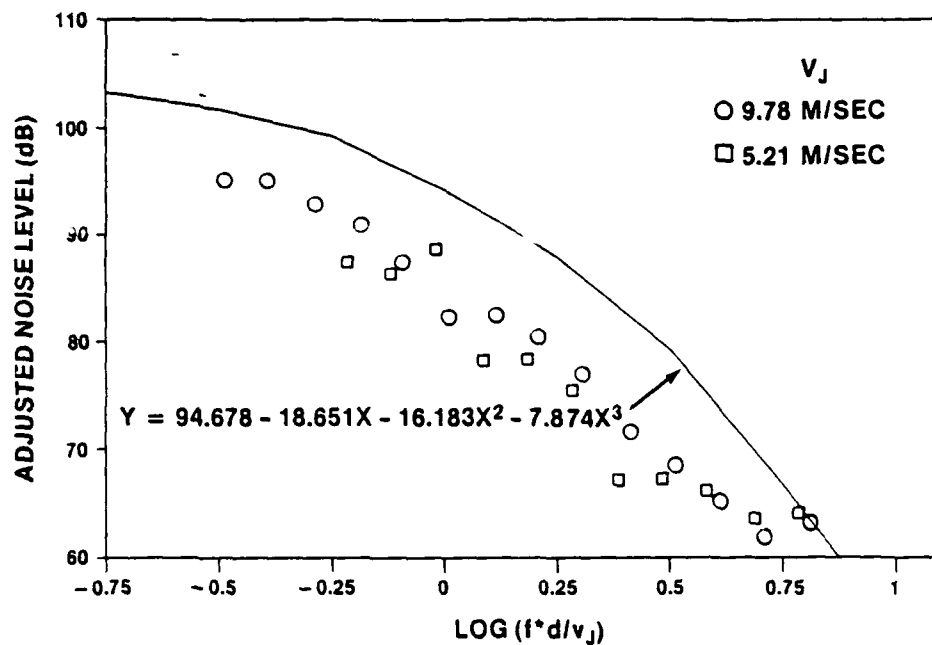


Figure 5-42a. Normalized Noise Spectra - 0.625-Inch Jet

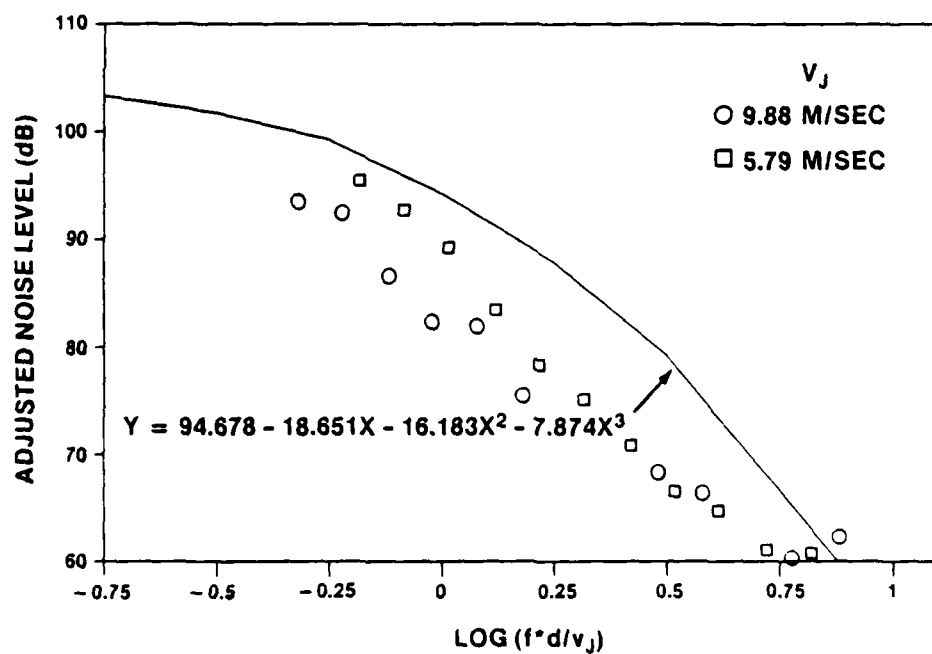


Figure 5-42b. Normalized Noise Spectra - 0.75-Inch Jet

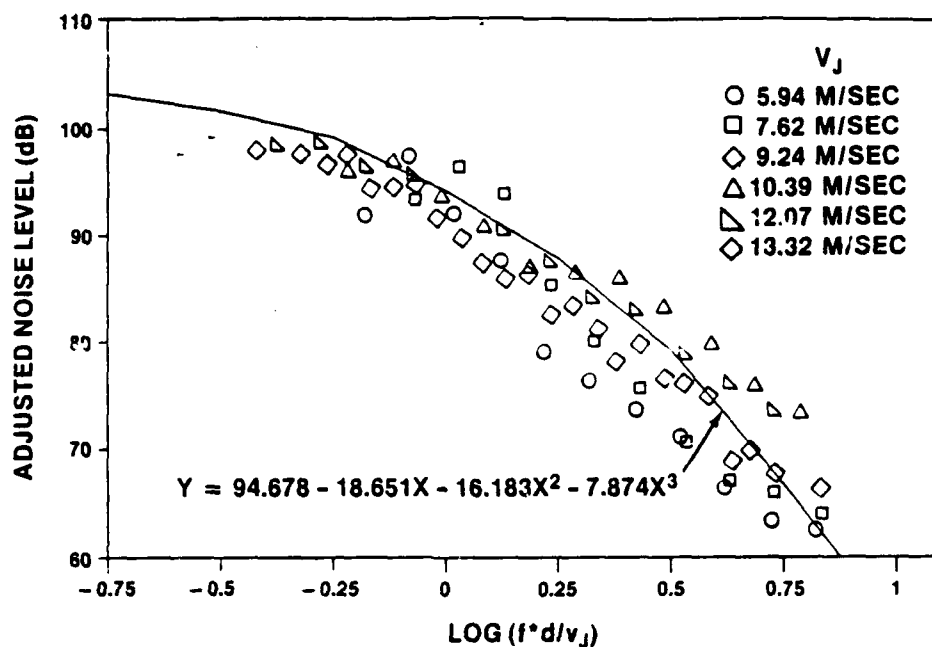


Figure 5-42c. Normalized Noise Spectra - 1.00-Inch Jet

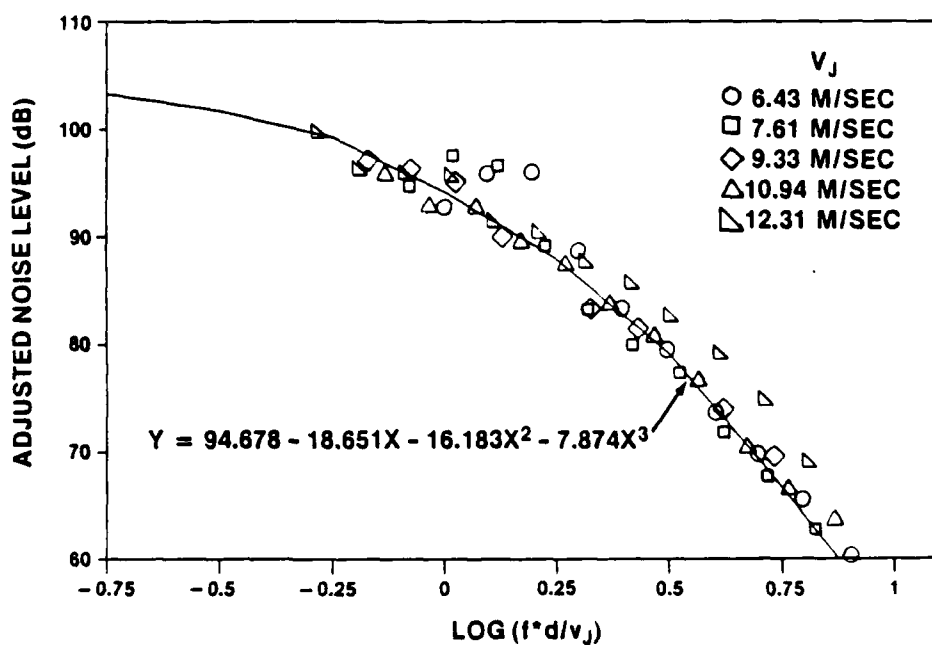


Figure 5-42d. Normalized Noise Spectra - 1.25-Inch Thin Plate

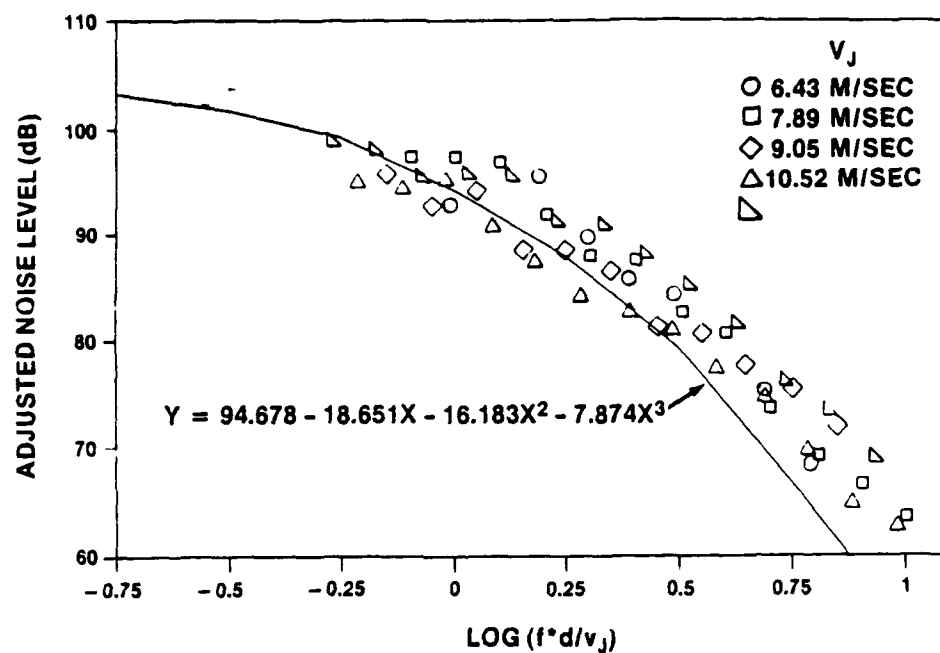


Figure 5-42e. Normalized Noise Spectra - 1.25-Inch Bevel Plate

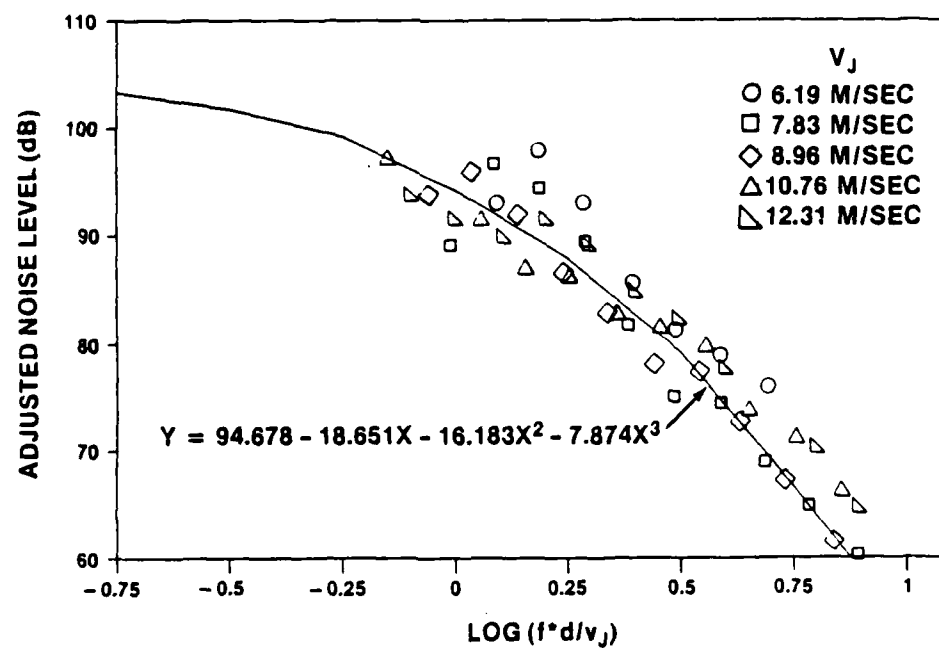


Figure 5-42f. Normalized Noise Spectra - 1.50-Inch Jet

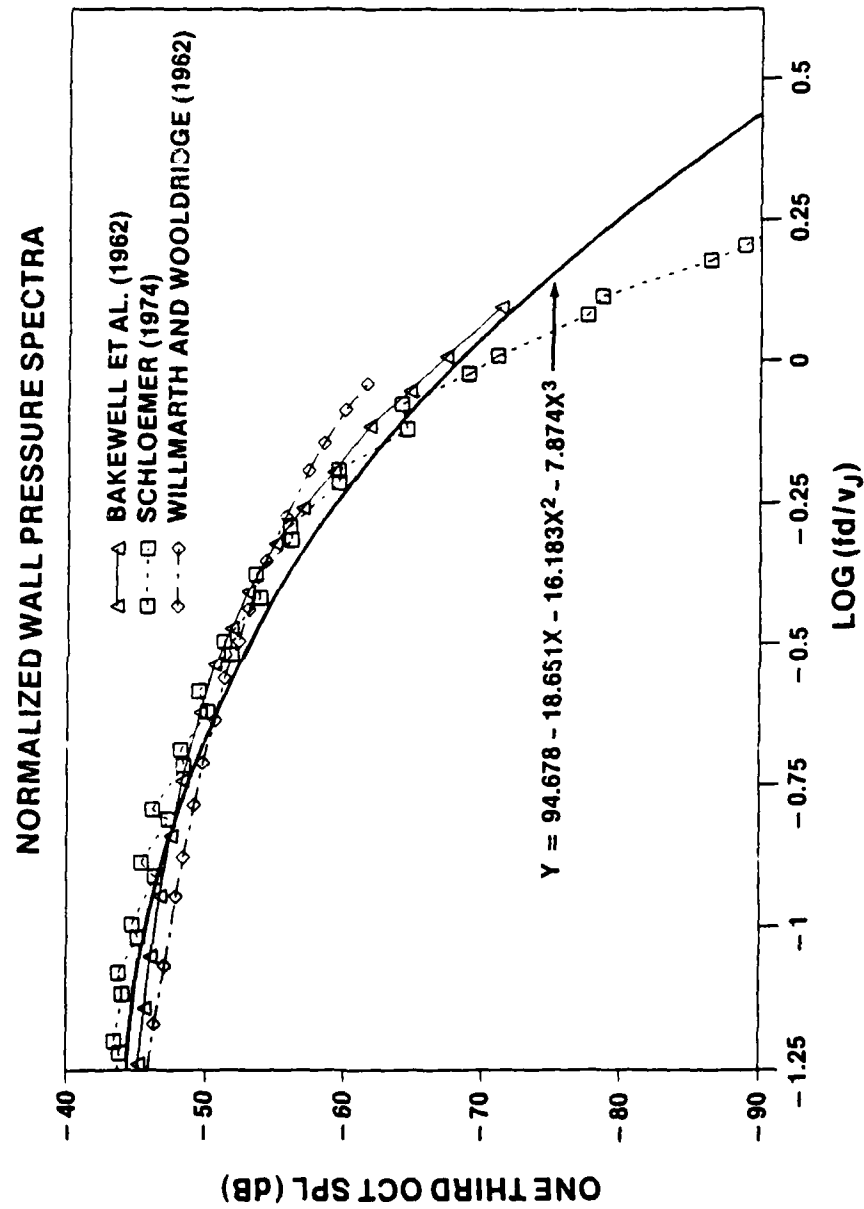


Figure 5-43. Normalized Noise Spectra Comparison

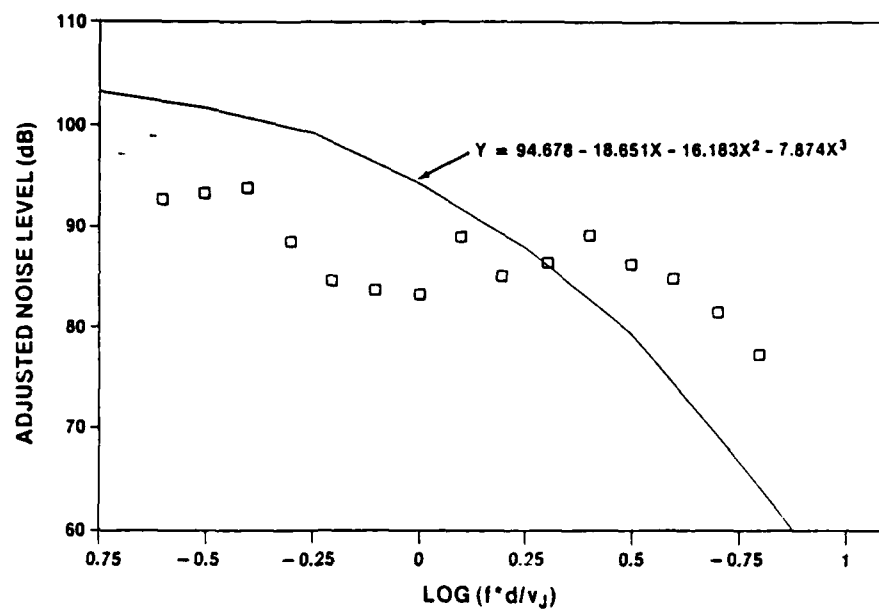


Figure 5-44a. Noise Spectra of Cavitating Jet - 0.625-Inch Jet

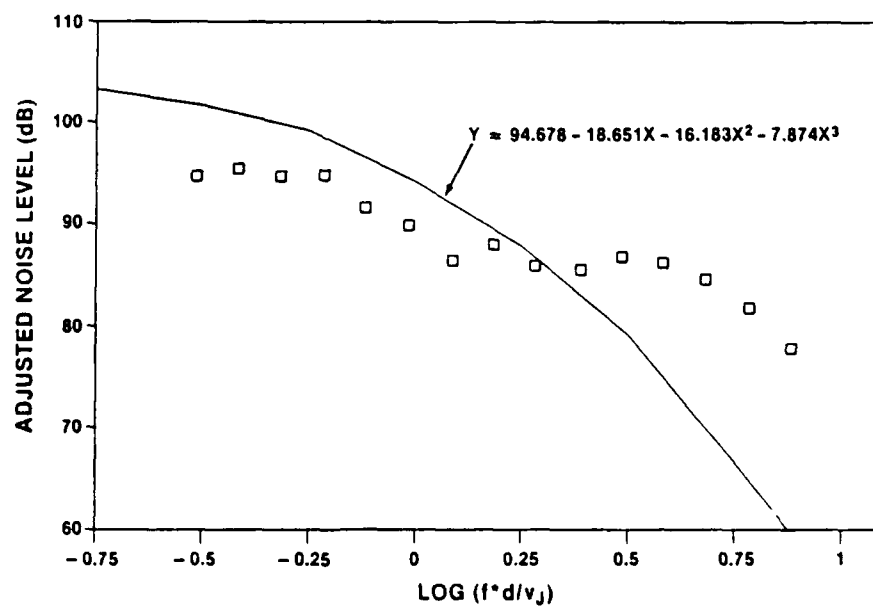


Figure 5-44b. Noise Spectra of Cavitating Jet - 0.75-Inch Jet

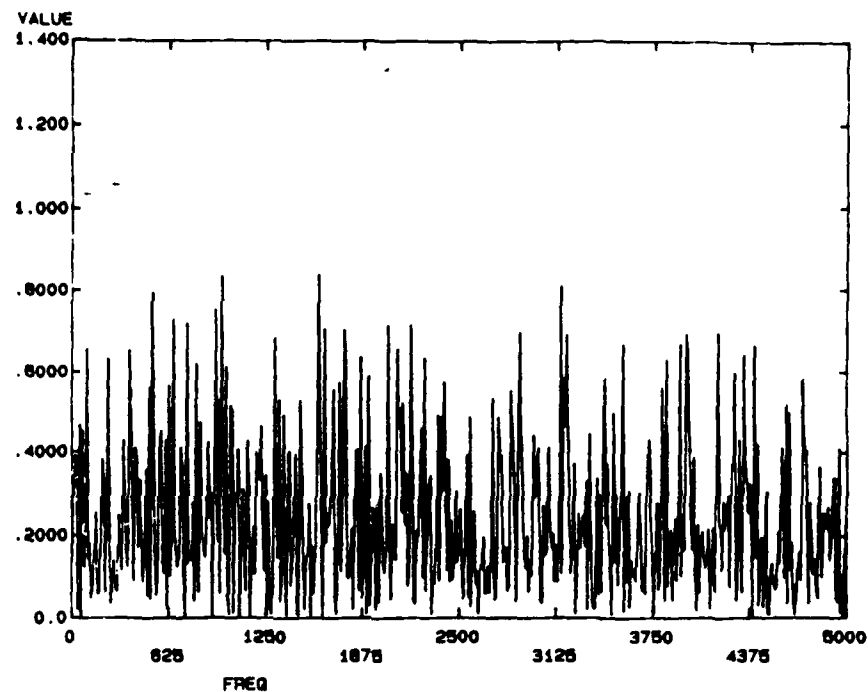


Figure 5-45a. Coherence Function u vs H3 - 0.625-Inch Jet

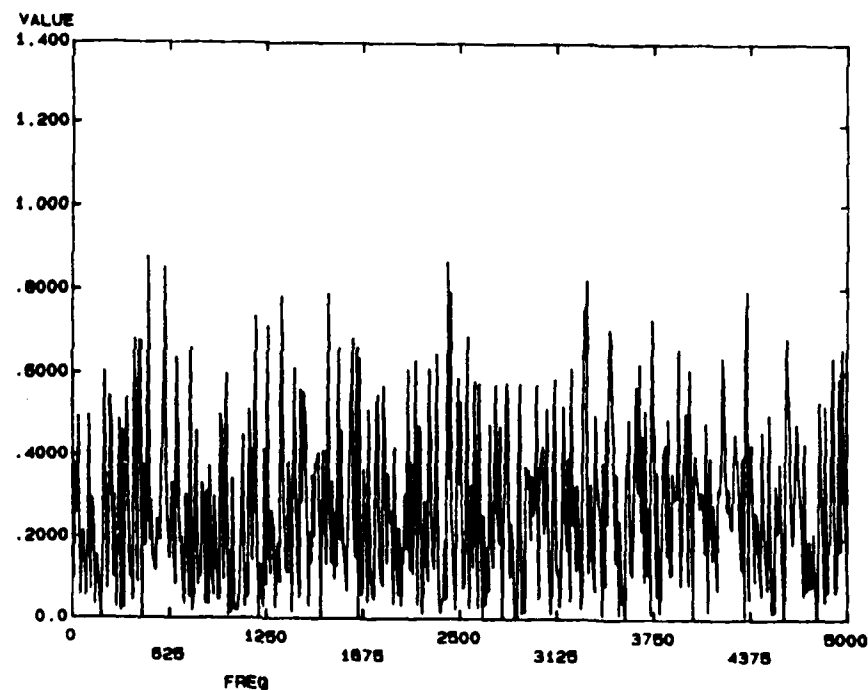


Figure 5-45b. Coherence Function v vs A3 - 0.625-Inch Jet

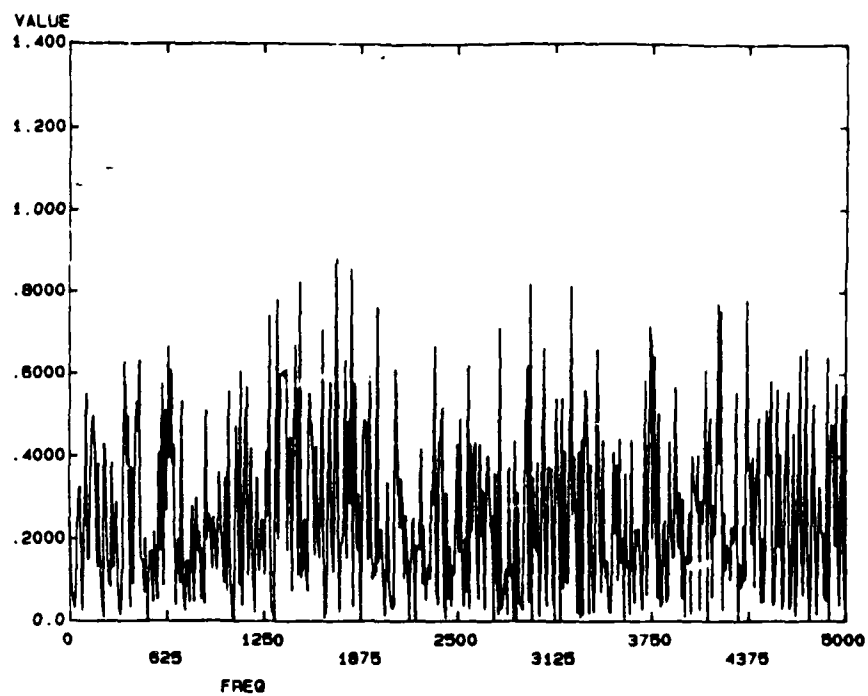


Figure 5-46a. Coherence Function u vs H3 - Pipe Flow

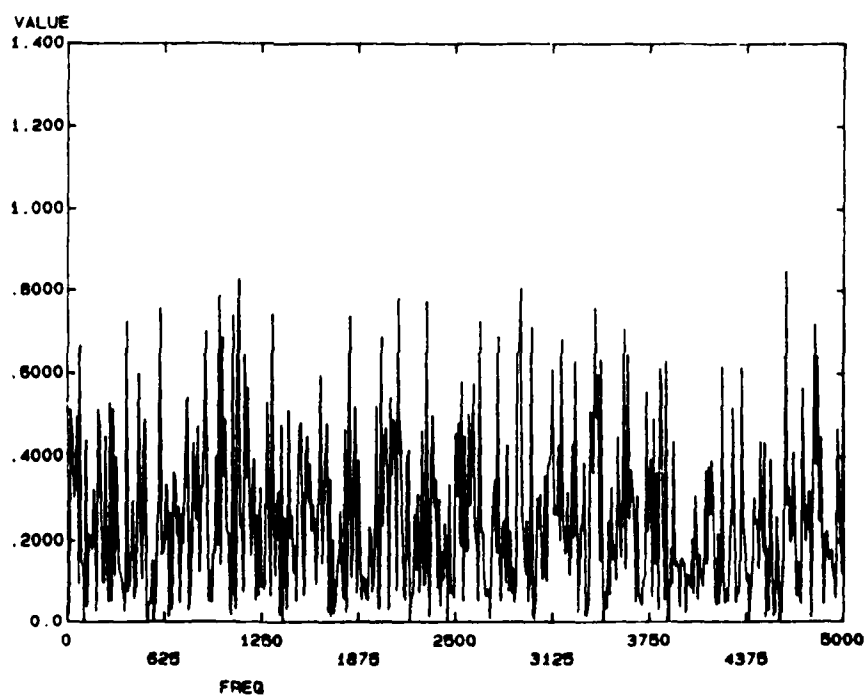


Figure 5-46b. Coherence Function v vs A3 - Pipe Flow

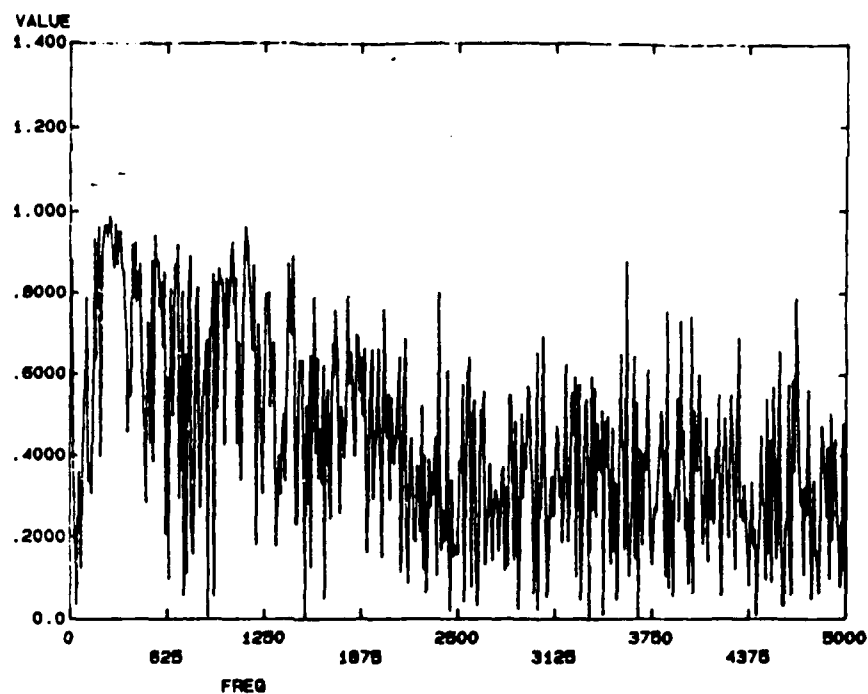


Figure 5-47a. Coherence Function H1 vs H3 - 0.625-Inch Jet

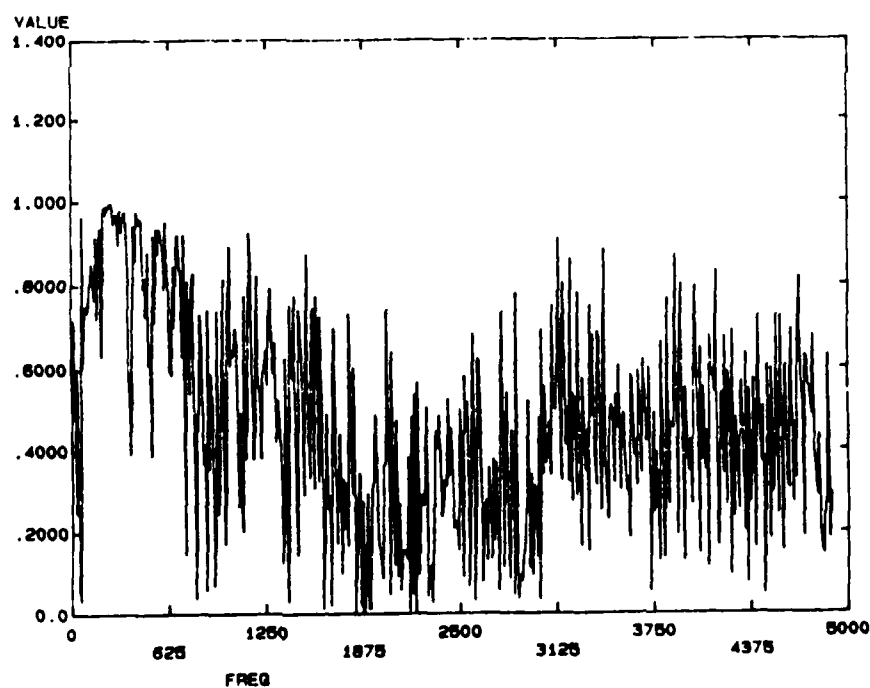


Figure 5-47b. Coherence Function H3 vs H5 - 0.625-Inch Jet

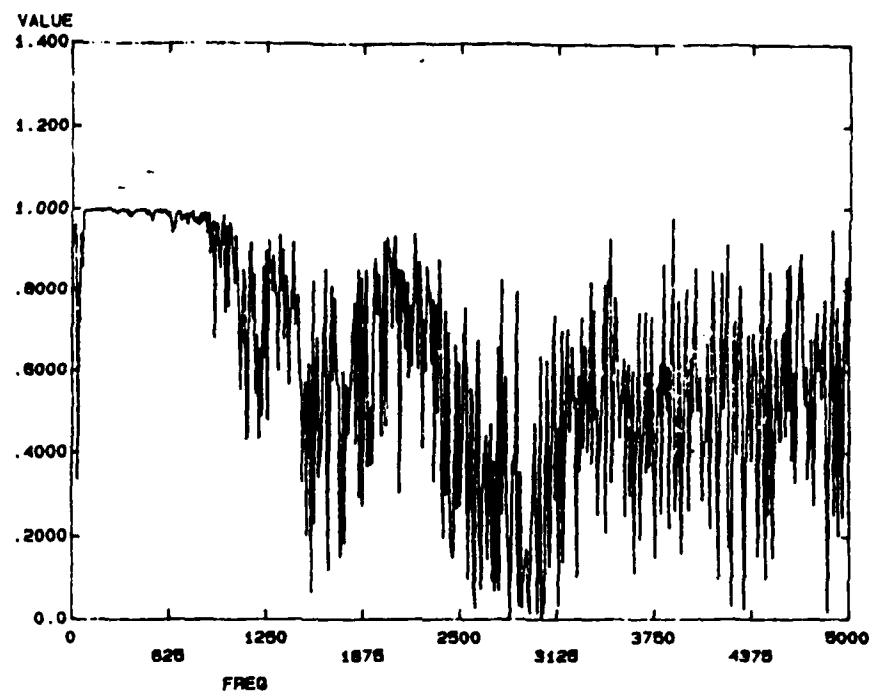


Figure 5-47c. Coherence Function H5 vs H7 - 0.625-Inch Jet

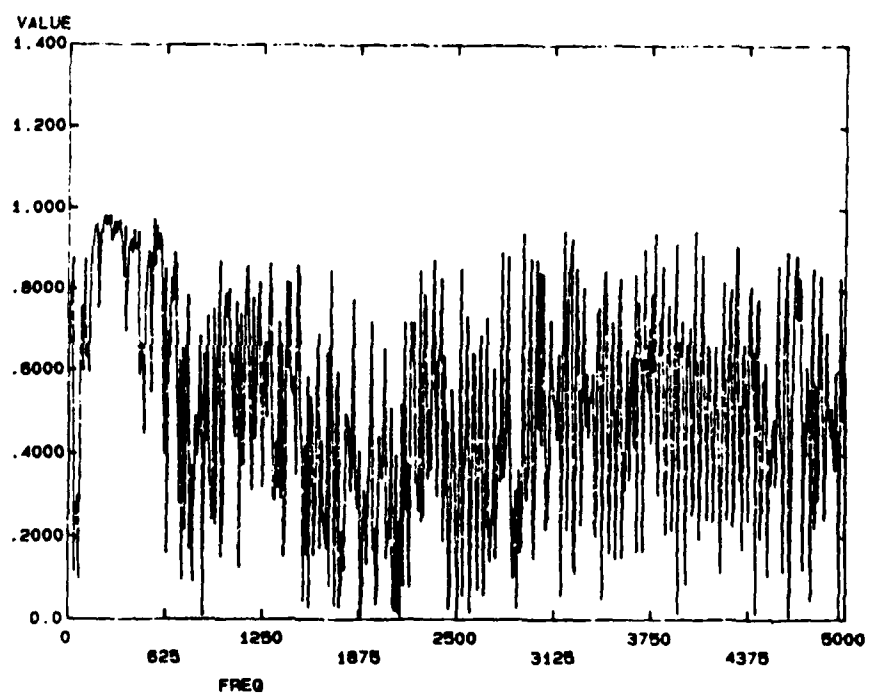


Figure 5-47d. Coherence Function H1 vs H5 - 0.625-Inch Jet

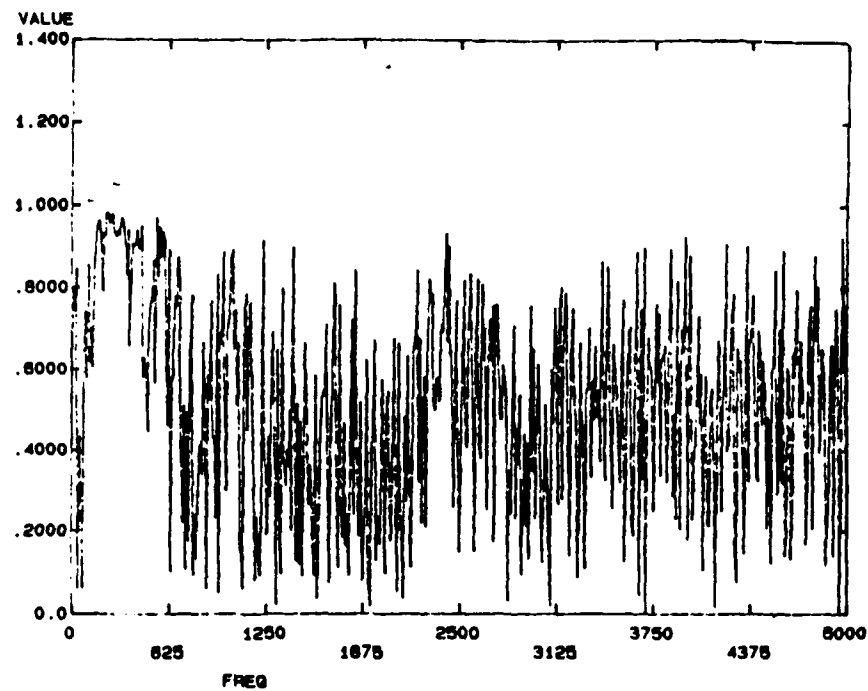


Figure 5-47e. Coherence Function H1 vs H7 - 0.625-Inch Jet

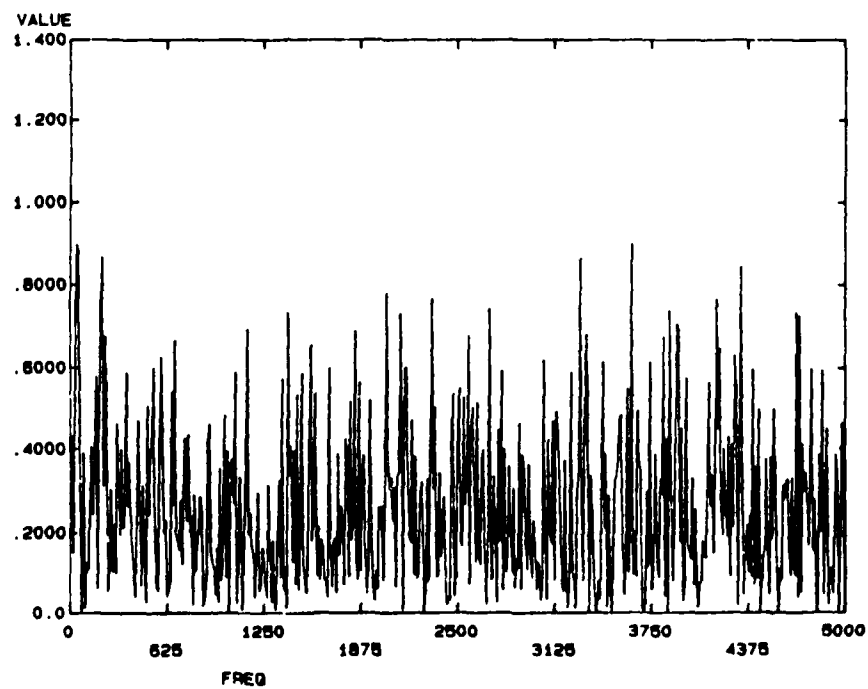


Figure 5-48a. Coherence Function H1 vs H3 - Pipe Flow

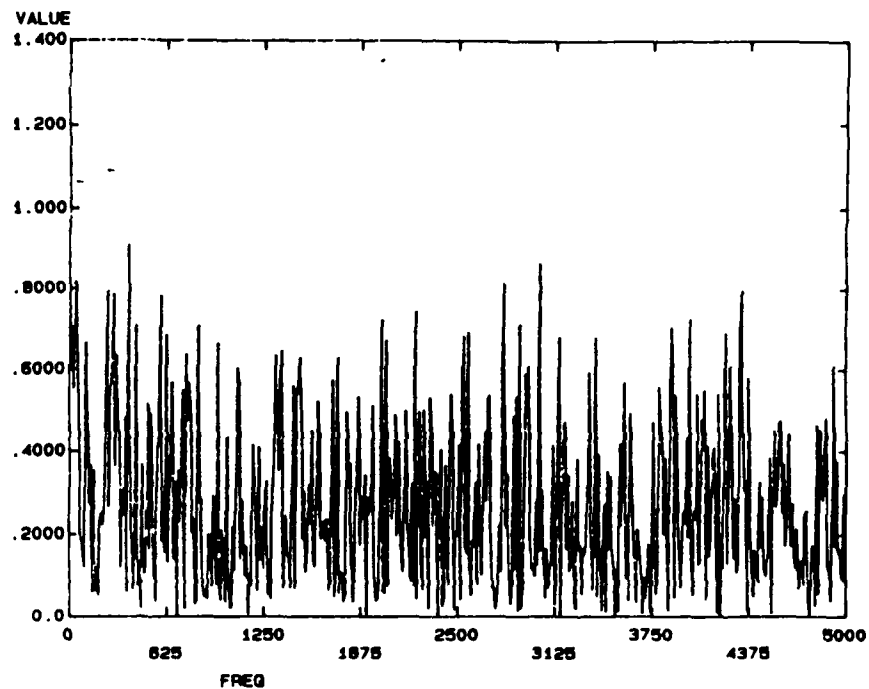


Figure 5-48b. Coherence Function H3 vs H5 - Pipe Flow

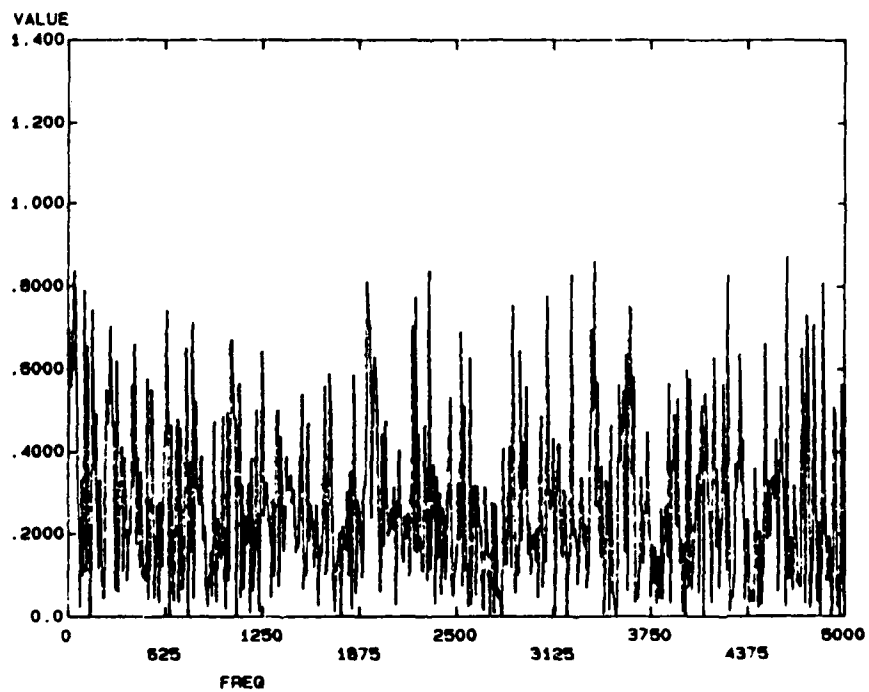


Figure 5-48c. Coherence Function H5 vs H7 - Pipe Flow

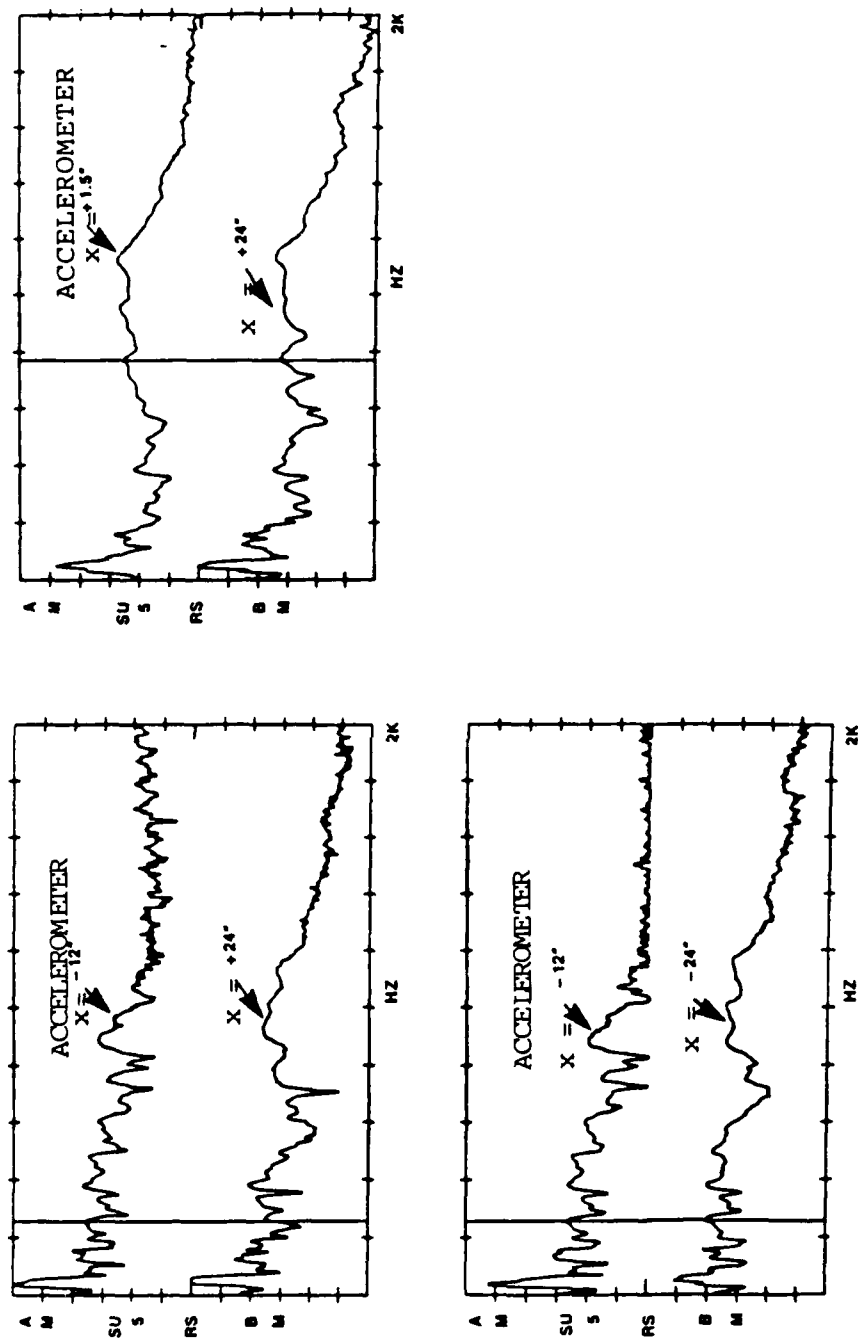


Figure 5-49. RMS Acceleration Spectra with Impact at $x = 0$ cm

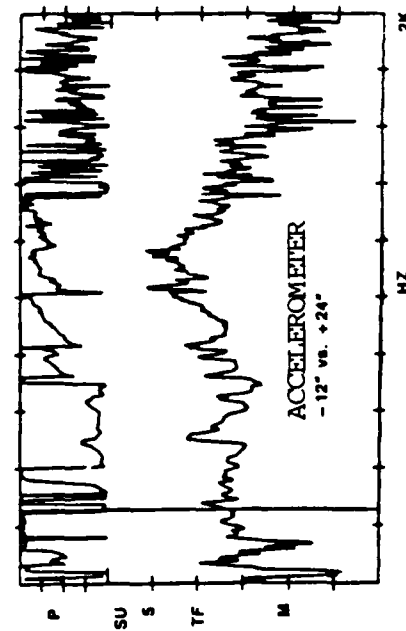
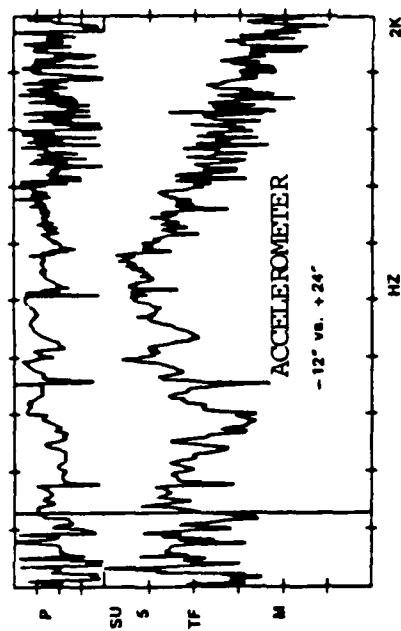
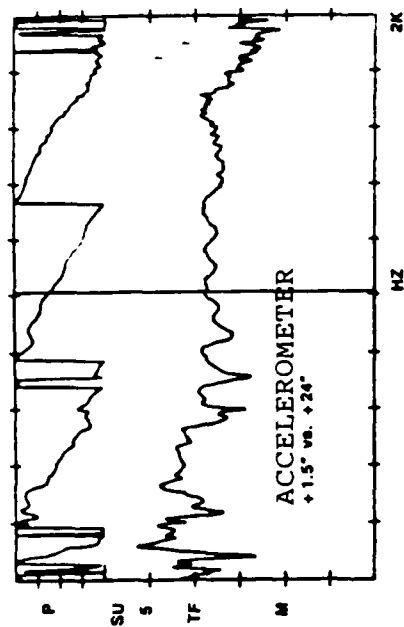


Figure 5-50. Transfer Functions of Accelerometer Signals
with Impact at $x = 0$ cm

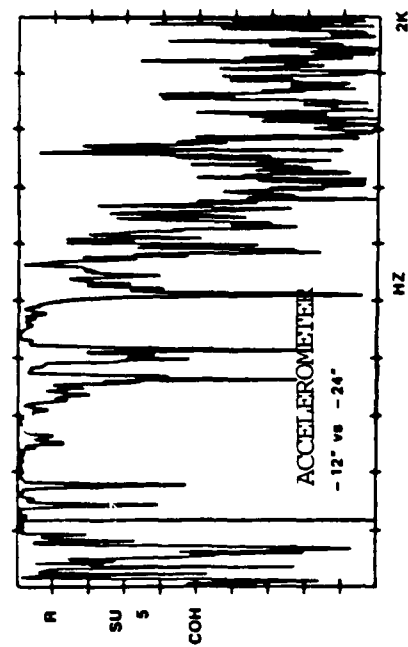
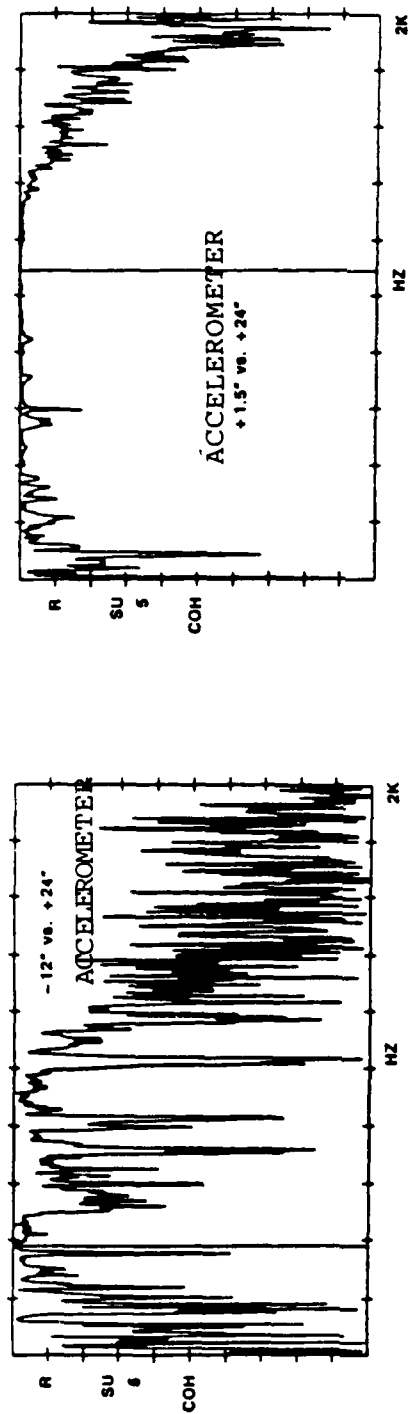


Figure 5-51. Coherence Functions of Accelerometer Signals

with Impact at $x = 0$ cm

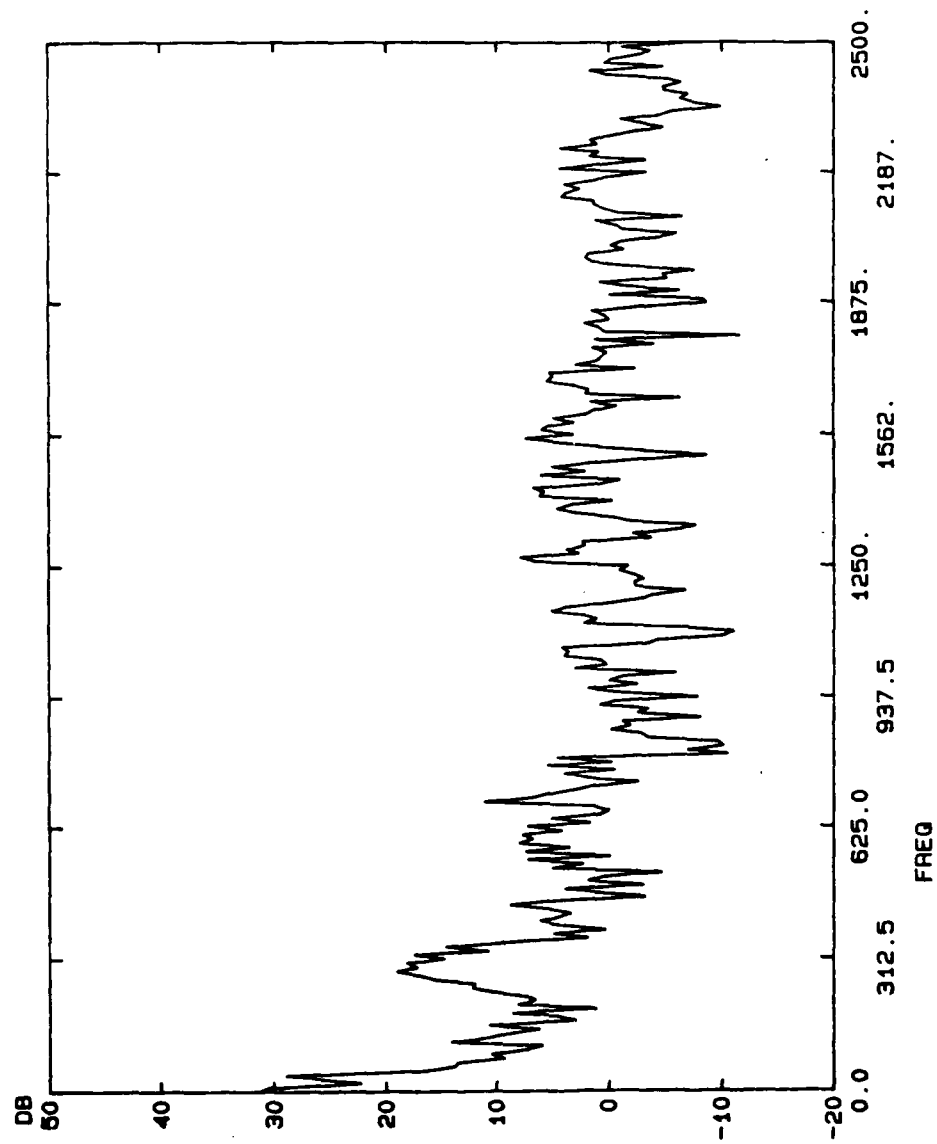


Figure 5-52. Pipe Wall Acceleration Spectrum - 0.625-Inch Jet

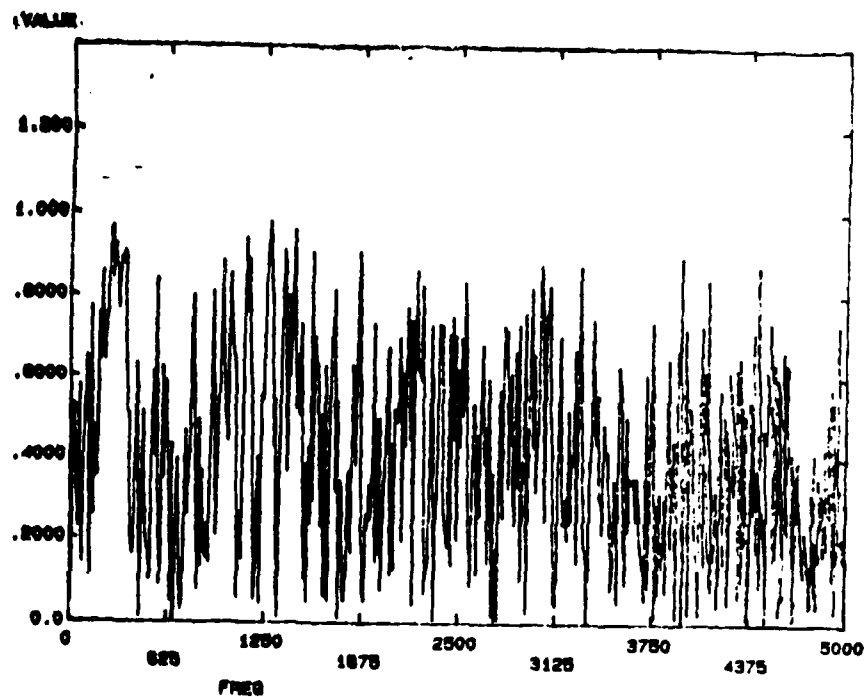


Figure 5-53a. Coherence Function A1 vs A3 - 0.625-Inch Jet

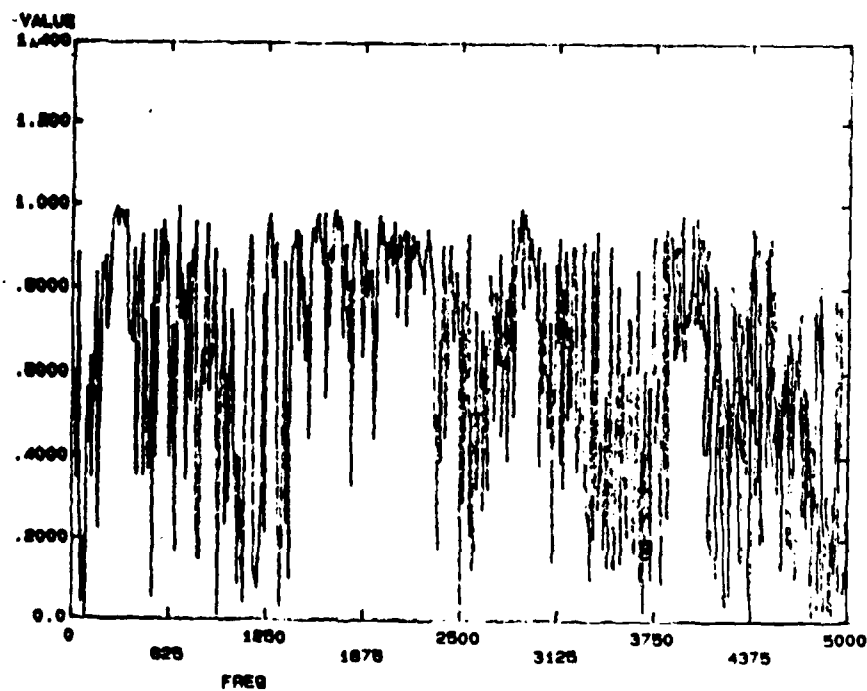


Figure 5-53b. Coherence Function A3 vs A5 - 0.625-Inch Jet

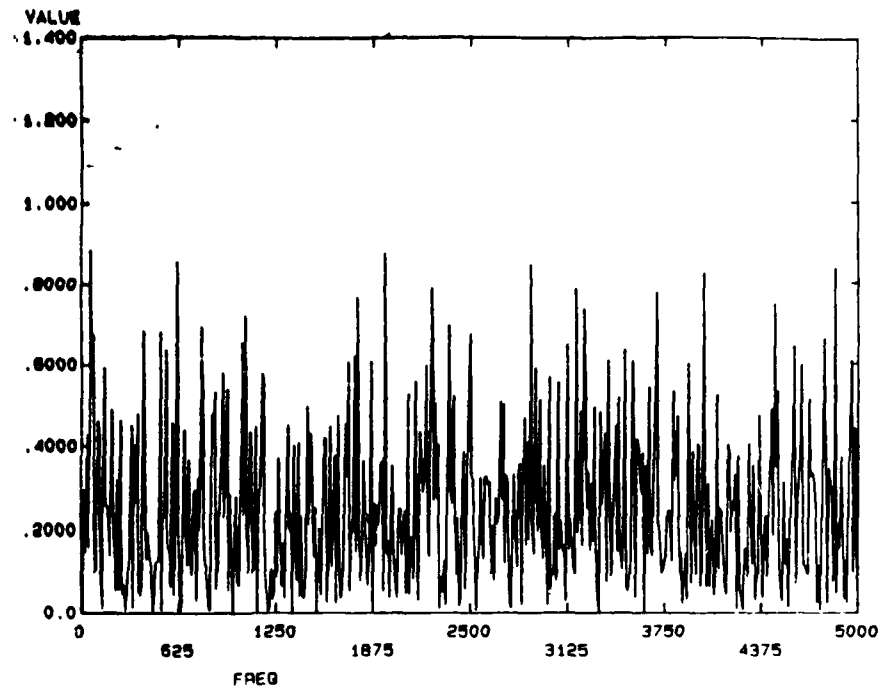


Figure 5-54. Coherence Function A3 vs A5 - Pipe Flow

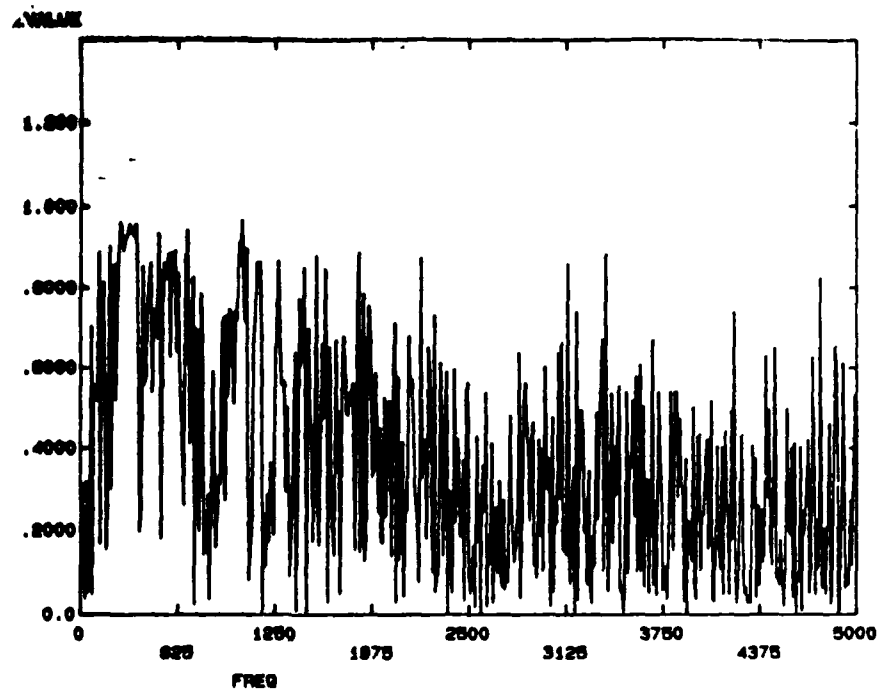


Figure 5-55a. Coherence Function H3 vs A3 - 0.625-Inch Jet

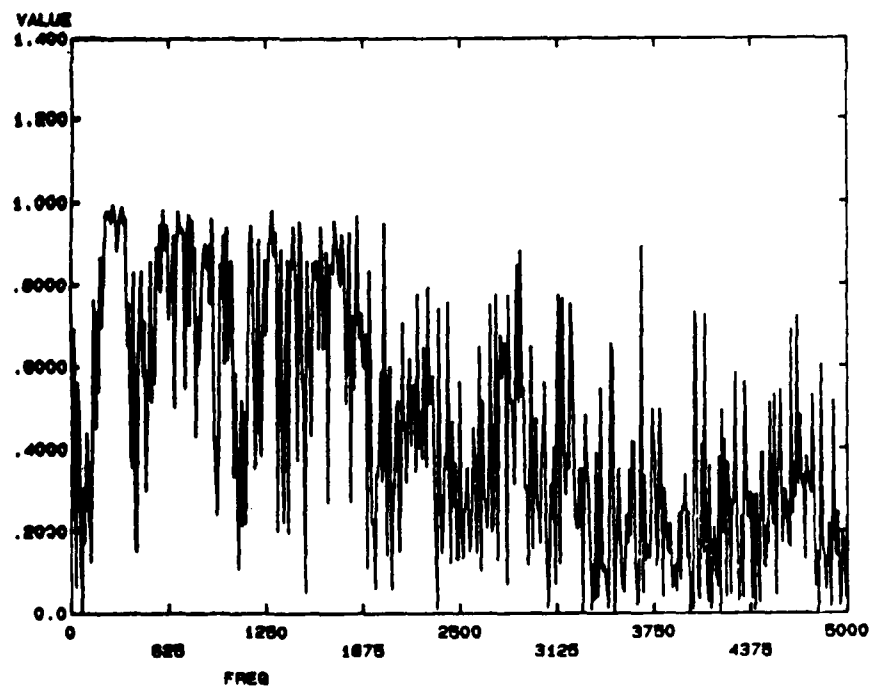


Figure 5-55b. Coherence Function H5 vs A5 - 0.625-Inch Jet

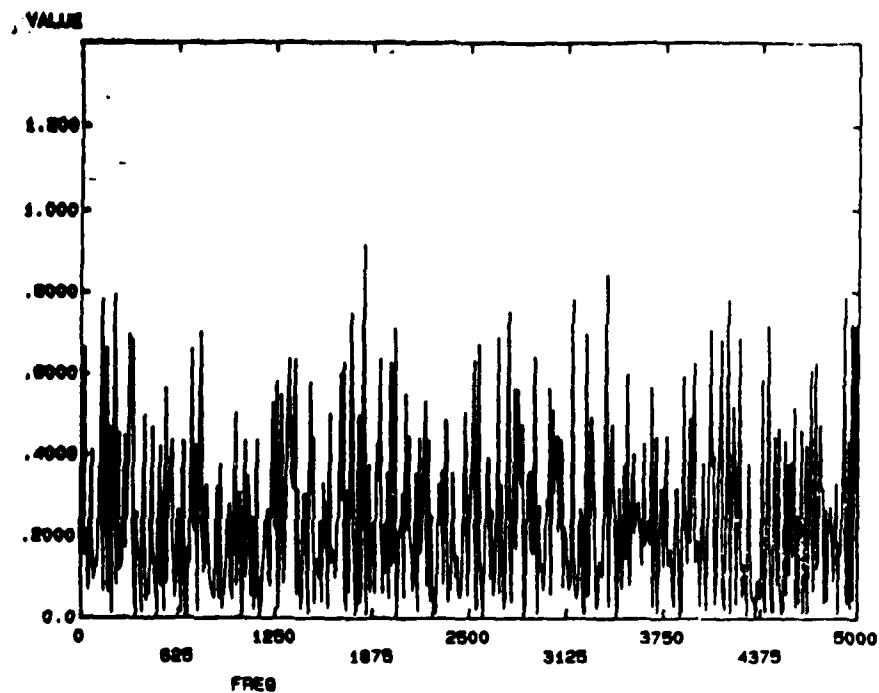


Figure 5-56a. Coherence Function H3 vs A3 - Pipe Flow

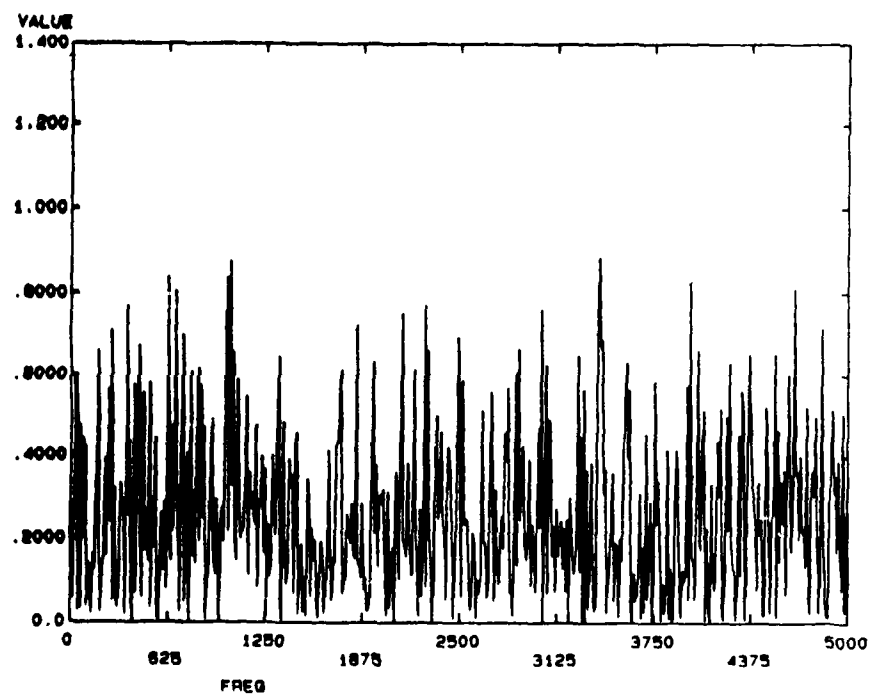


Figure 5-56b. Coherence Function H5 vs A5 - Pipe Flow

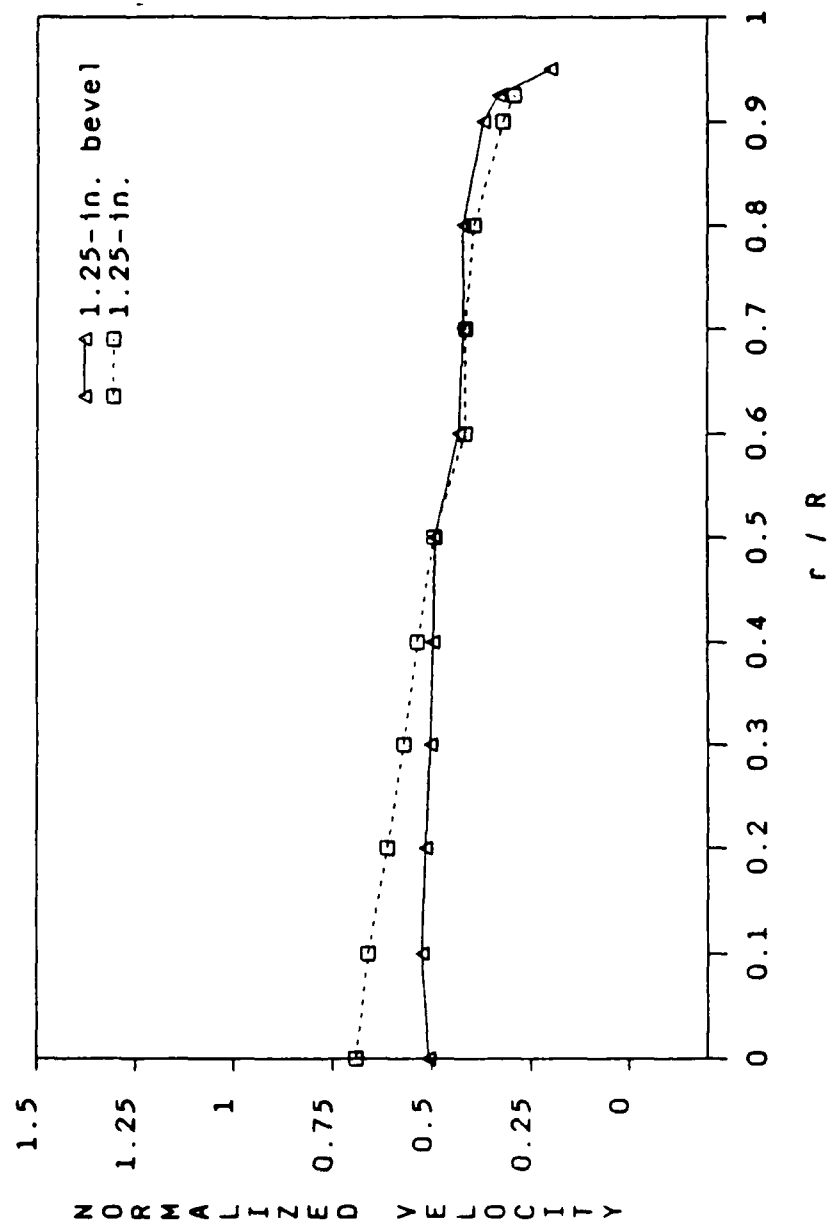


Figure 5-57. Velocity Profiles - 1.25-Inch Plate
with and without Bevel Edge

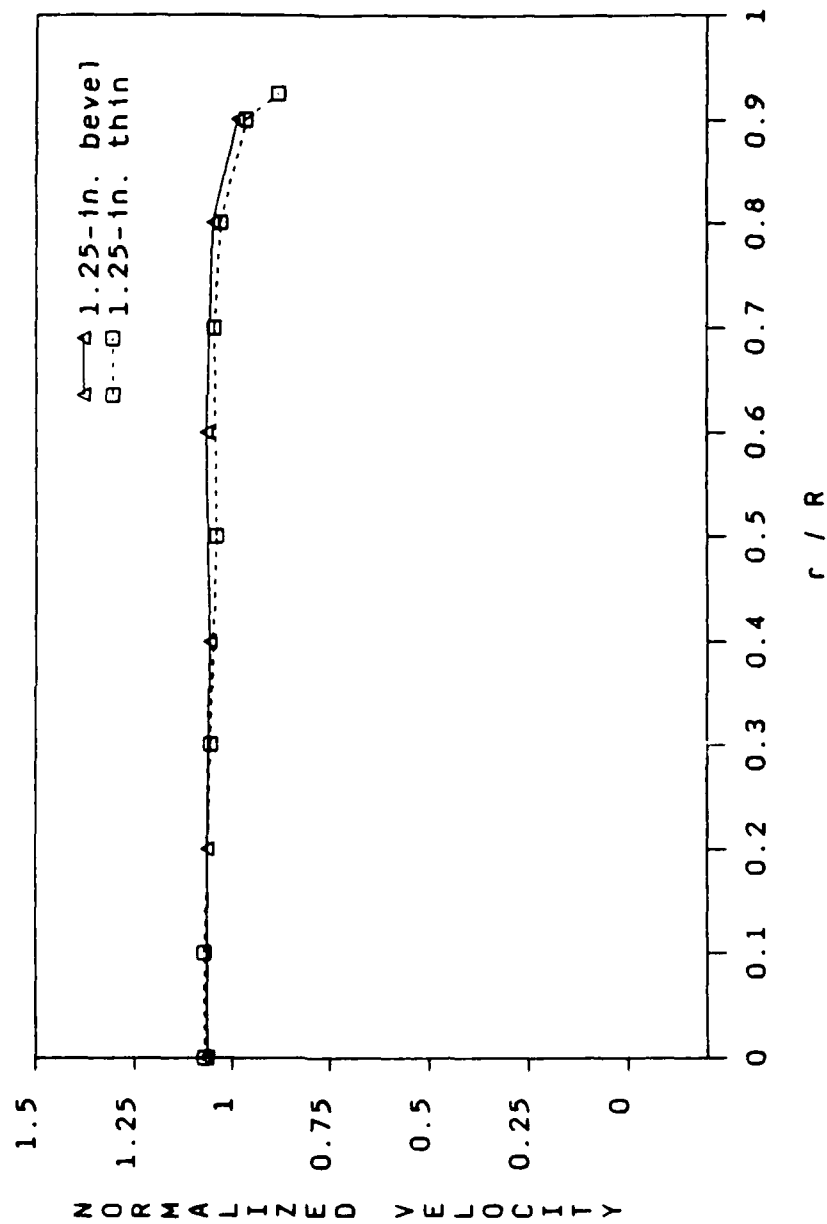


Figure 5-58. Velocity Profiles - 1.25-Inch Thin Plate
vs Bevel Edge Plate

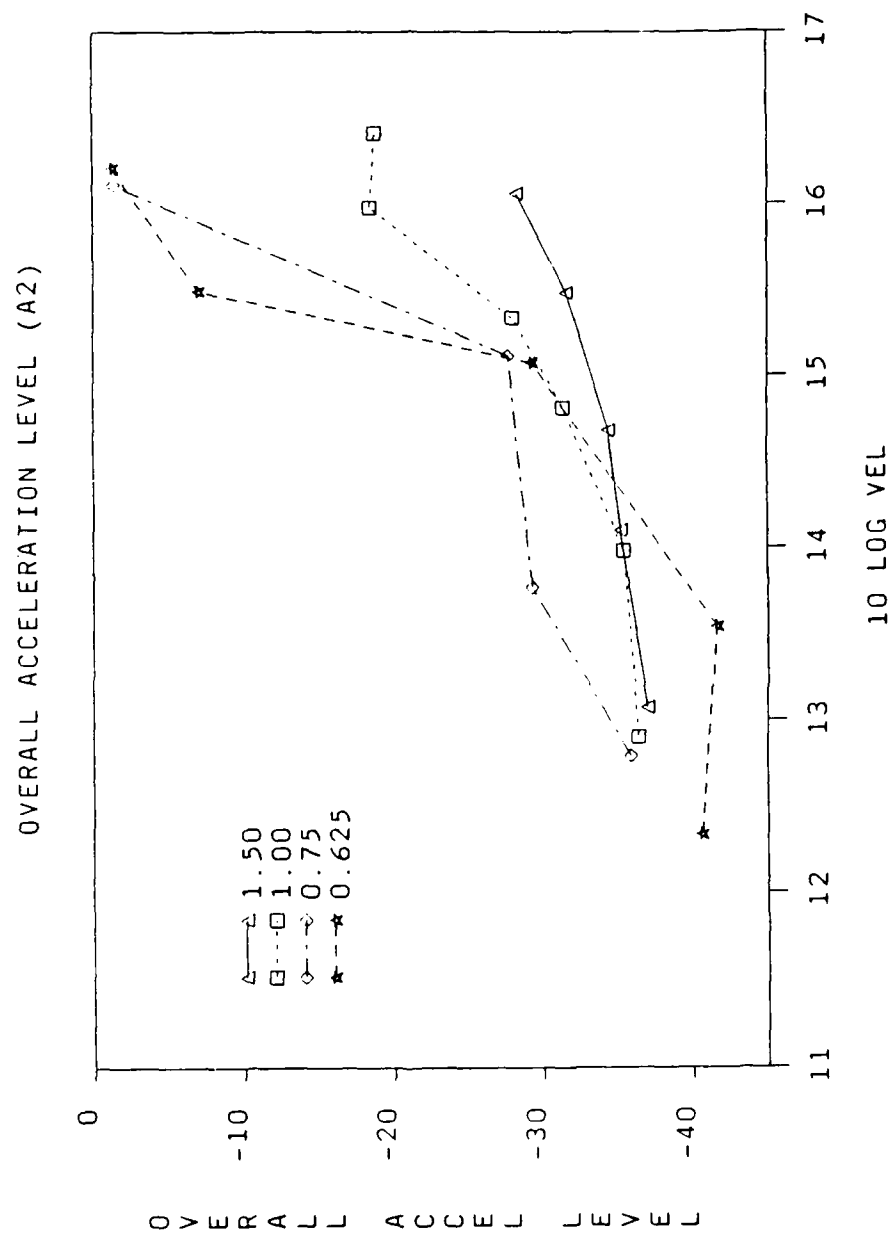


Figure 5-59. Overall Acceleration Level vs Velocity

CHAPTER 6

ANALYSIS AND NUMERICAL RESULTS

The theoretical development of the blocked surface pressure, pipe wall acceleration, and pressure contribution due to shell vibration was presented in chapter 3. In this chapter, results from the numerical calculations are presented and discussed. Calculations of the blocked surface pressure are presented first, followed by the pipe wall acceleration and pressure contribution from the wall vibration. Lastly, the numerical results of the wall pressure and acceleration are compared with the experimental data.

1. Fluid-Filled Shell Vibration

Consider the problem of fluid-filled shell vibration. For a free vibration solution to exist, the determinant of the elements of the differentiation operator, equation (16), must be equal to zero. Expansion of the determinant yields the characteristic equation. The characteristic equation of the coupled system is nonlinear due to the presence of the desired eigen roots in the argument of the Bessel functions in the fluid loading term. The roots of the characteristic equation were found by using a complex root searching technique as introduced by Fuller (1982). For the cases of purely real or imaginary values, a simple stepping procedure was used to locate a change of sign in the characteristic equation. The roots of the characteristic equation correspond to the structural wavenumber and are denoted as k_{ns} .

In the present study, efforts were focused on the calculations of the wall pressure and pipe wall response due to an axisymmetric turbulent jet inside the pipe. Before the analysis of the forced response of the

fluid-filled shell, it is necessary to consider the free vibration problem. Furthermore, the roots of the characteristic equation correspond to the poles of the complex integral that appears in the inverse Fourier transform. In evaluating the complex integral, the method of residues was used. This method involves the summation of residues at the poles. The roots of the characteristic equation for the various branches s were plotted against the normalized frequency.

Figure 6-1 shows the dispersion curves for the axisymmetric mode ($n = 0$) of a 5.1-cm (2-in.) diameter, 6.4-mm (0.25-in.) thick plexiglass shell. The frequency range of interest is from 100 to 2500 Hz. It should be noted that this frequency range is much below the ring, cut-off and critical frequencies. As shown in the figure, most of the dispersion curves are independent of frequency, except the first two branches ($s = 1$ and $s = 2$). The material properties used in the calculations are representative of the plexiglass test section used during phase II of the test program. Material properties are summarized in table 6-1.

Table 6-1. Material Properties for Numerical Calculations

Material	Young's Modulus (N/m^2)	Poisson's Ratio	Density (kg/m^3)	Wave Speed (m/sec)
Plexiglass	4.137×10^9	0.355	1388	1846
Water	-	-	1000	1500

2. Near-Field Jet Noise and Blocked Surface Pressure

The equation relating the near-field jet pressure fluctuations to the velocity fluctuations was presented in equation (12). In the rigid

wall case, the near-field pressure fluctuations are equivalent to the blocked surface pressure. As shown in equation (12), the blocked surface pressure is obtained by integrating the product of the source term and local weighting function $\partial^2 G / \partial x_i \partial x_j$ in the source region. The source term consists of the velocity fluctuations $u_i' u_j'$, time-averaged of $u_i' u_j'$, and the interaction of mean velocity and fluctuating velocity $2u_i' U_j$. The magnitude of the source term was determined experimentally, i.e., from the LDV data; and the weighting function as shown in equation (13) was derived analytically.

In general, the $2u_i' U_j$ is the dominant component in the source term. As discussed previously, near the jet exit the axial mean velocity U is much larger than the radial mean velocity V , and its velocity fluctuations u' and v' ; thus, the major contribution in the source term is from the $2u'U$ term. It should be noted that further downstream, the axial mean velocity U decays, and hence the $2u'U$ term may not be dominant. To illustrate the temporal characteristics of the velocity components, typical plots of u , u' , and $2u'U$ versus time are shown in figure 6-2.

Theoretically, the source term can be determined from the flow field data; however, it requires that the measurements of all points be taken simultaneously. During the test, the LDV measurements were taken at different points at different times. As shown in figure 6-2, the time history of the velocity components are relatively independent of the time interval. Accordingly, the flow field data were assumed to be stationary, and the source term was calculated using LDV measured data.

It was pointed out earlier that, in spite of the forward scattering mode and particle filtering efforts, the data rates of the LDV measurement were only up to 5000 samples per second. As compared with

other similar LDV systems, these data rates were relatively high. In overcoming the low data rate problem, various interpolation schemes were considered to enhance the velocity data. Since the source calculations were performed in the frequency domain, the interpolations were applied on a velocity versus time basis. Several interpolation schemes and various curve fittings were attempted.

Results showed the Lagrangian interpolation polynomial to be the most appropriate and the third order is sufficient. The third-order polynomial was based on a four-point interpolation scheme given by Abramowitz and Stegun (1964). A typical plot of velocity component $2u'U$ versus time is shown in figure 6-3. Figure 6-3a depicts the data as measured (no interpolation), and figure 6-3b represents the data with the third-order interpolation. The corresponding $2u'U$ velocity spectra without and with interpolation are shown in figures 6-4a and 6-4b, respectively. Note that without interpolation the velocity spectrum is flatter and shows more high-frequency components than the spectrum with interpolation. The high-frequency components are due to the varying nature of the discrete data points.

The local weighting function $\partial^2 G / \partial x_i \partial x_j$, as given by equation (13) is an oscillatory function. To illustrate the characteristics of the weighting function as a function of the number of terms m , several values were calculated and are shown in figures 6-5a through 6-5e. Note that in figure 6-5, as m increases, the number of peaks and valleys increases; and also the weighting is substantially large near the wall. It should be pointed out that the exponential term in equation (13) has a strong influence on the weighting function in the axial direction. Figures 6-6a through 6-6d show the amplitude of the weighting function with 32 terms as a function of x/R of 0.0, 0.02, 0.04, and 0.08. As

shown, the amplitude of the weighting function drops off rapidly with increasing x/R .

During the testing program, for each axial location x , the velocity measurements were taken at 11 radial points, i.e., values of r/R range from 0.0 to 0.925. Because of the oscillatory nature of the weighting function, spatial averaged values of the weighting function at each LDV measurement point were used in the blocked pressure calculations. The averaged values were obtained by integrating the weighting function in each annular area representing the particular measurement point. Figure 6-7 illustrates the division of the annular areas or bands. Calculations showed that the averaged weighting function approach was independent of the number of terms used in equation (13), and the amplitude of the weighting function was bounded near the wall. The value of m (number of terms) used in the numerical calculations was 32.

Based on the statistical approach as presented in section 4 of chapter 3, the cross spectral density of the surface pressure fluctuations were evaluated according to equation (30). In the calculations, it was assumed that the velocity fluctuations are uncorrelated in the radial direction. This assumption can be justified by the phase information of the $2u'U$ term. Typical plots of the magnitude and phase angle of the $2u'U$ term for the 0.625-in. jet are shown in figures 6-8a and 6-8b for two adjacent radial locations, i.e., $r = 0.0$ and 0.25 cm and at $x = 8$ cm. As shown, the phase angles are random which imply that the velocity fluctuations are uncorrelated. In the experimental study of confined jets conducted by Abdallah (1984), she also observed that the velocity fluctuations are uncorrelated in the radial direction.

As discussed previously, the blocked pressure was evaluated by

multiplying the source magnitude S_{ij} at each point of the flow field by the corresponding local weighting function $\partial^2 G / \partial x_i \partial x_j$ and integrating over the whole source volume. Because the local weighting function decays rapidly with x (see figures 6-6a through 6-6d), $\partial^2 G / \partial x_i \partial x_j$ was be approximated by a Dirac delta function in the x direction. With this approximation, equation (30) could be simplified and the mean squared blocked pressure can be expressed as equation (37).

Results of the mean squared blocked pressure spectra are plotted in figures 6-9 and 6-10 for the 0.625-in. diameter jet and pipe flow, respectively. In general, the spectral characteristics of the blocked surface pressure are very similar to the measured wall pressure. As discussed previously, the total wall pressure is the sum of blocked surface pressure and pressure contribution from the wall vibration. Therefore, wall pressure comparison cannot be made until the pressure contribution from the pipe wall vibration is quantified.

Results of the pressure calculations showed that the blocked pressure from sources at a specific x_0 indeed decays quite rapidly with distance $|x - x_0|$. For example, in figure 6-11, the blocked surface pressure decays more than 20 dB for relative x of 1.27 cm (0.5 in.). Plots of blocked pressure versus relative axial location for several frequencies are shown in figure 6-11. In general, the decay of blocked pressure is independent of frequency. These results support the use of the Dirac delta function as noted previously.

3. Fluid-Coupled Shell Vibration with Confined Jet Excitation

As discussed in section 3a of chapter 3, the pipe wall response was obtained by solving the characteristic or spectral equations of the fluid-filled shell vibration problem. The spectral radial displacement

has been given in equation (20). Consequently, the radial velocity and acceleration were obtained by differentiating equation (20).

To calculate the pipe wall acceleration, it is required to specify the blocked excitation pressure distribution as a function of x . As discussed previously, the blocked surface pressure decays rapidly and linearly with x . A special case was presented in section 5 of chapter 3, in which a relatively simple form of an amplitude modulated convecting wave field was used as the blocked surface pressure. Hence, the blocked excitation pressure distribution was assumed to be triangular as shown in figure 6-12. The width of the triangular distribution $2L$, is associated with the pressure correlation length.

The response of the pipe wall due to excitation by a harmonic ring load was calculated. A plot of the ratio of wall acceleration to peak pressure P_0 versus location is shown in figure 6-13 for several frequencies. As shown, the wall acceleration decays quite rapidly for x less than 2.54 cm (1 in.). It should be noted that the decay at high frequencies are less than the decay at low frequencies.

a. Deterministic Approach

The expression for pipe wall acceleration due to deterministic amplitude modulated convecting blocked pressure was presented in equation (36). In the evaluation of the sum of residues in equation (36), the summation was truncated at $s = 10$. It was found that higher order branch numbers would not contribute significantly to the residue sum, and $s = 10$ was sufficient for the computations.

Typical calculated wall acceleration spectra are shown in figures 6-14 and 6-15 for the 0.625-in. diameter jet and pipe flow, respectively. In the calculations, it was assumed that the pressure fluctuations are correlated in both radial and axial directions. For

comparison purpose, the measured wall acceleration spectra are also plotted in figures 6-14 and 6-15. As shown, the calculated wall acceleration spectra agree reasonably well with the experimental data.

b. Statistical Approach

Based on the statistical approach as presented in section 4 of chapter 3, the cross spectral density of the pipe wall velocity was evaluated according to equation (33). In the calculations, it was assumed that the pressure fluctuations are correlated in the x direction. The correlated pressure fluctuations reflect the occurrence of large-scale coherent structures in the jet developing region. As shown and discussed in chapter 5, the high coherence functions in wall pressure data are attributed to the large-scale coherent structures.

The expression for the pipe wall velocity due to an amplitude modulated convecting wave field was presented in equation (38). As discussed previously, the blocked pressure was assumed to have a triangular distribution. In the calculations the half width L , which here corresponds to the correlation length scale, was allowed to vary with frequency in a manner which is similar to the experimental results presented by Clinch (1969) for the pipe flow. The correlation length was assumed to be a function of the jet diameter. Specifically, the values of L range from about 3 jet diameters at 2 kHz to about 12 jet diameters at 100 Hz.

Typical calculated wall acceleration spectra are shown in figures 6-16 and 6-17 for the 0.625-in. diameter jet and pipe flow, respectively. Again for comparison purpose, the measured wall acceleration spectra are also plotted in figures 6-16 and 6-17. As shown, the calculated wall acceleration spectra agree well with the experimental data. As compared to the calculation based on the

deterministic approach (figure 6-14 versus figure 6-16), the statistical approach has better agreement with the experimental data.

4. Pipe Wall Pressure Due to Flexible Wall Vibration

The pressure contribution from the vibration of the shell wall was addressed in section 3b of chapter 3. The shell wall pressure calculations were obtained by solving the fluid-filled shell vibration problem with the blocked surface pressure as the excitation source. An expression relating the flexible wall pressure to the blocked pressure was given in equation (28). Note that the expression for wall pressure is very similar to that for wall acceleration, except that the residue term is different; that is, equation (28) versus equation (36). Again, in the evaluation of the sum of residues, the summation was truncated at $s = 10$.

A typical flexible wall pressure spectrum is shown in figure 6-18. As shown, the flexible wall pressure spectrum is lower than the blocked surface pressure, particularly at the low frequencies. For the range of frequencies of interest, the blocked surface pressure is dominant.

5. Comparison with Experimental Data - Jet Flow and Pipe Flow

a. Wall Pressure

The wall pressure was calculated by summing the blocked surface pressure and flexible wall pressure. Because the blocked surface pressure is dominant for the range of frequencies of interest, the flexible wall pressure has no significant contribution on the wall pressure calculations. In this section, wall pressure calculations based on the deterministic approach are presented first, then followed by the calculations based on the statistical approach.

The expressions for the blocked pressure and flexible wall pressure were presented in equations (12) and (28). In the deterministic case, it was assumed that the pressure fluctuations are correlated in both the radial and axial directions. Typical wall pressure spectra are shown in figures 6-19 and 6-20 for the 0.625-in. and 1.00-in. diameter jets, respectively. For comparison purpose, the measured wall pressure spectra are also plotted in figures 6-19 and 6-20. As shown, the calculated pressure spectra are slightly lower than the measured spectra.

The expression for the mean squared blocked pressure was presented in equation (37) for the statistical case. In the statistical case, it was assumed that the pressure fluctuations are uncorrelated in the radial direction, and the local weighting function $\partial^2 G / \partial x_i \partial x_j$ can be approximated by a Dirac delta function in the x direction. Typical comparisons of the calculated wall pressure with experimental data are shown in figures 6-21 through 6-26 for the various jets and flow conditions. As shown, the agreement is reasonably well, except for the pipe flow case in which the calculated spectrum is higher than the measured spectrum by about 6 db. In general, the calculated wall pressure spectra are higher than the measured spectra in the high frequencies. Because of the low data rates associated with the LDV data, it is expected that the accuracy of the calculated wall pressure spectra decreases for frequencies above 2 kHz.

b. Pipe Wall Acceleration

Additional spectra of pipe wall acceleration are given in figures 6-27 through 6-30. The calculations were based on the analysis from the statistical point of view. In general, the calculated wall acceleration spectra agree reasonably well with the acceleration measurements, with

exception of the 1.00-in. diameter jet (see figure 6-28). As shown in figure 6-28, the calculated values are higher than the measurement in the high-frequency region by as much as 10 dB. In most cases, the model overpredicts in the low frequencies, i.e., for frequencies less than 500 Hz. It should be pointed out that the first harmonics of the pump blade passage frequency can be observed in the low jet velocity cases (see figures 6-30 for example).

In summary, based on the turbulent flow field data, the wall pressure and wall acceleration spectra can be predicted reasonably well with the statistical approach. In the present study, calculations showed the blocked surface pressure is dominant as compared to the pressure due to pipe wall vibration. The blocked surface pressure decays faster than the wall acceleration with respect to the axial location. Numerical results have demonstrated that the noise model is capable of relating the flow field and acoustic field of confined jet flows under a range of jet velocities and area ratios. Furthermore, the analytical model can be used to quantify the near-field hydrodynamic pressure or blocked surface pressure, wall pressure due to pipe wall vibration, and pipe wall acceleration due to confined jet excitations. Although the analytical development and noise model focus on the prediction of the flow-induced noise and vibration of confined jets, during the course of this study, it has been revealed that this analytical development and noise model can also be applied to pipe flow.

DISPERSION CURVE N=0

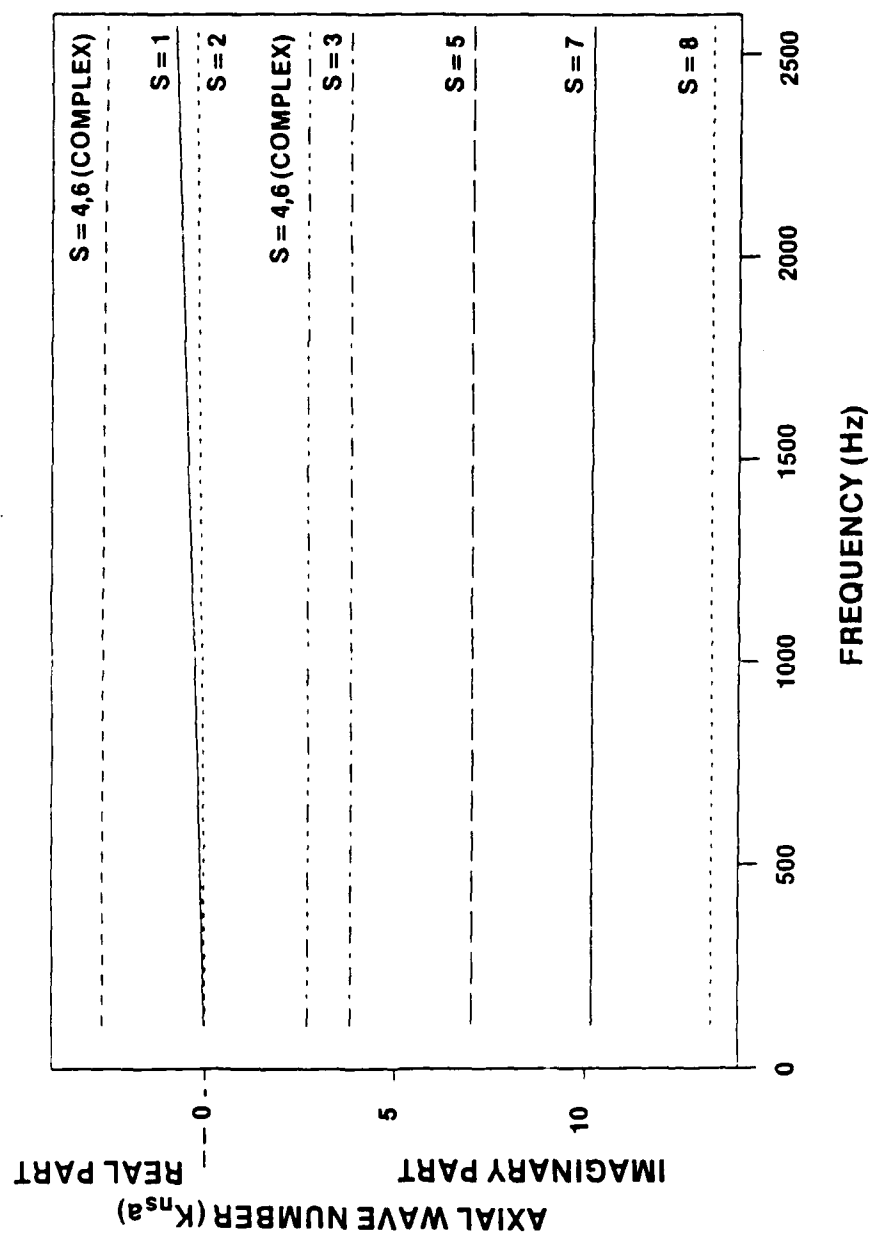


Figure 6-1. Dispersion Curve for Free Shell Vibration - Axisymmetric Mode $n = 0$

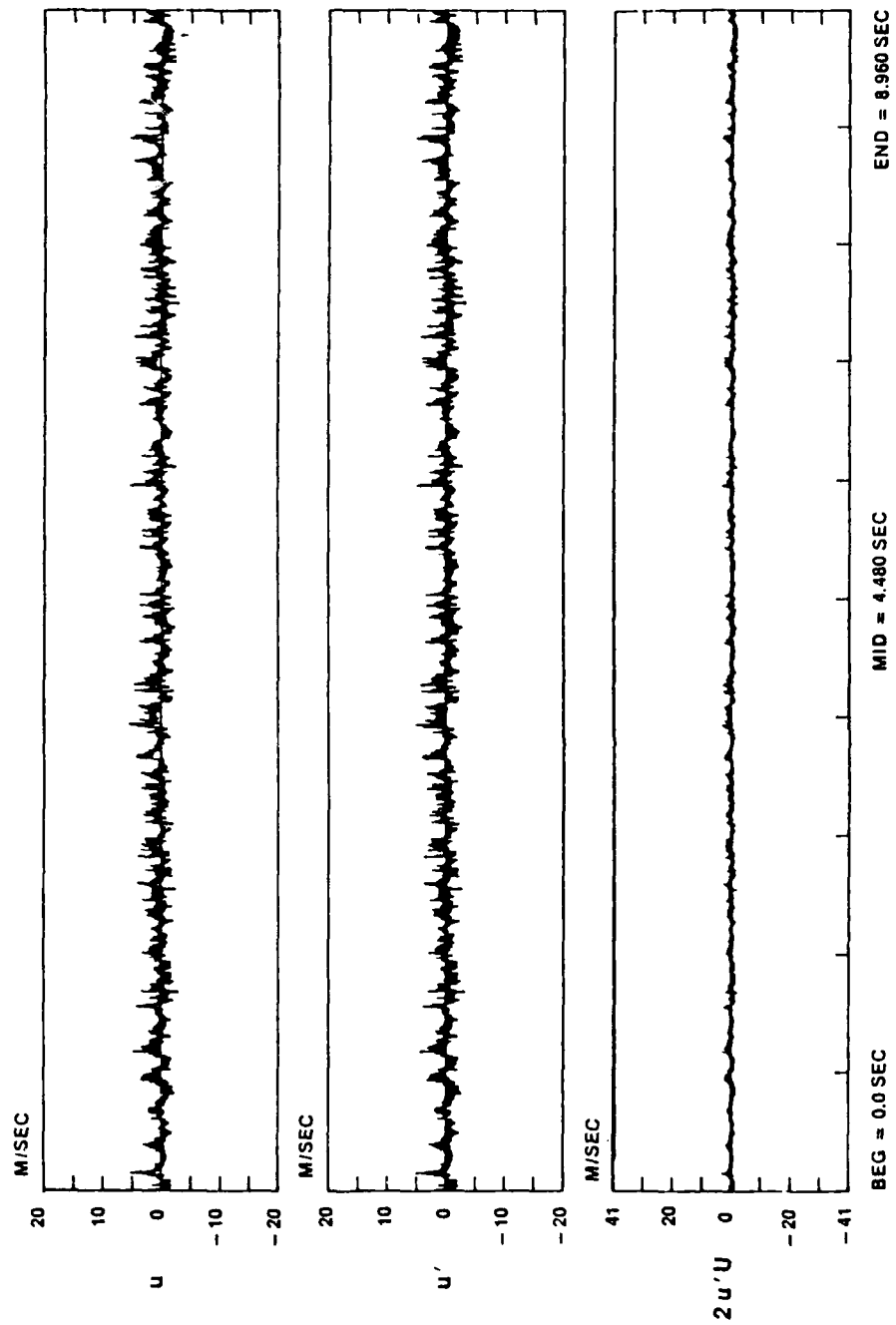


Figure 6-2. Velocity Components u , u' , $2u'u$ vs Time

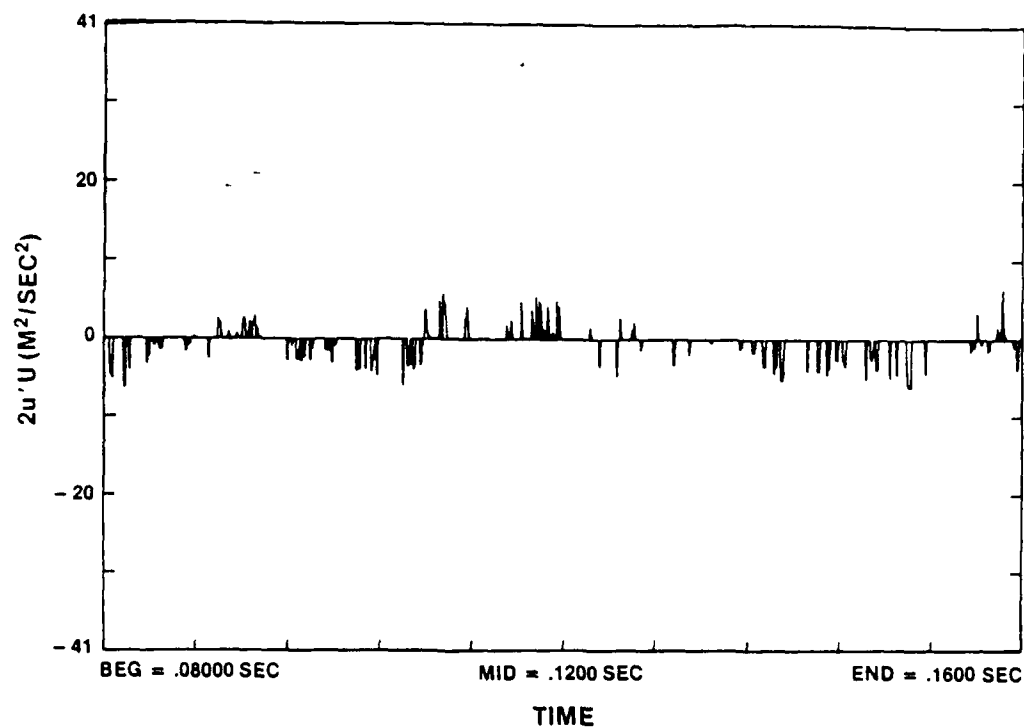


Figure 6-3a. Velocity Data without Interpolation

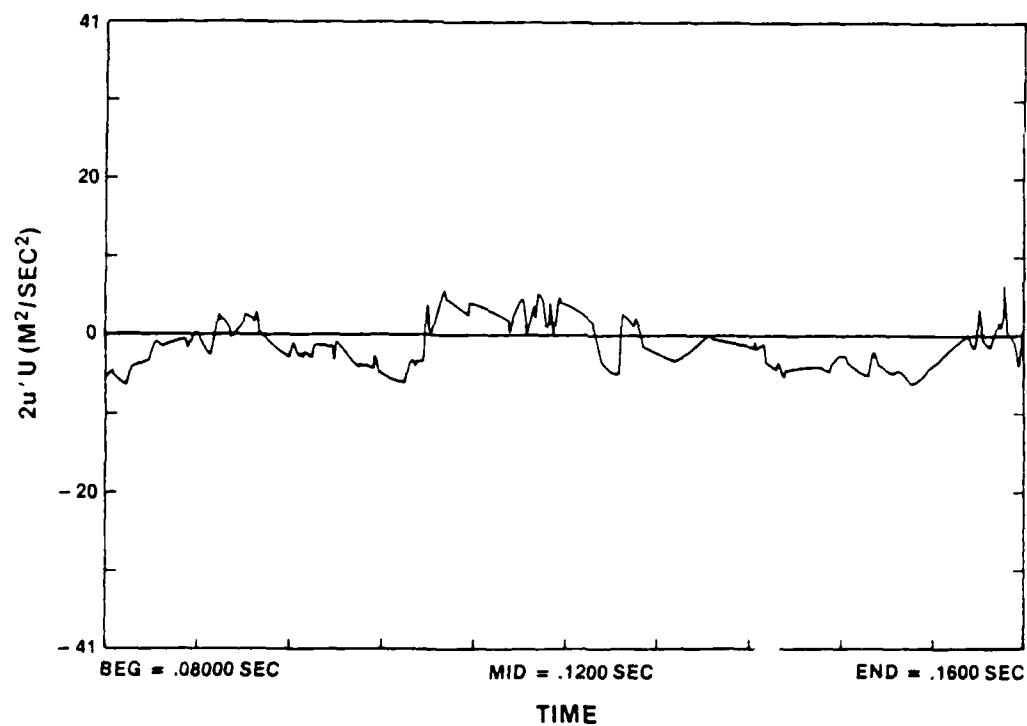


Figure 6-3b. Velocity Data with Interpolation

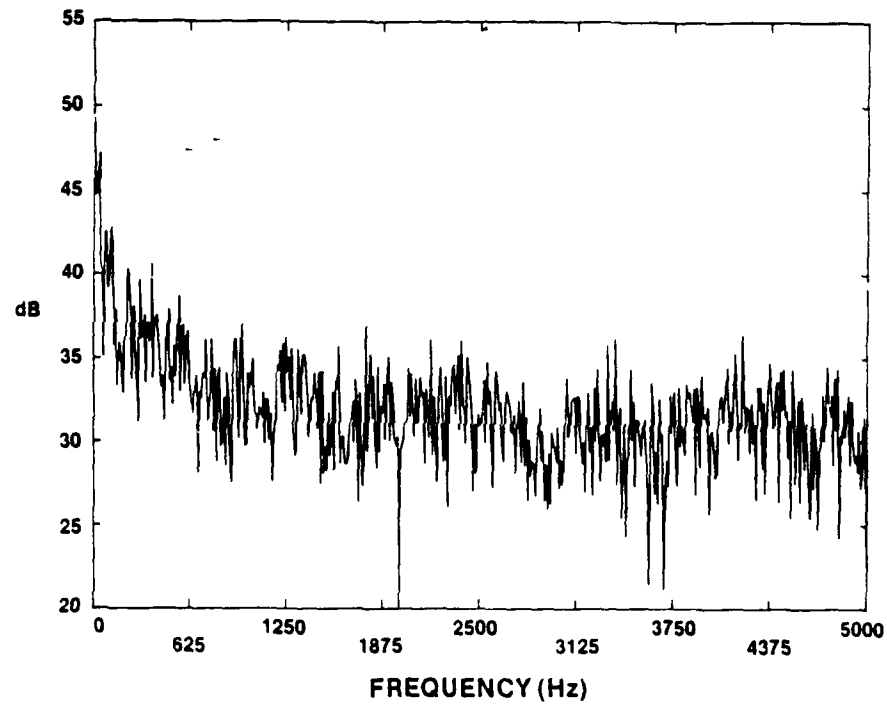


Figure 6-4a. Velocity Spectrum without Interpolation

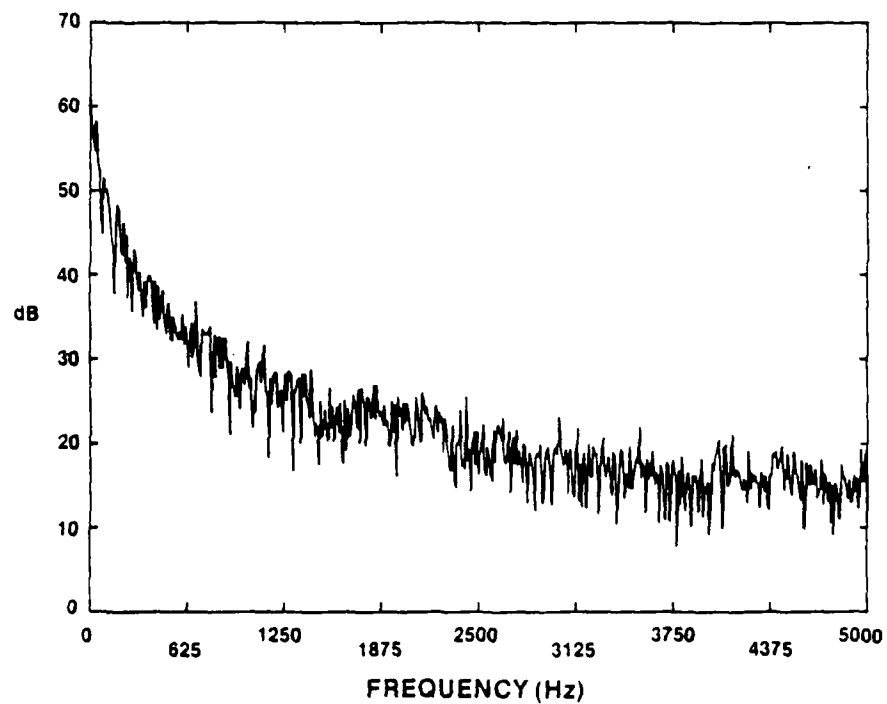


Figure 6-4b. Velocity Spectrum with Interpolation

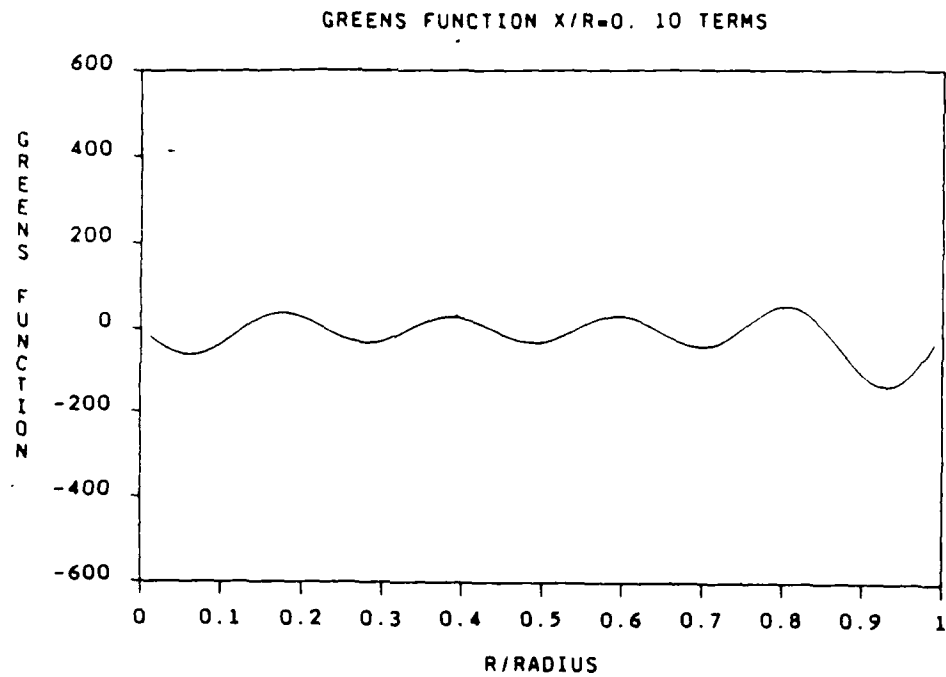


Figure 6-5a. Weighting Function- 10 Terms

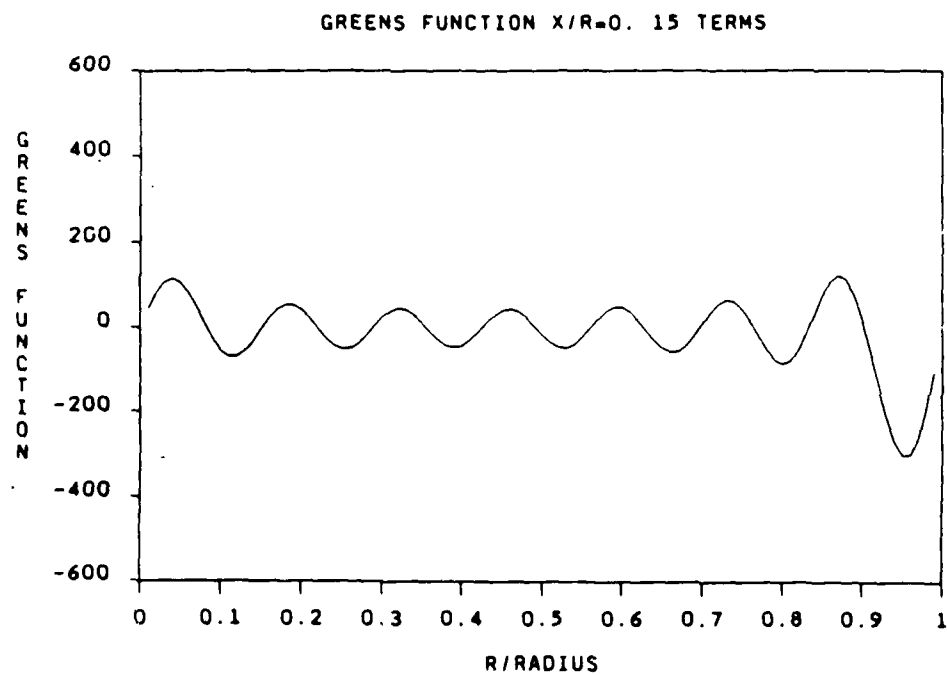


Figure 6-5b. Weighting Function- 15 Terms

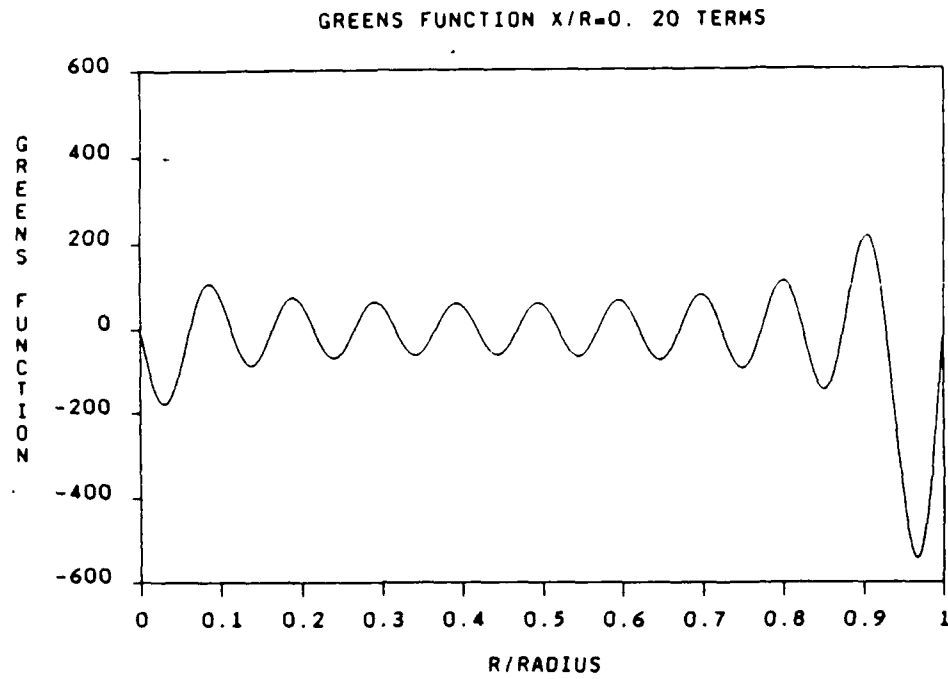


Figure 6-5c. Weighting Function- 20 Terms

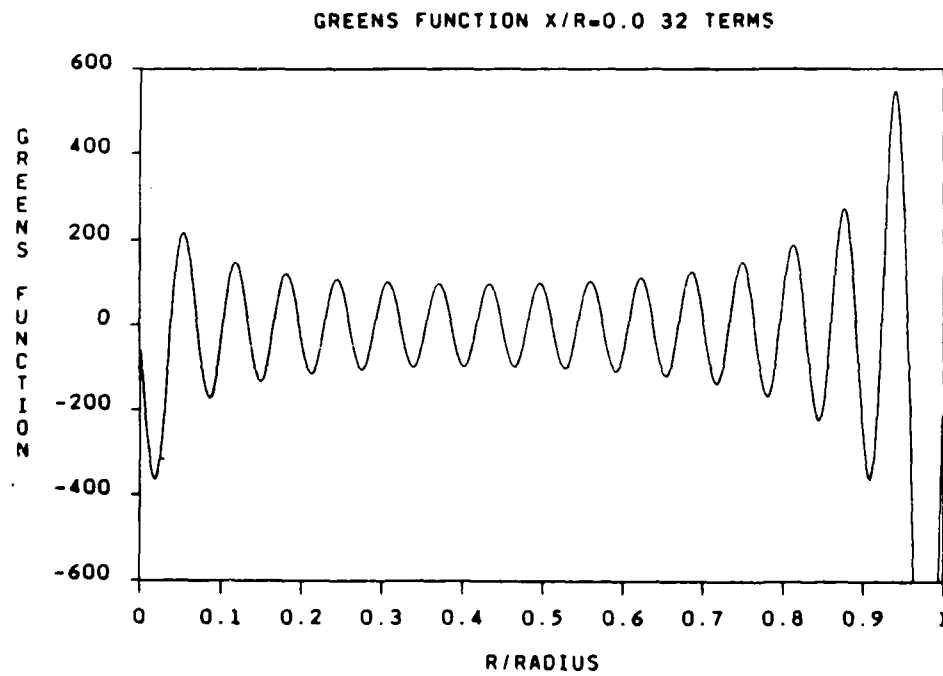


Figure 6-5d. Weighting Function- 32 Terms

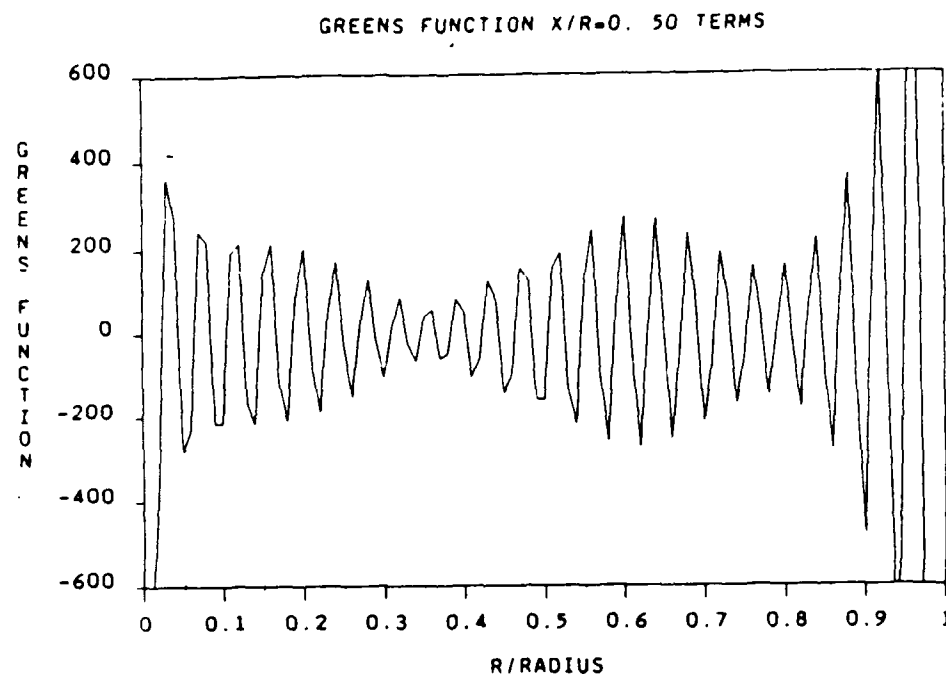


Figure 6-5e. Weighting Function- 50 Terms

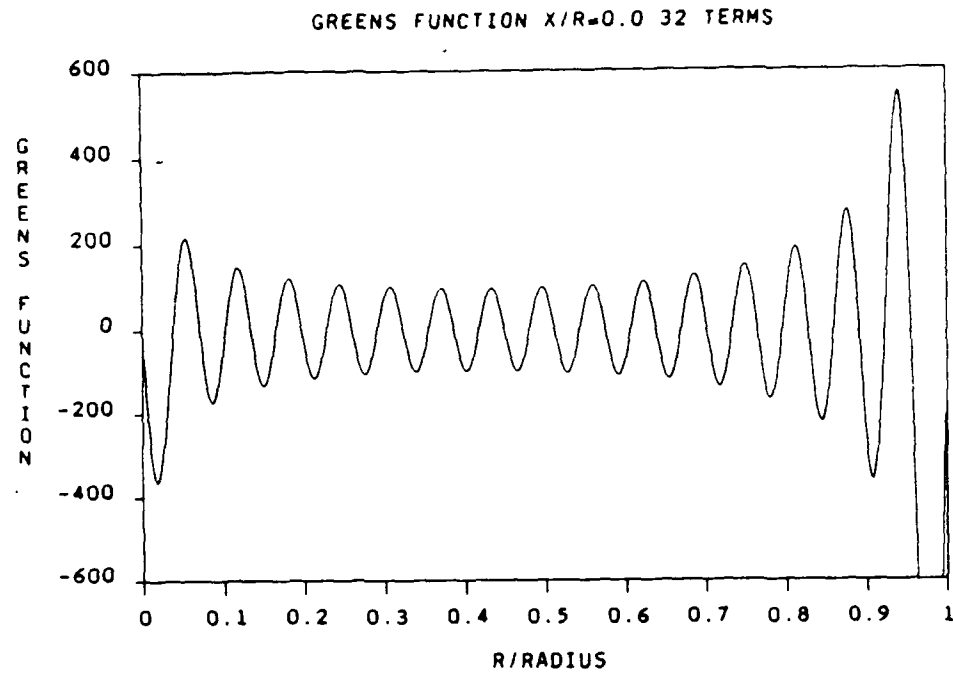


Figure 6-6a. Weighting Function- $x/R = 0.0$

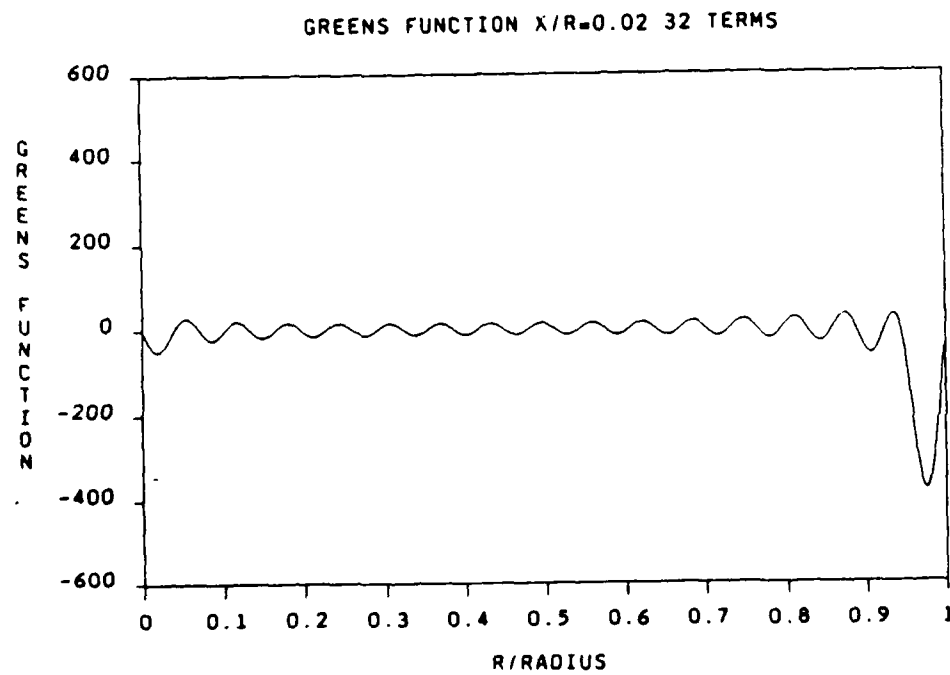


Figure 6-6b. Weighting Function- $x/R = 0.02$

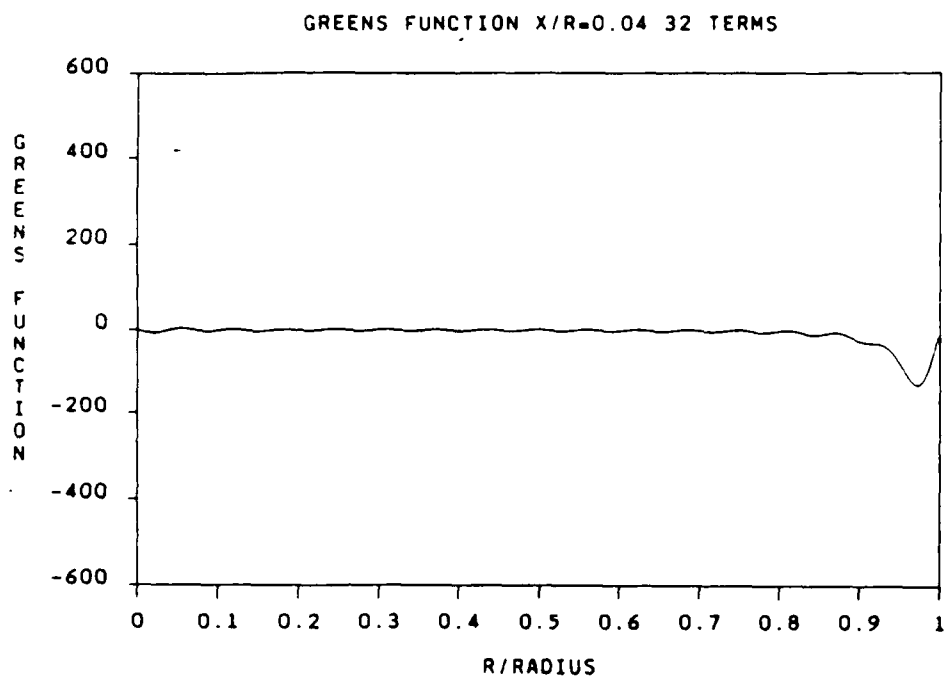


Figure 6-6c. Weighting Function- $x/R = 0.04$

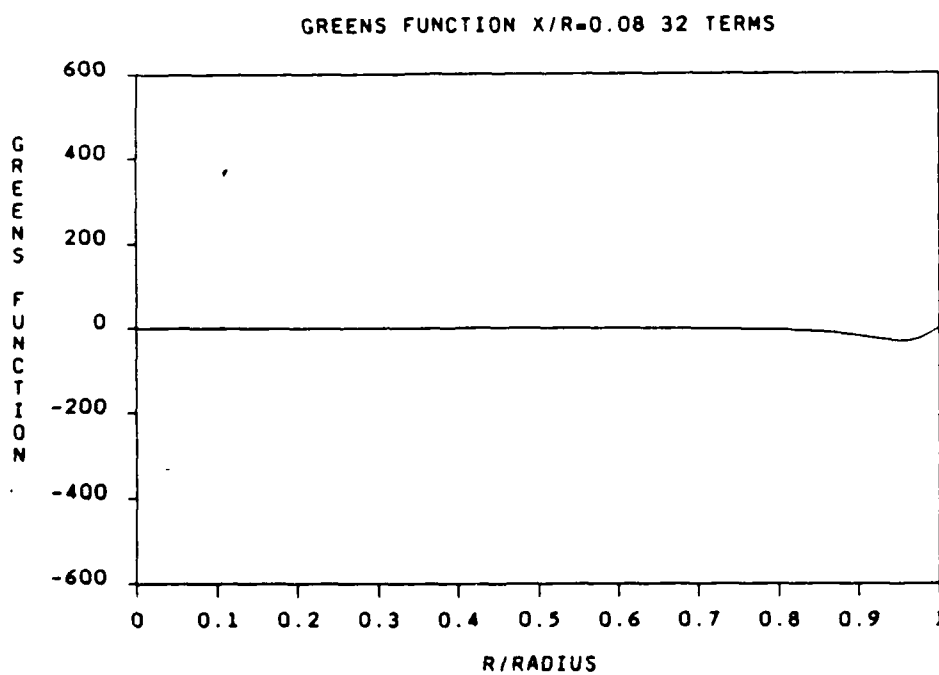


Figure 6-6d. Weighting Function- $x/R = 0.08$

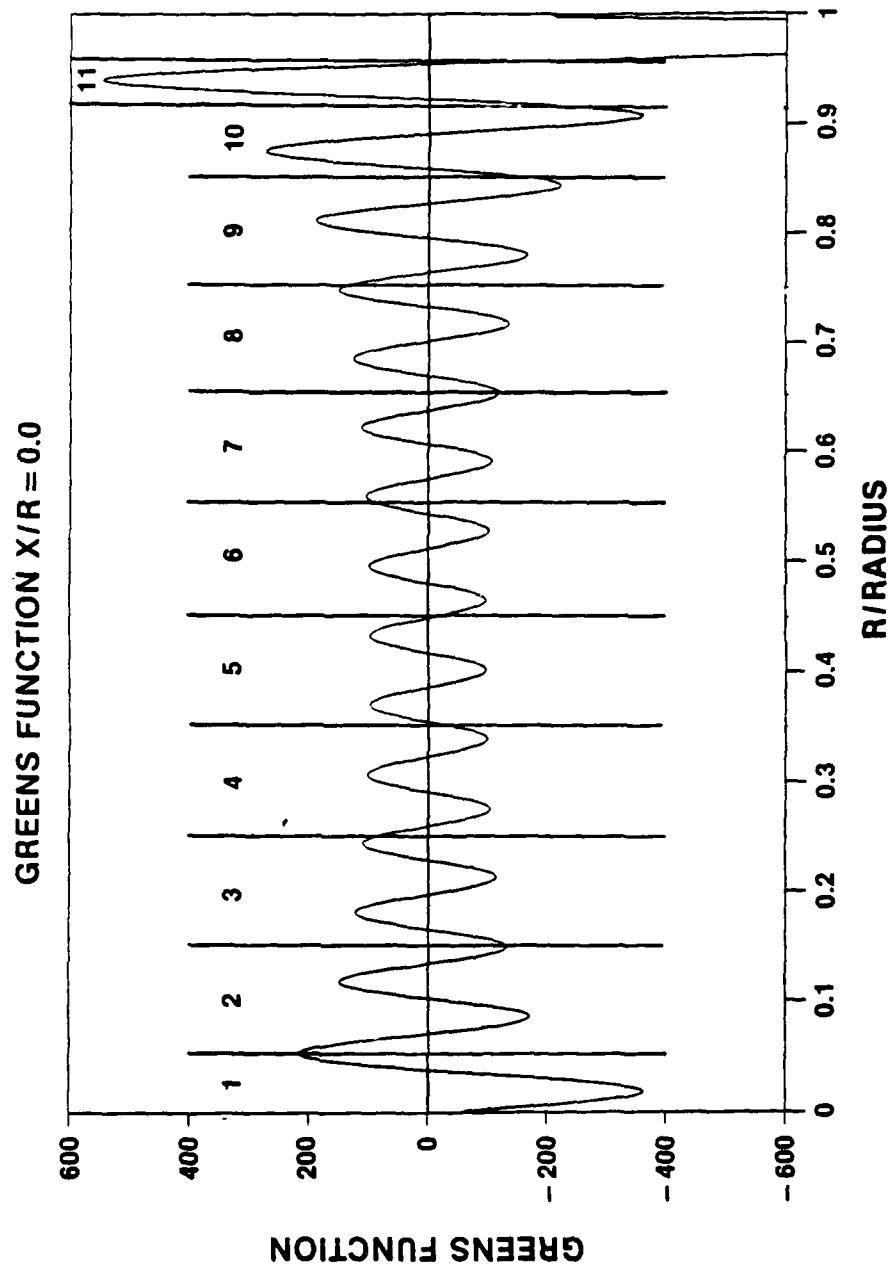


Figure 6-7. Division of Annular Bands

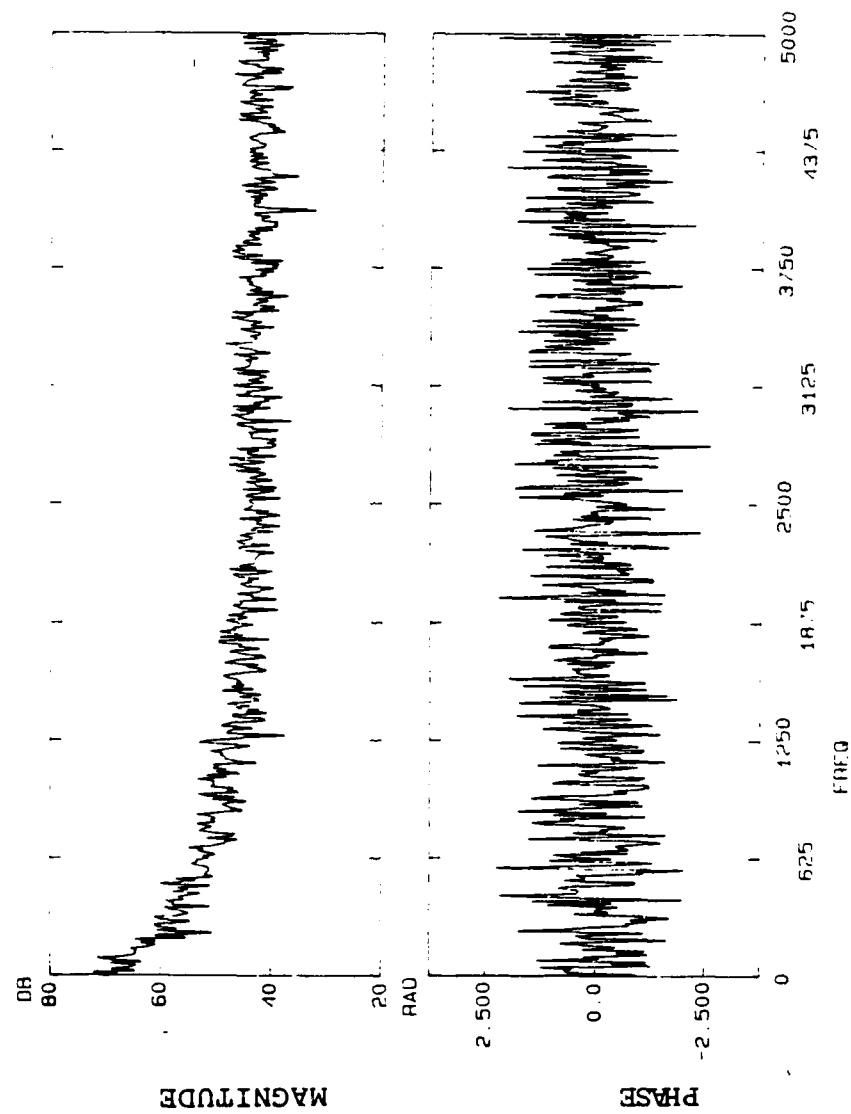


Figure 6-8a. Magnitude and Phase of $2u'u$ for 0.625-Inch Jet at $x = 0$ cm

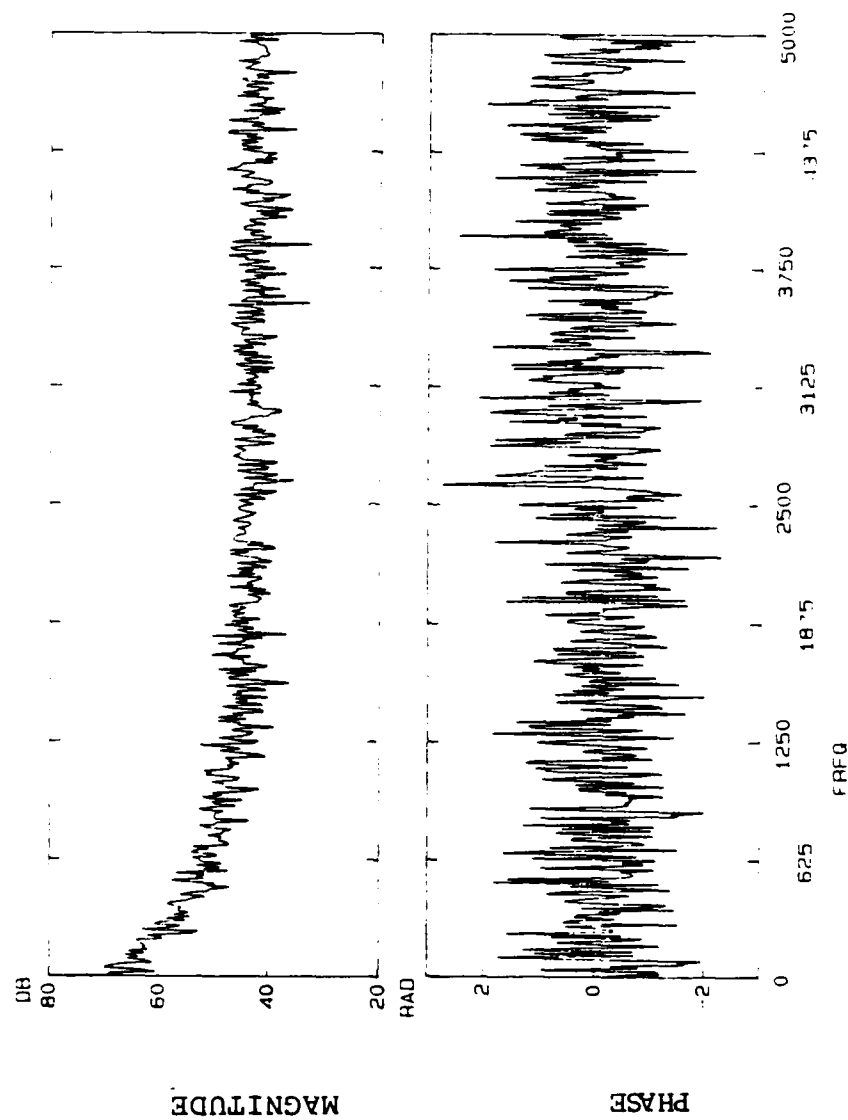


Figure 6-8b. Magnitude and Phase of $2u'u$ for 0.625-Inch Jet at $x=0.25$ cm

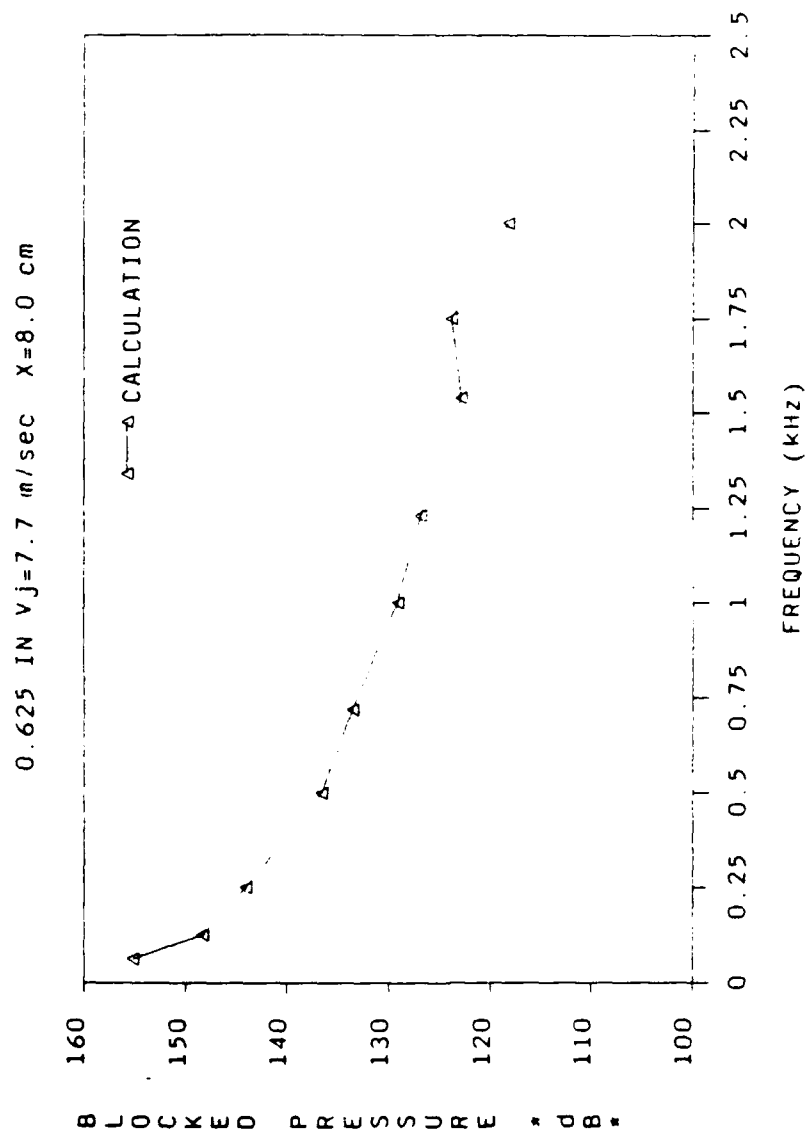


Figure 6-9. Blocked Surface Pressure for 0.625-Inch Jet

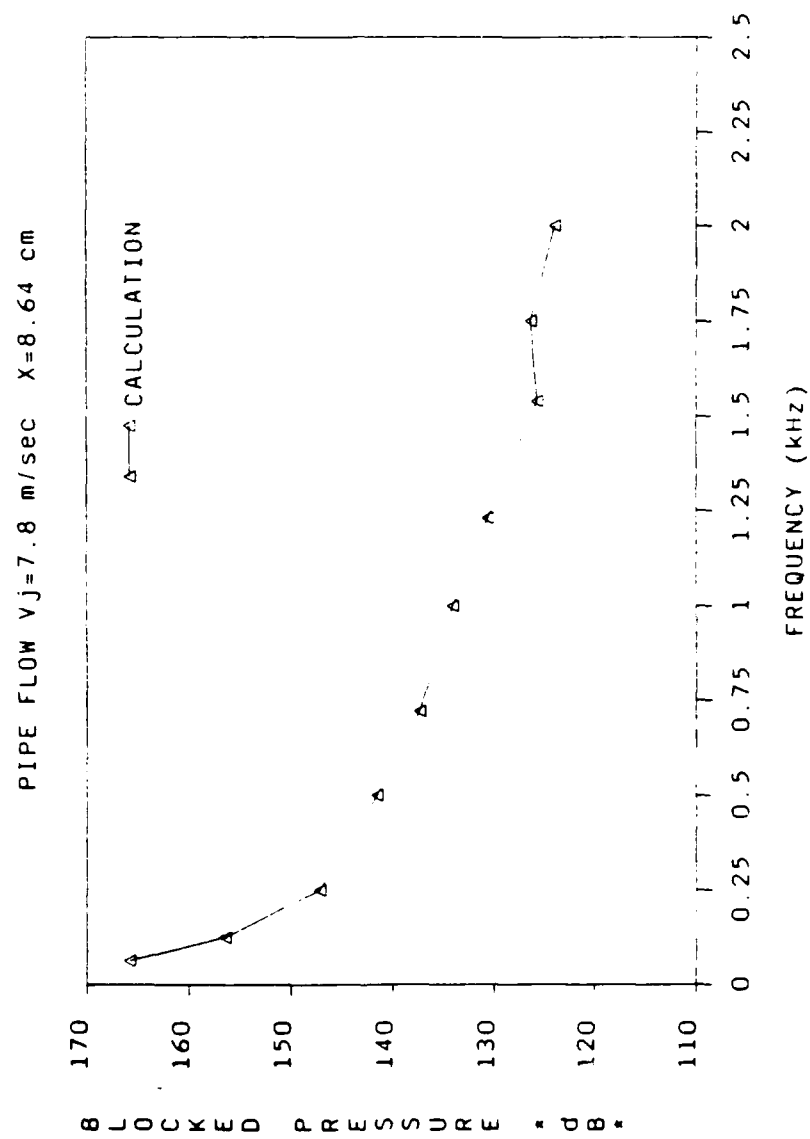


Figure 6-10. Blocked Surface Pressure for Pipe Flow

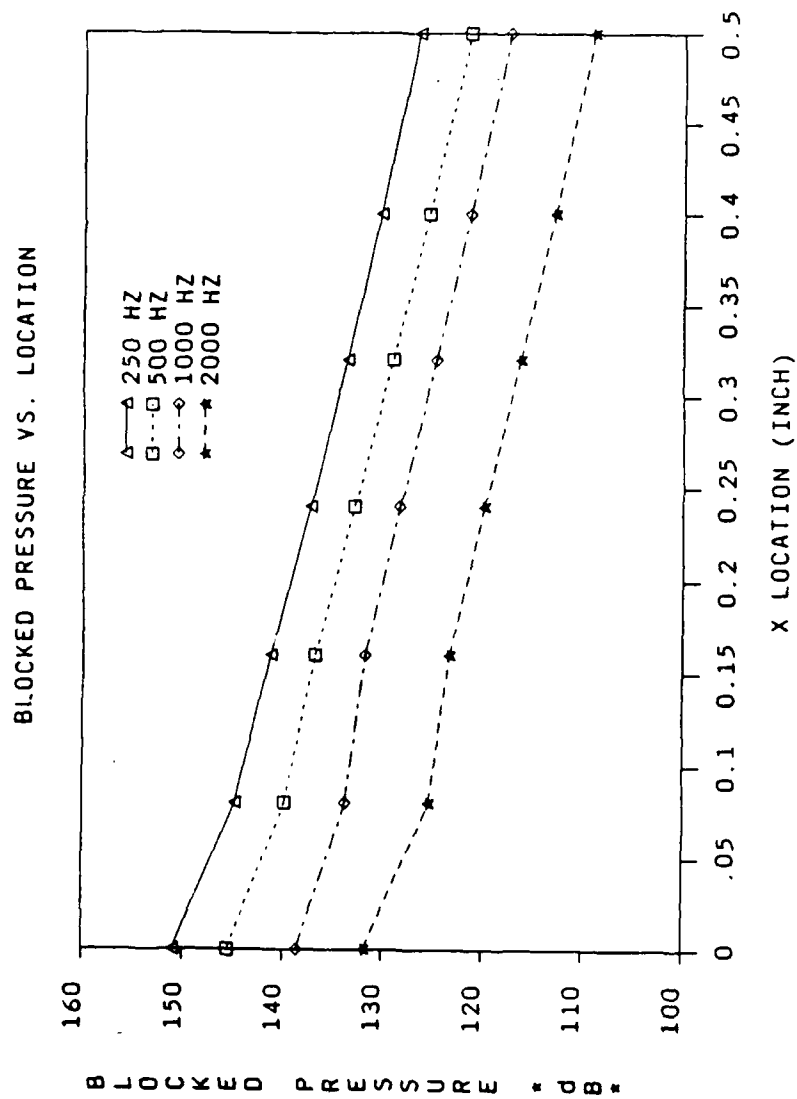


Figure 6-11. Blocked Surface Pressure vs Location

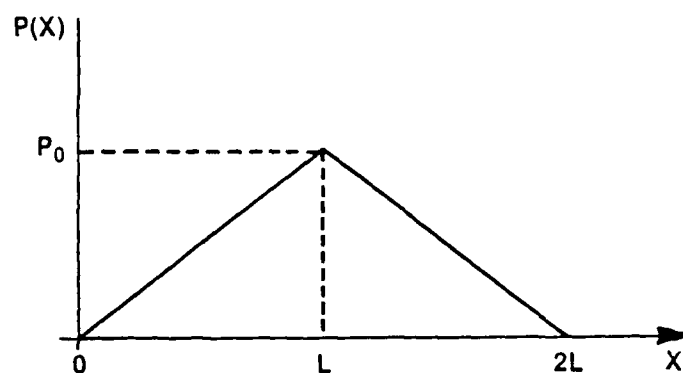


Figure 6-12. Triangular Blocked Pressure Distribution

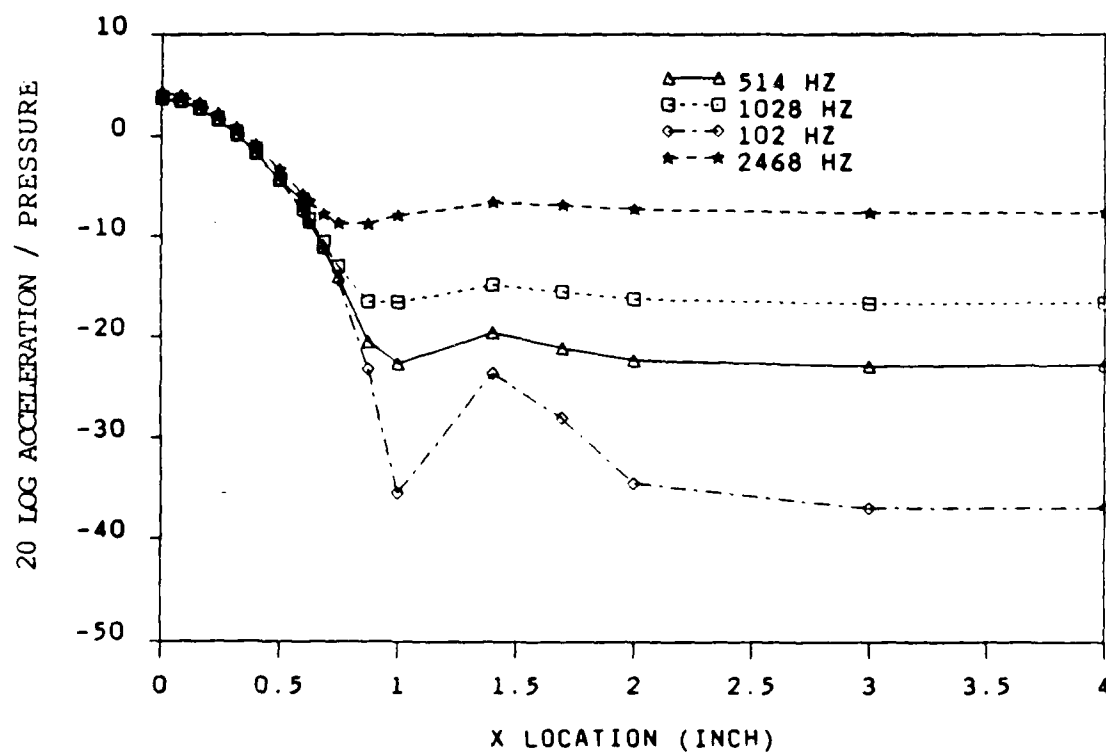


Figure 6-13. Wall Acceleration vs Location

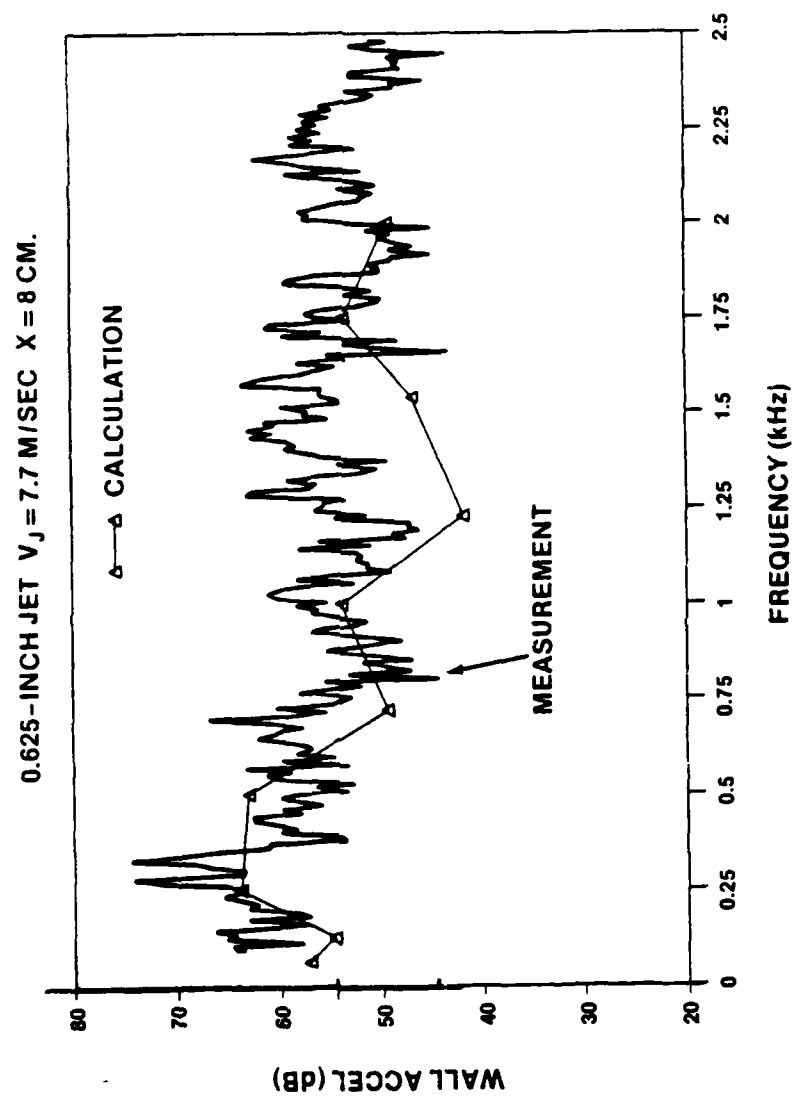


Figure 6-14. Wall Acceleration Spectrum for 0.625-Inch Jet
(Deterministic Approach)

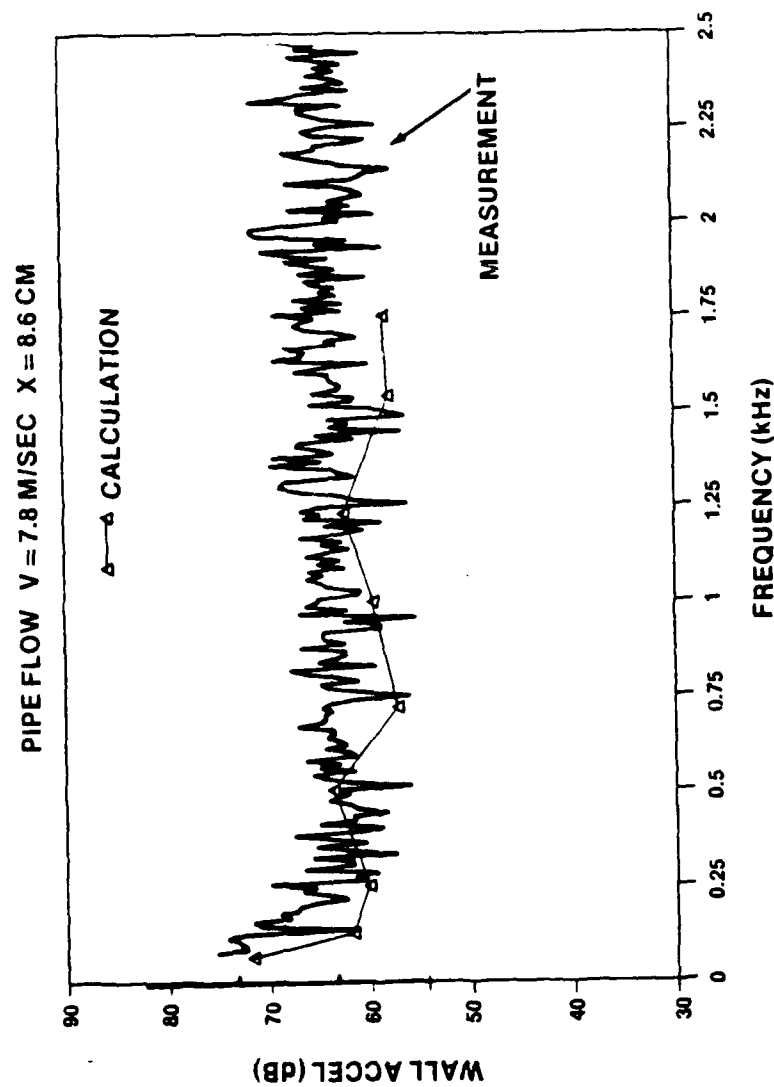


Figure 6-15. Wall Acceleration Spectrum for Pipe Flow
(Deterministic Approach)

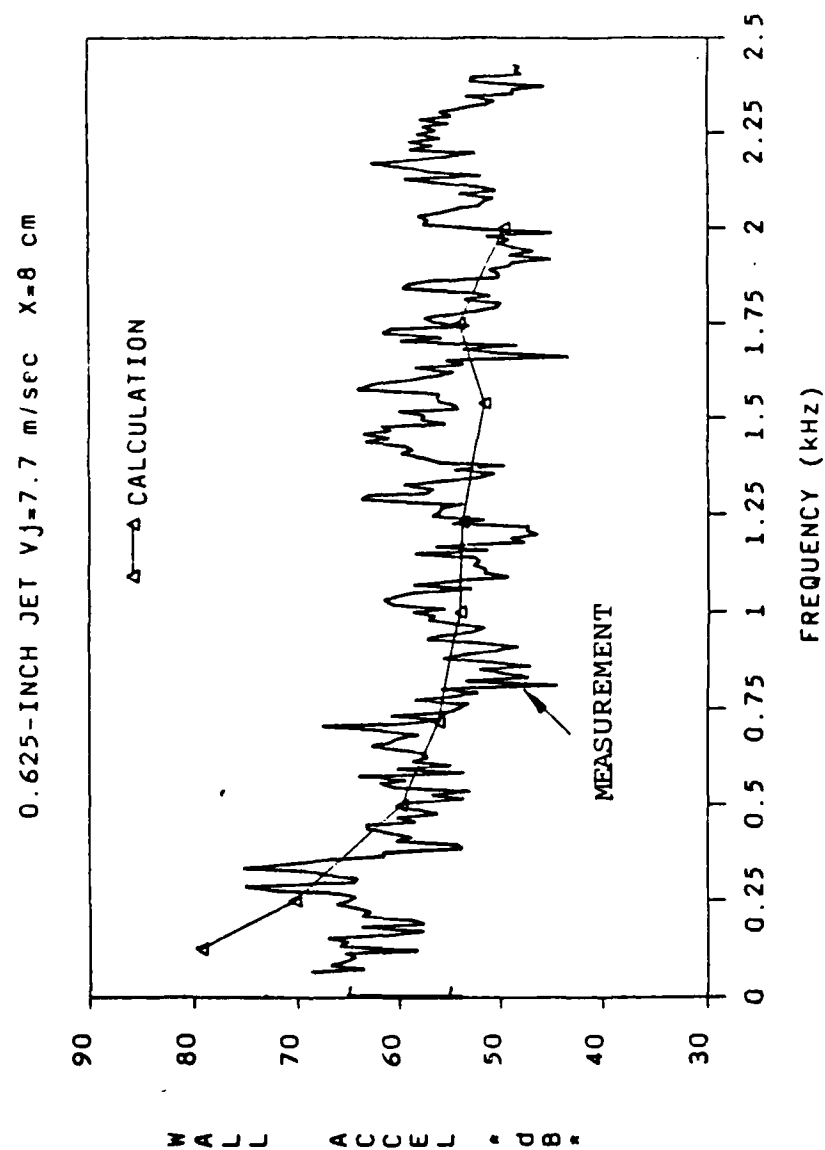


Figure 6-16. Wall Acceleration Spectrum for 0.625-Inch Jet
(Statistical Approach)

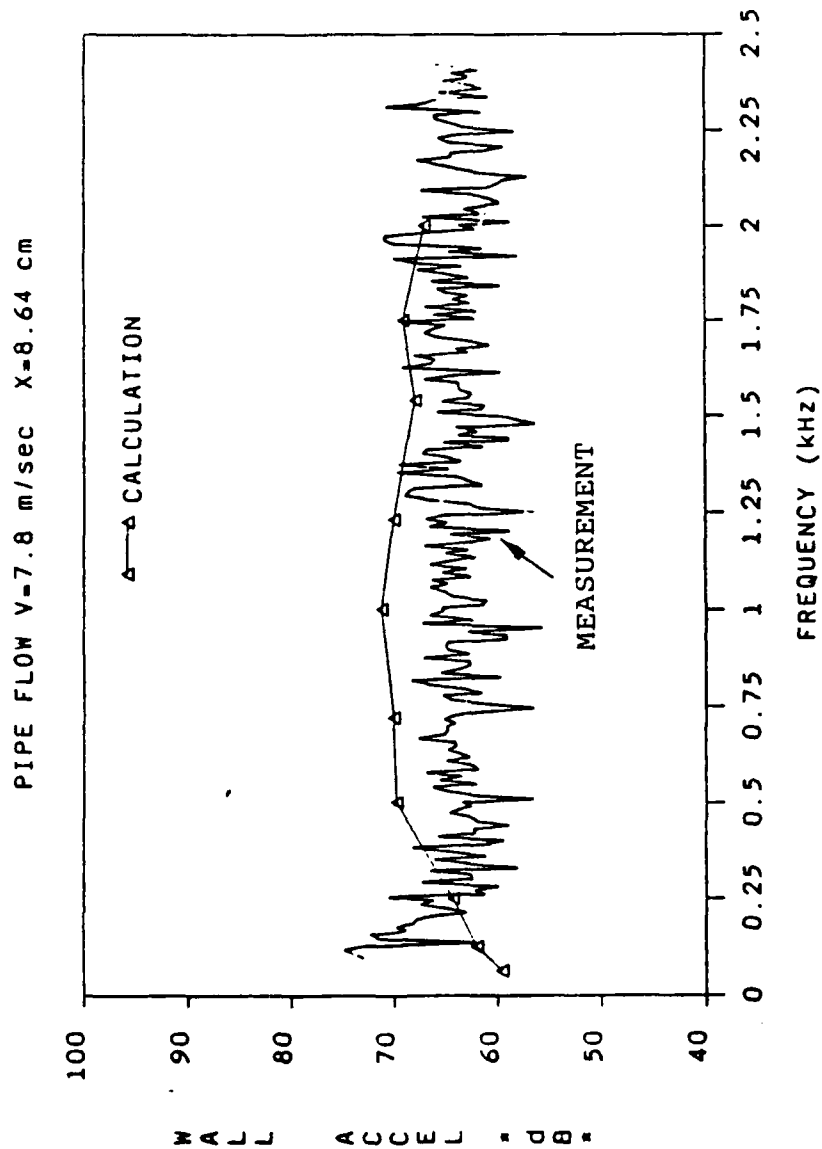


Figure 6-17. Wall Acceleration Spectrum for Pipe Flow
(Statistical Approach)

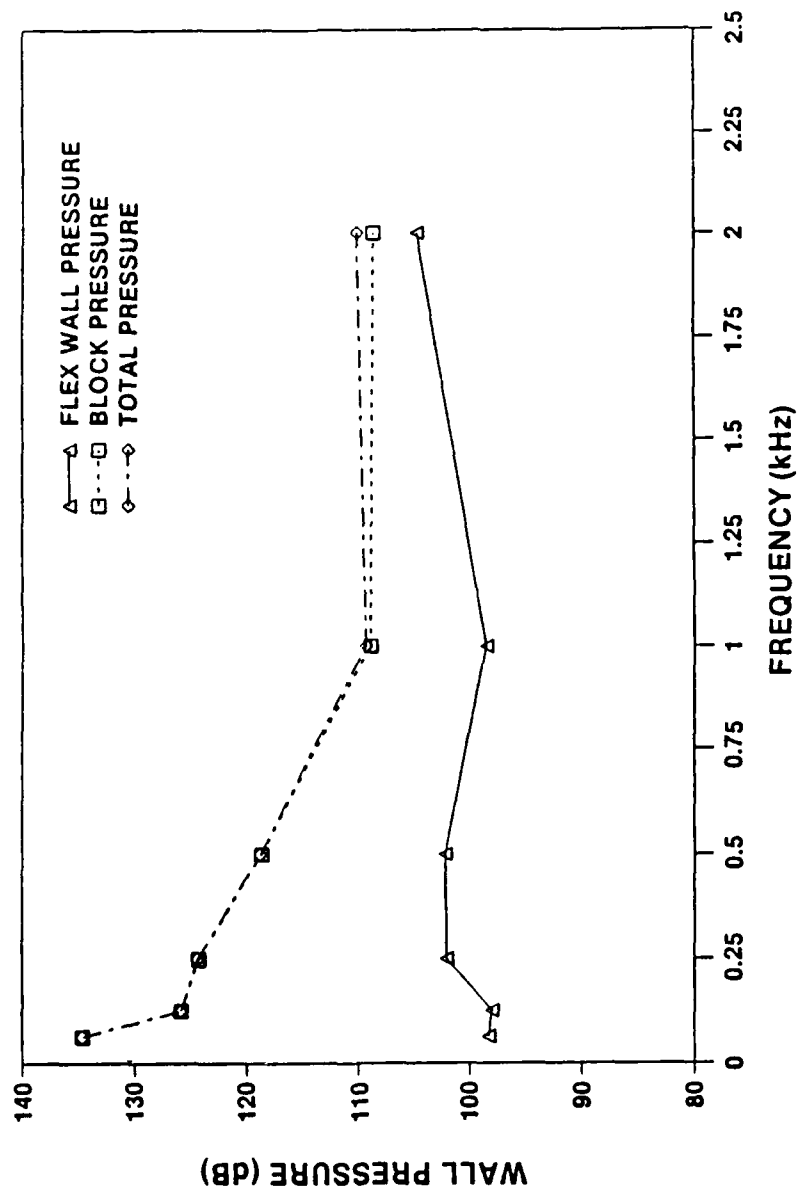


Figure 6-18. Flexible Wall Pressure Spectrum

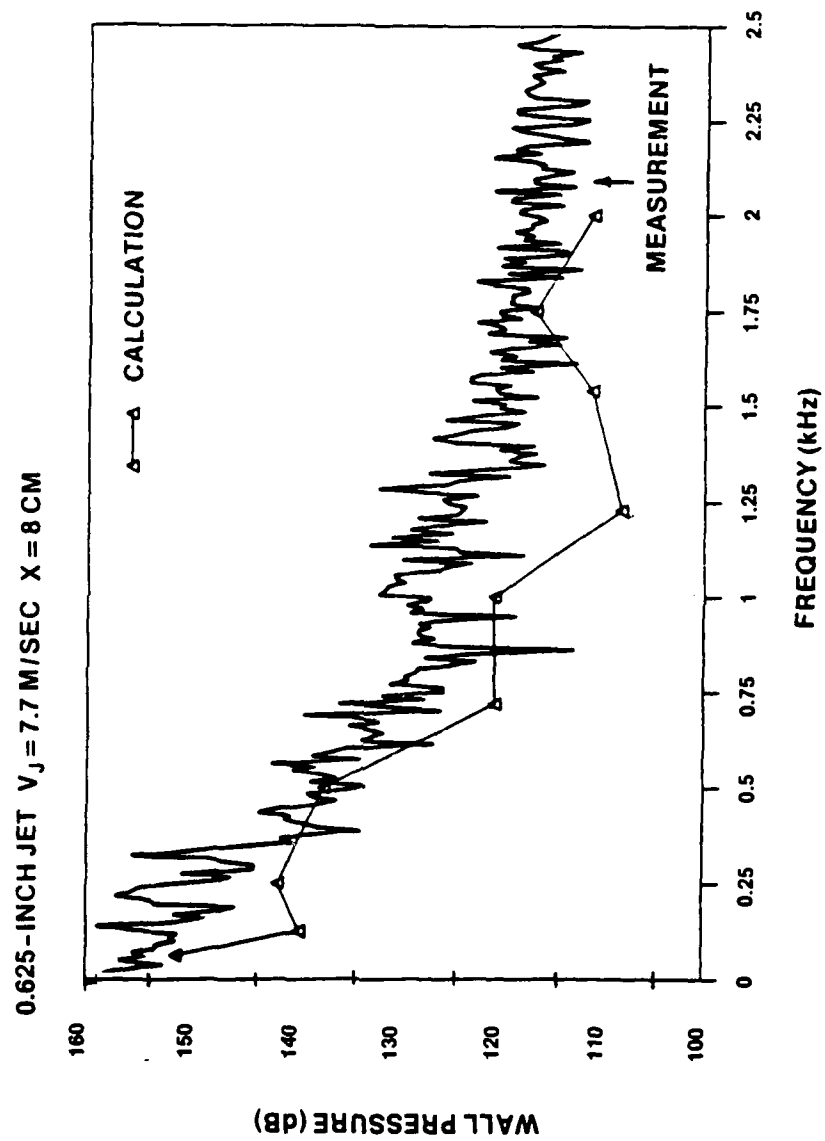


Figure 6-19. Wall Pressure Spectra Comparison - 0.625-Inch Jet
(Deterministic Approach)

1.00-INCH JET $V_J = 12.5 \text{ M/SEC}$ $X = 14.5 \text{ CM}$

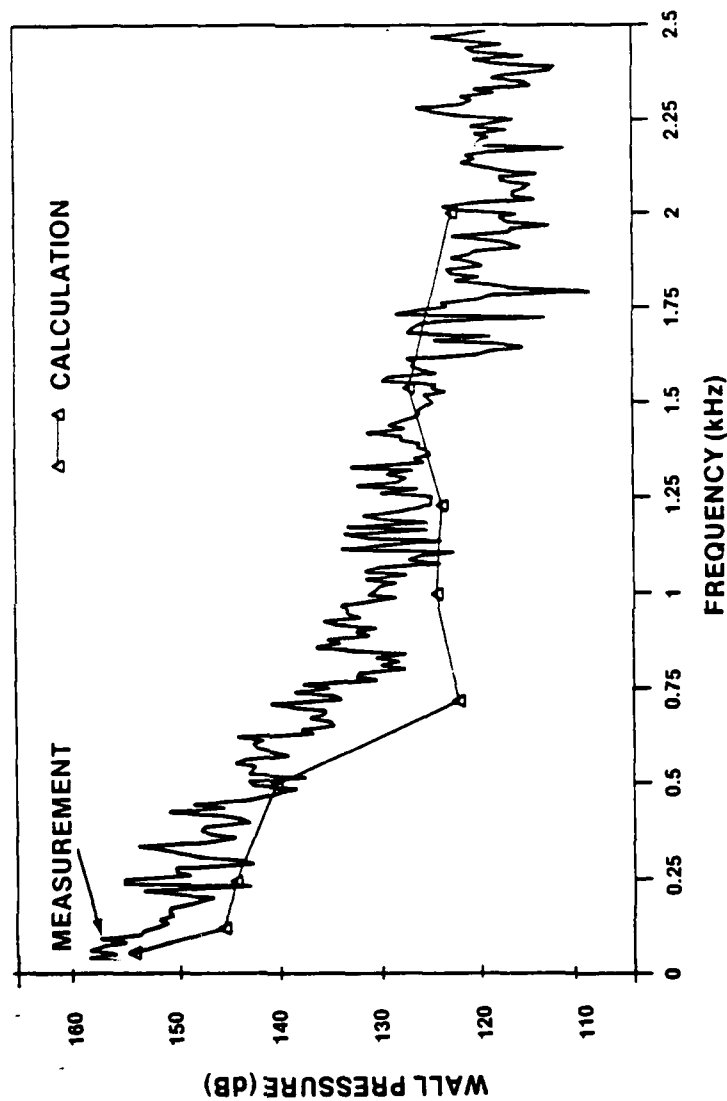


Figure 6-20. Wall Pressure Spectra Comparison - 1.00-Inch Jet
(Deterministic Approach)

PIPE FLOW $V_j = 7.8$ m/sec $X = 8.64$ cm

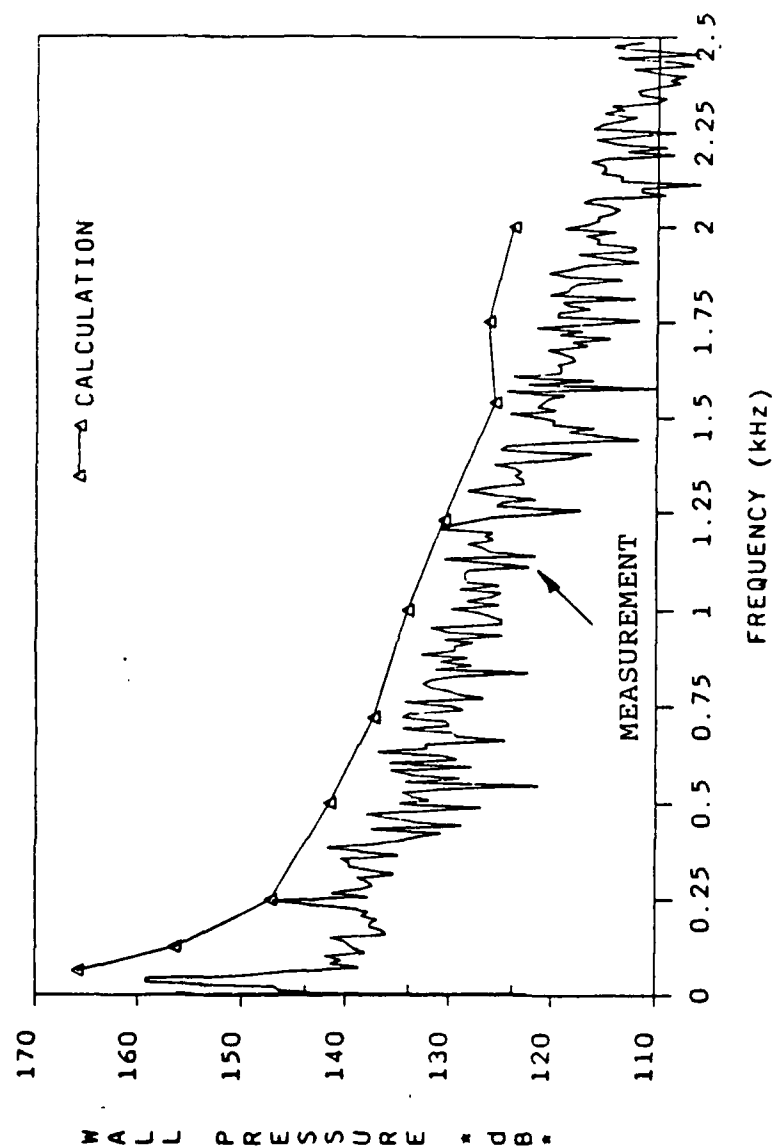


Figure 6-21. Wall Pressure Spectra Comparison - Pipe Flow

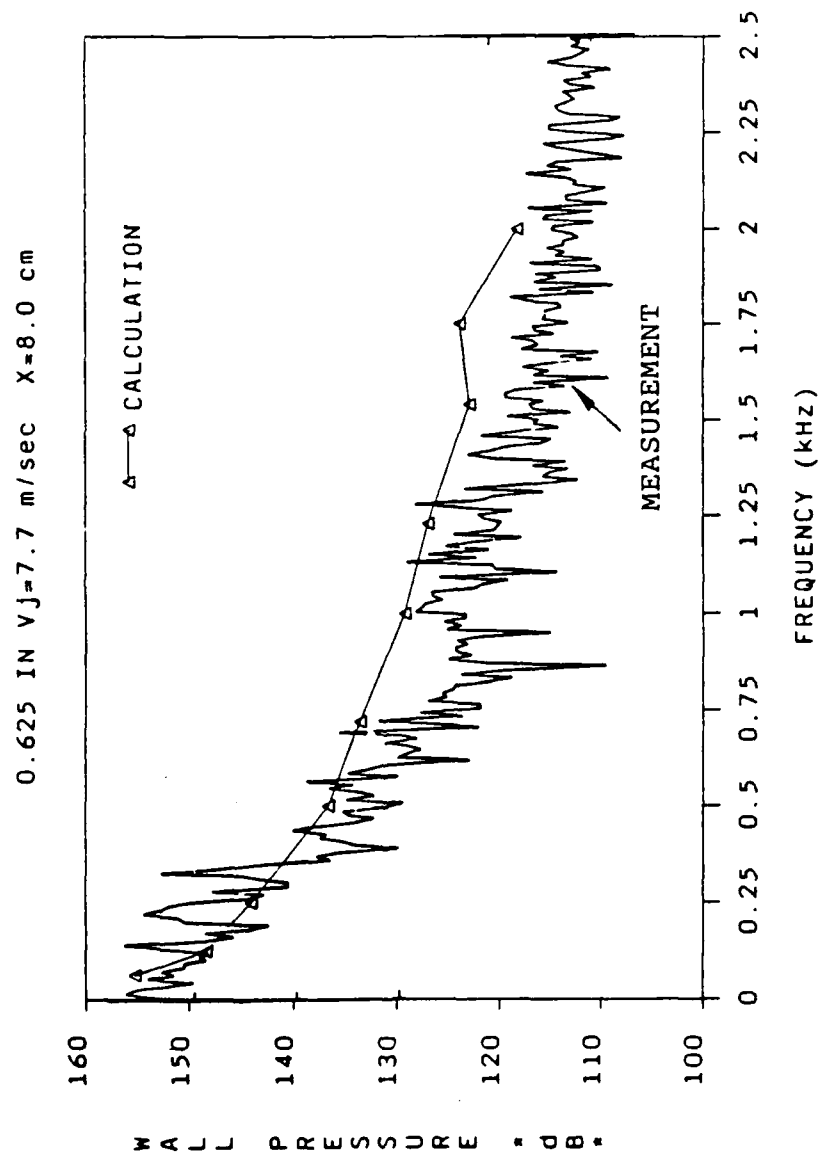


Figure 6-22. Wall Pressure Spectra Comparison - 0.625-Inch Jet

0.75 IN Vj=10.3 m/sec X=8.03 cm

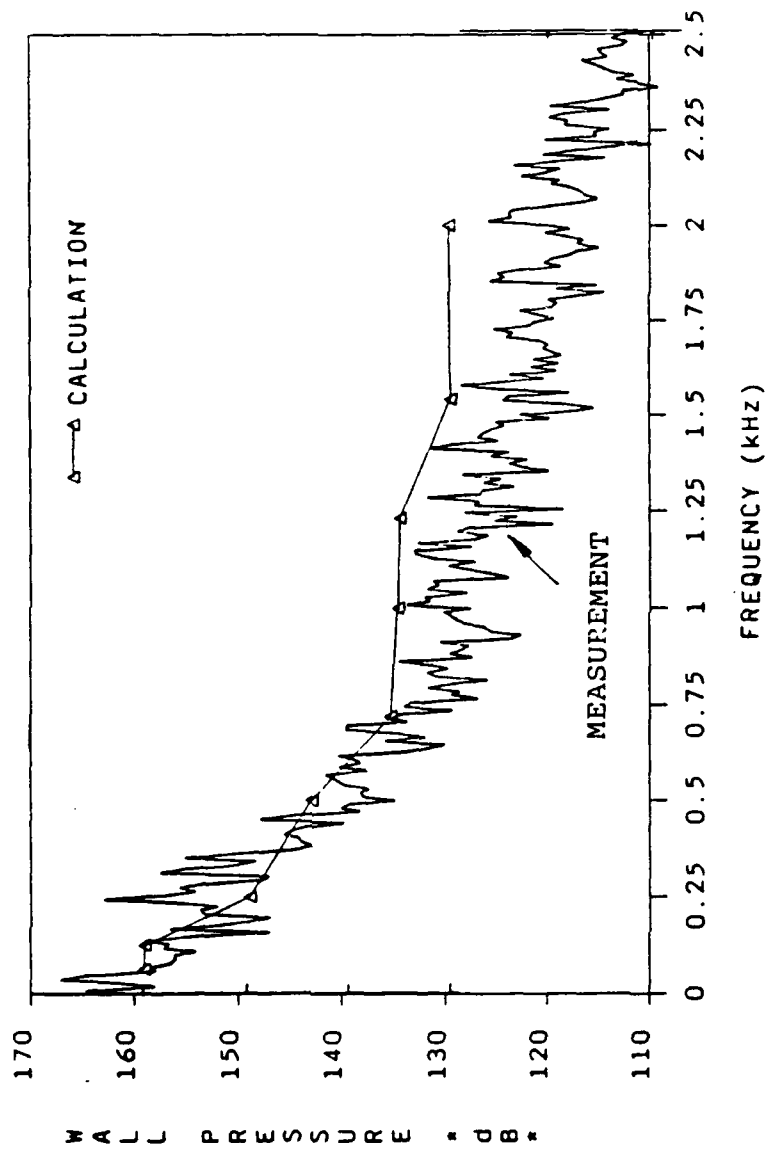


Figure 6-23. Wall Pressure Spectra Comparison - 0.75-Inch Jet

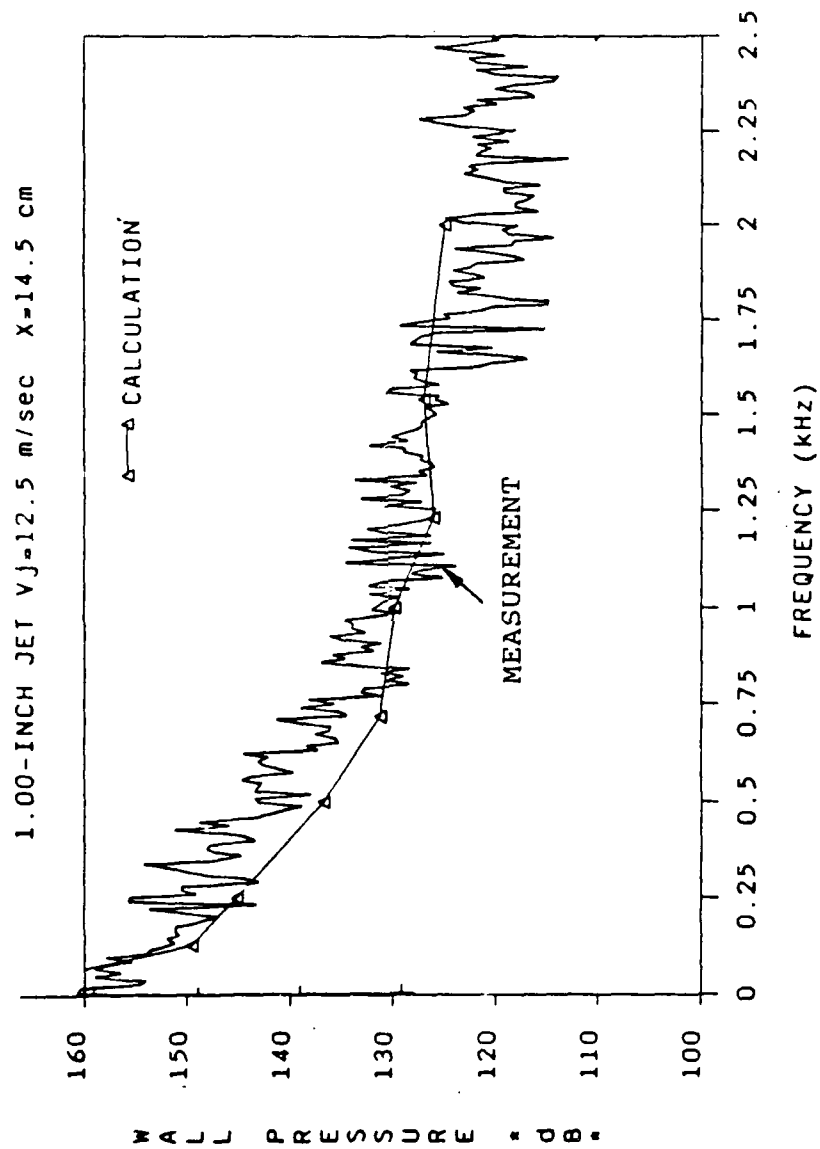


Figure 6-24. Wall Pressure Spectra Comparison - 1.00-Inch Jet

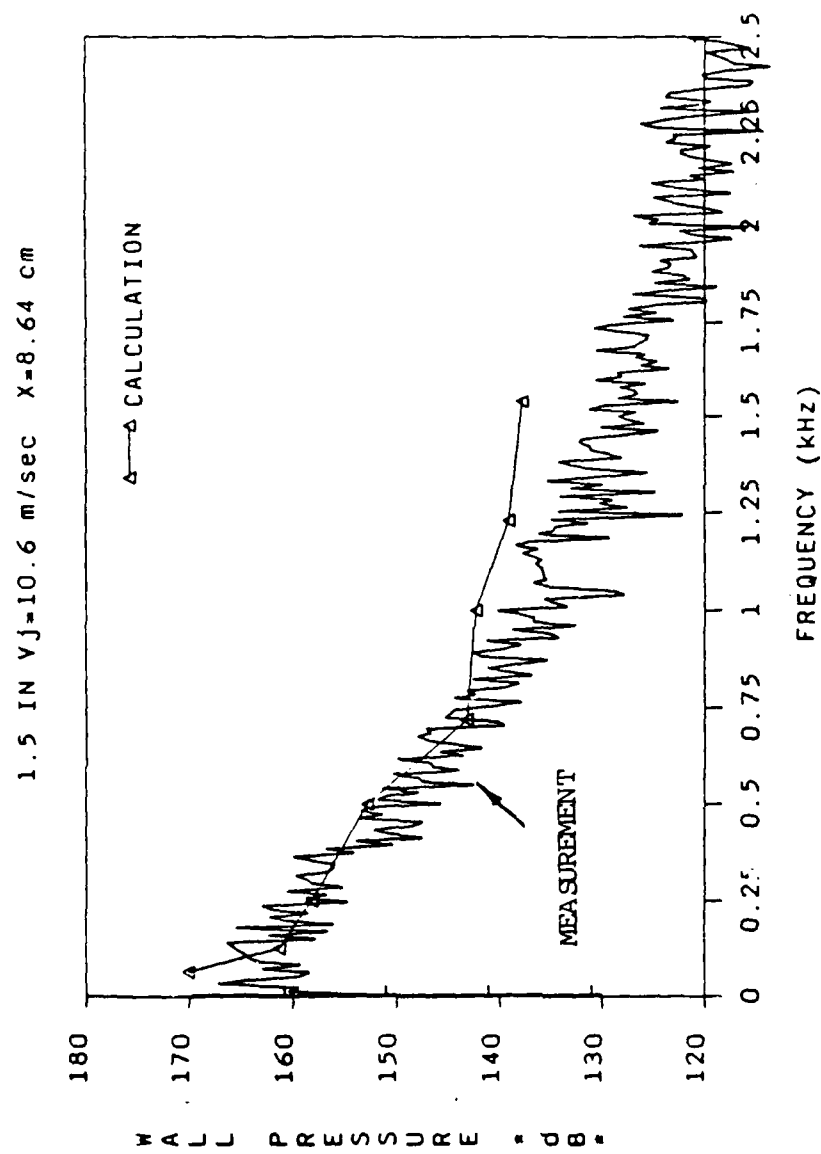


Figure 6-25. Wall Pressure Spectra Comparison - 1.50-Inch Jet

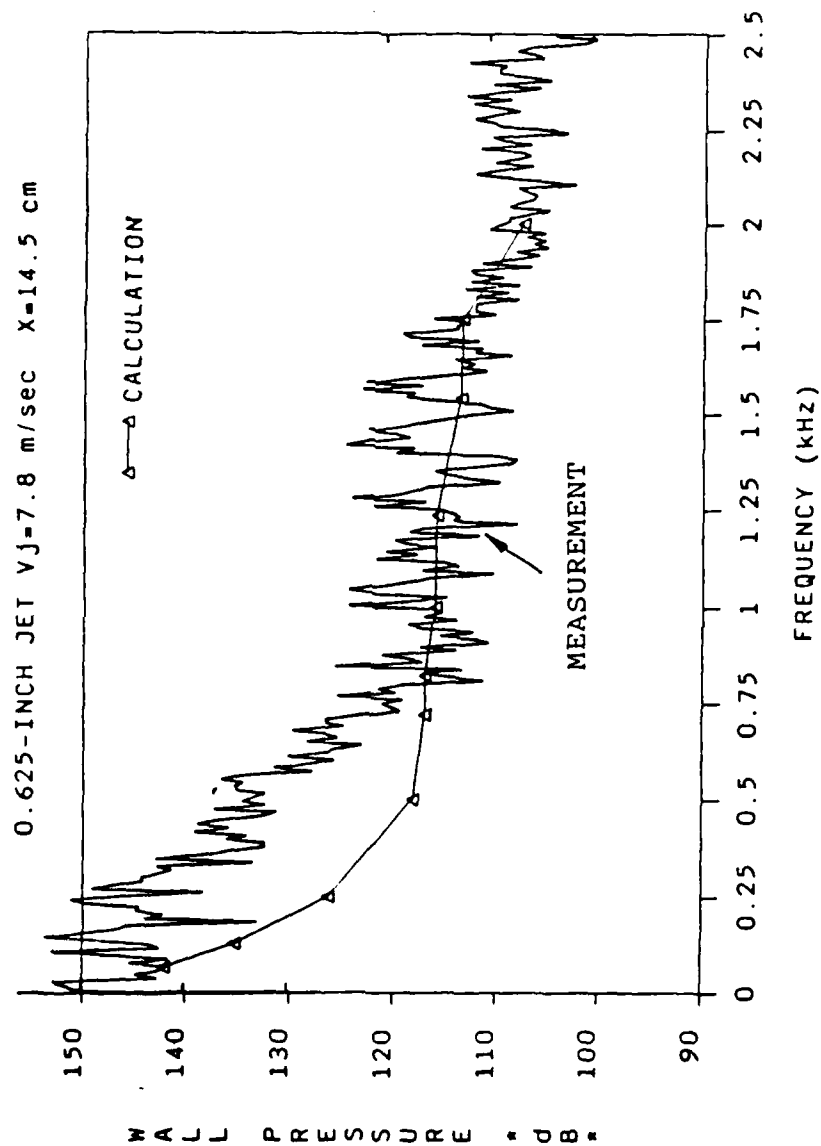


Figure 6-26. Wall Pressure Spectra Comparison - 0.625-Inch Jet

1.00-INCH JET $V_j=12.5$ m/sec $X=14.5$ cm

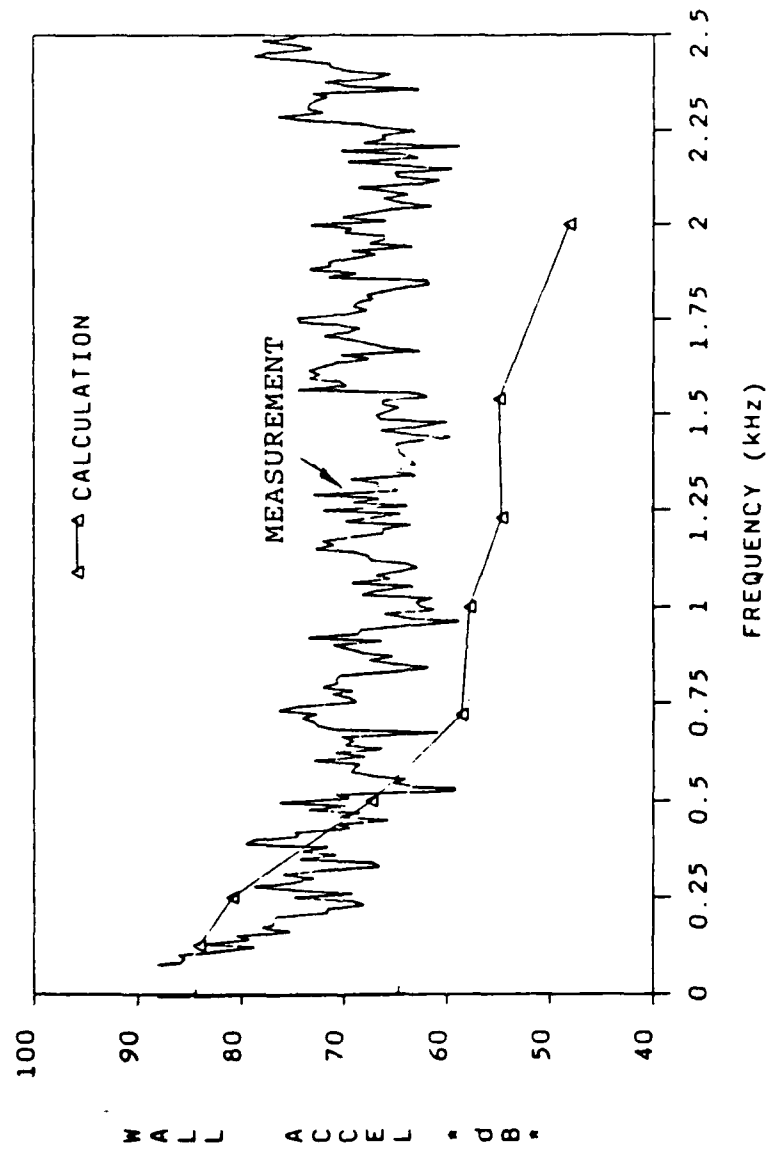


Figure 6-28. Wall Acceleration Spectrum for 1.00-Inch Jet

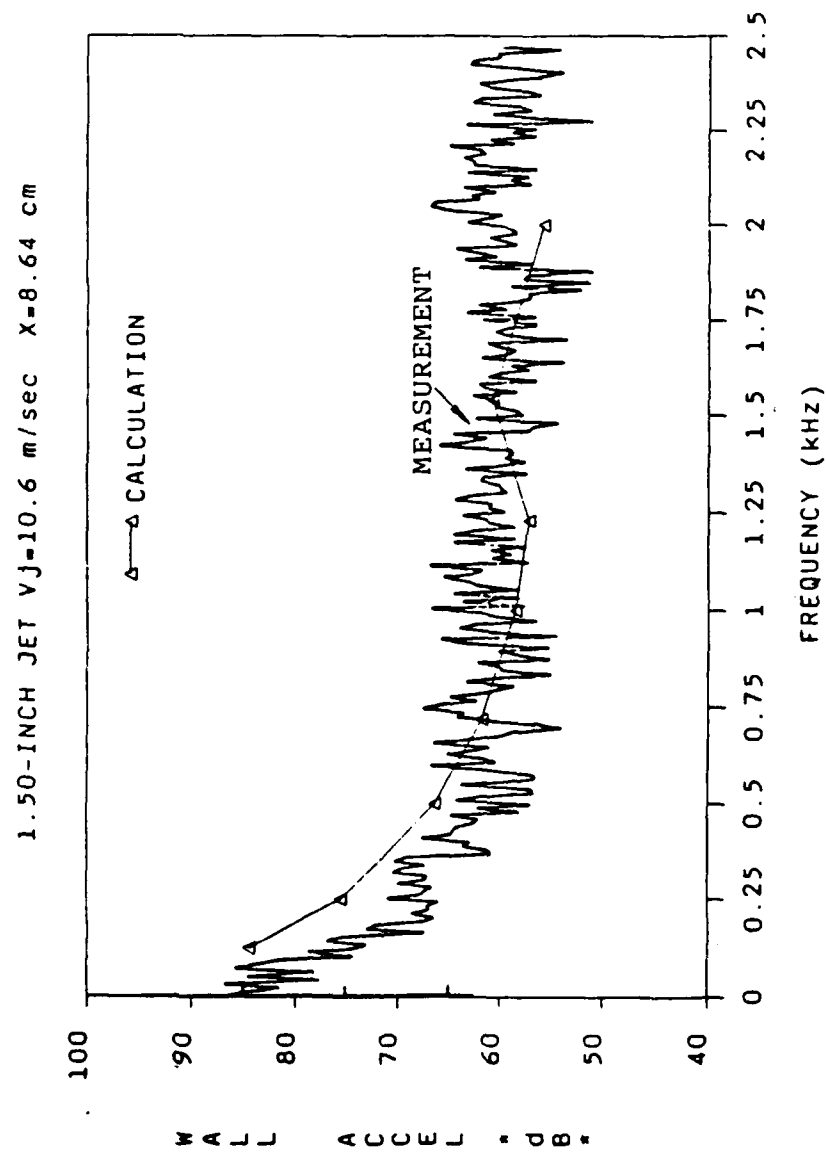


Figure 6-29. Wall Acceleration Spectrum for 1.50-Inch Jet

0.625-INCH JET $V_J=7.8$ m/sec $X=14.5$ cm

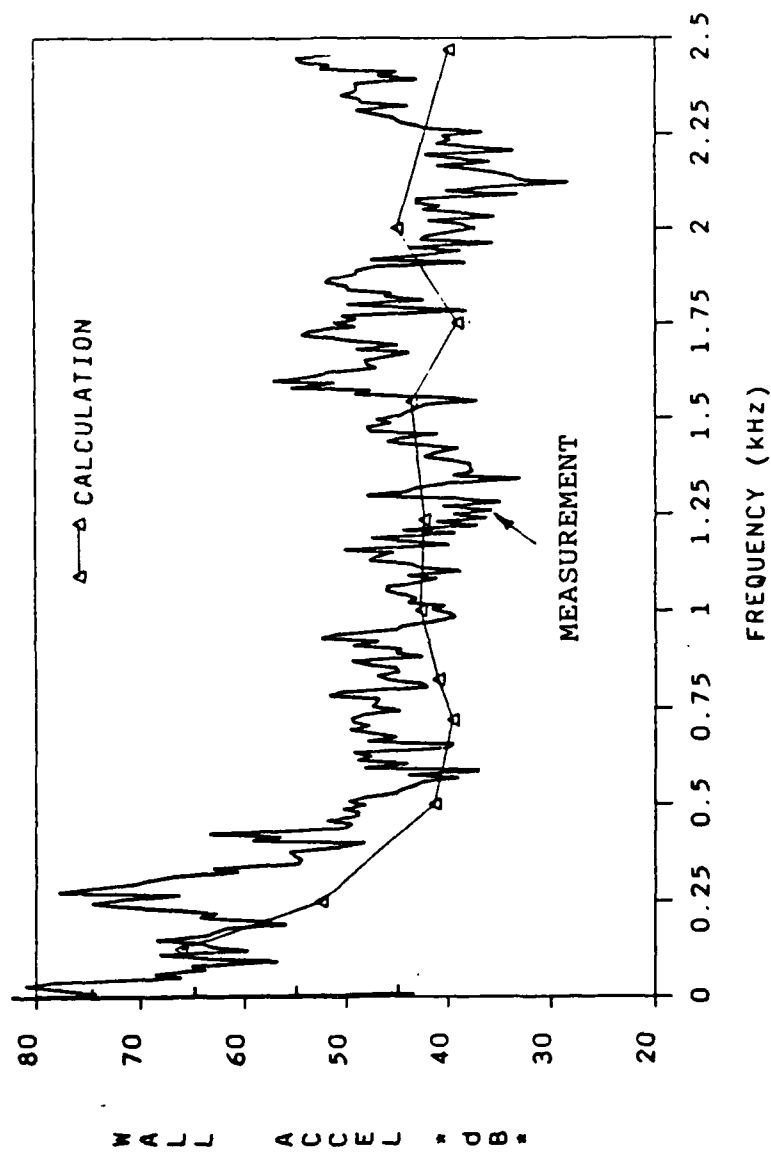


Figure 6-30. Wall Acceleration Spectrum for 0.625-Inch Jet

CHAPTER 7

CONCLUSIONS AND RECOMMENDATIONS

This study has addressed the subject of turbulence generated by confined jet flows in a cylindrical duct. An experimental investigation was conducted to characterize the noise generating mechanisms of a confined jet and to determine the noise source strength of confined jets with various configurations and area ratios. An analytical model was developed to study the effect of the turbulent jet flow field on the wall pressure and vibratory motion of the duct wall. Analytical and experimental results for wall pressure and acceleration were then compared for a wide range of parameters of interest.

Conclusions

The experimental investigation consisted of two phases, namely: phase I - study of the noise characteristics of various confined jet flows, and phase II - study of the flow and acoustic characteristics of circular confined jets with various area ratios. Conclusions regarding the experimental investigation can be summarized as follows:

1. The flow field of confined jets can be divided into the recirculation or developing region and the fully developed region. The developing region is characterized by reverse flow near the jet exit and relatively flat velocity further downstream. The fully developed region is characterized by a fully developed pipe flow velocity profile, which occurs at about 36 pipe diameters downstream. Results of the mean velocity profiles from the experiment compared reasonably well with the calculated velocity profiles using the two-equation (K and ϵ) model.

2. Turbulence intensity data showed that the peak radial velocity

fluctuations occurred at the shear layer region. The distribution functions of the axial velocities have a nearly Gaussian distribution, whereas the radial velocity distribution functions are more skewed. Frequency spectra of the axial velocities agree reasonably well with the wall pressure spectra, and the radial velocity spectra are in good agreement with the pipe wall acceleration spectra. The convection velocity of the noise-producing eddies was determined to be approximately 0.6 of the jet velocity.

3. Peak wall pressure fluctuations are located at the end of the jet's potential core, which is about 6 jet diameters downstream of the jet.

4. Correlations of wall pressure fluctuations with jet velocity showed a velocity to the 3.7th to 5.0th power relationship. As the jet diameter increases, the velocity exponent decreases.

5. A non-dimensional wall pressure spectrum was developed for the various confined jets by the Strouhal relationship. For circular jets, the length scale is the jet diameter; for more complicated jet geometries, the length scale is the hydraulic diameter. The collapsed wall pressure spectrum of the jets agrees well with the pressure spectrum of a turbulent boundary layer above a rigid plane. The wall pressure spectra of cavitating jets showed more high-frequency noise components.

6. Correlations of wall pressure fluctuations and pipe wall acceleration signals showed that jet flows generate more deterministic features than pipe flow. The coherence functions of the wall pressure and pipe wall acceleration signals are relatively high near the exit of the jet. The high coherence is probably due to the large-scale coherent structures.

7. Experimental results showed that the area ratio has significant

effects on the flow field and noise, whereas the effects of plate thickness and sharpness are insignificant.

A noise model was developed to calculate the wall pressure and the response of the pipe wall due to the turbulent jet flow in the pipe. An approach has been presented to evaluate the wall pressure fluctuations and pipe wall acceleration due to the excitation of turbulent jet flows. Based on flow field measurements, the blocked surface pressure was calculated using the Lighthill method, and then used to drive the fluid-filled shell. The wall pressure and pipe wall acceleration were determined by solving the coupled fluid solid interaction problem. The wall pressure was obtained by summing the blocked surface pressure and the pressure due to the wall vibration.

Principal results and conclusions to be drawn from the analytical study are as follows:

1. The source strength for the Lighthill method was calculated from the experimentally determined turbulence structure of the jet flow. The source term is controlled by the interaction of the mean axial velocity and axial velocity fluctuations.
2. The blocked surface pressure was obtained by integrating the product of the source term and the local weighting Green's function in the source region. Because the weighting function is an oscillatory function, spatial averaged values of the weighting function at each LDV measurement point were used in the blocked pressure calculations. The amplitude of the local weighting function increases toward the wall and decays rapidly in the axial direction. The blocked pressure is controlled by the sources near the wall since the values of the local weighting function are dominant near the wall region.

3. A deterministic amplitude modulated convecting wave field was used initially to simulate the moving acoustic sources of the jet. The amplitude modulation in the jet flow was represented by a triangular blocked excitation pressure. This form was representative of available experimental data.

4. The random nature of the turbulent jet was later incorporated into a statistical analysis of the jet sources. Specifically, the acoustic pressure was assumed to result from hydrodynamic pressure fluctuations which are uncorrelated in the radial direction, but are correlated in the axial direction near the jet exit. The uncorrelated pressure fluctuations in the radial direction reflect the random motion of the turbulent jet, whereas the correlated pressure fluctuations in the axial direction reflect the motion of the large-scale coherent structures near the jet exit.

5. The width of the triangular pressure distribution for the statistical calculations was chosen to represent the correlation length scale of the pressure fluctuations. The correlation length scale is a function of frequency. Specifically, the values of L range from about 3 jet diameters at 2 kHz to about 12 jet diameters at 100 Hz.

6. Numerical results showed that the blocked pressure is dominant as compared to the pressure due to the wall motion. The blocked pressure decays faster than the pipe wall acceleration with respect to the axial location. In the pipe wall response, the low frequencies decay faster than the high frequencies.

7. Numerical results have demonstrated that the noise model is capable of relating the flow field and acoustic field of confined jet flows. Results from the analytical model showed good agreement with the measured wall pressure and pipe wall acceleration. Comparisons with the

experimental data show that the calculated wall pressure and pipe wall acceleration based on the statistical analysis has better agreement than the calculations based on the deterministic analysis.

8. Although the analytical development and noise model focused on the prediction of flow-induced noise and vibration of confined jets, the analytical noise model can also be applied to the pipe flow noise prediction problem.

Recommendations for Further Study

Results of the experimental investigation have revealed some salient features of confined jet noise and vibration characteristics and shed some light on the understanding of piping system noise. Moreover, results of the numerical calculations have demonstrated the validity and capabilities of the analytical noise model. Nevertheless, it is apparent that certain extensions can be pursued. Accordingly, several recommendations are made for future work:

1. An area for future analytical work is the consideration of a finite length pipe and corresponding boundary conditions that are close in practical application.

2. A potentially rewarding area is the study of large-scale coherent structures in confined jets and their role in jet mixing and noise production.

3. A natural extension of the present study is the case of confined jet flows under transient conditions. This area is rather challenging, but could be very rewarding.

4. Another natural extension of this study is the development and application of noise control techniques on confined jet noise. An active noise control concept has been used and demonstrated in the

reduction of airborne noise in air ducting systems. This concept seems to have potential for reducing the noise associated with confined jets.

APPENDIX A

FORMULATION OF THE BLOCKED EXCITATION PRESSURE

In this section, derivation of the blocked excitation pressure is presented. The blocked excitation pressure (equation 35) is used to calculate the pipe wall response as described in section 5 of chapter 3.

Consider the vibration of a fluid-filled shell that is excited by a blocked pressure with an arbitrary pressure distribution as shown in figure A-1. For discussion purpose, the blocked pressure is divided into two segments at $x = x'$. The blocked pressure is specified by

$$p_b(x) = f_1(x) \quad \text{for} \quad 0 \leq x \leq x'$$

$$p_b(x) = f_2(x) \quad \text{for} \quad x' \leq x \leq 2L.$$

The acceleration response of the pipe wall due to blocked excitation pressure $p_b(x)$ can be expressed as

$$\ddot{W}(x) = \ddot{W}_1(x) + \ddot{W}_2(x),$$

where $W_1(x)$ and $W_2(x)$ are responses due to $f_1(x)$ and $f_2(x)$, respectively.

The wall acceleration response $\ddot{W}_1(x)$ can be simply calculated

according to section 3 of chapter 3. To transform the blocked pressure $f_2(x)$ for $x' \leq x \leq 2L$ to $f_1(x)$, the following steps are required:

1. Shift the origin by x' ;
2. Reflect $f_2(x-x')$ about $x = 0$;

3. Shift $f_2(x'-x)$ by $2L-x'$.

Steps 1 through 3 are shown graphically in figure A-2.

As a special case, consider the blocked pressure distribution as shown in figure A-3, and in particular for the case $x' = L$. The assumption of the triangular pressure distribution is based on the result from numerical calculations (see figure 6-11). The blocked pressure $f_2(x)$ can be transformed to $f_1(x)$ according to the procedure outlined previously.

It should be noted that $f_1(x)$ can be expressed as

$$\begin{aligned} f_1(x) &= g_1(x) + g_2(x) + g_3(x) \\ &= g_1(x) - g_1(x-L) - P_0 H(x-L), \end{aligned}$$

where $g_1(x) = P_0 x/L$; and $H(x)$ is the Heaviside function defined by

$H(x) = 1$ for $x > 0$ and $H(x) = 0$ for $x < 0$. Representation of $f_1(x)$ is depicted in figure A-4. The Fourier transform of $f_1(x)$ is

$$F_1(k_x) = G_1(k_x) [1 - \exp(-jk_x L)] - P_0 \exp(-jk_x L) / (jk_x) ,$$

(A-1)

where $G_1(k_x) = P_0 / [L (jk_x)^2]$. After substitutions, the triangular blocked excitation pressure can be expressed as

$$p_b = \frac{2P_0}{jk_u} \exp(-jk_u L) \left[\exp(jk_u L/2) \frac{\sin(k_u L/2)}{k_u L/2} - 1 \right] , \quad (A-2)$$

where L is the half width of the triangular pressure distribution; k_u is the wavenumber including the convection effect, and is defined as $k_u = \omega/V_c + k_{ns}$.

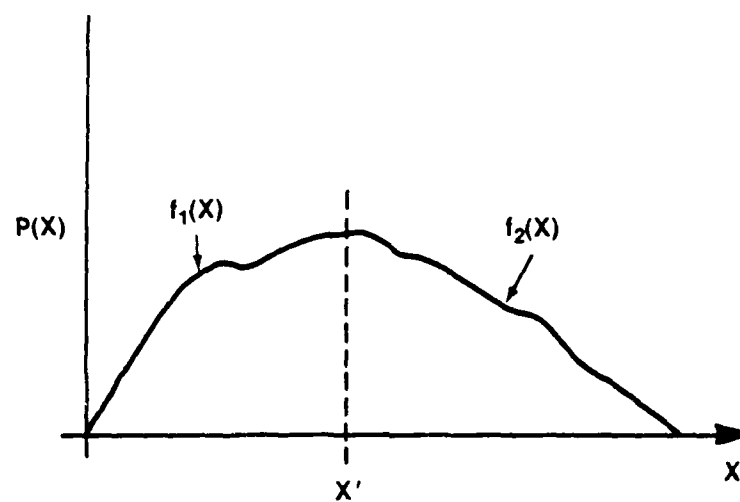


Figure A-1. Distribution of Blocked Excitation Pressure

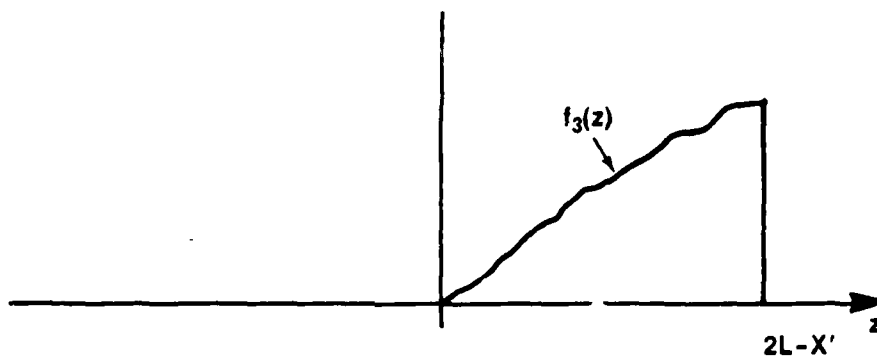
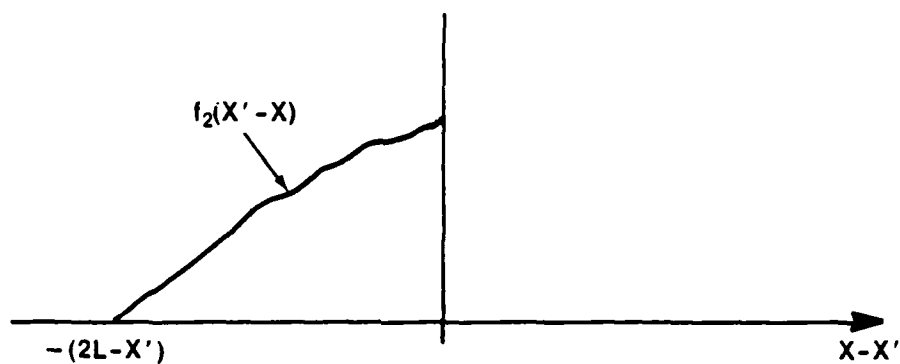
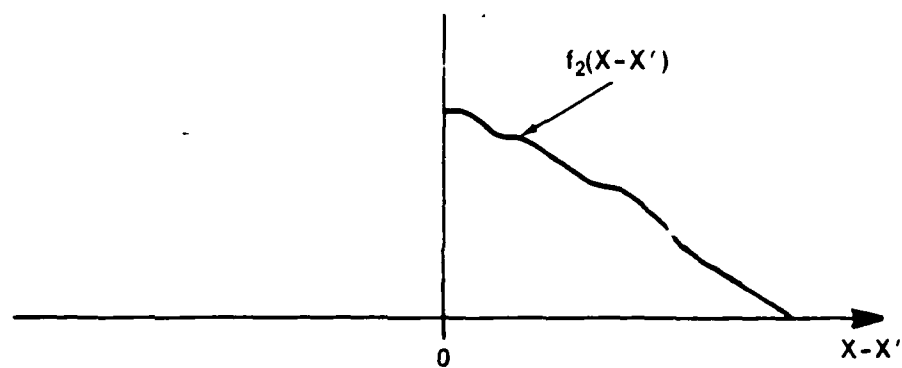


Figure A-2. Transformation of $f_2(x)$ to $f_1(x)$

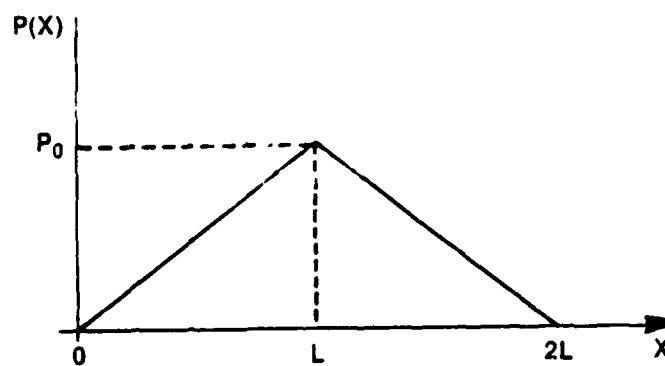


Figure A-3. Special Case - Triangular Blocked Pressure Distribution

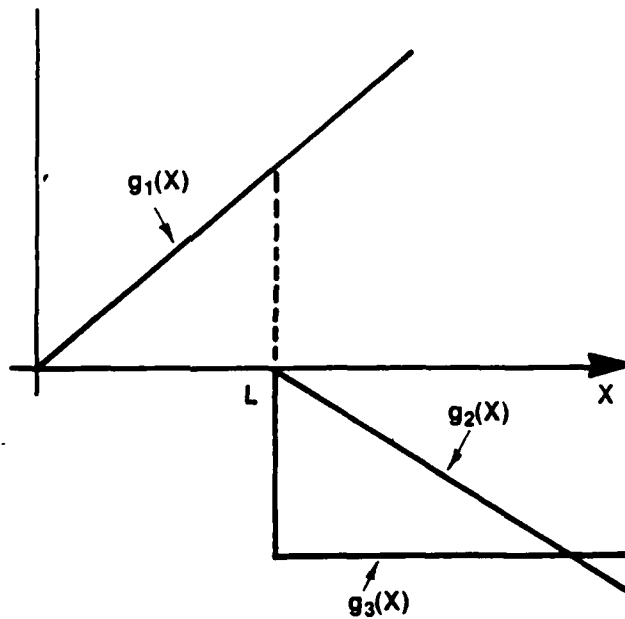
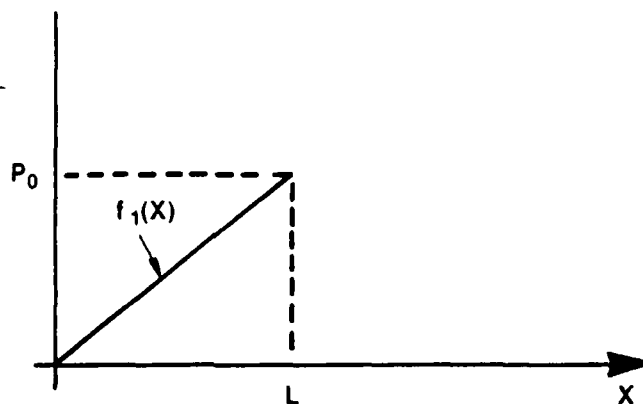


Figure A-4. Representation of $f_1(x)$

APPENDIX B

EXPERIMENTAL EQUIPMENT

Table B-1. List of Instrumentation - Phase I

Parameter	Instrumentation - Model and Description
Wall Pressure	Acoustic Research Corporation - Model LD-107 M2 Hydrophones Sensitivity: -210 dB re 1V/ μ Pa
Acceleration	Endevco - Model 2220 C Accelerometer Charge Sensitivity: 2.7 pC/g
Signal Conditioning for Hydrophones	Ithaco - Model P 14 Power Supply Ithaco - Model 455 Amplifiers, 10 Hz low frequency rolloff
Recording	Honeywell - Model 5600 B 14-Channel Recorder
Temperature	Honeywell - Model UDC 500 Universal Digital Controller, reading $\pm 0.1^\circ$
Pressure	Meriam Mercury Manometers large pressure differential - 120-in. manometer Reading ± 0.05 in. of Hg small pressure differential - 40-in. manometer Reading ± 0.01 in. of Hg
Frequency Analyses and Correlation	Nicolet - Model 660 B Dual-Channel FFT Spectrum Analyzer and Spectral Dynamics - Model SD-375 Dynamic Analyzer

Table B-2. List of Instrumentation - Phase II

Parameter	Instrumentation - Model and Description
Wall Pressure	Wilcoxon Research - Model H506-A Hydrophones Sensitivity: -210 dB re 1 V/ μ Pa
Acceleration	Endevco - Model 220 C Accelerometers Charge Sensitivity: 2.7 pC/g
Signal Conditioning for Hydrophones	Ectron - Model 563F Transducer Conditioners
Signal Conditioning for Accelerometers	Ithaco - Model 461 and 461M Charge Amplifiers
Recording	Honeywell - Model 5600 E 14-Channel Recorder
Digital Data Acquisition and Reduction	MASSCOMP 5500 Computer
Velocity (Axial and Radial Components)	TSI System Model 9100-11 3-beam, 2-Component Laser Doppler Velocimeter (LDV)
Flow Rate	Foxboro Model M/2800 Magnetic Flow Meter
Temperature	Cole Parmer - Model 8502-45 Fahrenheit Thermometer
Pressure	Kulite - Model XTM-190-100 Pressure Transducers
Frequency Analyses and Correlation	Nicolet - Model 660 B Dual-Channel FFT Spectrum Analyzer and B & K Model 2034 Frequency Analyzer

APPENDIX C

LDV DATA ACQUISITION AND REDUCTION

1. Instrumentation and Test Procedure

The TSI System 9100-11 is a three-beam, two-component laser Doppler velocimeter (LDV). The LDV system employed in this study used the dual-beam optics concept. It was configured for measurements of the axial and radial velocity components in the plexiglass test section. The setup was based on the system presented by Arnold et al. (1985). In the present study the LDV system was operated in a forward scatter mode, which resulted in much higher data rates. A detailed description of the LDV system is documented by Lefebvre (1987).

The arrangement of the LDV optics and laser are shown in figure C-1. The major components consisted of a Lexel 2-watt, argon-ion laser, which emitted a green beam having a wavelength of 514.5 nanometers; beam splitters to separate the beam from the laser into three separate beams all in the same plane; and two acousto-optic Bragg cells for frequency shifting the two outer beams. In addition, it had a 10-cm diameter focusing lens; a 5-cm diameter receiving lens; two photomultipliers; and two counter-type signal processors. The laser and optics were mounted on a traversing mechanism, which had a readability of 0.001 cm.

The two outer beams were frequency shifted by the Bragg cells. The top beam was shifted by 60 MHz and the bottom beam was shifted by 40 MHz. At the measurement point, the two outer beams and the center beam combined to form the fringe pattern. The measuring volume for this LDV system was 0.93 mm long in the radial direction by 0.161 mm high. The distance between fringes d_f is related to the half angle between the two outer beams $\phi/2$ and the wavelength of the laser light λ . The axial

velocity component u is perpendicular to the fringe pattern, and was obtained by measuring the frequency of scattered light generated by particles in the flow as they move past the fringes. The instantaneous axial velocity u was then calculated by the relationship $u = f_D \cdot d_f$, where f_D is the scattering or Doppler frequency seen by the laser counter processor minus the shift frequency.

During the measurement, the scattered light was detected in a forward scatter mode by the photomultiplier located behind the receiving lens. The signal from the photomultiplier was then filtered to separate the 100-MHz shifted axial velocity component signal from the 20-MHz shifted radial velocity component signal. Both signals were then processed separately by the counter-signal processors.

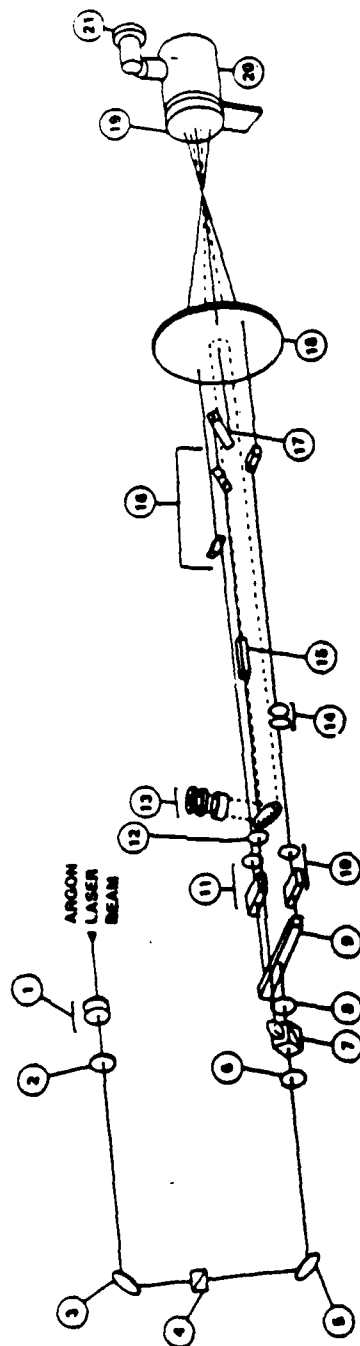
2. Data Acquisition and Reduction

The counter-signal processors provided a signal on output whenever valid data had been acquired and latched on to the processors' digital output buffers. A special electronic interface was used to link the processors and the MASSCOMP data acquisition system. This interface accepted the velocity data from each of the two counters and provided three output latch buffers or ports for three velocities. The first output port contained the axial velocity component updated at each data-ready signal. The remaining two ports were for the values of axial and radial velocity only when the data-ready signal from each processor was obtained within a time window that was user-selectable on the interface. These last two values are referred to as coincident velocity, i.e., u and v data measured simultaneously.

The alignment of the center beam was accomplished by using a TSI model 10925 calibrator. During the calibration, the focal point of the

three beams was positioned on the rubber scattering surface of the calibrator.

For velocity measurements, the traversing mechanism was traversed across the pipe in the direction of the center beam and always on the horizontal plane of the test section. Digital data of the axial velocity and radial velocity components were acquired by the MASSCOMP data acquisition system. The data were sampled at 10 kHz for 9 seconds. Simultaneously, analog data from hydrophones and accelerometers were also acquired. Computer programs were developed to reduce the digital data and preprocess the data for further data analyses and correlations using the Interactive Laboratory System (ILS) signal analysis software package (Signal Technology, 1986). Based on measurement accuracy of the LDV system and error analysis, the overall accuracy of the LDV measurements was estimated to be ± 1.0 percent for the axial velocity and ± 3.0 percent for the radial velocity.



ITEM	TM MODEL	DESCRIPTION
12	9182-12	POLARIZATION ROTATOR
13	9148, 9162	RECEIVING OPTICS
14	9175	BEAM STEEPER
15	9226	BEAM ANGLE ADJUSTER
16	9097	BEAM SHIFTER
17	9086	BEAM SHIFTER
18	9188-360	FOCUSING LENS
19	9118-360	RECEIVING LENS
20	9148	RECEIVING OPTICS
21	9162	PHOTO MULTIPLIER

ITEM	TM MODEL	DESCRIPTION
1	9189	COLLIMATOR
2	9181	POLARIZATION ROTATOR
3	9187	MIRROR
4	9128	ATTENUATOR
5	9187	MIRROR
6	9182-12	POLARIZATION ROTATOR
7	9216-1	BEAM SPLITTER
8	9182-12	POLARIZATION ROTATOR
9	9116-1	BEAM SPLITTER
10	9282-12	60 MHz BRAGG CELL
11	9182-12	60 MHz BRAGG CELL

Figure C-1. Schematic of Laser Doppler Velocimeter

APPENDIX D

SUMMARY OF FLOW CALCULATIONS USING THE K AND ϵ MODEL

The flow field of the confined jets and pipe flow was calculated using a two-dimensional, generalized computer program "Semi-Implicit Method for Pressure-Linked Equations (SIMPLE)." The procedure used in the computer program SIMPLE allows the solution of elliptic partial differential equations of the form:

$$\frac{\partial}{\partial t} (\rho \phi) + \text{DIV} (\rho \mathbf{u} \phi) = \text{DIV} (\Gamma_{\phi} \text{GRAD } \phi) + S_{\phi}, \quad (\text{D-1})$$

where the first, second, third, and fourth terms are the unsteady, convection, diffusion, and source terms, respectively. The variable ϕ is the flow parameter of interest. In fluid flow problems, ϕ usually represents the velocities or energy parameter, such as temperature, kinetic energy and dissipation. Equation (D-1) is solved with the necessary source term S_{ϕ} and flow boundary condition. A detailed discussion of the method SIMPLE is contained in Patankar (1979).

In the analysis, the governing equations are conservation of mass and momentum, and energy equation. For turbulent flows, the averaged form of the Navier-Stokes equation is used. The averaged form of the Navier-Stokes equation is similar to the momentum equation, with the exception that an additional term - Reynolds stress is introduced.

Turbulence Model

In overcoming the closure problem, additional transport equations are required to relate the Reynolds stress term. A popular approach to

this problem is the two-equation (K and ϵ) model. The Reynolds stress relates to the turbulence energy and dissipation via the turbulent viscosity μ_t . The turbulence energy K is given by

$$\rho \frac{DK}{Dt} = \frac{\partial}{\partial x_i} \left[\frac{\mu_t}{\sigma_k} \frac{\partial K}{\partial x_j} \right] + \mu_t \left[\frac{\partial u_i}{\partial x_j} + \frac{\partial u_j}{\partial x_i} \right] \frac{\partial u_i}{\partial x_j} - \rho \epsilon. \quad (D-2)$$

Similarly, the energy dissipation ϵ is expressed by

$$\rho \frac{D\epsilon}{Dt} = \frac{\partial}{\partial x_i} \left[\frac{\mu_t}{\sigma_\epsilon} \frac{\partial \epsilon}{\partial x_j} \right] + C_1 \frac{\epsilon}{K} - \mu_t \left[\frac{\partial u_i}{\partial x_j} + \frac{\partial u_j}{\partial x_i} \right] \frac{\partial u_i}{\partial x_j} - C_2 \frac{\rho \epsilon^2}{K}, \quad (D-3)$$

where C_1 and C_2 are constants which are determined experimentally. A detailed discussion of the K and ϵ model is provided by Jones and Launder (1972).

In the problem formulation, it is assumed that the jet and pipe flows are steady and axisymmetric (i.e., flow parameters depend on r and x). In addition, the fluid is incompressible ($\rho = \text{constant}$) and flows at constant temperature (isothermal flow).

Accordingly, the averaged Navier-Stokes equation can be written as:
In the radial, r direction

$$\begin{aligned} V_r \frac{\partial V_r}{\partial r} + V_x \frac{\partial V_r}{\partial x} = - \frac{1}{\rho} \frac{\partial p}{\partial r} + \nu \left[\frac{\partial^2 V_r}{\partial r^2} + \frac{1}{r} \frac{\partial V_r}{\partial r} - \frac{V_r}{r^2} + \frac{\partial^2 V_r}{\partial x^2} \right] \\ - \left[\frac{\partial}{\partial r} \overline{V_r'^2} + \frac{\partial}{\partial x} \overline{V_r' V_x'} + \frac{1}{r} \overline{V_r'^2} \right]; \end{aligned} \quad (D-4)$$

In the axial, x direction

$$v_r \frac{\partial v_x}{\partial r} + v_x \frac{\partial v_x}{\partial x} = - \frac{1}{\rho} \frac{\partial p}{\partial x} + \nu \left[\frac{\partial^2 v_x}{\partial r^2} + \frac{1}{r} \frac{\partial v_x}{\partial r} + \frac{\partial^2 v_x}{\partial x^2} \right]$$

$$- \left[\frac{\partial}{\partial r} v'_r v'_x + \frac{\partial}{\partial x} v'^2_x + \frac{1}{r} v'_r v'_x \right] . \quad (D-5)$$

The continuity equation is

$$\frac{\partial}{\partial r} (r v_r) + \frac{\partial}{\partial x} (r v_x) = 0 . \quad (D-6)$$

As expressed in equation (D-1), the flow parameter ϕ , diffusivity constant Γ_ϕ , and source term S_ϕ can be summarized as follows:

Equation	ϕ	Γ_ϕ	S_ϕ
Continuity	1	0	0
Navier-Stokes r:	V_r	μ_t	$\frac{\partial}{\partial x} \left[\mu_t \frac{\partial V_r}{\partial x} \right] + \frac{1}{r} \frac{\partial}{\partial r} \left[\mu_t r \frac{\partial V_r}{\partial r} \right] - \mu_t V_r / r^2$
Navier-Stokes x:	V_x	μ_t	$\frac{\partial}{\partial x} \left[\mu_t \frac{\partial V_x}{\partial x} \right] + \frac{1}{r} \frac{\partial}{\partial r} \left[\mu_t r \frac{\partial V_x}{\partial r} \right]$
Turbulence Energy,	K	μ_t / σ_k	$G - \rho \epsilon$
Energy Dissipation	ϵ	μ_t / σ_ϵ	$[C_1 G - C_2 \rho \epsilon] \epsilon / K$

where:

$$G = \mu_t \left[\frac{\partial u_i}{\partial x_j} + \frac{\partial u_j}{\partial x_i} \right] \frac{\partial u_i}{\partial x_j},$$

$C_1 = 1.44$, $C_2 = 1.92$, $\sigma_k = 0.9$, and $\sigma_\epsilon = 1.3$.

Additional equations, such as the turbulent viscosity, and the law of the wall were utilized in the computation and are summarized as follows:

$$K = 0.005 U^2$$

$$\epsilon = 0.1 K^2$$

$$\mu_t = C_\mu \rho K^2 / \epsilon, \quad C_\mu = 0.09$$

$$y^+ = \rho K^{0.5} (C_\mu)^{0.25} y / \mu$$

$$U^+ = 2.5 \ln (9y^+)$$

Detailed description of the computer program - SIMPLE, data inputs/outputs, and results from the computations are documented by Ng (1986).

BIBLIOGRAPHY

- Abdallah, S. A., "On the Wall Pressure Fluctuations and the Flow Field Structure Distal to a Modeled Stenosis," Ph.D. Thesis, University of Houston, 1984.
- Abramowitz, M. and Stegun, I. A., "Handbook of Mathematical Functions with Formulas, Graphs, and Mathematical Tables," National Bureau of Standards, 1964.
- Acton, E., "A Modelling of Large Eddies in An Axisymmetric Jet," J. Fluid Mech., vol. 98, 1980, pp. 1-31.
- Ahuja, K. K. and Blakney, D. F., "Tone Excited Jets, Part IV: Acoustic Measurements," J. Sound Vib., vol 102(1), 1985, pp. 93-117.
- Ahuja, K. K. and Whiffen, M. C., "Tone Excited Jets, Part II: Flow Visualization," J. Sound Vib., vol 102(1), 1985, pp. 63-69.
- Arnold, U., Stein, U., and Pasche, E., "First Experience with an On-Axis LDV-System in Spectral Applications to Open-Channel Flow," Proceedings of the Symposium on Laser Anemometry, 1985 ASME Winter Annual Meeting, November 1985.
- Au-Yang, M. K., "Dynamics of Coupled Fluid-Shells," J. of Vibration, Acoustics, Stress and Reliability in Design, vol. 108, 1986, pp.339-347.
- Bakevell, H. P., Carey, G. F., Libuha, J. J., Schloemer, H. H., and Von Winkle, W. A., "Wall Pressure Correlations in Turbulent Pipe Flow," USL Report 559, Navy Underwater Sound Laboratory, New London, CT, 20 August 1962.
- Bennett, J. C., Wagner, C. A., and Brondum, D. C., "A Model for Effects of Large-Scale Motion on Coaxial Jet Development," AIAA Paper 87-0380, Reno, Nevada, 1987.

- Blake, W. K., Mechanics of Flow-Induced Sound and Vibration, vol. 1 and 2, Academic Press, 1986.
- Blake, W. K. and Chase, D. M., "Wavenumber-Frequency Spectra of Turbulent-Boundary Layer Pressure Measured by Microphone Arrays," J. Acoust. Soc. Am., vol. 49(3), 1971, pp. 862-877.
- Bleich, H. H. and Baron, M. L., "Free and Forced Vibrations of an Infinitely Long Cylindrical Shell in an Infinite Acoustic Medium," J. Appl. Mech., 1954, pp. 167-177.
- Bradbury, L. J. S., et al., Turbulent Shear Flows 2 - Part IV: Coherent Structures, Springer-Verlag, 1980.
- Bradshaw, P., "Inactive Motion and Pressure Fluctuations in Turbulent Boundary Layers," NPL Aero. Report 1172, 1965.
- Bradshaw, P., "Turbulence in the Noise Producing Region of a Circular Jet," J. Fluid Mech., 1964, pp. 591-624.
- Brunn, H. H., "A Time-Domain Analysis of the Large-Scale Flow Structure in a Circular Jet, Part 1: Moderate Reynolds Number," J. Fluid Mech., vol. 83, 1977, pp. 641-671.
- Bull, M. K. and Agarwal, N. K., "The Mechanism of Pipe-Flow Noise Generation Due to Internal Flow Separation," Proceedings of 1984 International Conference on Noise Control Engineering, December 1984, pp. 261-264.
- Bull, M. K. and Norton, M. P., "The Proximity of Coincidence and Acoustic Cut-Off Frequencies in Relation to Acoustic Radiation from Pipes with Disturbed Internal Turbulent Flow," J. Sound Vib., vol. 69(1), 1980, pp. 1-11.
- Carey, G. F., Chlupsa, J. E. and Schloemer, H. H., "Acoustic Turbulent Water-Flow Tunnel," J. Acoust. Soc. Am., vol. 41, 1967, pp. 373-379.
- Chan, W. T. and Ko, N. W. M., "Coherent Structures in the Outer Mixing

- Region of Annular Jets," J. Fluid Mech., vol. 99, 1978, pp.515-533.
- Chase, D. M., "Modeling the Wavevector-Frequency Spectrum of Turbulent Boundary Layer Wall Pressure," J. Sound Vib., vol. 70, 1986, pp. 29-67.
- Clinch, J. M., "Measurements of the Wall Pressure Field at the Surface of a Smooth-walled Pipe Containing Turbulent Water Flow," J. Sound Vib., vol. 9, 1969, pp. 398-419.
- Clinch, J. M., "Prediction and Measurement of the Vibrations Induced in Thin-walled Pipes by the Passage of Internal Turbulent Water Flow," J. Sound Vib., vol. 12(4), 1970, pp. 429-451.
- Corcos, G. M., "The Resolution of Turbulent Pressures at the Wall of a Boundary Layer," J. Sound Vib., vol. 6, 1967, pp. 59-70.
- Crow, S. C., "Acoustic Gain of a Turbulent Jet," American Physics Society Meeting, University of Colorado, Boulder, Paper IE-6, 1972.
- Crow, S. C. and Champagne, F. H., "Orderly Structures in Jet Turbulence," J. Fluid Mech., vol. 48(3), 1971, pp. 547-591.
- Danilov, S. D. and Mironov, M. A., "Excitation of Axisymmetric Waves in a Thin Cylindrical Shell Filled with Fluid," Akust, Zh, 32, May-Jun 1986, pp. 387-389.
- Davies, P. O. A. L., Fisher, M. J. and Barratt, M. J., "The Characteristics of the Turbulence in the Mixing Region of a Round Jet," J. Fluid Mech., vol. 15, 1963, pp. 337-366.
- Dinkelacker, A., "Preliminary Experiments on the Influence of Flexible Walls on Boundary Layer Turbulence," J. Sound Vib., vol. 4, 1966, pp. 187-214.
- Dowling, A. P., "Flow-Acoustic Interaction Near a Flexible Wall," J. Fluid Mech., vol. 128, 1983, pp. 181-198.
- Drain, L. E., The Laser Doppler Technique, John Wiley & Sons, 1980.

- Durst, F., Melling, A. and Whitelaw, J. H., Principles and Practice of Laser-Doppler Anemometry, 2nd Edition, Academic Press, 1981.
- Dyer, I., "Measurement of Noise Sources in Ducts," J. Acoust. Soc. Am., vol. 30, no. 9, 1958, pp.833-841.
- Fagerlund, A. C., "A Theoretical and Experimental Investigation of the Effects of the Interaction between an Acoustic Field and Cylindrical Structure on Sound Transmission Loss," Ph.D. Thesis, University of Iowa, 1979.
- Fahy, F. J., "Response of a Cylinder to Random Sound in the Contained Fluid," J. Sound Vib., vol. 13(2), 1970, pp. 171-194.
- Fahy, F. J., Sound and Structural Vibration - Radiation, Transmission and Response, Academic Press, 1985.
- Farabee, T. M. and Casarella, M. J., "Measurements of Fluctuating Wall Pressure for Separated/Reattached Boundary Layer Flows," J. of Vibration, Acoustics, Stress, and Reliability in Design, vol. 108, 1986, pp. 301-307.
- Ffowcs Williams, J. E., "Boundary-Layer Pressures and the Corcos Model: A Development to Incorporate Low-Wavenumber Constraints," J. Fluid Mech., vol. 125, 1982, pp.9-25.
- Ffowcs Williams, J. E., "The Noise from Turbulence Convected at High Speed," Phil. Trans. Roy. Soc. Lond., ser A255: 1963, pp. 469-503.
- Ffowcs Williams, J. E. and Kempton, A. J., "The Noise from the Large-Scale Structure of a Jet," J. Fluid Mech., vol. 84, Part 4, 1978, pp. 673-694.
- Fuller, C. R., "Axisymmetric Wave Transmission Through Wall Thickness Discontinuities in Fluid-Filled Cylindrical Shells," Southampton University, Institute of Sound and Vibration Research, Report ISVR-TR-117, March 1981.

- Fuller, C. R. and Fahy, F. J., "Characteristics of Wave Propagation and Energy Distributions in Cylindrical Elastic Shells Filled with Fluid," J. Sound Vib., vol. 81, 1982, pp. 501-518.
- Fuller, C. R., "The Mobility of An Infinite Circular Cylindrical Elastic Shell Filled With Fluid," J. Sound Vib., vol. 87, 1983, pp. 409-427.
- Fuller, C. R., "Monopole Excitation of Vibrations in An Infinite Cylindrical Elastic Shell Filled With Fluid," J. Sound Vib., vol. 96, 1984, pp. 101-110.
- Fuller, C. R., "Radiation of Sound from An Infinite Cylindrical Elastic Shell Excited by An Internal Monopole Source," J. Sound Vib., vol. 109, 1986, pp. 259-275.
- Gatski, T. B. and Liu, J. T. C., "On the Interactions Between Large-Scale Structure and Fine-Grained Turbulence in a Free Shear Flow, III. A Numerical Solution," Phil. Trans. Roy. Soc. Lond., vol. 293, 1980, pp. 473-509.
- Gazis, D. C., "Exact Analysis of the Plane-Strain Vibrations of Thick-Walled Hollow Cylinders," J. Acoust. Soc. Am., vol. 30, No. 8, 1958, pp. 786-794.
- Geib, F. E., "Measurements on the Effects of Transducer Size on the Resolution of Boundary-Layer Pressure Fluctuations," J. Acoust. Soc. Am., vol. 46, 1969, pp. 253-261.
- Gilchrist, R. B. and Strawderman, W. A., "Experimental Hydrophone-Size Correction Factor for Boundary Pressure Fluctuations," J. Acoust. Soc. Am., vol. 38, 1965, pp. 298-302.
- Greenspon, J. E., "Vibrations of Thick and Thin Cylindrical Shells Surrounded by Water," J. Acoust. Soc. Am., vol. 33, no. 10, 1961, pp. 1321-1328.
- Greenspon, J. E., "Axially Symmetric Vibrations of a Thick Cylindrical

- Shell in an Acoustic Medium," J. Acoust. Soc. Am., vol. 32, no. 8, 1960, pp. 1017-1025.
- Haddle, G. P. and Skudrzyk, E. J., "The Physics of Flow Noise," J. Acoust. Soc. Am., vol. 46, no. 1, 1969, pp. 130-157.
- Hinze, J. O., Turbulence, McGraw Hill Book Co., 2nd edition, 1975, p. 513.
- Ho, C. M. and Nasseir, N. S., "Dynamics of an Impinging Jet, Part 1: The Feedback Phenomenon," J. Fluid Mech., vol. 105, 1981, pp. 119-142.
- Ho, C. M. and Huang, L. S., "Subharmonics and Vortex Merging in Mixing Layers," J. Fluid Mech., vol. 119, 1982, pp. 443-473.
- Hooper, J. D. and Rehme, K., "Large-Scale Structural Effects in Developed Turbulent Flow Through Closely-Spaced Rod Arrays," J. Fluid Mech., vol. 145, 1984, pp. 305-337.
- Hsu, J. C. and Clifton, R. J., "Waves in a Thin-Walled Tube due to Sudden Release of a Radial Ring Pressure," J. Acoust. Soc. Am., vol. 50, no. 1, 1971, pp. 230-240.
- Hussain, A. K. M. F., "Coherent Structures and Studies of Perturbed and Unperturbed Jets," Lecture Notes in Physics, vol. 136, 1980, pp. 252-291.
- James, J. H., "Computation of Acoustic Power, Vibration Response and Acoustic Pressures of Fluid-Filled Pipes," Admiralty Marine Technology Establishment, Teddington, AMTE Report TM82036, May 1982.
- Johnson, B. V. and Bennett, J. C., "Mass and Momentum Turbulent Transport Experiments with Confined Coaxial Jets," NASA Contractor Report, CR-165574, UTRC Report R81-915540-9, 1981.
- Jones, I. S. F., "Fluctuating Turbulent Stresses in the Noise-Producing Region of a Jet," J. Fluid. Mech., vol. 36, 1969, pp. 529-543.
- Jones, W. P. and Launder, B. E., "The Prediction of Laminarization with

- a Two-Equation Model of Turbulence," J. of Heat and Mass Transfer, vol. 15, 1972, pp. 301-314.
- Junger, M. C., "The Physical Interpretation of the Expression for an Outgoing Wave in Cylindrical Coordinates," J. Acoust. Soc. Am., vol. 25, no. 1, 1953, pp. 40-47.
- Junger, M. C., "Vibrations of Elastic Shells in a Fluid Medium and the Associated Radiation of Sound," J. App. Mech., vol. 19(4), 1952, pp. 439-445.
- Junger, M. C. and Feit, D., Sound Structures and Their Interaction, MIT Press, 2nd edition, 1986.
- Karvelis, A. V. and Reethof, G., "A Cross Correlation Technique for Investigating Internal Flow Noise," ASME Noise and Fluids Engineering, 1977, pp. 153-160.
- Keith, W. L. and Tourish J. P., "Hydrodynamic Characteristics of the Rectangular Test Section in the NUSC/NL Water Tunnel," Technical Report 8017, Naval Underwater Systems Center, New London, CT, August 1987.
- Keltie, R. F., "The Effects of Hydrostatic Pressure Fields on the Structural and Acoustic Response of Cylindrical Shells," J. Acoust. Soc. Am., vol 79(3), 1986, pp. 595-603.
- Kerschen, E. J. and Johnston, J. P., "Modal Content of Noise Generated by a Coaxial Jet in a Pipe," J. Sound Vib., vol. 76(1), 1981, pp. 95-115.
- Kerschen, E. J. and Johnston, J. P., "A Modal Separation Measurement Technique for Broadband Noise Propagating Inside Circular Ducts," J. Sound Vib., vol. 76(4), 1981, pp. 499-515.
- Kibens, V., "Discrete Noise Spectrum Generated by an Acoustically Excited Jet," AIAA Journal, vol. 18, no. 4, 1979, pp. 434-441.

- Kinsler, L. E. and Frey, A. R., Fundamentals Of Acoustics, 2nd Edition, John Wiley & Sons, Inc., 1962.
- Kline, S. J., Reynolds, W. C., Schraub, F. A., and Runstadler, P. W., "The Structure of Turbulent Boundary Layers," J. Fluid Mech., vol. 30, 1967, pp. 741-773.
- Ko, N. W. M. and Lam, K. M., "Flow Structures of a Basic Annular Jet," AIAA Journal, vol. 23, 1985, pp. 1185-1190.
- Kovaszny, L. S. G., Kibens, V. and Blackwelder, R. F., "Large Scale Motion in the Intermittent Region of a Turbulent Boundary Layer," J. Fluid Mech., 1970, pp. 283-325.
- Kraus, H., Thin Elastic Shells, John Wiley & Sons, Inc., 1967.
- Krothapalli, A., Baganoff, D. and Karamcheti, K., "Partially Confined Multiple Jet Mixing," AIAA Journal, vol. 19, no. 3, 1981, pp. 324-328.
- Kumar, R., "Dispersion of Axially Symmetric Waves in Empty and Fluid-Filled Cylindrical Shells," Acustica, vol. 27, 1972, pp. 317-327.
- Lam, K. M. and Ko, N. W. M., "Investigation of Flow Structures of a Basic Annular Jet," AIAA Journal, vol. 24, 1986, pp. 1488-1493.
- Laufer, J., "The Structure of Turbulence in Fully Developed Pipe Flow," NACA Report 1174, 1952.
- Laufer, J., "On the Generation of Jet Noise," AGARD, 1973.
- Lefebvre, P. J., "Characterization of Accelerating Pipe Flow," Ph.D. Thesis, University of Rhode Island, 1987.
- Leissa, A. W., "Vibration of Shells," NASA SP-288, 1973.
- Lepicovsky, J., Ahuja, K. K. and Burrin, R. H., "Tone Excited Jets, Part III: Flow Measurements," J. Sound Vib., vol. 102(1), 1985, pp. 71-91.

- Li, D., "Mechanical and Flow Excited Vibrations of Elastic Plate and Cylindrical Shells in Dense Fluids," Ph.D. Thesis, University of Rhode Island, 1986.
- Lighthill, M. J., "On Sound Generated Aerodynamically, I-General Theory," Proc. Roy. Soc. Lond., ser A211, 1952, pp. 564-587.
- Liu, J. T. C., "Development of Large Scale Wavelike Eddies and the Near Field Jet Noise," J. Fluid Mech., 1974, pp. 437-464.
- Loh, H. T., "Circular Pipe Wall Vibratory Response Excited by Internal Acoustic Fields," M.S. Thesis, Penn State University, 1981.
- Long, D. F. and Arndt, R. E. A., "Jet Noise at Low Reynolds Number," AIAA Journal, vol. 22, no. 2, 1984, pp. 187-193.
- Maidanik, G., "Flush-mounted Pressure Transducer Systems as Spatial and Spectral Filters," J. Acoust. Soc. Am., vol. 42, 1967, pp. 1017-1024.
- Mankbadi, R. and Liu, J. T. C., "A Study of the Interactions Between Large-Scale Coherent Structures and Fine-Grained Turbulence in a Round Jet," Phil. Trans. Roy. Soc. of Lond., vol. 298, January 1981, pp. 541-602.
- Meecham, W. C. and Ford, G. W., "Acoustic Radiation from Isotropic Turbulence," J. Acoust. Soc. Am., vol. 30, 1958, pp. 318-322.
- Merkine, L. O., "Problems in Non-linear Mechanic of Unstable Waves in Turbulent and Stratified Shear Flows, Part I: Development of the Noise Producing Large-Scale Structure in a Turbulent Jet," Ph.D. Thesis, Brown University, 1974.
- Moodie, T. B. and Haddow, J. B., "Dispersive Effects in Wave Propagation in Thin-Walled Elastic Tubes," J. Acoust. Soc. Am., vol. 64(2), 1978, pp. 522-528.
- Moore, C. J., "The Role of Shear-Layer Instability Waves in Jet Exhaust

- Noise," J. Fluid Mech., vol. 80, 1977, pp. 321-367.
- Morse, P. M. and Ingard, K. U., Theoretical Acoustics, McGraw Hill Book Co., 1968.
- Ng, K. W., "Aerodynamic Noise Generation in Control Valves," ASME Paper 80-WA/NC-8, 1980.
- Ng, K. W. and Sonderegger, H. R., "Hydrodynamic Noise Generation in Control Valves," Proceedings of 1982 International Conference on Noise Control Engineering, May 1982, pp. 91-94.
- Ng, K. W., "Calculation of Turbulent Jet Flows," Technical Memorandum 86-2035, Naval Underwater Systems Center, Newport, RI, June 1986.
- Norton, M. P. and Bull, M. K., "Mechanisms of the Generation of External Acoustic Radiation from Pipes due to Internal Flow Disturbances," J. Sound Vib., vol. 94(1), 1984, pp. 105-146.
- Norton, M. P. and Greenhalgh, R., "On the Estimation of Loss Factors in Lightly Damped Pipeline Systems: Some Measurement Techniques and Their Limitations," J. Sound Vib., vol. 105(3), 1986, pp. 397-423.
- Numachi, F., Yamabe, M. and Oba, R., "Cavitation Effect on the Discharge Coefficient of the Sharp-Edged Orifice Plate," ASME Journal of Basic Engineering, March 1960, pp. 1-11.
- Oba, R., Ito, Y. and Uranishi, K., "Effect of Polymer Additives on Cavitation Development and Noise in Water Flow Through an Orifice," ASME Journal of Fluids Engineering, vol. 100, December 1978, pp. 493-499.
- Olsen, W. A., Miles, J. H., and Dorsch, R. G., "Noise Generated by Impingement of a Jet upon a Large Flat Plate," NASA TN D-7075, 1972.
- Patankar, S. V., Numerical Heat Transfer and Fluid Flow, McGraw Hill, 1979.
- Powell, A., "On the Fatigue of Structures Due to Vibrations Excited by

- Random Pressure Fields," J. Acoust. Soc. Am., vol. 30, no. 12, 1958, pp. 1130-1135.
- Reethof, G., "Turbulence-Generated Noise I - Pipe Flow," Ann. Rev. Fluid Mech., 1978, pp. 333-367.
- Ribner, H. S., "The Generation of Sound by Turbulent Jets," Advances in Applied Mechanics, Academic Press, New York and London, 1964, pp. 103-182.
- Rijnja, H. A. J., "Flow Noise" Report No. PHL 1981-28, Physics Lab TNO, 1981.
- Roshko, A., "Structure of Turbulent Shear Flows: A New Look," AIAA Journal, vol. 14, no. 10, 1976, pp. 1349-1357.
- Rubinow, S. L. and Keller, J. B., "Wave Propagation in a Viscoelastic Tube containing a Viscous Fluid," J. Fluid Mech., vol. 88, part 1, 1978, pp. 181-203.
- Sarohia, V. and Massier, P.F., "Experimental Results of Large-Scale Structures in Jet Flows and Their Relation to Jet Noise Production," AIAA Journal, vol. 16, August 1978, pp. 831-835.
- Schloemer, H. H., "Installation of a Rectangular Test Section for Acoustic Water Tunnel Studies of Flow-Induced Noise," Technical Report 4763, Naval Underwater Systems Center, New London, CT, 1974.
- Signal Technology Inc., "ILS User's Guide V5.0," 1986.
- Skudrzyk, E., Simple and Complex Vibratory Systems, Penn State University Press, 1968.
- Stahl, B., "An Experimental Investigation of Noise Generated by Turbulence in a Pipe Flow Behind a Discontinuous Area Enlargement," DFVLR, Dissertation (D. of Eng.), November 1985.
- Stahl, B. and Arguello, G., "An Experimental Investigation of Noise Generation and Noise Reduction in a Pipe Flow Behind a Discontinuous

Area Enlargement," DFVLR, 1986.

Stepanishen, P. R., "Modal Coupling in the Vibration of Fluid-loaded Cylindrical Shells," J. Acoust. Soc. Am., vol. 71, 1982, pp. 813-823.

Tam, C. K. W., "Tone Excited Jets, Part V: A Theoretical Model and Comparison with Experiment," J. Sound Vib., vol. 102(1), 1985, pp. 119-151.

Tang, S. C., "Response of Viscoelastic Cylindrical Shells to Moving Loads," J. Acoust. Soc. Am., vol. 40, 1966, pp. 793-800.

Tanna, H. K. and Ahuja, K. K., "Tone Excited Jets, Part I: Introduction," J. Sound Vib., vol. 102(1), 1985, pp. 57-61.

Thomas, A. S. W. and Bull, M. K., "On the Role of Wall-Pressure Fluctuations in Deterministic Motions in the Turbulent Boundary Layer," J. Fluid Mech., vol. 128, 1983, pp. 283-322.

Townsend, A. A., The Structure of Turbulent Shear Flow, Cambridge University Press, 1956.

TSI Inc., "System 9100-11 : 5 beam, 3 component Laser Doppler Velocimeter Instruction Manual," 1982.

Walter, J. L., "Coincidence of Higher Order Modes - A Mechanism of the Excitation of Cylindrical Shell Vibrations Via Internal Sound," Ph.D. Thesis, Penn State University, 1979.

Willmarth, W. W. and Wooldridge, C. E., "Measurements of the Wall Beneath a Thick Turbulent Boundary Layer," J. Fluid Mech., 1962, pp. 187-210.

Winant, C. D. and Browand, F. K., "Vortex Pairing: The Mechanism of Turbulent Mixing Layer Growth at Moderate Reynolds Number," J. Fluid Mech., 1974, pp. 237-255.

Wynanski, I. J. and Champagne, F. H., "On Transition in Pipe, Part 1.

The Origin of Puffs and Slugs and the Flow in a Turbulent Slug,"

J. Fluid Mech., 1973, pp.281-335.

Zaman, K. B. M. Q., "Flow Field and Near and Far Sound Field of a Subsonic Jet," J. Sound Vib., vol. 106, 1986, pp. 1-16.

ABBREVIATIONS USED IN BIBLIOGRAPHY

ASME - American Society of Mechanical Engineers

AIAA Journal - Journal of American Institute of Aeronautics and
Astronautics

Ann. Rev. Fluid Mech. - Annual Review of Fluid Mechanics

J. Acoust. Soc. Am. - Journal of Acoustical Society of America

J. Appl. Mech. - Journal of Applied Mechanics

J. Fluid Mech. - Journal of Fluid Mechanics

J. Sound Vib. - Journal of Sound and Vibration

Phil. Trans. Roy. Soc. Lond. - Philosophical Transactions of
the Royal Society of London

Proc. Roy. Soc. Lond.- Proceedings of the Royal Society of London

INITIAL DISTRIBUTION LIST

Addressee	No. of Copies
DTIC	12
NAVSEA (SEA-56W13 (P. Crabb), SEA-05R32 (A. Smookler), SEA-55N)	3
DTRC, Annapolis (2743)	1
DTRC, Carderock (19, 1942(Dr. T. Farabee),1942(S. Fisher))	3
ONT (233(G. Remmers))	1
CNR (OCNR-12 (Dr. R. Hansen), OCNR-1132-SM (Dr. A. Tucker), OCNR-1125-OA (M. Blizzard))	3
URI (Dr. P. Stepanishen, Dr. F. White, Dr. M. Sadd, Dr. R. Lessmann, Dr. S. Letcher, Dr. H. Viets)	6
Penn State U (Dr. G. Reethof)	1